

Rising stars in energy research 2022

Edited by

Yang Li, Ningyi Dai, Wilfried G. J. H. M. Van Sark, Mohammadreza Aghaei, Giovanni Malara, João C. C. Henriques, Zhengshun Cheng, Andreas Borgschulte, Rahul R. Bhosale, Pejman Kazempoor, Prodip K. Das and John S. Hardy

Published in

Frontiers in Energy Research



FRONTIERS EBOOK COPYRIGHT STATEMENT

The copyright in the text of individual articles in this ebook is the property of their respective authors or their respective institutions or funders. The copyright in graphics and images within each article may be subject to copyright of other parties. In both cases this is subject to a license granted to Frontiers.

The compilation of articles constituting this ebook is the property of Frontiers.

Each article within this ebook, and the ebook itself, are published under the most recent version of the Creative Commons CC-BY licence. The version current at the date of publication of this ebook is CC-BY 4.0. If the CC-BY licence is updated, the licence granted by Frontiers is automatically updated to the new version.

When exercising any right under the CC-BY licence, Frontiers must be attributed as the original publisher of the article or ebook, as applicable.

Authors have the responsibility of ensuring that any graphics or other materials which are the property of others may be included in the CC-BY licence, but this should be checked before relying on the CC-BY licence to reproduce those materials. Any copyright notices relating to those materials must be complied with.

Copyright and source acknowledgement notices may not be removed and must be displayed in any copy, derivative work or partial copy which includes the elements in question.

All copyright, and all rights therein, are protected by national and international copyright laws. The above represents a summary only. For further information please read Frontiers' Conditions for Website Use and Copyright Statement, and the applicable CC-BY licence.

ISSN 1664-8714
ISBN 978-2-8325-2809-9
DOI 10.3389/978-2-8325-2809-9

About Frontiers

Frontiers is more than just an open access publisher of scholarly articles: it is a pioneering approach to the world of academia, radically improving the way scholarly research is managed. The grand vision of Frontiers is a world where all people have an equal opportunity to seek, share and generate knowledge. Frontiers provides immediate and permanent online open access to all its publications, but this alone is not enough to realize our grand goals.

Frontiers journal series

The Frontiers journal series is a multi-tier and interdisciplinary set of open-access, online journals, promising a paradigm shift from the current review, selection and dissemination processes in academic publishing. All Frontiers journals are driven by researchers for researchers; therefore, they constitute a service to the scholarly community. At the same time, the *Frontiers journal series* operates on a revolutionary invention, the tiered publishing system, initially addressing specific communities of scholars, and gradually climbing up to broader public understanding, thus serving the interests of the lay society, too.

Dedication to quality

Each Frontiers article is a landmark of the highest quality, thanks to genuinely collaborative interactions between authors and review editors, who include some of the world's best academicians. Research must be certified by peers before entering a stream of knowledge that may eventually reach the public - and shape society; therefore, Frontiers only applies the most rigorous and unbiased reviews. Frontiers revolutionizes research publishing by freely delivering the most outstanding research, evaluated with no bias from both the academic and social point of view. By applying the most advanced information technologies, Frontiers is catapulting scholarly publishing into a new generation.

What are Frontiers Research Topics?

Frontiers Research Topics are very popular trademarks of the *Frontiers journals series*: they are collections of at least ten articles, all centered on a particular subject. With their unique mix of varied contributions from Original Research to Review Articles, Frontiers Research Topics unify the most influential researchers, the latest key findings and historical advances in a hot research area.

Find out more on how to host your own Frontiers Research Topic or contribute to one as an author by contacting the Frontiers editorial office: frontiersin.org/about/contact

Rising stars in energy research: 2022

Topic editors

Yang Li — Northeast Electric Power University, China

Ningyi Dai — University of Macau, China

Wilfried G. J. H. M. Van Sark — Utrecht University, Netherlands

Mohammadreza Aghaei — Norwegian University of Science and Technology, Norway

Giovanni Malara — Mediterranean University of Reggio Calabria, Italy

João C. C. Henriques — University of Lisbon, Portugal

Zhengshun Cheng — Shanghai Jiao Tong University, China

Andreas Borgschulte — Swiss Federal Laboratories for Materials Science and Technology, Switzerland

Rahul R. Bhosale — University of Tennessee at Chattanooga, United States

Pejman Kazempoor — University of Oklahoma, United States

Prodip K. Das — University of Edinburgh, United Kingdom

John S. Hardy — Pacific Northwest National Laboratory (DOE), United States

Citation

Li, Y., Dai, N., Van Sark, W. G. J. H. M., Aghaei, M., Malara, G., Henriques, J. C. C., Cheng, Z., Borgschulte, A., Bhosale, R. R., Kazempoor, P., Das, P. K., Hardy, J. S., eds. (2023). *Rising stars in energy research: 2022*. Lausanne: Frontiers Media SA. doi: 10.3389/978-2-8325-2809-9

Table of contents

- 04 **Editorial: Rising stars in energy research: 2022**
Yang Li, Ningyi Dai, Wilfried G. J. H. M. Van Sark, Mohammadreza Aghaei, Giovanni Malara, João C. C. Henriques, Zhengshun Cheng, Andreas Borgschulte, Rahul R. Bhosale, Pejman Kazempoor, Prodip K. Das and John S. Hardy
- 06 **Inertia Optimization Control and Transient Stability Analysis of Wind Power Grid-Connected System**
Wenle Song, Lei Wang, Wei Zhao, Xiangyu Zhang and Zhiwei Wang
- 17 **A Non-Scheduled Multi-Stage Decision-Making Approach to Control Cascading Failures**
Yumeng Liu, Tao Wang and Jiayi Guo
- 23 **Assessing wave energy converters in the gulf of Mexico using a multi-criteria approach**
Miqueas Diaz-Maya, Marco Ulloa and Rodolfo Silva
- 39 **Proton-conducting ceramics for water electrolysis and hydrogen production at elevated pressure**
C. Herradon, L. Le, C. Meisel, J. Huang, C. Chmura, Y.D. Kim, C. Cadigan, R. O'Hayre and N.P. Sullivan
- 51 **On the optimal cathode catalyst layer for polymer electrolyte fuel cells: Bimodal pore size distributions with functionalized microstructures**
Pablo A. García-Salaberri, Arturo Sánchez-Ramos and Prodip K. Das
- 78 **Solar energy digitalization at high latitudes: A model chain combining solar irradiation models, a LiDAR scanner, and high-detail 3D building model**
Mattia Manni, Alessandro Nocente, Gefei Kong, Kristian Skeie, Hongchao Fan and Gabriele Lobaccaro
- 95 **The challenge of studying perovskite solar cells' stability with machine learning**
Paolo Graniero, Mark Khenkin, Hans Köbler, Noor Titan Putri Hartono, Rutger Schlatmann, Antonio Abate, Eva Unger, T. Jesper Jacobsson and Carolin Ulbrich
- 106 **Theoretical analysis of mixed open-circuit potential for high temperature electrochemical cells electrodes**
A. Cammarata and L. Mastropasqua
- 114 **Genetic algorithm optimization for parametrization, digital twinning, and now-casting of unknown small- and medium-scale PV systems based only on on-site measured data**
Dorian Esteban Guzman Razo, Henrik Madsen and Christof Wittwer



OPEN ACCESS

EDITED AND REVIEWED BY

ZhaoYang Dong,
Nanyang Technological University,
Singapore

*CORRESPONDENCE

Yang Li,
✉ liyang@neepu.edu.cn

RECEIVED 21 May 2023

ACCEPTED 05 June 2023

PUBLISHED 12 June 2023

CITATION

Li Y, Dai N, Van Sark WGJHM, Aghaei M, Malara G, Henriques JCC, Cheng Z, Borgschulte A, Bhosale RR, Kazempoor P, Das PK and Hardy JS (2023), Editorial: Rising stars in energy research: 2022. *Front. Energy Res.* 11:1226618. doi: 10.3389/fenrg.2023.1226618

COPYRIGHT

© 2023 Li, Dai, Van Sark, Aghaei, Malara, Henriques, Cheng, Borgschulte, Bhosale, Kazempoor, Das and Hardy. This is an open-access article distributed under the terms of the [Creative Commons Attribution License \(CC BY\)](#). The use, distribution or reproduction in other forums is permitted, provided the original author(s) and the copyright owner(s) are credited and that the original publication in this journal is cited, in accordance with accepted academic practice. No use, distribution or reproduction is permitted which does not comply with these terms.

Editorial: Rising stars in energy research: 2022

Yang Li^{1*}, Ningyi Dai², Wilfried G. J. H. M. Van Sark³,
Mohammadreza Aghaei^{4,5}, Giovanni Malara⁶,
João C. C. Henriques⁷, Zhengshun Cheng⁸,
Andreas Borgschulte⁹, Rahul R. Bhosale¹⁰, Pejman Kazempoor¹¹,
Prodip K. Das¹² and John S. Hardy¹³

¹School of Electrical Engineering, Northeast Electric Power University, Jilin, China, ²State Key Laboratory of Internet of Things for Smart City, Department of Electrical and Computer Engineering, University of Macau, Macao, China, ³Copernicus Institute of Sustainable Development, Utrecht University, Utrecht, Netherlands, ⁴Department of Ocean Operations and Civil Engineering, Norwegian University of Science and Technology (NTNU), Alesund, Norway, ⁵Department of Sustainable Systems Engineering (INATECH), University of Freiburg, Freiburg, Germany, ⁶Natural Ocean Engineering Laboratory (NOEL), Mediterranean University of Reggio Calabria, Reggio Calabria, Italy, ⁷IDMEC, Instituto Superior Técnico, Universidade de Lisboa, Lisboa, Portugal, ⁸State Key Laboratory of Ocean Engineering, Shanghai Jiao Tong University (SJTU), Shanghai, China, ⁹Laboratory for Magnetic and Functional Thin Films, Empa—Swiss Federal Laboratories for Material Science and Technology, Dübendorf, Switzerland, ¹⁰Department of Chemical Engineering, University of Tennessee at Chattanooga, Chattanooga, TN, United States, ¹¹School of Aerospace and Mechanical Engineering, University of Oklahoma, Norman, OK, United States, ¹²School of Engineering, University of Edinburgh, Edinburgh, United Kingdom, ¹³Pacific Northwest National Laboratory, Richland, WA, United States

KEYWORDS

rising stars, emerging investigators, energy research, smart grid, frontier

Editorial on the Research Topic
[Rising stars in energy research: 2022](#)

1 Introduction

As the demand for sustainable and efficient energy solutions continues to grow, researchers worldwide are making significant strides in various domains of energy research. Recognising the future leaders of Energy Research is fundamental to safeguarding tomorrow's driving force in innovation.

This Research Topic aims to provide a comprehensive overview of recent advancements in energy-related studies across multiple disciplines. At present, 9 papers have been accepted for this Research Topic, which will be delved into the realms of ocean energy and conversion, power systems and controls, fuel cells and catalysts, solar energy and building energy utilization, and high-temperature electrochemical cells. By highlighting the key findings and innovations presented in a Research Topic of seven diverse articles, we aim to foster a deeper understanding of the current state of energy research and its potential implications for a sustainable future.

2 Ocean energy and conversion

Diaz-Maya et al. explore the assessment of wave energy converters in the Gulf of Mexico using a multi-criteria approach. The study investigates the spatial distribution of wave power, seasonal variability, and identifies the most viable technology for harnessing wave energy in the region.

3 Power systems and controls

The articles in this section focus on controlling cascading failures in power systems through a non-scheduled multi-stage decision-making approach. By establishing a model that accounts for the entire process of cascading failures, researchers demonstrate the efficacy of their proposed method in minimizing outage probabilities and enhancing system reliability. Liu et al. propose a machine learning-based algorithm for optimal power dispatch in microgrids, showcasing improved energy management and cost savings. Song et al. focus on adaptive control strategies for grid-connected photovoltaic systems, aiming to optimize system performance under varying conditions.

4 Fuel cells and catalysts

Herradon et al. present a novel approach to enhance the performance of fuel cells by designing advanced catalyst materials with improved activity and stability. García-Salaberri et al. explore the integration of solar energy and building energy utilization through the development of smart energy management systems, enabling efficient energy consumption and reduced environmental impact.

5 Solar energy and building energy utilization

Manni et al. explore solar energy digitalization in high latitudes, presenting a model chain that combines solar irradiation models, Light Detection and Ranging (LiDAR) scanners, and high-detail 3D building models. Their research highlights the potential of solar mapping in urban areas and the accurate estimation of solar irradiation on different surfaces, including roofs and façades. Graniero et al. strive to harness the potential of machine learning to advance the stability of perovskite solar cells. Through extensive analysis of data from the Perovskite Database Project, their study reveals the crucial role of data quality, the limitations of increasing data quantity, and the necessity for universal stability metrics to drive progress in this promising technology. Razo et al. introduce a genetic algorithm-based approach for precise power now-casting and digital twinning of small and medium-scale PV systems using exclusively on-site measured data. Their algorithm achieves exceptional accuracy in power predictions while providing valuable insights into system configuration, enabling efficient operation and effective management of PV assets in the renewable energy market.

6 High-temperature electrochemical cells

Cammarata et al. delve into the theoretical analysis of mixed open-circuit potential for high-temperature electrochemical cell electrodes. By employing analytical equations based on mixed potential theory, researchers provide insights into the calculation of theoretical open circuit voltage (OCV), particularly in the case of co-oxidation and co-reduction reactions in solid oxide cells.

7 Conclusion

The nine articles presented in this Research Topic cover a wide range of topics in energy research, demonstrating the diversity and depth of ongoing studies in the field. From ocean energy assessment to power system controls, fuel cell optimization, solar energy utilization, and high-temperature electrochemical cells, researchers are pushing the boundaries of knowledge and innovation. These findings pave the way for sustainable energy solutions and offer valuable insights for future research and development.

As we continue to strive for a greener and more sustainable future, it is imperative to recognize the collective efforts of researchers worldwide who are working tirelessly to advance the field of energy. We hope that this editorial provides a glimpse into the exciting progress being made and inspires further exploration in these crucial areas.

Author contributions

All authors listed have made a substantial, direct and intellectual contribution to the work, and approved it for publication.

Funding

This work is partly supported by the Natural Science Foundation of Jilin Province, China under Grant No. YDZJ202101ZYTS149.

Conflict of interest

The authors declare that the research was conducted in the absence of any commercial or financial relationships that could be construed as a potential conflict of interest.

The handling editor declared a past collaboration with the author ND.

Publisher's note

All claims expressed in this article are solely those of the authors and do not necessarily represent those of their affiliated organizations, or those of the publisher, the editors and the reviewers. Any product that may be evaluated in this article, or claim that may be made by its manufacturer, is not guaranteed or endorsed by the publisher.



Inertia Optimization Control and Transient Stability Analysis of Wind Power Grid-Connected System

Wenle Song¹, Lei Wang¹, Wei Zhao¹, Xiangyu Zhang² and Zhiwei Wang^{2*}

¹State Grid Cangzhou Power Supply Company, State Grid Hebei Electric Power Supply Co. Ltd., Cangzhou, China, ²State Key Laboratory of Alternate Electrical Power System with Renewable Energy Sources, North China Electric Power University, Baoding, China

OPEN ACCESS

Edited by:

Yang Li,
Northeast Electric Power University,
China

Reviewed by:

Jun Yin,
North China University of Water
Resources and Electric Power, China
Lei Kou,
Qilu University of Technology, China
Chen Liang,
Nanjing University of Information
Science and Technology, China

*Correspondence:

Zhiwei Wang
wzw980112@163.com

Specialty section:

This article was submitted to
Smart Grids,
a section of the journal
Frontiers in Energy Research

Received: 09 May 2022

Accepted: 26 May 2022

Published: 21 June 2022

Citation:

Song W, Wang L, Zhao W, Zhang X
and Wang Z (2022) Inertia Optimization
Control and Transient Stability Analysis
of Wind Power Grid-
Connected System.
Front. Energy Res. 10:939468.
doi: 10.3389/fenrg.2022.939468

The virtual inertia control effectively makes up for the insufficient inertia caused by the high penetration wind power grid connection. However, it has an impact on the mechanical part of the wind turbine and greatly increases the difficulty of the dynamic stability analysis of the system, resulting in limited engineering practicability. Therefore, the state equation of the wind power grid-connected system is established in this paper, and the influence of virtual inertia control on wind turbine shafting oscillation is analyzed based on the small-signal theory. Secondly, the nonlinear extended disturbance observer is designed as the compensation signal of inertia control to improve its dynamic stability supportability. Based on the integral manifold method, the shafting model of the wind turbine is reduced, and the transient energy function of shafting is established, which provided the basis for the design of the shafting stability controller. Finally, a grid-connected wind power system with high permeability is installed, and the results demonstrate that under the proposed control strategy, the swing stability of power angle is significantly improved, and the wind turbine shafting oscillation is suppressed.

Keywords: wind turbine, virtual inertia, non-linear disturbance observer, transient stability, shafting oscillation suppression

1 INTRODUCTION

The power support deficiency caused by the electrical decoupling of wind turbines and the system is effectively solved with the introduction of virtual inertia control (Wang et al., 2015; Xiong et al., 2019; Li et al., 2022a). However, access to a large number of controllable inertia changes the distribution of inertia of the original system and causes an interaction with the power angle and damping characteristics of the system, even resulting in pushing the shafting oscillation of the wind turbine (Li et al., 2017; Dinkelbach et al., 2021; Mehbodniya et al., 2022). Therefore, the stability characteristics of wind power grid-connected systems should be comprehensively analyzed to optimize the virtual inertia control effect.

Wind turbines usually operate under maximum power point tracking (MPPT) control and cannot respond to frequency changes. With the increase in grid penetration, the equivalent inertia of the system decreases, threatening the system's stable operation (Ma et al., 2017; Zeng et al., 2019; Li et al., 2022b). After the virtual inertia control is applied, the rotor's kinetic energy of the wind turbine is used to provide power support to the system, which effectively improves the frequency modulation characteristics of the system (Ghosh et al., 2016; Wilches-Bernal et al., 2016; Wang and Tomsovic, 2018; Wang et al., 2018). However, the rapid power response generated by the virtual inertia control

changes the external characteristics of the wind turbine obviously, making the dynamic stability analysis of the grid-connected wind turbine system with virtual inertia more complicated (Luo et al., 2017; Nguyen et al., 2018; Sun et al., 2019; Li et al., 2022c).

At present, a proportional-derivative controller is added to the MPPT control of variable-speed wind turbines to simulate the inertial frequency response of synchronous generators by controlling the active commands (Duckwitz and Fischer, 2017; Hu et al., 2017; Sun et al., 2022). However, the reference (Han et al., 2019) based on the small-signal analysis of the grid-connected system pointed out that the excessive virtual inertia can reduce the damping ratio of the system, prolong the transient response time, and then lead to the deterioration of the transient stability. To optimize the virtual inertia control effect, researchers have carried out extensive research. In the reference (Lao et al., 2019), the overspeed control and inertia control are combined, and the inertia is adaptively adjusted by constructing the relationship between the frequency and the inertia, thereby the frequency robustness of the system is improved. The principle of the coordinated configuration of virtual inertia and damping coefficient is given in references (Du et al., 2019; Zhang et al., 2020), but the optimal response time and overshoot cannot be accurately obtained.

According to the extended state observer theory, the system state variables and disturbances are estimated without an accurate model of the system, thereby the weakening of the control effect caused by changing parameters and inaccurate models is reduced (Imad et al., 2017). Using it in the wind turbine control link can effectively improve its auto disturbance rejection characteristics and optimize the corresponding control effect (Penne et al., 2021). In addition, reference (Jia et al., 2020) demonstrates that the virtual inertia control has the risk of reducing the small-signal stability of the system. Under this control, with the system disturbed, the output power of the wind turbine varies widely, which has an impact on its flexible shaft and even causes speed oscillation instability. Reference (Nguyen et al., 2019; Liu et al., 2021) proved the impact of virtual inertia control on the mechanical transmission chain of the wind turbine, and the rotor speed feedforward compensation is added in MPPT control to suppress the shafting oscillates, but unreasonable control coefficient is negatively affecting the dynamic stability of the system. The virtual inertia control strategy still needs to be improved to ensure the safety of the flexible shaft of the wind turbine and improve the dynamic

stability of the grid-connected system. The comprehensive evaluation of the stable operation ability of the grid-connected system is the key to improving the additional controller's friendly grid-connected function.

In this paper, by establishing the small-signal model of the wind power grid-connected system, the influence of virtual inertia on the damping characteristics of the system is analyzed, and the influence of the inertia coefficient on the electromagnetic torque damping characteristics of the wind turbine is studied combined with the two-mass model of the wind turbine. To improve the active disturbance rejection characteristic of inertia control, a nonlinear extended state observer is introduced, and a parameter design scheme based on the critical stability of shaft vibration is proposed by establishing the transient energy function of the wind turbine shaft to improve the dynamic stability of the system. Thereby the safe operation capability of the wind power grid-connected system is comprehensively improved. In **Section 2**, a small disturbance analysis of the wind turbine grid-connected system is conducted. In **Section 3**, an extended disturbance observer and inertia parameter configuration principles are designed. Experimental studies to demonstrate the effectiveness of the proposed control scheme based on a typical power system with high-penetration wind power are presented in **Section 4**. Conclusions are presented in **Section 5**.

2 SMALL SIGNAL ANALYSIS OF WIND TURBINE GRID-CONNECTED SYSTEM

The variable speed wind turbine with virtual inertia control absorbs or releases the rotational kinetic energy by changing the wind turbine speed, adjusting the output power, and responding to the change of system frequency. Take a permanent magnet synchronous generator (PMSG) as an example. **Figure 1** shows the active power control structure of the variable speed wind turbine, including MPPT control and virtual inertia controller module. Under the per-unit system, the active power control instruction of the wind turbine is the sum of the MPPT control reference instruction and the active power increment generated by the inertia controller, which can be expressed as (Wang et al., 2018)

$$P_{ew} = k_m \omega_w^2 - k_v p (\omega_s - \omega_n) \quad (1)$$

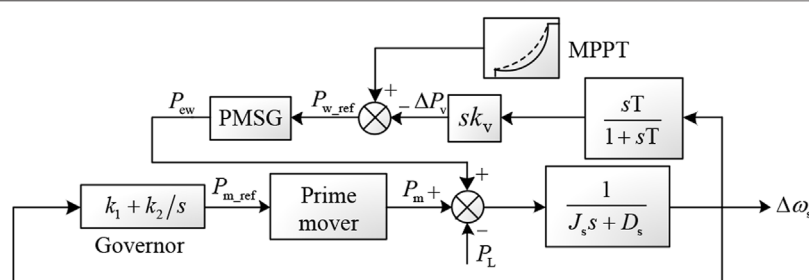


FIGURE 1 | Diagram of active power control of the system with virtual inertia.

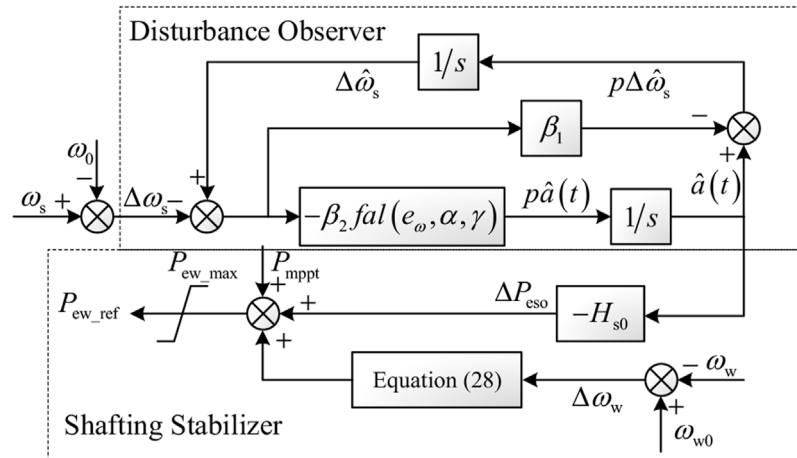


FIGURE 2 | Diagram of virtual inertia control based on extended disturbance observer.

where k_m is the MPPT coefficient of the wind turbine; k_v is the inertia control coefficient. ω_w is the angular velocity of the wind turbine; ω_s and ω_n are the angular velocity of the system synchronous generator and the rated angular velocity of the system, respectively. p is the differential operator.

The following two mass shafting models are established to analyze the dynamic stability of wind turbine shafting (Gaidi et al., 2017).

$$\begin{cases} H_r p \omega_r = P_r / \omega_r - K_s \theta \\ H_w p \omega_w = K_s \theta - (k_m \omega_w^2 - k_v p \omega_s) \\ p \theta = \omega_r - \omega_w \end{cases} \quad (2)$$

where ω_r is the angular velocity of the wind turbine; θ is the torque angle of shafting; H_r and H_w are the inertia of the wind turbine and generator, respectively; K_s is the stiffness coefficient shafting; P_r is the mechanical power captured by the wind turbine.

Ignoring the damping coefficient D_s of synchronous generator, the equivalent second-order rotor motion equation of generator can be expressed as

$$H_s p \omega_s = k_1 (\omega_n - \omega_s) + k_2 x - P_e \quad (3)$$

where H_s is the equivalent inertial time constant of the system; P_e is the electromagnetic power output by the synchronous generator; x represents the output state variable of the

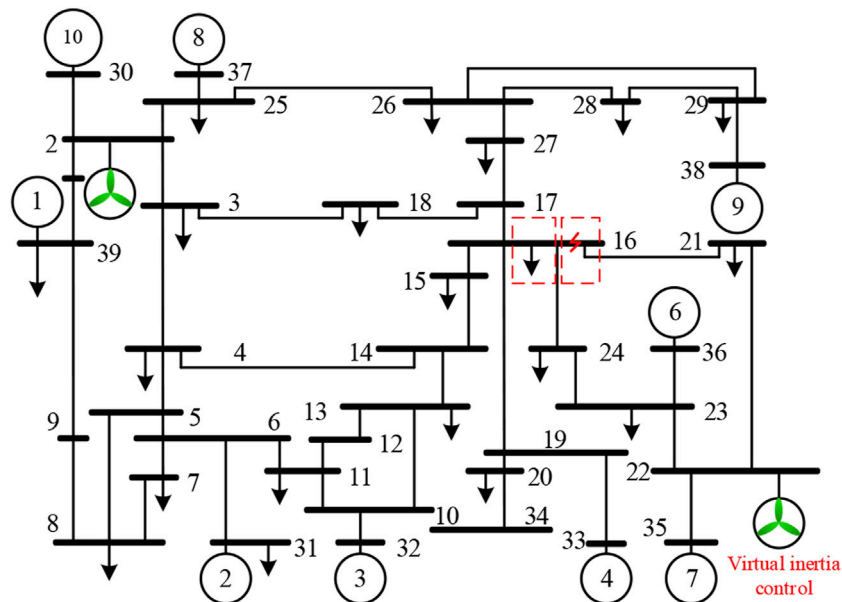


FIGURE 3 | Diagram of the simulation system with the wind turbine.

TABLE 1 | The parameters of the 2 MW PMSG.

Parameters	Value	Parameters	Value
R_s/pu	0.011	L_s/pu	0.102
R_r/pu	0.01	L_r/pu	0.11
L_m/pu	3.36	K_s/pu	8.0
J_w/pu	0.5	J_r/pu	6.5

TABLE 2 | The parameters of synchronous generators.

Parameters	Value	Parameters	Value
X_d/pu	1.8	X'_d/pu	0.3
X''_d/pu	0.25	X_q/pu	1.7
X'_q/pu	0.55	X''_q/pu	0.25
T_{d0}/s	8.0	T'_{d0}/s	0.4
T''_{d0}/s	0.03	T''_{q0}/s	0.05
J_{s1}/pu	2.5	J_{s2}/pu	10.5

governor, $dx/dt = \omega_n - \omega_s$; k_1 is the proportional coefficient; k_2 is the integral coefficient of the governor.

Considering the system power balance, substituting Eq. 1 into Eq. 3, the equation can be expressed as follows

$$\left(H_s + \frac{k_v}{S_B}\right)p\omega_s = k_1(\omega_n - \omega_s) + k_2x - \frac{U_n^2}{rS_B} + \frac{k_m\omega_g^2}{S_B} \quad (4)$$

where U_n represents the terminal voltage of the load connection point; r is the load equivalent resistance; S_B is the system capacity reference value.

Combining Eq. 2 and Eq. 4, the small-signal equation of the wind turbine grid-connected system with virtual inertia control can be expressed as

$$\begin{bmatrix} p\Delta\omega_s \\ p\Delta x \\ p\Delta\omega_r \\ p\Delta\omega_w \\ p\Delta\theta \end{bmatrix} = \begin{bmatrix} a_{11} & a_{12} & 0 & a_{14} & 0 \\ -1 & 0 & 0 & 0 & 0 \\ 0 & 0 & a_{33} & 0 & a_{35} \\ a_{41} & a_{42} & 0 & a_{44} & a_{45} \\ 0 & 0 & 1 & -1 & 0 \end{bmatrix} \begin{bmatrix} \Delta\omega_s \\ \Delta x \\ \Delta\omega_r \\ \Delta\omega_w \\ \Delta\theta \end{bmatrix} \quad (5)$$

where $H_G = H_s + k_v S_B$; $a_{11} = -k_1 S_B / (H_G S_B)$; $a_{12} = -k_2 / (H_G S_B)$; $a_{14} = 2k_m \omega_{w0} / (H_G S_B)$; $a_{33} = -P_{r0} / (H_r \omega_{w0}^2)$; $a_{35} = -K_s / H_r$; $a_{41} = -k_1 k_v S_B / (H_w H_G)$; $a_{42} = -k_2 k_v / (H_w H_G)$; $a_{44} = 2k_m \omega_{w0} k / H_w$; $k = k_v / (H_G S_B) - 1$; $a_{45} = K_s / H_w$.

As the virtual inertia is introduced into the power system, the variable inertia distribution significantly affects system damping. Assuming the constant wind speed, the motion equation of the synchronous generator should be expressed as

$$H_G p^2 \Delta\delta_s + k_1 p \Delta\delta_s - k_2 \Delta\delta_s = 0 \quad (6)$$

By solving the differential equation shown in Eq. 6, the real part expression of the characteristic root of the system is obtained as:

$$\sigma_{1,2} = -\frac{k_1}{2H_G} = -\frac{k_1}{2(H_s + k_v S_B)} \quad (7)$$

According to Eq. 7, the introduction of k_v makes the equivalent inertial time constant of the system H_G increase, but the damping ratio of the synchronous generator is reduced and the characteristic roots gradually move towards the imaginary axis. Therefore, an unreasonable inertia control

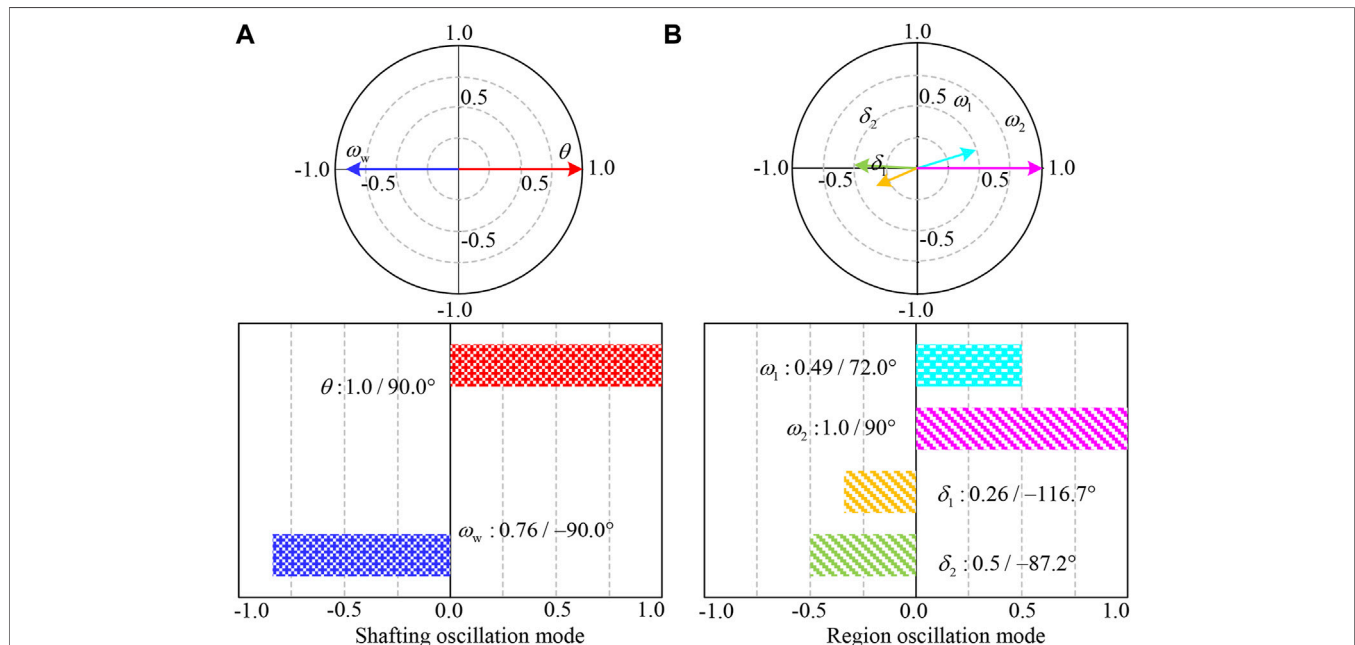


FIGURE 4 | Figure shows the oscillation mode diagram of the wind turbine under the control of constant inertia, in which the (A) is the shafting oscillation mode of the wind turbine, and the (B) is the oscillation mode between the internal regions of the system.

TABLE 3 | Variations of the shafting oscillation mode.

Case	Eigenvalues	Oscillation Frequency/Hz	Damping ratio/%
Case 1	$-0.691 + j13.680$	2.177	5.041
Case 2	$-0.545 + j16.857$	2.683	3.051
Case 3	$-0.921 + j11.361$	1.808	8.080

TABLE 4 | Variations of the region oscillation mode.

Case	Eigenvalues	Oscillation Frequency/Hz	Damping ratio/%
Case 1	$-0.313 + j5.881$	0.936	5.310
Case 2	$-0.341 + j5.036$	0.802	6.760
Case 3	$-0.962 + j4.925$	0.784	19.170

coefficient can even have a negative damping effect on the power angle oscillation of the synchronous generator. In addition, the virtual inertia control of the wind turbine affects the system's dynamic characteristics and causes the stability of wind turbine shafting. Therefore, the analysis of the influence of the inertia response power of the wind turbine on shafting torsional vibration is extremely important for the safe popularization of control technology.

After the Laplace transformation of **Eq. 5**, ω_w can be expressed as follows

$$s\Delta\omega_w = \left[\frac{a_{14}(a_{41} - a_{42}/s)}{s - a_{11} + a_{12}/s} + a_{44} \right] \Delta\omega_w + a_{45}\Delta\theta \quad (8)$$

The coefficient of $\Delta\omega_w$ in **Eq. 8** is defined as a'_{44} , and the shafting state equation of the wind turbine with inertial control can be sorted out as

$$\begin{bmatrix} s\Delta\omega_r \\ s\Delta\omega_w \\ s\Delta\theta \end{bmatrix} = \begin{bmatrix} a_{33} & 0 & a_{35} \\ 0 & a'_{44} & a_{45} \\ 1 & -1 & 0 \end{bmatrix} \begin{bmatrix} \Delta\omega_r \\ \Delta\omega_w \\ \Delta\theta \end{bmatrix} \quad (9)$$

The natural oscillation frequency of wind turbine shafting is about 1–2 Hz; therefore, the equation $a'_{44} \approx a_{44}$ is valid. Since the inertia of the wind turbine is much greater than the inertia of the generator, i.e., $H_w \ll H_r$, as a state variable with the characteristics of rapid change, ω_w can be approximated by an integral manifold to replace, thus reducing the order of **Eq. 9**, to obtain the approximate expression of the analytical solution of the shafting state equation. Assume that the integral manifold of the state variable ω_w is given by

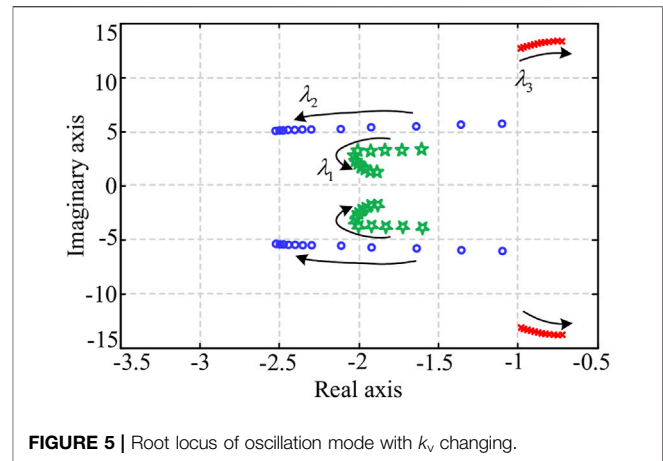
$$\Delta\omega_w = h(\Delta\omega_r, \Delta\theta, \varepsilon) \quad (10)$$

where ε is an infinitesimal quantity.

Let $\varepsilon = H_w/(mH_r)$, where $m \gg 2$, and the power series expansion of **Eq. 10** is given by

$$\Delta\omega_w = h = h_0 + \varepsilon h_1 + \varepsilon^2 h_2 + \dots o(\varepsilon^n) \quad (11)$$

Substituting **Eq. 11** into **Eq. 9** and the expression is obtained as

**FIGURE 5** | Root locus of oscillation mode with k_v changing.

$$\varepsilon \frac{\partial h}{\partial \Delta\omega_w} p \Delta\omega_w + \varepsilon \frac{\partial h}{\partial \Delta\theta} p \Delta\theta = \frac{1}{mH_r} (S_1 h + S_2 \Delta\theta) \quad (12)$$

where,

$$\begin{cases} \frac{d\Delta\theta}{dt} = \Delta\omega_r - h_0 - \varepsilon h_1 - \varepsilon^2 h_2 \dots \\ \frac{\partial h}{\partial \Delta\omega_w} = \frac{\partial h_0}{\partial \Delta\omega_w} + \varepsilon \frac{\partial h_1}{\partial \Delta\omega_w} + \varepsilon^2 \frac{\partial h_2}{\partial \Delta\omega_w} + \dots \\ \frac{\partial h}{\partial \Delta\theta} = \frac{\partial h_0}{\partial \Delta\theta} + \varepsilon \frac{\partial h_1}{\partial \Delta\theta} + \varepsilon^2 \frac{\partial h_2}{\partial \Delta\theta} + \dots \end{cases}$$

The coefficients of ε^0 , ε^1 , and ε^2 on both sides of **Eq. 12** should be equal, and then the function h can be obtained as

$$\begin{cases} h_0 = -\frac{S_2}{S_1} \Delta\theta = \frac{K_s}{2k_m \omega_{w0} k} \Delta\theta \\ h_1 = -\frac{mH_r K_s}{2k_m^2 \omega_{w0}^2 k^2} \Delta\omega_r + \frac{mH_r K_s^2}{4k_m^3 \omega_{w0}^3 k^3} \Delta\theta \end{cases} \quad (13)$$

Substituting **Eq. 13** into **Eq. 11**, the state variable $\Delta\omega_w$ can be approximated as

$$\Delta\omega_w \approx K_A \Delta\theta + K_B \Delta\omega_r \quad (14)$$

where $K_A = \frac{K_s}{2k_m \omega_{w0}} + \frac{H_w K_s^2}{4k_m^3 \omega_{w0}^3 k^3}$, $K_B = -\frac{H_w K_s}{2k_m^2 \omega_{w0}^2 k^2}$.

After reducing the order of the system's state equation combined with **Eq. 14**, the characteristic equation can be expressed as

$$\lambda^2 + (K_A - a_{33})\lambda - K_A a_{33} - (1 - K_B)a_{35} = 0 \quad (15)$$

Therefore, the real part of the characteristic root corresponding to the shafting oscillation mode is given by

$$\sigma_{1,2} = -\frac{1}{4} \left(\frac{K_s}{k_m \omega_{w0}} + \frac{H_w K_s^2}{2k_m^3 \omega_{w0}^3 k^3} \right) - \frac{P_0}{4H_r \omega_{r0}^2} \quad (16)$$

According to **Eq. 16**, the inertia control coefficient k_v affects the shafting oscillation mode of the wind turbine. As the control coefficient k_v increases, k also increases, $\sigma_{1,2}$ approaches the virtual axis of the state plane, and the dynamic stability of wind turbine shafting decreases. Therefore, a new virtual

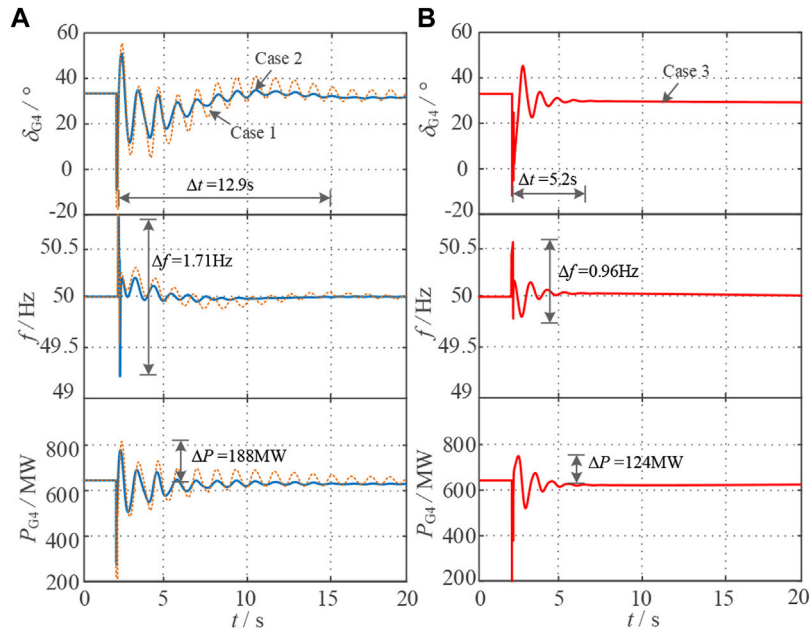


FIGURE 6 | Figure shows the dynamic response curve of the system under short-circuit fault, in which no control is applied to the wind turbine in case 1, the traditional constant inertia control is applied to the wind turbine in case 2, and the optimal control proposed in this paper is applied to the wind turbine in case 3. In order to highlight the contrast effect, the response curves under case 1 and 2 are drawn as **(A)**, and the response curves under case 3 are drawn as **(B)**.

inertia control method is needed to increase the equivalent inertia of the system without causing the shaft oscillation instability of the wind turbine.

3 VIRTUAL INERTIA OPTIMIZATION BASED ON EXTENDED OBSERVER

Considering the slowly changing characteristics of wind speed, the complexity of inertia control parameters is mainly affected by the penetration rate of wind power in the system. If the estimated inertia is set to H_{s0} , the first equation in Eq. 8 is given by

$$p\Delta\omega_s = \frac{1}{H_s} \Delta P_e + \left(\frac{1}{H_s} - \frac{1}{H_{s0}} \right) \Delta P_v + \frac{1}{H_{s0}} \Delta P_v \quad (17)$$

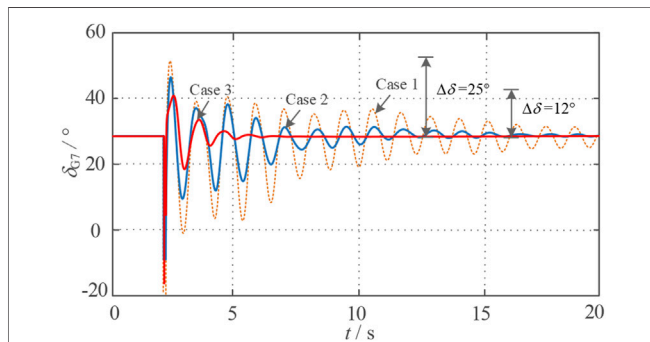


FIGURE 7 | Dynamic responses of G_7 after short circuit fault.

where,

$$\Delta P_e = k_2 \Delta \delta_s - k_1 \Delta \omega_s + \frac{2k_m \omega_{w0}}{S_B} \Delta \omega_w$$

The frequency variation is significantly affected by the system disturbance power and the controller inertia response. The expanded disturbance observer can expand the unknown disturbance affecting the controlled output of the system into new state variables. By adjusting the control coefficient, the output observation signal is gradually close to the original system state variables to realize the observation of system state variables and unknown disturbances.

For the first-order nonlinear uncertain system shown in the above equation, the expansion state variable is constructed as

$$a(t) = \frac{1}{H_s} \Delta P_e + \left(\frac{1}{H_s} - \frac{1}{H_{s0}} \right) \Delta P_v \quad (18)$$

Let the control input $u = \Delta P_v$ and the input coefficient $b = 1/H_{s0}$, the extended disturbance observer can be constructed as follows

$$\begin{cases} e_\omega = \Delta \hat{\omega}_s - \Delta \omega_s \\ p\Delta \hat{\omega}_s = \hat{a}(t) + bu - \beta_1 e_\omega \\ p\hat{a}(t) = -\beta_2 \text{fal}(e_\omega, \alpha, \gamma) \end{cases} \quad (19)$$

where β_1 and β_2 are the adjusting gains of the nonlinear disturbance observer; α is a nonlinear factor, which generally is 0.5. γ is the filter factor related to the sampling step size of the system. $\text{fal}(e_\omega, \alpha, \gamma)$ is a nonlinear function, which is expressed as

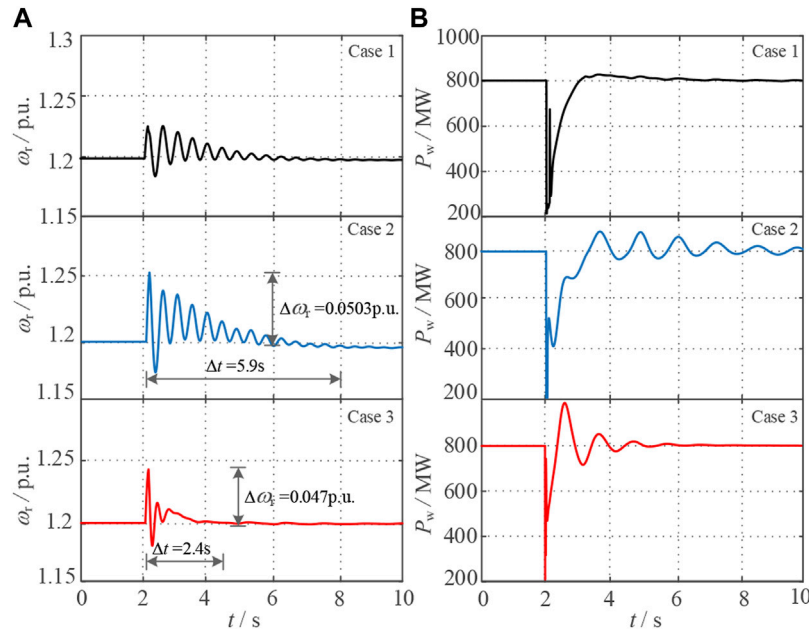


FIGURE 8 | Figure shows the transient response curve of the wind turbine, in which (A) is the rotational speed curve of the wind turbine under the three simulation test cases, and (B) is the output power curve of the wind turbine.

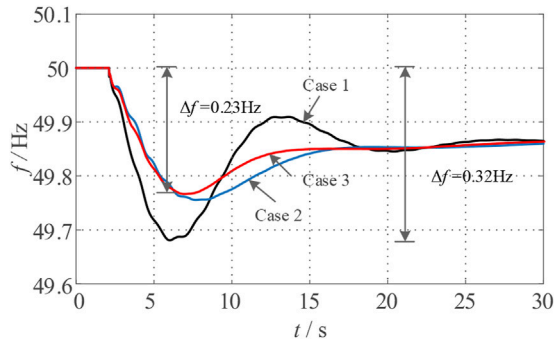


FIGURE 9 | Frequency responses of the system after the load increase.

$$fal(e_\omega, \alpha, \gamma) = \begin{cases} |e_\omega|^\alpha \text{sign}(e_\omega), & |e_\omega| > \gamma \\ \frac{e_\omega}{\gamma^{1-\alpha}}, & |e_\omega| \leq \gamma \end{cases} \quad (20)$$

By adjusting the parameters of the expanded disturbance observer, β_1 , β_2 , α , γ reasonably, the observed value can approach the actual value quickly and ensure the observation precision of the observer. According to Eq. 17 and Eq. 18, with the disturbance observer, the unbalanced power of the system caused by virtual inertia control can be expressed as

$$\Delta P_{\text{eso}} = -H_{s0}a(t) \approx -H_{s0}\hat{a}(t) \quad (21)$$

In the process of dynamic regulation, it is necessary to set the control parameters of the shafting stabilizer to avoid the threat of

shafting torsional vibration caused by additional power control of the wind turbine. Let $\omega_\theta = \omega_r - \omega_w$, simplify Eq. 2, then the equivalent two-mass block shafting model of the wind turbine can be expressed as

$$p\omega_\theta + \frac{K_s}{H_t}\theta = \frac{P_{r0}}{\omega_r H_r} + \frac{k_m \omega_w^2}{H_w} - \frac{k_v}{H_w} p\omega_s \quad (22)$$

where $H_t = H_r \times H_w / (H_r + H_w)$.

Taking the virtual inertia control into account, the power balance equation of the single infinite power grid can be expressed as follows

$$p\omega_s = \frac{S_B}{H_s S_B + k_v} \left(k_m \omega_w^2 - \frac{U_n^2}{r} \right) \quad (23)$$

The wind turbine is controlled by an additional shafting stabilizer, and substituting the above equation is into Eq. 22, after linearization, the expression is given by

$$p\Delta\omega_\theta + (c_1 + k_{ss})\Delta\omega_g + c_2\Delta\omega_r + c_3\Delta\theta = 0 \quad (24)$$

where, $c_1 = 2k_m \omega_{w0} [(k_v / (H_s + k_v / S_B)) - 1] / H_w$; $c_2 = P_0 / (H_r \omega_{w0}^2)$; $c_3 = K_s / H_t$; k_{ss} is the control coefficient of shafting stabilizer.

Since $\Delta\omega_r$ is in the opposite phase to $\Delta\omega_w$, and $\Delta\omega_w = n\Delta\omega_r$, the expression of $\Delta\omega_\theta$ can be expressed as

$$\Delta\omega_\theta = \begin{cases} -(n+1)\Delta\omega_w/n \\ (n+1)\Delta\omega_r \end{cases} \quad (25)$$

where n is defined as the speed ratio between a low-speed and a high-speed shaft.

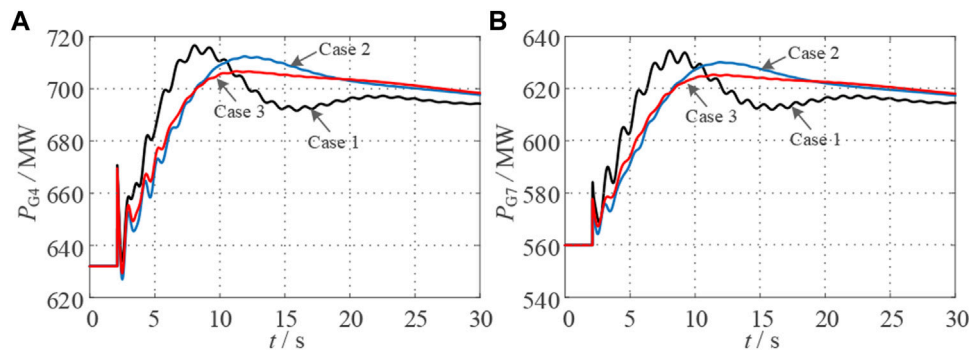


FIGURE 10 | (A) shows the output power curve of the synchronous machine G_4 after a sudden load increase, and **(B)** shows the output power curve of the synchronous machine G_7 .

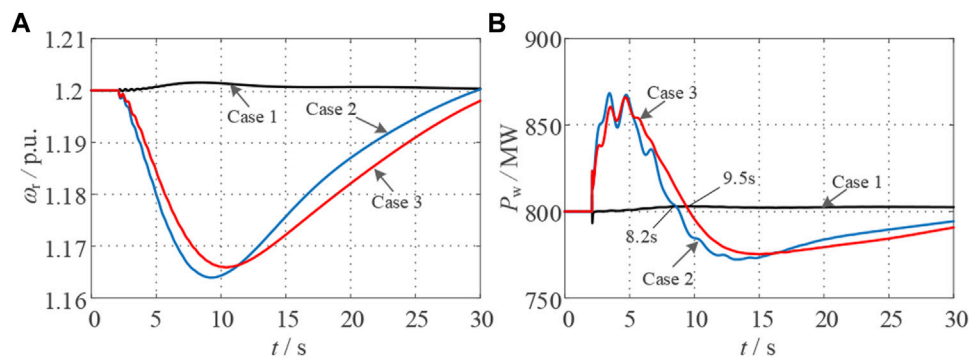


FIGURE 11 | (A) shows the change curve of the rotational speed of the wind turbine after a sudden load increase, and **(B)** shows the output power curve of the wind turbine.

Substituting **Eq. 25** into **Eq. 24**, the small-signal equation of state about θ is given by

$$p^2 - \left[\frac{c_2}{1+n} \frac{n(c_1 - k_s)}{1+n} \right] p + c_3 \Delta \theta = 0 \quad (26)$$

The Lyapunov energy function of the wind turbine shafting system is constructed as

$$V(\Delta \omega_\theta) = \frac{1}{2} \times (\Delta \omega_\theta)^2 \geq 0 \quad (27)$$

The shaft stiffness of the vital connecting parts inside the wind turbine is limited. Considering the most conservative case, when the shaft system stiffness is close to 0, and the nonlinear system is stable in the dynamic process, the first derivative of $V(\Delta \omega_\theta)$ satisfies the **Eq. 28** according to the Lyapunov stability criterion. Therefore, the control coefficient configuration criterion of the stabilizer is shown in **Eq. 29**

$$\frac{dV(\Delta \omega_\theta)}{dt} = \left[\frac{n(c_1 - k_{ss})}{1+n} - \frac{c_2}{1+n} \right] \Delta \omega_\theta^2 \leq 0 \quad (28)$$

$$k_{ss} \geq 2k_m \omega_{w0} \left(\frac{k_v}{H_G S_B} - 1 \right) - \frac{P_{r0}}{nH_r \omega_{r0}^2} \quad (29)$$

According to **Eq. 29**, the control coefficient k_{ss} is set corresponding to the critical stability of the torsional vibration mode of wind turbine shafting to limit the adverse effects brought by inertia adjustment power and ensure reliable damping of shafting oscillation of wind turbine.

By analyzing the influence of virtual inertia on system shafting stability, a virtual inertia compensation control strategy based on an extended disturbance observer is proposed, as shown in **Figure 2**. As the system is disturbed and the frequency fluctuates, the angular velocity ω_s and the expansion variable $a(t)$ are collected and input to the expanded disturbance observer. By setting its adjusting parameters k_{ss} reasonably, the estimated value of the system frequency and unbalanced power is rapidly approaching the actual value, and the compensation value of the output power of the inertia controller is calculated. Through **Eq. 29**, the control parameters of the shafting stabilization stabilizer are set, which are added with the power instruction of MPPT control and sent to the wind turbine to dynamically adjust the active power output of the wind turbine, change the power distribution of the system, and improve the system frequency supportability and shafting stability.

4 VERIFICATION AND ANALYSIS

4.1 System Structure

As shown in **Figure 3**, a 39-node New England system with the wind turbine interconnected system is established to validate the effectiveness of the proposed control strategy. The test system contains ten synchronous generators with a rated capacity of 200 MW, and two PMSG-based wind farms with 400 turbines with a rated capacity of 2MW, which are connected to the system through the bus B_3 and B_{22} , respectively. Specific simulation parameters are shown in **Tables 1, 2**.

The nonlinear factor α is set as 0.5, and the filtering factor $\gamma = 1000$ h. Since the convergence effect of the expanded observer is affected by the gain coefficients β_1 and β_2 , online debugging is carried out according to the estimation accuracy requirements of the observer, so that the estimated value of the output of the observer can approach the actual value at a faster speed. As $\beta_1 = 30$ and $\beta_2 = 120$, the observer can get a better convergence effect without causing a high-frequency flutter phenomenon.

4.2 The Modal Analysis

The simulation model of the system shown in **Figure 3** is built in the DigSILENT/PowerFactory, and the modal analysis of the system is conducted under the initial steady-state conditions of the system. Without virtual inertia control, the characteristic roots of the shafting oscillation mode of DFIG and the low-frequency oscillation mode of the synchronous generator in the region are $-0.691 + j13.680$ and $-0.313 + j5.881$, respectively. The corresponding phasor diagram and bar diagram of the participating factors is shown in **Figure 4**, respectively.

According to the oscillation mode diagram, the shafting oscillation of the wind turbine is mainly affected by the torque angle of shafting and the angular velocity of the generator. The participation factors of the internal oscillation modes in the grid-connected system are rotor angles and angular velocities of the two synchronizers, which are consistent with the theoretical analysis results.

To verify the effect of the optimized inertia control scheme designed in this paper, the control coefficient k_v of constant virtual inertia is set to 30, and the shafting oscillation information of wind turbines and the information on the system static stability are calculated. As shown in **Table 3**, under constant inertia control, the oscillation frequency of wind turbine shafting increases greatly, which threatens the safe operation of the vital connecting parts. Compared with it, the optimized inertia control scheme designed in this paper can improve the damping ratio of the shafting oscillation mode of the wind turbine and the low-frequency oscillation mode of the system, and the oscillation frequency is also reduced **Table 4**. Therefore, the optimized inertia control can effectively improve the static stability of the grid-connected system based on ensuring the operating life of the wind turbine.

Regulating the control coefficient of inertia k_v increases from 0 to 30, the characteristic root track corresponding to

each oscillation mode of the system is shown in **Figure 5**. Where λ_1 represents the region low-frequency oscillation mode, λ_2 represents the local low-frequency oscillation mode, and λ_3 represents the shafting oscillation mode of the wind turbine. As k_v increases from 0 to 15, λ_1 and λ_2 move away from the imaginary axis. If k_v continues to increase, the low-frequency oscillation in the region of the grid-connected system intensifies, and the overall stability decreases. The larger k_v is, the greater the active power output fluctuation of the wind turbine is, and the lower the oscillation stability of its shafting is, which is consistent with the theoretical analysis in **Section 2**.

4.3 Dynamic Response Under Short Circuit Fault

In the following experimental tests, three control schemes are compared to verify the influence of virtual inertia control on the dynamic stability of the system. A three-phase short-circuit fault lasting 0.1 s is set at bus B_{16} , and the wind speed is kept constant at 9 m/s during the fault process.

The dynamic response comparison curve of system power angle δ_{G4} , frequency f , and active power output of synchronous generator P_{G4} are shown in **Figure 6**. It can be seen from **Figure 6A** that the traditional constant inertia control effectively increases the inertial time constant of the system, so the amplitude of the first swing of the power angle decreases after the fault. Although the fluctuation amplitude of the system frequency and power has decreased, the lower damping ratio makes the oscillation time longer, and the transient stability of the system still has a large room for improvement.

As can be seen from **Figure 6B**, after the optimized control strategy designed in this paper, is adopted, the time of the first pendulum oscillation of the system power angle is reduced by 59%, the maximum peak-to-peak value of the frequency fluctuation is reduced by 0.75 Hz, and the active power output of the synchronous generator G_4 is reduced by 64 MW. It can be seen from **Figure 7** that the amplitude of the first swing of the power angle is decreased by 52%, and the recovery time is shortened with the damping characteristics significantly improved.

Under the short-circuit fault, the response curves of the electromagnetic power of PMSG P_w and generator rotor speed ω_w are shown in **Figure 8**. The active power of the wind turbine is significantly adjusted by the constant inertia control during the system short-circuit fault, so the electromagnetic power and speed of the wind turbine fluctuate greatly, which is not conducive to the dynamic stability of the wind turbine shafting. Under the optimized inertia control strategy, the wind turbines optimize the active output and dynamic compensation system of the power deficiency by estimating system unbalanced power. Therefore, the recovery time of the wind turbine speed is shortened by 3.5 s, and the fluctuation amplitude of the speed is reduced by 6%. Meanwhile, the system dynamic stability is improved, and the shaft stability of wind turbines is assured.

4.4 Dynamic Response After the Load Event

To verify the frequency regulation performance of the designed inertia optimization control strategy, the initial conditions of the simulation system are changed, the load at B16 is set to suddenly increase by 1200 MW at 2 s, and the dynamic response of the system is obtained as shown in **Figures 9–11**.

It can be seen from **Figure 9** that, compared with no additional control, the frequency drop amplitude under constant inertia control is reduced by 28%, but the frequency recovery time is longer. The optimized inertia control can speed up the transient process of the system and improve the dynamic stability of the system while assisting the frequency adjustment of the system. As shown in **Figures 10, 11**, after the optimized inertia control proposed in this paper is applied, the rotor speed fluctuation amplitude of the wind turbine is reduced by 4%, and its output power changes more smoothly, which significantly improves the stability of the wind turbine and effectively shares the frequency modulation of the synchronous generator pressure.

5 CONCLUSION

In this paper, the influence of inertia control on the system and wind turbine shafting dynamic stability is analyzed by establishing the state equation of the grid-connected system of the wind turbine, and the optimal control strategy of inertia is designed. The conclusions are as follows:

1) The virtual inertia control of variable-speed wind turbines can effectively improve the system inertia weakening caused by wind turbine grid connection, but the increase of the system equivalent inertia time constant will lead to a decrease in the system damping ratio and slow power oscillation attenuation. The integral manifold method is used to reduce the order of the small-signal model of the wind turbine shafting. With the increase of the differential control coefficient k_v , the vibration modal characteristic root of the wind turbine shafting is close to the imaginary axis. Under virtual inertia control, wind turbines

have an extensive range of power regulations and frequent rotational speed changes impact the mechanical life of wind turbine shafting.

2) Virtual inertia control based on a nonlinear disturbance observer is designed to optimize the virtual inertia control strategy, compensate for the support power output by the wind turbine, and reduce the virtual inertia based on ensuring the frequency modulation effect by estimating the unbalanced power generated by the system in the disturbance process. Thereby the system damping characteristics are improved, and the grid-friendly function of additional inertia control is improved. By establishing the critical stability transient energy function of the wind turbine shafting, the setting range of the k_{ss} control coefficient of the shafting stabilizer is given, to ensure the stability of the wind turbine oscillation.

DATA AVAILABILITY STATEMENT

The original contributions presented in the study are included in the article/Supplementary Material, further inquiries can be directed to the corresponding author.

AUTHOR CONTRIBUTIONS

XZ provides the original idea; Partial theoretical analysis is implemented by WZ and LW; Simulation is realized by WS, ZW wrote the paper and proofread it. All authors have read and agreed to the published version of the manuscript.

FUNDING

This work is supported by the Science and technology project of State Grid Hebei Electric Power Co. Ltd. No. kj 2021-045.

REFERENCES

- Dinkelbach, J., Nakti, G., Mirz, M., and Monti, A. (2021). Simulation of Low Inertia Power Systems Based on Shifted Frequency Analysis. *Energies* 14, 1860. doi:10.3390/en14071860
- Du, W., Dong, W., Wang, H., and Cao, J. (2019). Dynamic Aggregation of Same Wind Turbine Generators in Parallel Connection for Studying Oscillation Stability of a Wind Farm. *IEEE Trans. Power Syst.* 34 (6), 4694–4705. doi:10.1109/tpwrs.2019.2920413
- Duckwitz, D., and Fischer, B. (2017). Modeling and Design of $\$/dt\$$ -Based Inertia Control for Power Converters. *IEEE J. Emerg. Sel. Top. Power Electron.* 5 (4), 1553–1564. doi:10.1109/jestpe.2017.2703814
- Gaidi, A., Lehouche, H., Belkacemi, S., Tahraoui, S., Loucif, M., and Guenounou, O. (2017). “Adaptive Backstepping Control of Wind Turbine Two Mass Model,” in 2017 6th International Conference on Systems and Control (ICSC), 168–172.
- Ghosh, S., Kamalasadan, S., Senroy, N., and Enslin, J. (2016). Doubly Fed Induction Generator (DFIG)-Based Wind Farm Control Framework for

- Primary Frequency and Inertial Response Application. *IEEE Trans. Power Syst.* 31 (3), 1861–1871. doi:10.1109/tpwrs.2015.2438861
- Han, D., Fang, J., Yu, J., Tang, Y., and Debusschere, V. (2019). “Small-Signal Modeling, Stability Analysis, and Controller Design of Grid-Friendly Power Converters with Virtual Inertia and Grid-Forming Capability,” in 2019 IEEE Energy Conversion Congress and Exposition (ECCE), 27–33.
- Hu, J., Sun, L., Yuan, X., Wang, S., and Chi, Y. (2017). Modeling of Type 3 Wind Turbines with Df/dt Inertia Control for System Frequency Response Study. *IEEE Trans. Power Syst.* 32 (4), 2799–2809. doi:10.1109/tpwrs.2016.2615631
- Imad, A., El Hani, S., and Echchaachouai, A. (2017). “Robust Active Disturbance Rejection Control of a Direct Driven PMSG Wind Turbine,” in 2017 International Renewable and Sustainable Energy Conference (IRSEC), 1–6.
- Jia, Y., Huang, T., Li, Y., and Ma, R. (2020). Parameter Setting Strategy for the Controller of the DFIG Wind Turbine Considering the Small-Signal Stability of Power Grids. *IEEE Access* 8, 31287–31294. doi:10.1109/access.2020.2973281
- Lao, H., Zhang, L., Zhao, T., and Zou, L. (2019). “Frequency Regulation Strategy for DFIG Combining Over-speed Control and Adaptive Virtual Inertia,” in 2019 IEEE Innovative Smart Grid Technologies - Asia (ISGT Asia), 1663–1666.

- Li, D., Zhu, Q., Lin, S., and Bian, X. Y. (2017). A Self-Adaptive Inertia and Damping Combination Control of VSG to Support Frequency Stability. *IEEE Trans. Energy Convers.* 32 (1), 397–398. doi:10.1109/tec.2016.2623982
- Li, Y., Li, J., and Wang, Y. (2022a). Privacy-preserving Spatiotemporal Scenario Generation of Renewable Energies: A Federated Deep Generative Learning Approach. *IEEE Trans. Ind. Inf.* 18 (4), 2310–2320. doi:10.1109/tii.2021.3098259
- Li, Y., Li, K., Yang, Z., Yu, Y., Xu, R., and Yang, M. (2022c). Stochastic Optimal Scheduling of Demand Response-Enabled Microgrids with Renewable Generations: An Analytical-Heuristic Approach. *J. Clean. Prod.* 330, 129840. doi:10.1016/j.jclepro.2021.129840
- Li, Y., Wang, R., and Yang, Z. (2022b). Optimal Scheduling of Isolated Microgrids Using Automated Reinforcement Learning-Based Multi-Period Forecasting. *IEEE Trans. Sustain. Energy* 13 (1), 159–169. doi:10.1109/tste.2021.3105529
- Liu, B., Zhao, J., Huang, Q., Milano, F., Zhang, Y., and Hu, W. (2021). Nonlinear Virtual Inertia Control of WTGs for Enhancing Primary Frequency Response and Suppressing Drivetrain Torsional Oscillations. *IEEE Trans. Power Syst.* 36 (5), 4102–4113. doi:10.1109/tpwrs.2021.3055262
- Luo, K., Shi, W., Shi, W., Chi, Y., Wu, Q., and Wang, W. (2017). Stability and Accuracy Considerations in the Design and Implementation of Wind Turbine Power Hardware in the Loop Platform. *Csee Jpes* 3 (2), 167–175. doi:10.17775/cseejpes.2017.0021
- Ma, J., Qiu, Y., Li, Y., Zhang, W., Song, Z., and Thorp, J. S. (2017). Research on the Impact of DFIG Virtual Inertia Control on Power System Small-Signal Stability Considering the Phase-Locked Loop. *IEEE Trans. Power Syst.* 32 (3), 2094–2105. doi:10.1109/tpwrs.2016.2594781
- Mehbodniya, A., Paeizi, A., Rezaie, M., Azimian, M., Masrur, H., and Senjyu, T. (2022). Active and Reactive Power Management in the Smart Distribution Network Enriched with Wind Turbines and Photovoltaic Systems. *Sustainability* 14, 4273. doi:10.3390/su14074273
- Nguyen, N., Almasabi, S., and Mitra, J. (2018). Impact of Correlation between Wind Speed and Turbine Availability on Wind Farm Reliability. *IEEE Trans. Industry Appl.* 55 (3), 2392–2400. doi:10.1109/ias.2018.8544643
- Nguyen, N., Almasabi, S., and Mitra, J. (2019). Impact of Correlation between Wind Speed and Turbine Availability on Wind Farm Reliability. *IEEE Trans. Ind. Appl.* 55 (3), 2392–2400. doi:10.1109/tia.2019.2896152
- Penne, M., Qiao, W., Qu, L., Qu, L., Huang, R., and Huang, Q. (2021). “Active Disturbance Rejection Control of Doubly-Fed Induction Generators Driven by Wind Turbines,” in 2021 IEEE Energy Conversion Congress and Exposition (ECCE), 965–972.
- Sun, L., Liu, K., Hu, J., and Hou, Y. (2019). Analysis and Mitigation of Electromechanical Oscillations for DFIG Wind Turbines Involved in Fast Frequency Response. *IEEE Trans. Power Syst.* 34 (6), 4547–4556. doi:10.1109/tpwrs.2019.2923012
- Sun, M., Sun, Y., Chen, L., Zou, Z., Min, Y., Liu, R., et al. (2022). Novel Temporary Frequency Support Control Strategy of Wind Turbine Generator Considering Coordination with Synchronous Generator. *IEEE Trans. Sustain. Energy* 13 (2), 1011–1020. doi:10.1109/tste.2022.3142914
- Wang, S., and Tomsovic, K. (2018). A Novel Active Power Control Framework for Wind Turbine Generators to Improve Frequency Response. *IEEE Trans. Power Syst.* 33 (6), 6579–6589. doi:10.1109/tpwrs.2018.2829748
- Wang, X., Song, P., Sun, D., and Liu, H. (2018). “Frequency Regulation Characteristics Optimization and Analysis of DFIG- VSG Based on Rotor Inertia Control,” in 2018 China International Conference on Electricity Distribution (CICED), 2051–2055.
- Wang, Y., Meng, J., Zhang, X., and Xu, L. (2015). Control of PMSG-Based Wind Turbines for System Inertial Response and Power Oscillation Damping. *IEEE Trans. Sustain. Energy* 6 (2), 565–574. doi:10.1109/tste.2015.2394363
- Wilches-Bernal, F., Chow, J. H., and Sanchez-Gasca, J. J. (2016). A Fundamental Study of Applying Wind Turbines for Power System Frequency Control. *IEEE Trans. Power Syst.* 31 (2), 1496–1505. doi:10.1109/tpwrs.2015.2433932
- Xiong, L., Li, P., Wu, F. W., and Wang, J. (2019). Stability Enhancement of Power Systems with High DFIG-Wind Turbine Penetration via Virtual Inertia Planning. *IEEE Trans. Power Syst.* 34 (2), 1352–1361. doi:10.1109/tpwrs.2018.2869925
- Zeng, X., Liu, T., Wang, S., Dong, Y., and Chen, Z. (2019). Comprehensive Coordinated Control Strategy of PMSG-Based Wind Turbine for Providing Frequency Regulation Services. *IEEE Access* 7, 63944–63953. doi:10.1109/access.2019.2915308
- Zhang, X., Zhu, Z., Fu, Y., and Li, L. (2020). Optimized Virtual Inertia of Wind Turbine for Rotor Angle Stability in Interconnected Power Systems. *Electr. Power Syst. Res.* 180, 106157. doi:10.1016/j.epr.2019.106157

Conflict of Interest: Authors WS, LW, and WZ were employed by the company State Grid Cangzhou Power Supply Company State Grid Hebei Electric Power Supply Co Ltd.

The remaining authors declare that the research was conducted in the absence of any commercial or financial relationships that could be construed as a potential conflict of interest.

Publisher’s Note: All claims expressed in this article are solely those of the authors and do not necessarily represent those of their affiliated organizations, or those of the publisher, the editors and the reviewers. Any product that may be evaluated in this article, or claim that may be made by its manufacturer, is not guaranteed or endorsed by the publisher.

Copyright © 2022 Song, Wang, Zhao, Zhang and Wang. This is an open-access article distributed under the terms of the Creative Commons Attribution License (CC BY). The use, distribution or reproduction in other forums is permitted, provided the original author(s) and the copyright owner(s) are credited and that the original publication in this journal is cited, in accordance with accepted academic practice. No use, distribution or reproduction is permitted which does not comply with these terms.



A Non-Scheduled Multi-Stage Decision-Making Approach to Control Cascading Failures

Yumeng Liu^{1*}, Tao Wang² and Jiayi Guo¹

¹Department of Electrical Engineering, North China Electric Power University-Baoding, Baoding, China, ²Department of Mathematics and Physics, North China Electric Power University-Baoding, Baoding, China

OPEN ACCESS

Edited by:

Yang Li,
Northeast Electric Power University,
China

Reviewed by:

Jun Yin,
North China University of Water
Resources and Electric Power, China
Chen Liang,
Nanjing University of Information
Science and Technology, China
Jia Cui,
Shenyang University of Technology,
China

*Correspondence:

Yumeng Liu
lym_yomand@163.com

Specialty section:

This article was submitted to
Smart Grids,
a section of the journal
Frontiers in Energy Research

Received: 02 May 2022

Accepted: 30 May 2022

Published: 07 July 2022

Citation:

Liu Y, Wang T and Guo J (2022) A Non-Scheduled Multi-Stage Decision-Making Approach to Control Cascading Failures.
Front. Energy Res. 10:934213.
doi: 10.3389/fenrg.2022.934213

The control research on cascading failures is critical to ensure the reliability of power supply. A path-driven multi-stage corrective control model for the whole process of cascading failures is established to eliminate the risk of cascading failure. For the cascading failure process caused by overloading, the selection criterion for subsequent outage is defined according to the mechanism of propagation of cascading failures. The path-driven constraints and power relaxation constraints are extracted based on the selection criterion for a subsequent outage. A model coupled with non-scheduled multi-stage decision-making is designed by considering the flexibility of control action implementation to optimize the sum of control cost and load-shedding risk for elimination of cascading failures. The verification results show that the proposed method can reduce the probability of outages of tripped branches and successfully eliminate cascading failure.

Keywords: cascading failure, path-driven, multi-stage decision-making, control, power system

1 INTRODUCTION

Due to human factors and external environmental factors such as natural disasters, large-scale blackouts remain difficult to avoid for modern power systems, as evinced by the many large-scale blackouts that have occurred around the world in recent years (Hines et al., 2009; Xue and Xiao, 2013). Most blackouts are found to be caused by cascading failures (Wong et al., 2007; Zeng et al., 2015; Nagpal et al., 2018). Specifically, local disturbances such as generator and transmission line outages can result in a series of successive outages through network connections, resulting in great economic losses and negative social influence. Therefore, it has important significance to quickly and accurately predict the cascading failure process and establish a targeted framework of defense for the predicted cascading failure.

According to the different modeling ideas, there are mainly two types of control approaches for cascading failure. The first type of control method is from the perspective of macroscopic system theory (Lin et al., 2018; Kornbluth et al., 2021). The control methods based on macroscopic system theory focusing on load optimization (Tu et al., 2013) and network structure reinforcement (Liu et al., 2019) are taken as preventative actions to release system operating stress and avoid blackouts. Those methods are applied to provide a reference for power system planning and design; however, it is difficult to realize cascading failure control in practical operation of the power system. Therefore, the research on cascading failure control in power systems is mainly based on reductionism, which consists of initial disturbances and control considering cascading effects.

Security constrained optimal power flow (Capitanescu et al., 2011) is a deterministic model for initial disturbances, including prevention (Azzolin et al., 2018) and correction (Bi et al., 2018),

according to the timing of the implementation of control actions. The deterministic method lacks risk awareness, and overly conservative control schemes can increase control costs. Risk is a comprehensive measure of probability and results in uncertain events, including risk identification, risk assessment, and risk control. Among them, the risk identification and assessment of cascading failures have been widely discussed, and considerable results have been achieved. In addition, mathematical programming, reinforcement learning methods, and deep learning approaches (Li et al., 2022) are used to solve the above model. However, the risk control of cascading failures is still confined to the preventive control of cascading failures or the corrective control of a given cascading failure stage, especially for the initial outage. Zhai et al. (2019) compared two corrective control models of cascading failures: non-recurring corrective control and that of two consecutive cascading failure stages. The simulation results show that the two consecutive stages perform better than non-recurring corrective control. However, corrective actions are taken only at two consecutive stages, which reduces the flexibility around control timing. Subsequently, Gan et al. (2020) proposed a multi-stage corrective control model to study the predicted cascading failure. The mechanism of propagation of the cascading failure process caused by overload is not considered in the control model, that is, the influence of a control action on the branch outage probability and the constraints between outage probability of the tripped branches and in-service branches. Although the resulting control schemes can reduce the outage probability of a tripped branch, the outage probability of an in-service branch may increase significantly, even exceeding the outage probability of the tripped branch. Therefore, it is important to explore how to correct a given cascading failure process under the constraints of the cascading failure propagation mechanism. In this report, an optimal control considering the constraints of the cascading failure mechanism of propagation, the so-called path-driven MSCC, is presented to protect power systems against cascading failure.

This report is organized as follows. **Section 2** presents an analysis of the interaction between the MSCC and the cascading effect. Extraction of path-driven constraints and power relaxation constraints is based on the mechanism of propagation of cascading failures in **Section 3**. And **Section 4** discusses the effects of the above two constraints on the control scheme obtained by the path-driven MSCC. **Section 5** concludes the report.

2 INTERACTION BETWEEN CASCADING FAILURE PROCESS AND MSCC

For cascading failures caused by overload, when a branch is randomly selected as the initial disturbance, the outage probability of in-service branches can be calculated by (1), given by Zima and Andersson (2005). The selection criterion for a subsequent outage (Wei et al., 2018) is adopted, i.e., choosing the branch with largest $p_{i,k}$ among all branches as the tripped branch at the $(k+1)^{\text{th}}$ stage:

$$p_{i,k} = \begin{cases} 0, & F_{i,k} \leq F_i^{\text{rated}} \\ \frac{1}{F_i^{\text{max}} - F_i^{\text{rated}}} (F_{i,k} - F_i^{\text{rated}}), & F_i^{\text{rated}} < F_{i,k} \leq F_i^{\text{max}} \\ 1, & F_{i,k} > F_i^{\text{max}}. \end{cases} \quad (1)$$

In actual operation, the change of active power injections, demand response, and topology optimization can be used to correct power flow on the branches. The outage probability of in-service branches and their maximum values are also changed, as given by (1). Thus, the control action can affect the outage probability of tripped branches and even change the branches that tripped during the cascading failure process. Similarly, the network topology determined by tripped branches also affects the distribution of nodal power injections on the branches. The interaction between the cascading failure process and the MSCC continues until there are no overloaded lines in the power system.

3 PATH-DRIVEN MSCC MODEL

In this section, the path-driven MSCC for the whole cascading failure process is proposed, in which path-driven constraints and power relaxation constraints are taken into consideration at each cascading stage.

3.1 Objective Function

The goal of MSCC is to minimize the load-shedding risk caused by cascading failures with the lowest control cost, and the objective function f is calculated as follows:

$$\min f = \sum_{k=1}^{v_{\text{con}}} \left(\prod_{m=1}^k \pi_m \right) \left(\sum_g \alpha_g PGD_{g,k} + \sum_n \beta_n LD_{n,k} \right), \quad (2)$$

where v_{con} denotes the total number of cascading stages with corrective control actions; because the proposed multi-stage control is designed to eliminate cascading failures, v_{con} is an unknown variable and less than the total number of cascading stages l without corrective control. π_k is the maximum of an overloaded branch probability at the $(k-1)^{\text{th}}$ cascading stage, i.e., $\pi_k = \max(p_{i,k-1})$. Therefore, the multiplication of π_k over stages is the probability of cascading failure. $PGD_{g,k}$ and $LD_{n,k}$ are the power generation adjustment at unit g and load shedding at node n at the k^{th} cascading stage. α_g and β_n are the cost coefficients of $PGD_{g,k}$ and $LD_{n,k}$, respectively.

3.2 Path-Driven Constraints

In this report, the research object is the predicted cascading failure process, so the same subsequent outage selection criteria should be used in both the cascading failure prediction and the cascading failure control processes; therefore, the outage probability of the tripped branch must satisfy path-driven constraints in the MSCC model of cascading failure, given by

$$p_{i,k} \geq p_{e,k} \quad \forall e \in E_k, \quad (3)$$

where E_k is the set of in-service branches. The physical meaning of Eq. 3 is that the outage probability of predicted outage branch i

at the k th stage is greater than that of other in-service branches in power systems. Eq. 3 ensures that corrective control actions can only affect the probability of an outage on a tripped branch without changing the tripped branch subject to the subsequent outage selection criteria described above.

3.3 Power Relaxation Constraints

To balance cost and load-shedding risk in corrective control, the corresponding power relaxation coefficients γ_1 and γ_2 are set for predicted tripped branches and other in-service branches. As the control relaxation coefficient decreases, the upper capacity of the power flow allowed on branches is gradually reduced in the corrective control model. At each cascading stage, the power relaxation constraints are expressed as

$$\begin{cases} |F_{i,k}| \leq \gamma_1 F_i^{\text{rated}} & k = 1, 2, \dots, v_{\text{con}} - 1 \\ |F_{i,k}| \leq F_i^{\text{rated}} & k = v_{\text{con}}, \end{cases} \quad (4)$$

$$\begin{cases} |F_{e,k}| \leq \gamma_2 F_e^{\text{rated}} & k = 1, 2, \dots, v_{\text{con}} - 1 \\ |F_{e,k}| \leq F_e^{\text{rated}} & k = v_{\text{con}}, \end{cases} \quad (5)$$

where $F_{i,k}$ and $F_{e,k}$ are the active power flows on predicted tripped branches and other in-service branches, respectively. Eqs 4–5 represent power flow on branches being allowed to exceed its threshold in the former ($v_{\text{con}}-1$) stages; meanwhile, there may be differences in the degree of power relaxation for predicted tripped branches and other in-service lines.

3.4 Power Flow Constraints

At each cascading stage, the proposed model is subject to the following power flow constraints:

$$P_{n,k} = \sum_{Fr(i)} F_{i,k} - \sum_{T(i)} F_{i,k}, \quad (6)$$

$$PG_g^{\min} \leq PG_{g,k} \leq PG_g^{\max}, \quad (7)$$

$$0 \leq PGD_{g,k} \leq PGD_g^{\max}, \quad (8)$$

$$0 \leq LD_{n,k}, \quad 0 \leq \sum_{m=1}^k LD_{n,m} \leq PD_n^{\max}, \quad (9)$$

where $PG_{g,k}$, PG_g^{\min} , and PG_g^{\max} are power generated by unit g and its minimum and maximum capacities, respectively. PGD_g^{\max} and PD_n^{\max} are the maximum allowable power generation adjustment of unit g and maximum allowable load shedding of node n , respectively. Eq. 6 is the power balance equation. Eqs 7–8 limit power outputs of the generators and their power output adjustment, respectively. Eq. 9 is the load-shedding limit.

Eqs 2–9 imply that, due to the uncertainty of v_{con} , the path-driven MSCC model is a non-scheduled multi-stage decision-making optimization for the whole process of cascading failure. It is worth noting that control action implementation is not confined to one or more given cascading failure stages. So, there is a choice to take control actions at each cascade stage.

3.5 Solving the Path-Driven MSCC Model

The proposed model is a non-linear programming problem which is difficult to be solved directly. Therefore, we draw on the idea of the two-layer decomposition optimization scheme

proposed by Liu et al. (2015), and the genetic algorithm (Shi et al., 2021) is used to solve it. The upper-level model optimizes the outage probability of predicted tripped branch for each cascading stage, and the obtained values are imported into the lower-level model. Output adjustment of unit and load shedding are optimized in the lower-level model.

4 EXAMPLE ANALYSIS

4.1 Validation of Path-Driven MSCC Model

The IEEE 39 Bus System is employed to validate the proposed method and analyze the corresponding results. The IEEE 39 Bus System consists of 10 units, 39 buses, and 46 branches. In addition, the system load in normal operation is 6,254.2 MW, and the total installed capacity is 7367 MW. The transmission capacity of branch is set to 95% of its original value, and the transmission capacity of branch 17–18 is modified to 300 MW. The active adjustment of the unit is 15% of the unit capacity; α_g and β_n are set to 1 \$/MW and 100 \$/MW, respectively (Carreras et al., 2001). Power relaxation coefficients γ_1 and γ_2 are both set to 1.4. The tripping of branch 1–2 is selected as the initial disturbance, and subsequently, the power flow on branch 2–3 with its rated capacity of 475 MW increases from 450.81 to 757.62 MW. The cascading effect continues to propagate until the grid is decoupled, and the cascading failure process is denoted as $I_a = \{1-2, 2-3, 17-18, 15-16, 1, 1, 1, 1\}$. Figure 1A presents the connection states of IEEE 39 Bus Systems after suffering the cascading failure process I_a . In Figure 1, the blue balls are the unit nodes, while black ones are the load nodes and red branches characterize overloaded branches. It is worth noting that the IEEE 39 node system not only is decoupled into two islands but also contains an overloaded branch in each island.

The proposed model is applied to devise the control schemes for the cascading failure process I_a . With corrective control, the cascading failure process is truncated from I_a to $I_b = \{1-2, 2-3, 17-18, 1, 0.48, 0.31\}$, and the connection states of IEEE 39 Bus Systems after suffering the cascading failure process I_b are shown in Figure 1B. As can be seen from Figure 1B, with corrective control, there are no multiple islands and overloaded branches in IEEE 39 Bus Systems, indicating that path-driven MSCC can successfully eliminate cascading failures in three cascading stages.

4.2 Effect of V_{con}

Due to the uncertainty of v_{con} , the proposed path-driven MSCC model is a non-scheduled multi-stage decision-making optimization facing the whole cascading failure process. In other words, the optimal control approach is designed to correct the cascading effect within the first l cascading stages. This non-scheduled model is compared with the scheduled model (i.e., v_{con} is restricted to a certain value), and the results are summarized in Table 1.

If v_{con} is restricted to 1, after implementing the corrective action, the power flow on branch is less than its threshold and the cascading process caused by overloaded branches ends. The MSCC will be transformed to non-recurring corrective control, and path-driven MSCC is superior to non-recurring corrective control in terms of

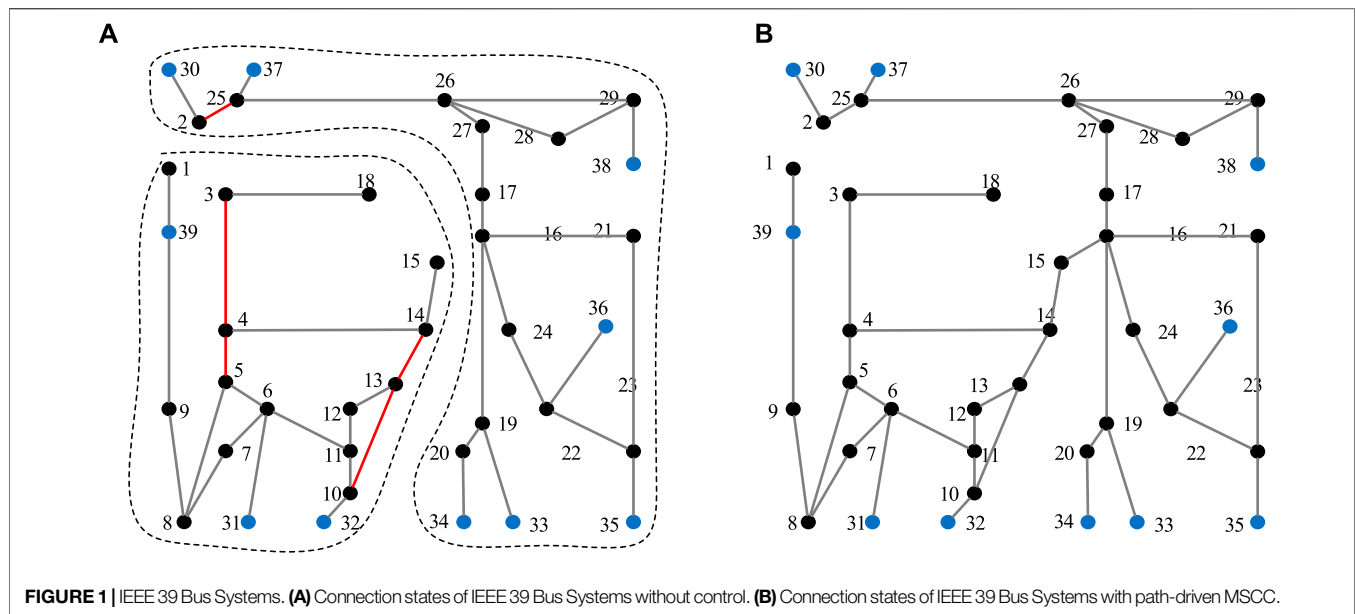


TABLE 1 | Effect of v_{con} on the performance of the scheduled MSCC model.

v_{con}	Cascading failure process	Load-shedding risk	Objective function
1	{1–2,1}	448.54	45,760.86
2	{1–2,2–3,1,0.43}	115.43	12,310.87
3	{1–2,2–3,17–18,1,0.48,0.31}	106.05	11,412.95
4	{1–2,2–3,17–18,15–16,1,0.47,0.26,0.01}	109.47	11,749.17

TABLE 2 | Branch outage probability ranking with the control actions obtained by Model 2.

Ranking	$k = 1$		$k = 2$		$k = 3$		$k = 4$	
	Branch	Outage probability	Branch	Outage probability	Branch	Outage probability	Branch	Outage probability
1	1–2	1	2–3	0.49	17–18	0.46	4–14	0.21
2	1–2	1	6–11	0.14	—	—	6–11	0.03
3	1–2	1	—	—	—	—	15–16	0.01

The data listed in bold are the predicted tripped branches and its outage probability.

load-shedding risk and objective function. For the scheduled MSCC model, when $v_{con} = 3$, the values of the above two indicators are the lowest at 11,412.95 and 106.05, respectively. With the scheduled constraints, the MSCC model needs to be solved repeatedly according to the value of v_{con} , and the solution time gradually increases as v_{con} increases. Then, the optimization results with different v_{con} values are compared, and the optimal solution is obtained. The non-scheduled MSCC model proposed in this report can be solved once to obtain the optimal solution.

4.3 Effect of Path-Driven Constraint

If the path-driven constraint is not considered in path-driven MSCC, i.e., the constraint (Eq. 3) is removed, the model is denoted as Model 2. Table 2 shows the branch outage probability ranking with the control scheme obtained by Model 2. The data listed in bold are the predicted tripped branches and their outage probability. Notably, the

initial disturbance is the selected outage, so there is no ranking of branch outage probability at the first cascading stage.

After control action is implemented at the third cascading stage, the outage probability of predicted tripped branch 15–16 is 0.01. In contrast, the branch with maximum outage probability is branch 4–14, and its outage probability is significantly greater than that of predicted tripped branch 15–16. From the defined criterion for candidate outage, branch 4–14 is chosen to serve as the tripped branch at the next cascading stage, so the cascading failure process will deviate from the original predicted cascading process.

Furthermore, under the corrective control obtained by using Model 2, the cascading failure process considering the selection criterion for subsequent outage is $I_c = \{1-2, 2-3, 17-18, 4-14, 6-11, 1, 0.49, 0.46, 0.21, 1\}$. It can be seen from I_c that although the control scheme obtained by Model 2 can reduce the outage probability of a tripped branch, there are still overloaded

TABLE 3 | Comparison of different control models.

Model	Load shedding (MW)	Risk of load shedding	Objective function
1	281.85	106.05	11,412.95
3	299.89	128.25	13,608.48

branches in the network even after four cascading stages, that is, Model 2 cannot eliminate cascading failure processes.

4.4 Effects of Power Relaxation Constraints

In this part, the power relaxation coefficient is modified to 1, denoted as Model 3. Model 3 is solved and compared with the results of Model 1, as summarized in **Table 3**.

As can be seen from **Table 3**, compared with Model 3, Model 1 provides better performance in terms of load shedding, risk of load shedding, and objective function. This is because the control scheme obtained by Model 3 needs to shed more load to satisfy the constraint whereby the power flow on a branch cannot exceed the pre-set threshold for in-service branches other than on the branch predicted to trip. As the transmission capacity of branch is further reduced, it may appear that Model 1 can provide an effective control scheme, while Model 3 fails to obtain a corrective control scheme. This is because in extreme operating conditions, when the control action is implemented to eliminate the power flow overload of one branch, it may inevitably cause the power flow overload of other branches. Therefore, the power relaxation constraints can not only help to obtain an available control scheme in extreme conditions but also reduce the control cost.

5 CONCLUSION

A path-driven multi-stage corrective control method considering the uncertainty of v_{con} is proposed to eliminate

the cascading failure process. According to the mechanism of propagation of cascading failures, path-driven constraints and power relaxation constraints are extracted. Adjustments of nodal power injections including unit output adjustment and load shedding are considered corrective controls, and the proposed model is optimized by minimizing the sum of the expected control cost and load-shedding risk. The results verified that the path-driven MSCC method can correct the cascading failure process in an effective and cooperative manner. The effects of the uncertainty of v_{con} , path-driven constraints, and power relaxation constraints on the applicability and effectiveness of control scheme are discussed. When path-driven constraints are not considered, the obtained control scheme may fail due to change of cascading failure paths. When power relaxation constraints or the uncertainty of v_{con} is not considered, the resulting solutions are too conservative.

DATA AVAILABILITY STATEMENT

The raw data supporting the conclusions of this article will be made available by the authors, without undue reservation.

AUTHOR CONTRIBUTIONS

YL and TW performed the methodology. YL was involved in data analysis and writing the original draft. TW supervised the work. JG reviewed and edited the paper.

FUNDING

This research was funded by the National Natural Science Foundation of China under Grant No. 52107092.

REFERENCES

- Azzolin, A., Dueñas-Osorio, L., Cadini, F., and Zio, E. (2018). Electrical and Topological Drivers of the Cascading Failure Dynamics in Power Transmission Networks. *Reliab. Eng. Syst. Saf.* 175, 196–206. doi:10.1016/j.ress.2018.03.011
- Bi, R., Lin, T., Chen, R., Ye, J., Zhou, X., and Xu, X. (2018). Alleviation of Post-contingency Overloads by SOCP Based Corrective Control Considering TCSC and MTDC. *IET Gener. Transm. Distrib.* 12 (9), 2155–2164. doi:10.1049/iet-gtd.2017.1393
- Capitanescu, F., Martinez Ramos, J. L., Panciatici, P., Kirschen, D., Marano Marcolini, A., and Platbrood, L. (2011). State-of-the-art, Challenges, and Future Trends in Security Constrained Optimal Power Flow. *Electr. Power Syst. Res.* 81 (8), 1731–1741. doi:10.1016/j.epsr.2011.04.003
- Carreras, B., Lynch, V., Sachtjen, M., Dobson, I., and Newman, D. (2001). "Modeling Blackout Dynamics in Power Transmission Networks with Simple Structure," in Proceedings of 34th IEEE Hawaii International Conference on System Sciences, Maui, Hawaii, July, 2011, 719–727. doi:10.1109/HICSS.2001.926275
- Gan, G., Geng, G., Gao, B., Zhong, W., Jiang, Q., and Huang, D. (2020). Blocking Control of Power System Cascading Failures Considering Line Outages Probability. *Power Syst. Techn.* 44 (1), 266–272. doi:10.13335/j.1000-3673.pst.2018.2244
- Hines, P., Apt, J., and Talukdar, S. (2009). Large Blackouts in North America: Historical Trends and Policy Implications. *Energy Policy* 37 (12), 5249–5259. doi:10.1016/j.enpol.2009.07.049
- Kornbluth, Y., Cwlich, G., Buldyrev, S., Soltan, S., and Zussman, G. (2021). Distribution of Blackouts in the Power Grid and the Motter and Lai Model. *Phys. Rev. E* 103 (3), 032309. doi:10.1103/PhysRevE.103.032309
- Li, Y., Li, J., and Wang, Y. (2022). Privacy-Preserving Spatiotemporal Scenario Generation of Renewable Energies: A Federated Deep Generative Learning Approach. *IEEE Trans. Industrial Inf.* 18 (4), 2310–2320. doi:10.1109/TII.2021.3098259
- Lin, Y., Burghardt, K., Rohden, M., Noel, P., and D'Souza, R. (2018). Self-Organization of Dragon King Failures. *Phys. Rev. E* 98 (2), 022127. doi:10.1103/PhysRevE.98.022127
- Liu, W., Lin, Z., Wen, F., Chung, C., Xue, Y., and Ledwich, G. (2015). Sectionalizing Strategies for Minimizing Outage Durations of Critical Loads in Parallel Power System Restoration with Bi-level Programming. *Int. J. Electr. Power Energy Syst.* 71, 327–334. doi:10.1016/j.ijepes.2015.03.004
- Liu, D., Tse, C., and Zhang, X. (2019). Robustness Assessment and Enhancement of Power Grids from a Complex Network's Perspective Using Decision Trees. *IEEE Trans. Circuits Syst. II Exp. Briefs.* 66 (5), 833–837. doi:10.1109/TCSII.2019.2909523

- Nagpal, M., Martinich, T., Jiao, Z., Manuel, S., and Zhang, H. (2018). Lessons Learned from a Regional System Blackout and Restoration in BC Hydro. *IEEE Trans. Power Deliv.* 33 (4), 1954–1961. doi:10.1109/TPWRD.2017.2768046
- Shi, K., Liu, H., Wang, L., Bie, Y., and Yang, Y. (2021). Theoretical Design of a Multilayer Based Spectrally Selective Solar Absorber Applied under Ambient Conditions. *Front. Energy Res.* 9, 795261. doi:10.3389/fenrg.2021.795261
- Tu, J., Xin, H., Wang, Z., Gan, D., and Huang, Z. (2013). On Self-Organized Criticality of the East China AC-DC Power System-The Role of DC Transmission. *IEEE Trans. Power Syst.* 28 (3), 3204–3214. doi:10.1109/TPWRS.2013.2251913
- Wei, X., Zhao, J., Huang, T., and Bompard, E. (2018). A Novel Cascading Faults Graph Based Transmission Network Vulnerability Assessment Method. *IEEE Trans. Power Syst.* 33 (3), 2995–3000. doi:10.1109/TPWRS.2017.2759782
- Wong, J., Su, C., and Liu, C. (2007). Study on the 729 Blackout in the Taiwan Power System. *Int. J. Electr. Power Energy Syst.* 29 (8), 589–599. doi:10.1016/j.ijepes.2007.02.001
- Xue, Y., and Xiao, S. (2013). Generalized Congestion of Power Systems: Insights from the Massive Blackouts in India. *J. Mod. Power Syst. Clean. Energy* 1 (2), 91–100. doi:10.1007/s40565-013-0014-2
- Zeng, B., Ouyang, S., Zhang, J., Shi, H., Wu, G., and Zeng, M. (2015). An Analysis of Previous Blackouts in the World: Lessons for China's Power Industry. *Renew. Sustain. Energy Rev.* 42, 1151–1163. doi:10.1016/j.rser.2014.10.069
- Zhai, C., Zhang, H., Xiao, G., and Pan, T. (2019). A Model Predictive Approach to Protect Power Systems against Cascading Blackouts. *Int. J. Electr. Power Energy Syst.* 113, 310–321. doi:10.1016/j.ijepes.2019.05.029
- Zima, M., and Andersson, G. (2005). “On Security Criteria in Power Systems Operation,” in *Proceeding of IEEE Power Engineering Society General Meeting*, San Francisco, USA, June, 2005, 3089–3093. doi:10.1109/PES.2005.1489533
- Conflict of Interest:** The authors declare that the research was conducted in the absence of any commercial or financial relationships that could be construed as a potential conflict of interest.
- Publisher's Note:** All claims expressed in this article are solely those of the authors and do not necessarily represent those of their affiliated organizations, or those of the publisher, the editors, and the reviewers. Any product that may be evaluated in this article, or claim that may be made by its manufacturer, is not guaranteed or endorsed by the publisher.
- Copyright © 2022 Liu, Wang and Guo. This is an open-access article distributed under the terms of the Creative Commons Attribution License (CC BY). The use, distribution or reproduction in other forums is permitted, provided the original author(s) and the copyright owner(s) are credited and that the original publication in this journal is cited, in accordance with accepted academic practice. No use, distribution or reproduction is permitted which does not comply with these terms.*



OPEN ACCESS

EDITED BY

Giovanni Malara,
Mediterranea University of Reggio
Calabria, Italy

REVIEWED BY

Purnima Jalihal,
National Institute of Ocean Technology,
India
Andrea Scialò,
Mediterranea University of Reggio
Calabria, Italy

*CORRESPONDENCE

Marco Ulloa,
mulloa@ipn.mx

SPECIALTY SECTION

This article was submitted to Wave and
Tidal Energy,
a section of the journal
Frontiers in Energy Research

RECEIVED 27 April 2022

ACCEPTED 01 August 2022

PUBLISHED 31 August 2022

CITATION

Diaz-Maya M, Ulloa M and Silva R (2022),
Assessing wave energy converters in the
gulf of Mexico using a multi-
criteria approach.
Front. Energy Res. 10:929625.
doi: 10.3389/fenrg.2022.929625

COPYRIGHT

© 2022 Diaz-Maya, Ulloa and Silva. This
is an open-access article distributed
under the terms of the [Creative
Commons Attribution License \(CC BY\)](#).
The use, distribution or reproduction in
other forums is permitted, provided the
original author(s) and the copyright
owner(s) are credited and that the
original publication in this journal is
cited, in accordance with accepted
academic practice. No use, distribution
or reproduction is permitted which does
not comply with these terms.

Assessing wave energy converters in the gulf of Mexico using a multi-criteria approach

Miqueas Diaz-Maya¹, Marco Ulloa^{1*} and Rodolfo Silva²

¹Instituto Politécnico Nacional, CICATA-Altamira, Altamira, Mexico, ²Instituto de Ingeniería, Universidad Nacional Autónoma de México, Mexico City, Mexico

The wave power in the Gulf of Mexico was analyzed, using 42 years (1979–2020) of simulated data, with ERA-5 winds to force the WAVEWATCH III wave model. The model was successfully validated with three NDBC buoys, 42,055, 42,001 and 42,002. Comparison of significant wave heights obtained from the Jason-2, Cryosat-2, and Saral satellites showed good mean correlation coefficients and root mean squares. The spatial distribution of wave power was studied, as well as its seasonal variability. The region studied has moderate availability of wave power with marked seasonality. A multi-criteria MCA approach, including both sea state and wave energy converters (WECs), was then applied. Nine virtual sites were selected for the study and the AAHPA device gave best results in 7 virtual sites and the Wavestar device in the remaining two. The technology of these two devices, a system of oscillating buoys, is the most viable technology for the Gulf of Mexico.

KEYWORDS

wave power, wave energy converters, wavewatch III, gulf of Mexico, multi-criteria approach

Introduction

The availability of energy is an important factor in the development of any country's economy and in the welfare of its people. However, the unsustainable use of energy resources impacts the environment, human health, and economic progress (Pérez-Denicia et al., 2017). In 2020 in Mexico, most energy was generated from oil 59.8%, followed by natural gas at 23.2%, renewable energy 10.5%, coal 3.6%, and nuclear 2.0%. Of the renewable sources geothermal energy, solar and wind accounted for 3.4%, hydroelectric 1.3% and biomass 5.7% (SENER, 2020). As the demand for electricity in Mexico continues to grow, our commitment to try to decrease the amount of energy produced from fossil fuels is becoming vital, and therefore all the available clean energy resources must be considered. Marine energy from waves, currents, tides, thermal gradient and salinity gradient must be assessed. Among these, wave energy has greatest potential (Soerensen and Weinstein, 2008), partly because it is more predictable than other renewables, such as wind or solar (Kamranzad and Hadadpour, 2020).

Global assessments of the annual mean wave power estimate maximum values in the Gulf of Mexico (GoM) to be 5–10 kW/m (Cornett, 2008; Mørk et al., 2010; Gunn and

Stock-Williams, 2012; Rusu and Rusu, 2021). In water depths of over 40 m, Guillou and Chapalain (Guillou and Chapalain, 2020) found an annual mean power of less than 8 kW/m in the GoM, which coincides with that of Appendini et al. (Appendini et al., 2015). Off the Mexican coast in the GoM, Félix et al. (Félix et al., 2018) found that the multi annual wave energy potential excluding storms, is 18.0 MW, with 24.2 MW, including storms ($H_s = 4$ m). More specifically, Hernández-Fontes et al. (Hernández-Fontes et al., 2019) stated that the wave power availability for a wave power threshold of over 5 kW/m is available 60–70% of the time off the states of Quintana Roo and Tamaulipas. It should be pointed out that numerical results of Hernández-Fontes et al. (Hernández-Fontes et al., 2019) were not validated with wave measurements.

The GoM has significant urban and industrial development, and thus a substantial base of electricity consumers, as well as almost 1900 oil platforms that require an electricity supply (Bureau of Safety and Environmental Enforcement, 2020). However, the GoM is not considered to offer steady wave power for energy harnessing, due to hurricane risk and the variability of the potential resource (annual index exceeding 1.0) (Cornett, 2008; Guillou and Chapalain, 2020). Guiberteau et al. (Guiberteau et al., 2015), however, suggested that the Power Buoy and Pelamis wave energy converters (WECs), are capable of adapting to the variability and to capture wave energy to provide some electricity to the oil platforms in the GoM. Haces-Fernández et al. (Haces-Fernández et al., 2018) also suggests that the combination of Pelamis and wind power is a good option.

In the present quest for sustainable energy resources, the adaptation of WEC technologies for low-medium wave power regions has become a topic of research. If these regions cannot supply electricity to large centers of consumption, then perhaps the wave energy harvested can meet local needs. This study explores various WEC technologies for harnessing wave energy in the GoM, at sites associated with oil exploration and exploitation. A multi-criteria analysis was used to select the most viable WEC technology. The WAVEWATCH III wave model (WW3) was used, validated with National Buoy Data Center (NDBC) data and satellite altimetry data. The results obtained for 1979–2020 (42 years) allowed us to study interannual variations in wave parameters in the deep waters of the GoM. A numerical characterization of the wave power was carried out, and site selection and WECs were evaluated.

Materials and methods Section of this paper describes the implementation and methodology of the model. In *Results and discussion* Section the model validation, the wave power analysis and the analysis of the different WECs using the multi-criteria approach (MCA, also known as MCA factor) are shown.

Materials and methods

This section is divided into three stages: the implementation and validation of the WW3 model for 1979–2020 is described, a

brief description of the wave power in the GoM is given and, finally, the analysis of WECs at various sites is presented, using the MCA.

Study area

The GoM is a semi-enclosed sea (Figure 1) with moderate waves, reaching significant wave heights of about 1 m (Ojeda et al., 2017). The extreme waves generated in the GoM are primarily due to frontal systems, tropical cyclones and winds with southern and southeastern components known as “Suradas”. The cold fronts in the area can lead to abrupt temperature changes (up to 20°C in 24 h) and rainfall of 200 mm day⁻¹ with strong winds and thus large waves (Pérez et al., 2014). The cold front season usually lasts from October to April, with the most intense period being between December and March (Appendini et al., 2014). Meteorological data from 1981 to 2010 (CONAGUA, 2019) shows that on average there are 44 cold fronts per season. The North Atlantic tropical cyclone season is from June 1 to November 30, with most tropical cyclones directly affecting the Mexican coast in September (Rosengaus et al., 2014). Hurricane winds vary in severity and direction (Young and Burchell, 1996). The “Suradas” are associated with high-pressure systems that can occur at any time of the year, mostly affecting Veracruz, Campeche, Yucatán and Quintana Roo. These anticyclonic systems provide warm, stable conditions although, but the speed of the dry winds can reach over 60 kmh⁻¹ (CENAPRED, 2019).

Numerical model

The analysis undertaken here relies on hindcast data from the WW3 version 6.07 [WAVEWATCH III Development Group (WW3DG, 2019)], a third-generation wave model forced with reanalysis winds from 1979 to 2020. This model solves the random phase spectral action density balance equation for wavenumber-direction spectra (Massel, 1996). The output wave parameters of the model are the significant wave height, peak period and peak directions recorded with a time resolution of one hour.

Model set up

The WW3 model for the GoM is built on a structured mesh with a resolution of 0.1875°. The wave spectrum was discretized in 24 uniformly distributed directions and 29 frequencies distributed in a logarithmic mesh covering the interval of 0.06623–0.9551 Hz, with a frequency increase factor set at 1.1. Bathymetric and obstacle grids have a resolution of 15 arc-seconds from the GEBCO database [GEBCO Compilation

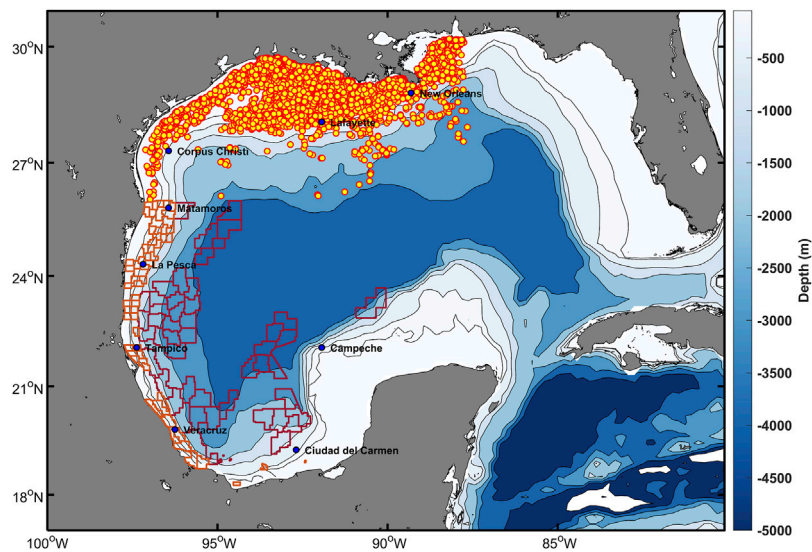


FIGURE 1

Study area, showing US offshore oil platforms (yellow dots) and oil exploitation areas in the GoM (Comisión Nacional de Hidrocarburos, CNH) in both shallow and deep water (orange and red respectively), and virtual sites (blue dots).

Group (GEBCO, 2021)]. Coastline and island data are from the high-resolution GSHHS model database (Wessel and Smith, 1996). The wind forcing is from ERA5 (Copernicus Climate Change Service (C3S), 2017) from the European Center for Mid-Range Climate Forecasting (ECMWF). This dataset, covering the period from 1979 to 2020, has temporal and spatial resolutions of one hour and 0.28° , respectively. The source term package ST4 by Ardhuin et al. (Ardhuin et al., 2010) was used to improve the duplication of wave parameters (Kalourazi et al., 2021). The time steps for the global, spatial, intra-spectral propagation and the source term integration are 1800 s, 900 s, 1350 s and 15 s.

Validation

Validation of the WW3 model was carried out by comparing the model predictions against altimetry (Jason-2, Cryosat-2 and Saral satellites) and buoy data from the NOAA Deep Sea National Buoy Data Center (NDBC) (Figure 2). The satellite data are from the Sea State project (Piollé et al., 2020) of the IFREMER-Climate Change Initiative (CCI). The WW3 results were interpolated linearly over spatial and temporal scales based on the positions of satellite trajectory observations for the periods: 01/01/2009–31/12/2017, Jason-2, 01/01/2011–31/12/2017, Cryosat-2, and 01/01/2014–31/12/2018, Saral. The altimeter data is the “along track” type, implying that when there are no altimeter data, there is no data from the model in some time periods. In the case of NDBC buoys, validation was performed according to hourly data for the significant wave height (H_s) and dominant period (T_p) over the 10-year period 2008–2017. To analyse deviations of simulated wave

variables from satellite data and buoy observations, the following statistical metrics were used: mean bias, root mean square error (RMSE) and Pierson correlation coefficient (CC). They are defined as follows:

$$\text{Bias} = \bar{s} - \bar{o}, \quad (1)$$

$$\text{RMSE} = \sqrt{\sum_{i=1}^N (s_i - o_i)^2 / N}, \quad (2)$$

$$\text{CC} = \sum_{i=1}^N (s_i - \bar{s}) (o_i - \bar{o}) / \sigma_s \sigma_o, \quad (3)$$

where N is the number of available observations, the overbar indicates a mean value, s_i indicates the simulated variable and o_i the observed variable, and σ_s and σ_o are, in respective order, the standard deviation of the simulated and observed variables.

Wave energy resource assessment

Following model validation, a total of 42 years from 1979 to 2020 was simulated. The wave power density (P) in kW/m for deep water conditions is given by:

$$P = \frac{\rho g^2}{32\pi} T_e H_s^2 \quad (4)$$

where ρ is the density of seawater ($\frac{\text{kg}}{\text{m}^3}$), g is the gravity acceleration ($\frac{\text{m}}{\text{s}^2}$), T_e is the wave energy period (s), H_s is the significant wave height (m) and $T_e = 0.86 T_p$ (Guillou, 2020), with T_p being the dominant wave period (s).

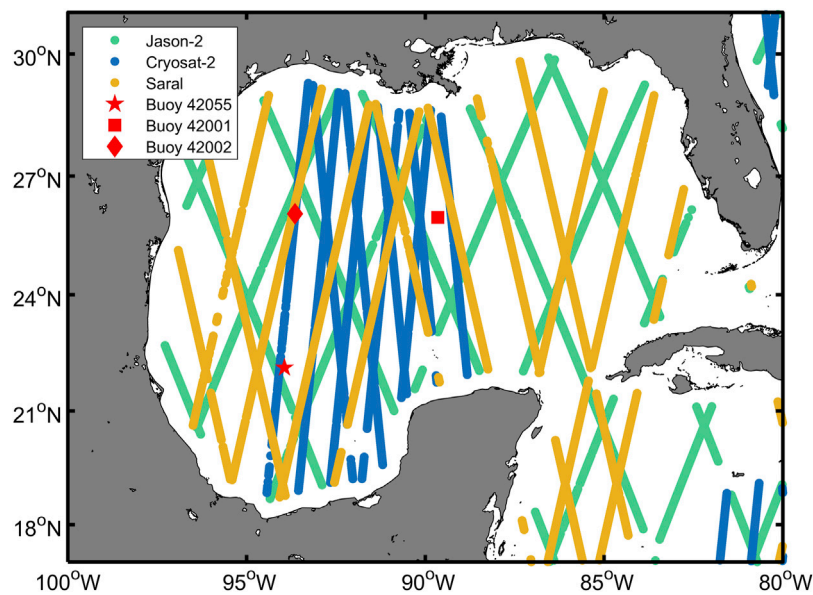


FIGURE 2
Satellite trajectories from 1st to 10th of January 2015 and NDBC buoy positions.

TABLE 1 Main characteristics of the WECs selected.

Device	Rated power (kW)	Classification	Matrix resolution	References
Pelamis	750	Attenuator	0.5 m × 0.5 s	Carcas, (2003)
OE buoy	2880	Oscillating water column	0.5 m × 1.0 s	Babarit et al. (2012)
Oceantec	500	Attenuator	0.5 m × 1.0 s	Patel et al. (2020)
Langlee	1665	Oscillating water surge converter	0.5 m × 1.0 s	Babarit et al. (2012)
Wavestar	600	Point absorber	0.5 m × 1.0 s	(Marquis et al., 2012; Ambühl et al., 2016; Heo and Koo, 2021)
Oyster	290	Terminator	0.5 m × 1.0 s	Silva et al. (2013)
AAHPA	178	Point absorber	1.0 m × 1.0 s	Aderinto and Li, (2020)

Characteristics of the selected WECs

Seven different WECs were selected for this work: Pelamis, OE Buoy, Oceantec, Langlee, Wavestar, Oyster and AAHPA. These WECs operate using different principles. Table 1 presents the main characteristics of these WECs: power rating, operating principle and power matrix resolution. The manufacturers of the WECs specify these performance characteristics in terms of a power matrix. This gives a representation of the WEC response in terms of average power output, using the two sea state parameters (H_s and T_e or T_p). The power captured by the WEC is the product of the power matrix of the device and the number of sea state hours represented by the sea state matrix of H_s and T_e or T_p . The usefulness/applicability of the WECs evaluated depends on them being able to operate at their rated power for as long as possible in the GoM. Because the average

wave regime in the GoM is lower than the regime these WECs were designed for, the part of the power matrix with highest powers of each device is not exploited. Thus, the device with most potential is the AAHPA prototype, an oscillating buoy specifically designed for the wave conditions in South Texas.

Pelamis device

The Pelamis is a WEC consisting of a series of semi-submerged cylindrical sections, connected by hinged joints. It resists the wave-induced movement of the joints by means of hydraulic rams that pump oil at high pressure from motors running electric generators (Carcas, 2003). In 2008, 3 Pelamis devices were tested in Agucadoura (Portugal). In 2009–2010 another trial was carried out in the United Kingdom with a second generation device and another

was installed in 2012 by Scottish Power. In 2014, the company went into receivership and the intellectual property was transferred to the Scottish government body: Wave Energy Scotland (EMEC, 2022).

OE buoy device

The OE Buoy is an oscillating water column device, developed by Ocean Energy Ltd., Ireland. It has a semi-submerged open chamber below the sea surface with an air pocket held above the water column. The airflow is converted into electrical energy as the column is oscillated by incoming waves that pass the air through a two-way turbine (Babarit et al., 2012). In its early stages, a 1:50 scale model of the device was tested in Ireland, and later, a 1:15 scale model was successfully tested in France, followed by ocean trials. In 2011, a 28-tonne 1:4 scale model was installed in Galway Bay, Ireland, providing energy production data (Lavelle and Kofoed, 2011; Ocean Energy Ireland, 2017).

Oceantec device

The WEC Oceantec is an attenuator device. It extracts energy from the waves in a gyroscopic device, using the relative inertial motion caused by the waves. This motion powers an electrical generator through a series of transformation stages. The gyroscopic device is housed within a structure, or hull, that stays aligned with the wave front, giving a pitch movement. The structure containing the absorber element and the other elements is vessel-shaped and can be scaled in size, to suit the wave conditions at a given site. The mooring system consists of four lines that allow the WEC to cope with the incident wave and maximizes the absorption of directional wave energy (Patel et al., 2020). Tests were carried out in 2008, off the north coast of Spain (Salcedo et al., 2009).

Langlee device

This oscillating wave surge converter extracts kinetic energy from the orbital motion of water particles excited by waves, through a series of hinged flaps located just below the water surface. It has a series of pairs of flaps that are placed symmetrically opposite each other, mounted on a semi-submerged, floating steel frame. At suitable wavelengths, the symmetry helps to minimize the forces acting on the structure and moorings, while the flaps must complement each other to extract the maximum amount of energy (Babarit et al., 2012). The device was developed by Langlee Wave Power, based in Norway. In 2012 they conducted scale model tests at the Plataforma Oceánica de Canarias (PLOCAN) facility (Langlee Wave Power AS, 2013).

Wavestar device

The Wavestar device is a point absorber. It is essentially a group of floats that rise and fall with the movement of the waves. A hydraulic system transfers this movement, converting it into

the rotational motion of an electric generator. The Wavestar can be installed on shore, inland, or in shallow waters, or it can be adapted for deep waters, and can work in combination with at least one wind turbine (Marquis et al., 2012). In extreme events that threaten the system, the bridge is raised to a safe height, as are the arms (Drew et al., 2009; Aderinto and Li, 2019). The Wavestar system was developed in Denmark in 2000 and in 2004 a 1:40 scale model was tested in the wave tank at Aalborg University to verify the performance of the concept and document the energy data obtained. In 2005, a 1:10 scale model was constructed for ocean testing at Nissum Bredning, a coastal lagoon in Denmark where the swell size is approximately 1:10, compared to the North Sea. The device was successfully installed in 2006, accumulating 15,000 operational hours and withstanding over 15 storms with no damage to the system (WaveStar, 2019). In 2010, a 1:2 scale model was installed at a depth of 6 m. There were two versions of this 110 kW-capacity device, with different numbers of floats. The power matrix used in this research corresponds to the 20-float version with a nominal power of 600 kW.

OYSTER device

The Oyster is a device of oscillating fins fixed to the bottom. The floating hinged flipper moves back and forth with the movement of the waves, and the two hydraulic pistons pump water at high pressure to a shore-based hydroelectric station that drives an electricity-producing generator (Silva et al., 2013). The Oyster device was developed in Scotland from 2005 by the Aquamarine Power company. The first full-scale device was tested in Orkney, Scotland, and the first Oyster was installed with the help of the European Marine Energy Centre (EMEC) in 2009 (Cameron et al., 2010).

AAHPA device

The AAHPA device was designed for the wave conditions in South Texas (GoM). It consists of a cylindrical buoy that oscillates vertically through a fixed, solid frame during its interaction with the waves. The cylinder is hollow, with an inlet and an outlet that have one-way valves near to the submerged base of the device. The valves open at a certain critical wave period and close when the wave period falls to less than this. This allows resonance at two different wave frequencies. It does not have a specific mechanism for converting mechanical wave energy into electrical energy, and it is known as a self-adjusting WEC because it changes its inertia by ballasting and deballasting with seawater. As yet, this device is only a conceptual design; no tests have been performed yet.

The devices selected were designed for areas of high energy, so it is not possible to harness their full rated power. However, by studying sites with less energy important information can be gleaned for future technological development. For example, the design loads of the WEC is reduced and its probabilities of survival are increased. In addition, installation, commissioning

and maintenance are simpler, safer and less costly than at higher power sites. In areas with low power, the annual variation of sea wave energy is generally lower, while the tidal range is low (as in the GoM), facilitating the installation, operation and maintenance of these WECs (Foteinis, 2022).

Multi-criteria approach

The multi-criteria approach (MCA) index was introduced by (Kamranzad and Hadadpour, 2020) and later modified by (Kamranzad et al., 2021). It is used to compare energy extraction using different WECs at specific sites. The calculation of the index involves different variables: the exploitable energy at the site (E_e), the accessibility, the availability, the energy production of the WECs (E_o), calculated from the sea state matrix of each site and the power matrix of the WECs, the monthly variability index (MV_{E_o}) and the 99th percentile of H_s ($H_{s,99}$). However, it does not take into account factors such as the levelized cost of energy, lifetime of devices, installation and operation costs, distance to energy consumption centres, and other important factors. Therefore, this method is mainly used to compare the type of technology that might be suitable at a given site, it is a decision-making tool to compare the suitability of WECs/sites. Although the choice is limited by the above factors, the MCA index can be used to rank the performance of WECs, not only in terms of their energy output, but also their stability. Nine sites, close to oil platforms in the GoM, were selected (Figure 1).

The total and exploitable wave energy per unit area (E_t and E_e , respectively) are given by:

$$E_t = P_{\text{mean}} t \quad (5)$$

$$E_e = P_{\text{mean}} t_e \quad (6)$$

where t is the total hours per year (8760 h), t_e is the theoretical exploitable time, that is the total hours corresponding to $P > 2 \text{ kW/m}$ (Zheng et al., 2013), and P_{mean} is the mean wave power.

Accessibility refers to the percentage of time that marine conditions are favorable for the operation and maintenance of WEC activities offshore. The wave height threshold taken into account is that of Lavidas et al. (Lavidas et al., 2018), ranging from 1.5 to 4 m with increments of 0.5 m. Availability is calculated according to the percentage of time that the wave resource is favorable to WEC operations. As a result of Lavidas et al. (Lavidas et al., 2018), we are considering WECs suitable for high and low resources in terms of a wave height cut-in ($H_{\text{cut-in}}$) and cut-off ($H_{\text{cut-off}}$) of 0.5 and 4 m respectively. The analysis of extreme events is based on the 99th and 95th percentiles of H_s .

The performance of each WEC at the different sites is assessed in relation to energy production (E_o).

$$E_o = \sum_{i=1}^{n_T} \sum_{j=1}^{n_H} P_{ij} P_{ij} \quad (7)$$

where, n_T and n_H represent n bin of T_p or T_e and H_s , respectively, p_{ij} represents the percentage of occurrences in each sea state is determined by H_s and the energy period T_e , and P_{ij} is the rated power matrix supplied by each WEC manufacturer.

Energy production of a WEC at a given site is estimated from Eq. 7, which uses the power matrix of a device with the sea state matrix. The values of Table 3 were estimated by multiplying the expected energy production of each interval of the power matrix by the expected number of hours/year of occurrence of that interval. For this purpose, the wave climate data were represented using a sea state matrix with the same resolution (i.e. same size of height and period intervals) as the power matrix of each WEC, to show the different wave conditions at each of the sites. The annual energy production was then calculated by summing the records for each year, and finally, the average annual production was estimated by taking the 42-years average of the dataset. Energy production was calculated on a monthly and an annual basis. The general characteristics of the WECs selected are described in Table 1 and the power matrices of the WECs were obtained from the references consulted. It is important to note that the power matrix used for the AAHPA device is approximate, derived from the results of the work of (Aderinto and Li, 2020).

The variability of the wave resource follows the monthly variability index (MV) provided by (Cornett, 2008).

$$MV = \frac{P_{M1} - P_{M12}}{\bar{P}} \quad (8)$$

where P_{M1} and P_{M12} are the mean power of the waves for the most and the least energetic month respectively, and \bar{P} is the mean wave power.

Combination of all the above factors constitutes the multi-criteria factor for the selection of a wave energy harvesting site (Kamranzad et al., 2021),

$$MCA = \left(\frac{\frac{E_e}{\max(E_e)} \times \text{accessibility}_{(H_s < 1.5)} \times \text{availability} \times \frac{E_o}{\max(E_o)} \times \frac{\min(H_{s,99})}{H_{s,99}}}{MV_{E_o}} \right) \quad (9)$$

where annual values of $H_s < 1.5$ are considered for accessibility. A higher MCA value indicates a better match for a location/WEC combination, allowing a classification of the WEC performance, according to its energy production and stability.

Results and discussion

Validation

The results obtained from the WW3 model were successfully validated in terms of 10 years daily means of H_s and T_p from the buoy 42,055 (Figure 3 and Table 2). The highest waves and periods occur in winter, coinciding with the passage of cold

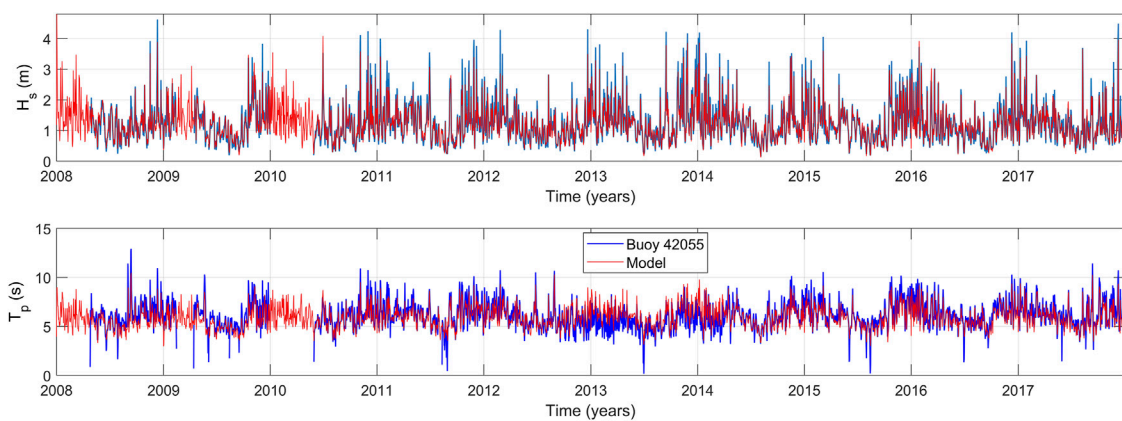


FIGURE 3

Comparison between simulated and observed wave parameters from NDBC buoy 42,055 for 2008–2017.

TABLE 2 Validation metrics based on NDBC buoys and satellite data.

Buoy	Variable	Bias	RMSE	CC
42,055	Hs (m)	0.02	0.22	0.95
	Tp (s)	0.38	0.9	0.84
42,001	Hs (m)	0.02	0.21	0.95
	Tp (s)	0.61	1.25	0.70
42,002	Hs (m)	0.04	0.21	0.95
	Tp (s)	0.54	1	0.81
Jason-2	Hs (m)	−0.26	0.33	0.92
Cryosat-2	—	−0.2	0.29	0.93
Saral	—	−0.24	0.31	0.93

fronts (CF). In summer, periods of calm can be disrupted by tropical cyclones (Figure 4). The WW3 model tends to underestimate the maximum significant height of the buoys, measured in extreme events (Figure 5), probably due to the underestimation of the ERA5 maximum winds. Overall, both the modelled and *in situ* data from the NDBC buoys in the GoM show good correlation coefficients (> 0.9 for H_s and ≥ 0.7 for T_p) and root mean square errors (< 0.3 m and < 1.3 s). To simplify, the results for buoy 42,002 are not presented. The statistical metrics obtained are comparable to those found in other works using the WW3 model (e.g. (Sangalugeme et al., 2018; Sun et al., 2020)). However, the variation in the correlation coefficients for T_p reflects the failure of the model to represent local extreme events and long period swells accurately. For both NDBC buoy and altimetry in the GoM, the values in Table 2 indicate good agreement between the model data and the *in-situ* observations.

Figure 6 shows the comparison of the time series of H_s from the Jason-2 satellite with the WW3 model, which are in good agreement. The significant height of the satellite is in positive

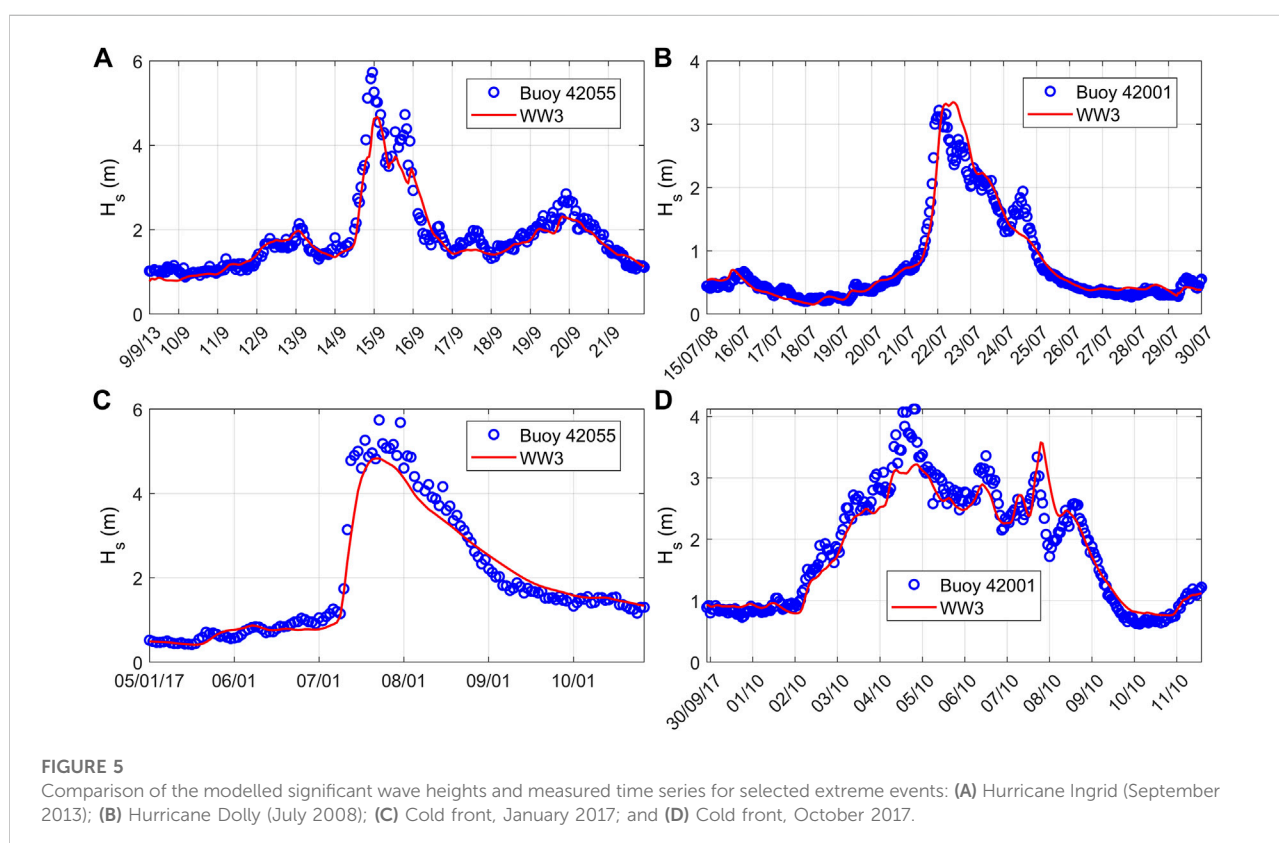
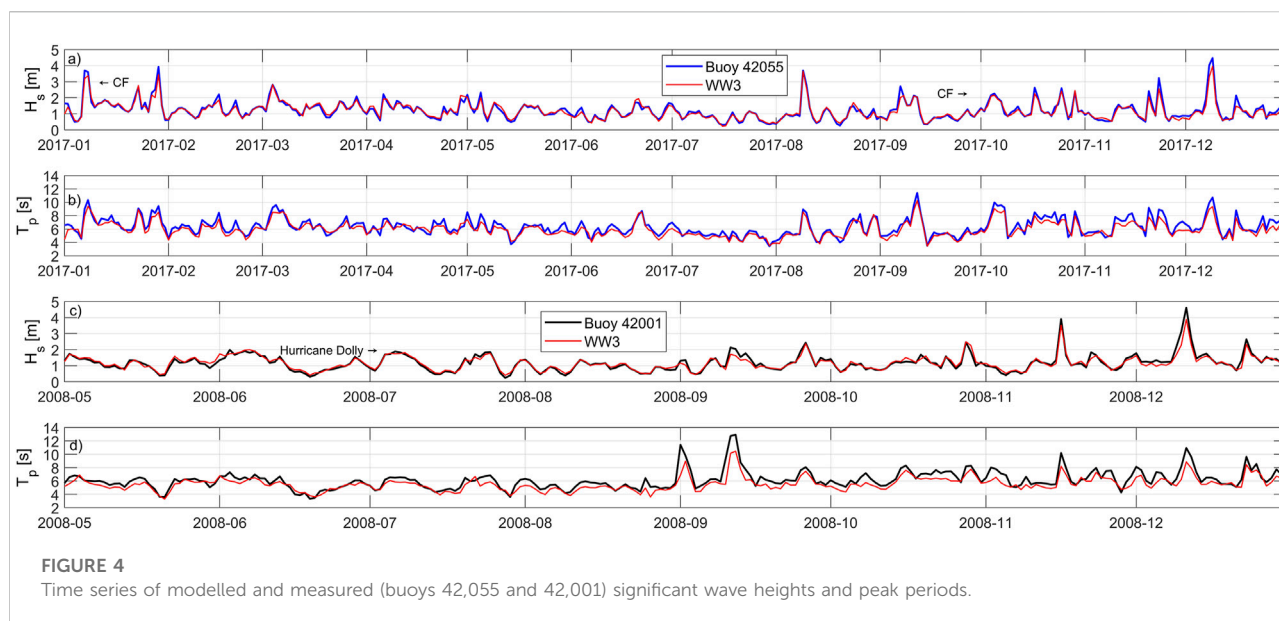
correlation with the modelled significant height (Figure 7). Referring to the data in Table 2 the negative bias implies that the model tends to underestimate the satellite data. For H_s , CC is greater than 0.9 and RMSE is roughly 0.3 m.

Wave power spatial distribution and wave climate characteristics

In this section the results of the theoretical wave power in the GoM, that is, the spatial distribution of the mean wave power, the percentiles of the wave power and the seasonality of the mean wave power are described.

In general, mean wave power in the GoM is low. It is seen in Figure 8 that the highest mean wave power is off the west coast of the GoM (> 5 kW/m). Data from the virtual buoys, shown in Figure 1, shows that in deep water the mean wave power is about 2–5 kW/m, while closer to the coast, the mean wave power is less than 2 kW/m.

Figure 9 depicts the 25th, 50th, 75th and 99th percentiles of wave power for the 42-years interval. The maximum values for all percentiles are in the northwest of the GoM, at approximately the same position as the wave power mean maximums. The latter coincides with the results of Haces-Fernández et al. (Haces-Fernández et al., 2018) and Félix et al. (Félix et al., 2018) who identified the west of the GoM as promising for the harnessing of wave energy for electricity. Nevertheless, with the exception of the 99th percentile, maximum values are found on the coast of Veracruz. The 50th percentile, the median, does not exceed 3 kW/m in the entire GoM. For the 75th percentile, the same distribution occurs with maximum values in the west of the GoM. However, maximum values can reach 6 kW/m. Regarding the 99th percentile, the observed values are between 10 and 55 kW/m, with a maximum of 55 kW/m in the southwest of the GoM.



The mean wave power for each season of the year was also calculated, based on the 42-year period (Figure 10). The season with the highest wave power is winter, with an average of 6 kW/m

and maximum values in excess of 8 kW/m. In autumn and spring, the mean wave power is 4 kW/m with maximum values of 5.5 kW/m. The least energetic season is the summer

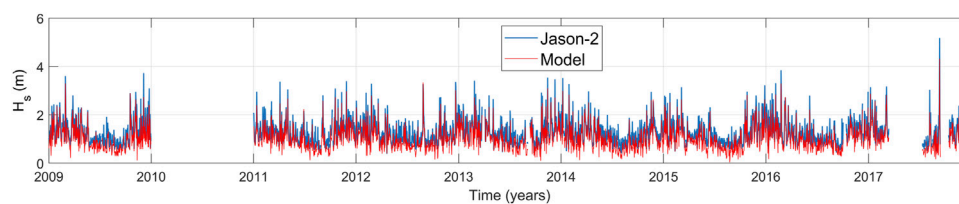


FIGURE 6

Time series of modelled and measured significant wave heights from the Jason-2 satellite.

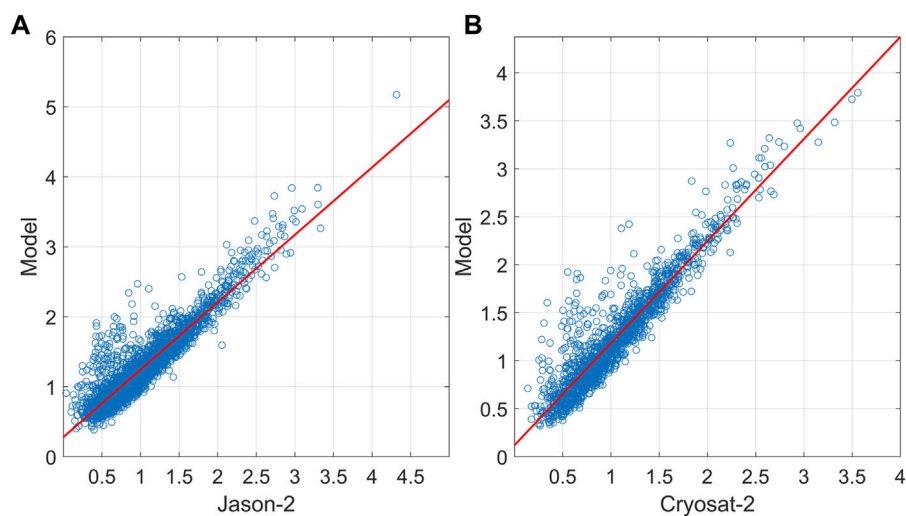


FIGURE 7

Scatter plots of the significant wave heights of modelled and satellite data: (A) Jason-2; (B) Cryosat-2.

with a mean of 2 kW/m and minimum values of up to 0.5 kW/m. The findings reported here agree with those of Félix et al. (Félix et al., 2018) and the global trend (Cornett, 2008; Gunn and Stock-Williams, 2012).

MCA factor

The results of the MCA factor, shown in this section encompass essential aspects for estimating long-term energy potential for possible WEC devices and sites. The MCA factor includes aspects such as total and exploitable wave energy at the site, accessibility, availability, annual energy production, monthly variability, as well as extreme values. The results shown are for 9 sites in the GoM, selected for their proximity to oil activity (Figure 1) where electricity generated from wave energy would make a considerable contribution to the carbon footprint. Nearby locations to these platforms areas were used to aid identification:

New Orleans (New), Lafayette (Laf), Corpus Christi (Cor), Matamoros (Mat), La Pesca (Pes), Tampico (Tam), Veracruz (Ver), Ciudad del Carmen (Car) and Campeche (Cam).

The annual exploitable energy (E_e) considers the average power and the number of hours that the power is over 2 kW/m (Lavidas et al., 2018). The E_e varies between 11.9 (Lafayette) and 30.5 MWh/m (Matamoros) (Figure 11A), although La Pesca, Corpus Christi and Campeche also have high E_e values. The ratio of exploitable energy to total energy ($\frac{E_e}{E_t}$) is 40–67%, with Matamoros having the highest value and Lafayette the lowest (Figure 11B). The values seen in the GoM are high compared to those for the Caspian Sea, Persian Gulf and Gulf of Oman (Kamranzad and Hadadpour, 2020) where the highest value was 19%. However, another study in the Indian Ocean (Amrutha and Sanil Kumar, 2022) found sites with values of up to 99.7%. Therefore, the GoM is considered to have a moderate ratio of exploitable to total energy ($\frac{E_e}{E_t}$).

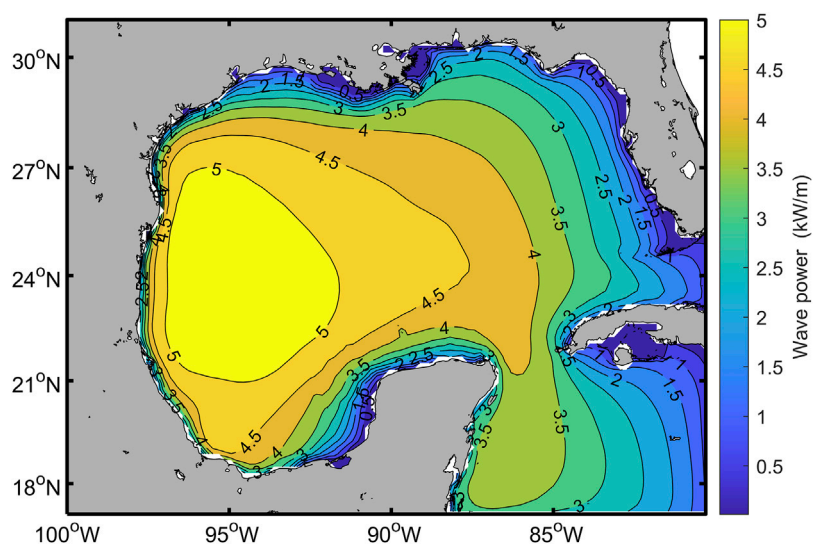


FIGURE 8
Spatial distribution of mean wave power.

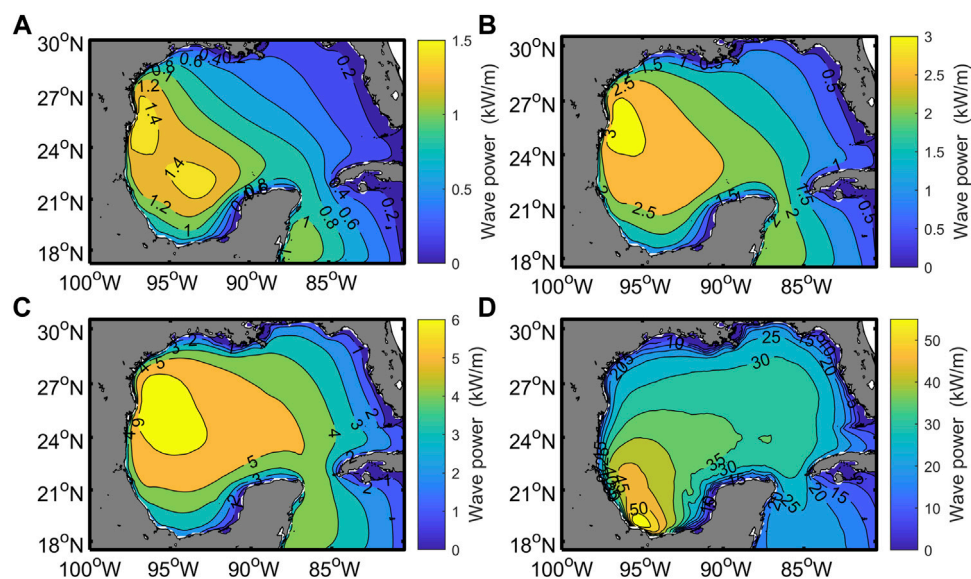


FIGURE 9
Wave power (kW/m) percentile maps: (A) 25th; (B) 50th; (C) 75th; and (D) 99th. Note the scale in the colour bands is different.

Another factor considered in the MCA is accessibility, defined as the percentage of time in which it is possible to operate a device at a given site, or perform maintenance operations. This parameter is determined according to H_s thresholds. Figure 11C shows accessibility values on an annual scale in the categories defined. For the 9 sites considered, the H_s is less than 2 m 94% of the time. Values of $H_s < 1.5$ m at the 9 sites

vary between 72.5 and 88.8% of the time and are used to calculate the MCA factor. The WECs would be accessible most of the time, except during extreme events.

Figure 11D shows the availability values, indicating the percentage of time when the wave resource favors the operation of the WEC devices. Availability is greater than 74% at all sites. The highest and lowest values are at La Pesca

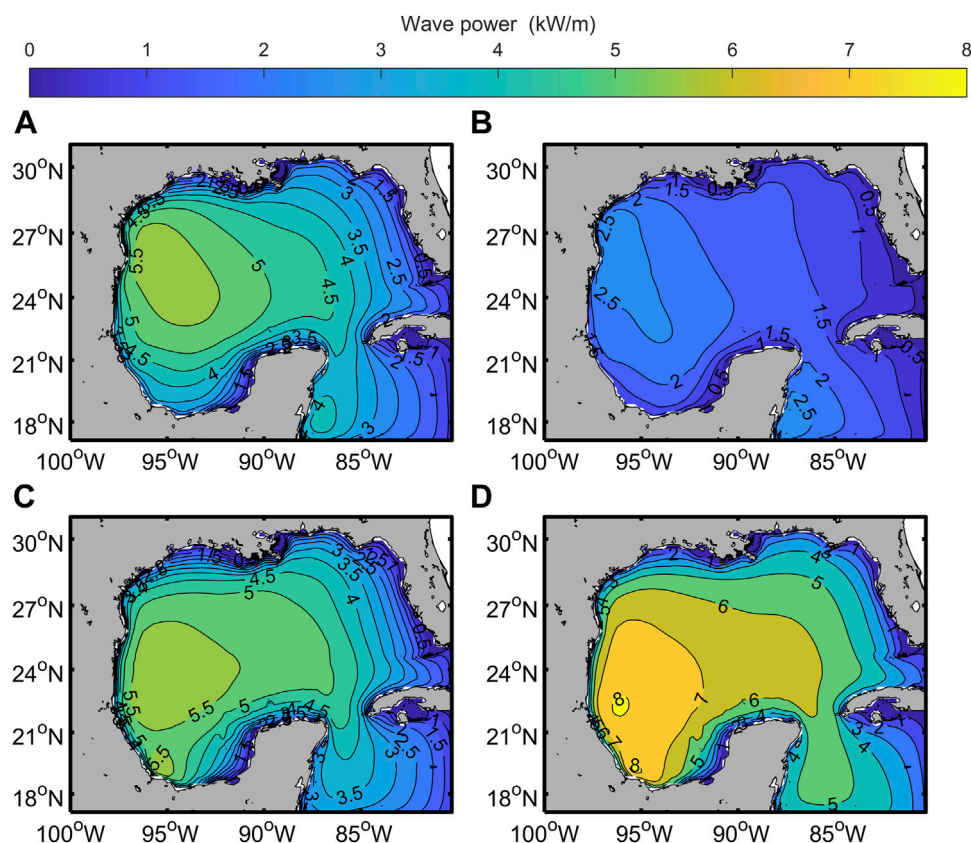


FIGURE 10
Seasonal mean wave power maps: (A) spring; (B) summer; (C) autumn; and (D) winter.

and Lafayette, respectively. The values for these sites are high compared to the annual availability value reported of 55.21% in the Gulf of Oman (Kamranzad and Hadadpour, 2020) and various sites in the Indian Ocean (Amrutha and Sanil Kumar, 2022), which range from 50% to about 97%. The H_{99} percentile value is also considered in the MCA factor. For the sites studied, this is 2.74 m for Corpus Christi and 3.15 m for Campeche. The range of values is narrow (Figure 11E).

Table 3 shows the annual energy production (E_o), a parameter that allows the local conditions at the study sites for the WECs to be evaluated. The E_o values for the various WECs are between 83 (OE Buoy) and 1733 MWh (Wavestar). For all WECs, except the OE Buoy, the Matamoros site has the highest E_o values.

In addition to the annual energy production (E_o), the variability of energy at the site must be considered. The variability indexes calculated for each device and the 9 sites are shown in Figure 12. The AAHPA device has the lowest monthly MVI_{E_o} variability at all the sites. The MVI_{E_o} intervals are between 2.2 (OE Buoy at the Ciudad del Carmen site) and 0.55 (OE Buoy at the Lafayette site). The more northerly sites

(New, Laf, Cof, Mat, Pes) have lower MVI_{E_o} values than those in the south.

The MCA factor was calculated for all sites (Figure 13), allowing comparison of the performance of the WECs at each study site. For 7 sites, the AAHPA is the most suitable WEC, followed by the Wavestar at the other two sites. Corpus Christi site and the sites in Tamaulipas have the highest values of the MCA factor.

The Wavestar WEC is described as a point absorber (Marquis et al., 2012; Ambühl et al., 2016; Heo and Koo, 2021), oscillating body system or wave activated system (Chen et al., 2018; Curto et al., 2021), or attenuator (Amrutha and Sanil Kumar, 2022). It is essentially a group of floats whose operation does not depend on the direction of the waves, ascending and descending with the upward and downward motion of the waves. This device is small in size, compared to the wavelength, with smaller horizontal dimensions than the vertical. It can float on the sea surface or below the water, relying on the pressure differential (Drew et al., 2009; Aderinto and Li, 2019; Farrok et al., 2020). It is promising as a WEC prototype, capable of changing the inertia of the oscillating body using seawater as ballast and de-ballasting to

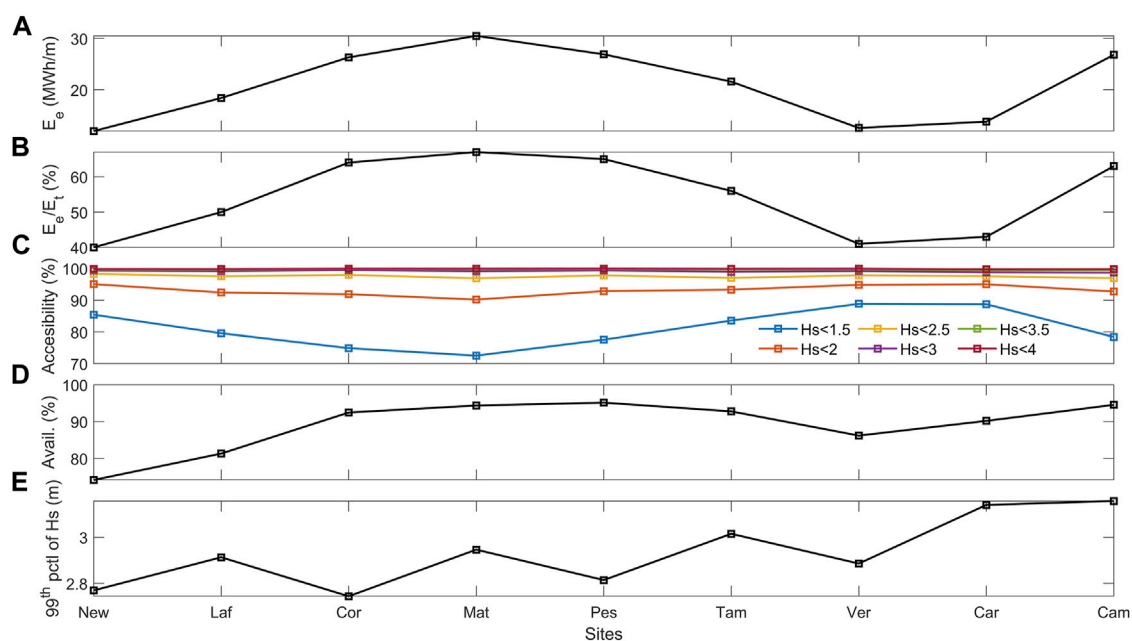


FIGURE 11

(A) Annual Exploitable energy; (B) percentage of the ratio of exploitable energy to total energy; (C) annual accessibility; (D) annual availability; and (E) 99th percentile values of H_s for different locations in 9 sites in the GoM.

TABLE 3 Annual energy production at each site in the GoM.

		New Orleans	Lafayette	Corpus Christi	Matamoros	La Pesca	Tampico	Veracruz	Ciudad del Carmen	Campeche
E_o (MWh)	Pelamis	117	156	177	213	188	191	150	144	191
	OEBuoy	83	98	103	125	116	131	116	120	131
	Oceantec	324	451	545	638	551	490	333	300	500
	Langlee	230	310	370	419	368	319	216	225	362
	Wavestar	1029	1322	1609	1733	1594	1414	1108	1040	1526
	Oyster	146	204	245	284	242	218	157	145	229
	AAHPA	193	243	284	303	275	240	180	179	277

achieve resonance with two different wave frequencies (Aderinto and Li, 2020).

In areas with a high wave climate, the movements of WECs are limited in storms, to ensure their survival (Stuhlmeier and Xu, 2018); they do not generate electricity. However, in low-energy areas, such as GoM, storm survival is not a major issue (Lavidas, 2019). However, existing types of WECs would only fully function during relatively infrequent high-energy storms and waves (Foteinis et al., 2017), since low-energy waves could not drive them. The reason for this is that the power matrix of the European WECs cannot be used to capacity with the average sea state of the GoM. The range of significant heights and energy

periods obtained for the sea state matrix was $0 < H_s < 3.5$ m, $0 < T_p < 9$. In the WECs evaluated in this research, approximately 60–80% of the power matrices cannot be used, as the nominal power and peak powers are in higher ranges than GoM sea state matrices. The storm fronts that affect the GoM for half of the year, can be used to harvest energy (cold fronts and tropical cyclones), through semi-submerged devices, such as oscillating buoys.

The power matrices of the converters evaluated in this research: Pelamis, OE Buoy, Oceantec, Langlee, WaveStar, Oyster and AAHPA, are added as a [Supplementary Material](#).

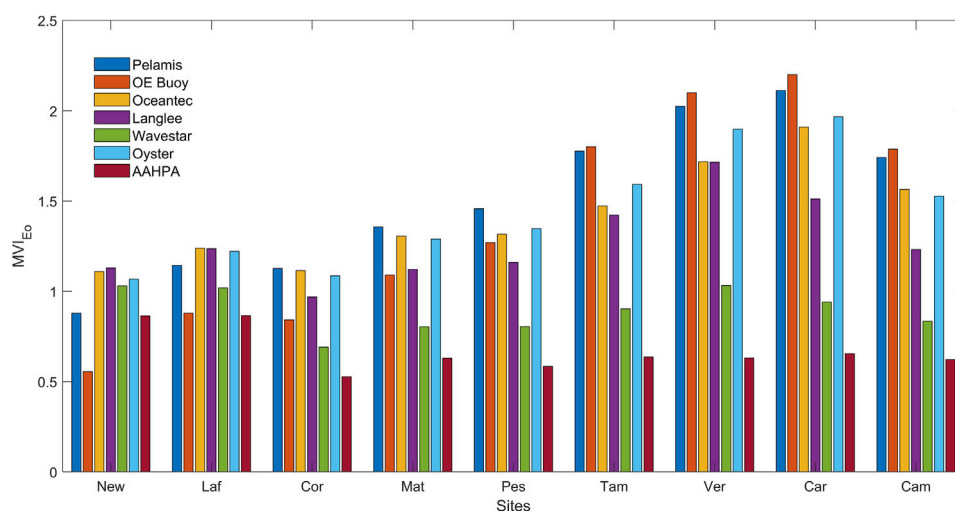


FIGURE 12
Monthly variability of E_0 of different WECs for the 9 sites.

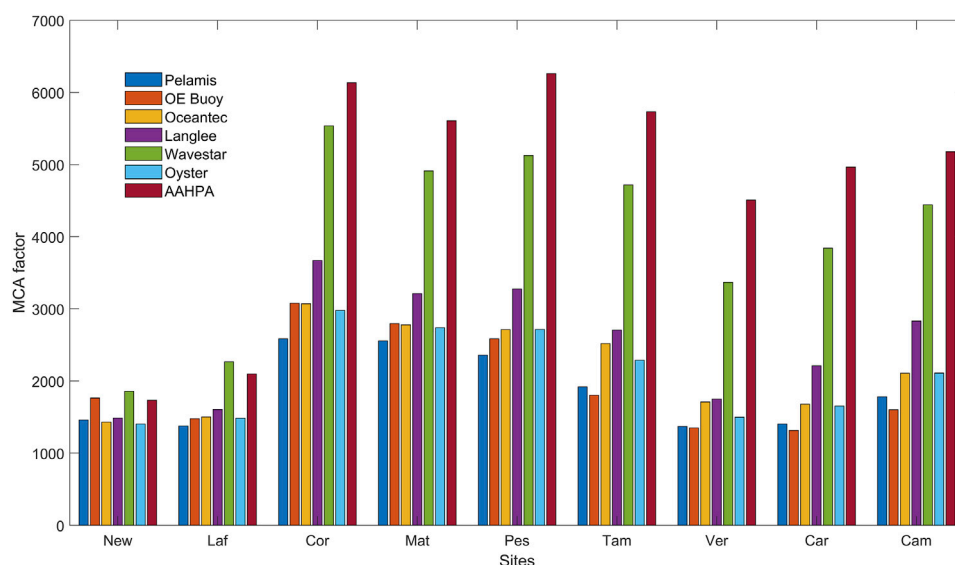


FIGURE 13
Multi-Criteria-Approach factor of different WECs for the 9 sites.

Conclusion

From analysis of wave power in the GoM, using simulated data from the WW3 numerical model with ERA-5 wind-forcing, good mean correlation coefficients and root mean squares were found when compared to the significant heights obtained from the Jason-2, Cryosat-2, and Saral satellites. While the WW3 model tends to underestimate storms, such

as atmospheric frontal systems and hurricanes, the mean wave power was found to be 4 kW/m (variation coefficient 2), indicating unstable wave conditions. The month with the highest mean wave power was January (5.5 kW/m) and the lowest was July (2.5 kW/m). Winter was the most energetic season in the GoM, and summer the least. The monthly and seasonal variability in wave power was moderate.

Using the multi-criteria approach, AAHPA and Wavestar technology were found to be the most viable WEC devices at most of the GoM sites evaluated in this study. The functioning of these two WECs work uses an oscillating buoy. For the offshore sites assessed, Corpus Christi, Matamoros, La Pesca, and Tampico had the highest MCA values. A farm of submerged, wave activated devices would seem to be the most feasible alternative. These could provide electricity for nearby oil rigs, e.g., lighting, communications and impressed current cathodic protection to prevent underwater corrosion. Other possible end-uses could be the supply of electricity to power the electric motors used by fleets of fishing vessels, either via supply stations or by electricity repositories. For nearshore sites, oscillating buoys are probably suitable, offering similar services. In addition to these end-uses of the electricity generated by wave power, water desalination plants in the area could also benefit from more sustainably produced energy.

The provision of electricity from the harnessing of wave power to isolated and socially marginalized communities around the 9 sites assessed would also be a possible goal. As of now, there are no wave powered energy generating plants in the GoM, as indeed is the case in the rest of the world.

If we are to meet the commitments made in the various internationally signed treaties to produce more energy from sustainable, clean sources, and to reduce our dependency on fossil fuels, every potential avenue must be evaluated. We believe that there is a future for marine energy, particularly wave powered electricity generation in the GoM. Nevertheless, substantial wave-to-wire simulations and economic assessments are still required to improve the attractiveness of such projects. Investigation into capital and operational expenditures, as well as levelized cost of energy studies are vital to assure commercial success.

The GoM, in common with many other places in the world, has not been considered suitable for wave energy harvesting as it does not have high energy potential. Existing European WECs do not work efficiently with the low energy waves of the GoM, and would have to be adapted, elevating costs and thus becoming less attractive to potential investors. However, this study shows that for areas with prevailing wave periods of 5–8 s, floating buoy systems are viable, technically and economically in the near future.

Data availability statement

The raw data supporting the conclusion of this article will be made available by the authors, without undue reservation.

Author contributions

MD-M.: conceptualization, methodology, software, validation, formal analysis, investigation, writing—original draft preparation, visualization. MU: conceptualization, methodology, formal analysis, investigation, writing—original draft preparation, writing—review and editing, supervision, funding acquisition. RS: conceptualization, formal analysis, writing—review and editing, supervision, funding acquisition.

Funding

This research was funded by the Fondo de Sustentabilidad CONACYT-SENER (Consejo Nacional de Ciencia y Tecnología-Secretaría de Energía) through the Centro Mexicano de Innovación en Energías del Océano (CEMIE-Océano), Grant Number 249795.

Acknowledgments

MD-M is grateful for the support provided by the CONACyT doctoral scholarship.

Conflict of interest

The authors declare that the research was conducted in the absence of any commercial or financial relationships that could be construed as a potential conflict of interest.

Publisher's note

All claims expressed in this article are solely those of the authors and do not necessarily represent those of their affiliated organizations, or those of the publisher, the editors and the reviewers. Any product that may be evaluated in this article, or claim that may be made by its manufacturer, is not guaranteed or endorsed by the publisher.

Supplementary material

The Supplementary Material for this article can be found online at: <https://www.frontiersin.org/articles/10.3389/fenrg.2022.929625/full#supplementary-material>

References

- Aderinto, T., and Li, H. (2020). Conceptual design and simulation of a self-adjustable heaving point Absorber based wave energy converter. *Energies* 13 (8), 1997. doi:10.3390/en13081997
- Aderinto, T., and Li, H. (2019). Review on power performance and efficiency of wave energy converters. *Energies* 12 (22), 4329. doi:10.3390/en12224329
- Ambühl, S., Kramer, M., and Dalsgaard Sørensen, J. (2016). Structural reliability of plain bearings for wave energy converter applications. *Energies* 9 (2), 118. doi:10.3390/en9020118
- Amrutha, M. M., and Sanil Kumar, V. (2022). Evaluation of a few wave energy converters for the Indian shelf seas based on available wave power. *Ocean. Eng.* 244, 110360. doi:10.1016/j.oceaneng.2021.110360
- Appendini, C. M., Torres-Freyermuth, A., Salles, P., López-González, J., and Mendoza, E. T. (2014). Wave climate and trends for the Gulf of Mexico: A 30-yr wave hindcast. *J. Clim.* 27 (4), 1619–1632. doi:10.1175/JCLI-D-13-00206.1
- Appendini, C. M., Urbano-Latorre, C. P., Figueroa, B., Dagua-Paz, C. J., Torres-Freyermuth, A., and Salles, P. (2015). Wave energy potential assessment in the Caribbean Low Level Jet using wave hindcast information. *Appl. Energy* 137, 375–384. doi:10.1016/j.apenergy.2014.10.038
- Ardhuin, F., Rogers, E., Babanin, A. V., Filipot, J.-F., Magne, R., Roland, A., et al. (2010). Semiempirical dissipation source functions for ocean waves. Part I: Definition, calibration, and validation. *J. Phys. Oceanogr.* 40 (9), 1917–1941. doi:10.1175/2010jpo4324.1
- Babarit, A., Hals, J., Muliawan, M. J., Kurniawan, A., Moan, T., and Krokstad, J. (2012). Numerical benchmarking study of a selection of wave energy converters. *Renew. Energy* 41, 44–63. doi:10.1016/j.renene.2011.10.002
- Bureau of Safety and Environmental Enforcement (2019). How many platforms are in the Gulf of Mexico? [Online]. Available at: <https://www.bsee.gov/faqs/how-many-platforms-are-in-the-gulf-of-mexico>.
- Cameron, L., Doherty, R., Henry, A., Doherty, K., Van't Hoff, J., Kaye, D., et al. (2010). "Design of the next generation of the Oyster wave energy converter," in *3rd international conference on ocean energy* (Spain: ICOE Bilbao), 1e12.
- Carcas, M. C. (2003). The OPD Pelamis WEC: Current status and onward programme (2002). *Int. J. Ambient Energy* 24 (1), 21–28. doi:10.1080/01430750.2003.9674899
- Centro Nacional de Prevención de desastres (CENAPRED) (2019). Vientos del sur, surada. [Online]. Available at: <https://www.gob.mx/cenapred/articulos/vientos-del-sur-surada> (Accessed February 17, 2022).
- Chen, W.-x., Gao, F., and Meng, X.-d. (2018). Oscillating body design for a 3-DOF wave energy converter. *China Ocean. Eng.* 32 (4), 453–460. doi:10.1007/s13344-018-0047-4
- CONAGUA, S. (2019). *Reporte del Clima en México*. reporte anual [Online]. Available at: <https://smn.conagua.gob.mx/tools/DATA/Climatolog%C3%ADa/Diagn%C3%B3stico%20Atmosf%C3%A9rico/Reporte%20del%20Clima%20en%20M%C3%A9xico/Anual2019.pdf>.
- Copernicus Climate Change Service (C3S) (2019). "ERA5: Fifth generation of ECMWF atmospheric reanalyses of the global climate," in *Copernicus climate change Service climate data store (CDS)*. [Online]. Available at: <https://cds.climate.copernicus.eu/cdsapp#!/home>.
- Cornett, A. M. (2008). "A global wave energy resource assessment," in *The eighteenth international offshore and polar engineering conference*. ISOPE-I-08-370.
- Curto, D., Franzitta, V., and Guercio, A. (2021). sea wave energy: A review of the current technologies and perspectives. *Energies* 14 (20), 6604. doi:10.3390/en14206604
- Drew, B., Plummer, A. R., and Sahinkaya, M. N. (2009). A review of wave energy converter technology. *Proc. Institution Mech. Eng. Part A J. Power Energy* 223 (8), 887–902. doi:10.1243/09576509JPE782
- EMEC (2022). *Pelamis wave power*. [Online]. Available at: www.emec.org.uk/about-us/wave-clients/pelamis-wave-power (Accessed 07 15, 2022).
- Farrok, O., Ahmed, K., Tahlil, A. D., Farah, M. M., Kiran, M. R., and Islam, M. R. (2020). Electrical power generation from the oceanic wave for sustainable advancement in renewable energy technologies. *Sustainability* 12 (6), 2178. doi:10.3390/su12062178
- Felix, A., Mendoza, E., Chávez, V., Silva, R., and Rivillas-Ospina, G. (2018). Wave and wind energy potential including extreme events: A case study of Mexico. *J. Coast. Res.* 85 (1), 1336–1340. doi:10.2112/SI85-268.1
- Foteinis, S., Hancock, J., Mazarakis, N., Tsoutsos, T., and Synolakis, C. E. (2017). A comparative analysis of wave power in the nearshore by WAM estimates and *in-situ* (AWAC) measurements. The case study of Varkiza, Athens, Greece. *Energy* 138, 500–508. doi:10.1016/j.energy.2017.07.061
- Foteinis, S. (2022). Wave energy converters in low energy seas: Current state and opportunities. *Renew. Sustain. Energy Rev.* 162, 112448. doi:10.1016/j.rser.2022.112448
- GEBCO Compilation Group (GEBCO) (2021). GEBCO 2021 grid. [Online]. Available at: https://www.gebco.net/data_and_products/gridded_bathymetry_data/.
- Guiberteau, K., Lee, J., Liu, Y., Dou, Y., and Kozman, T. A. (2015). Wave energy converters and design considerations for Gulf of Mexico. *Distributed Generation Altern. Energy J.* 30 (4), 55–76. doi:10.1080/21563306.2015.11667613
- Guillou, N., and Chapalain, G. (2020). Assessment of wave power variability and exploitation with a long-term hindcast database. *Renew. Energy* 154, 1272–1282. doi:10.1016/j.renene.2020.03.076
- Guillou, N. (2020). Estimating wave energy flux from significant wave height and peak period. *Renew. Energy* 155, 1383–1393. doi:10.1016/j.renene.2020.03.124
- Gunn, K., and Stock-Williams, C. (2012). Quantifying the global wave power resource. *Renew. Energy* 44, 296–304. doi:10.1016/j.renene.2012.01.101
- Haces-Fernandez, F., Li, H., and Ramirez, D. (2018). Assessment of the potential of energy extracted from waves and wind to supply offshore oil platforms operating in the Gulf of Mexico. *Energies* 11 (5), 1084. doi:10.3390/en11051084
- Heo, S., and Koo, W. (2021). Dynamic response analysis of a wavestar-type wave energy converter using augmented formulation in Korean nearshore areas. *Processes* 9 (10), 1721. doi:10.3390/pr9101721
- Hernández-Fontes, J. V., Felix, A., Mendoza, E., Cueto, Y. R., and Silva, R. (2019). On the marine energy resources of Mexico. *J. Mar. Sci. Eng.* 7 (6), 191. doi:10.3390/jmse7060191
- Kalourazi, M. Y., Siadatmousavi, S. M., Yeganeh-Bakhtiyari, A., and Jose, F. (2021). WAVEWATCH-III source terms evaluation for optimizing hurricane wave modeling: A case study of hurricane ivan. *Oceanologia* 63 (2), 194–213. doi:10.1016/j.oceano.2020.12.001
- Kamranzad, B., and Hadadpour, S. (2020). A multi-criteria approach for selection of wave energy converter/location. *Energy* 204, 117924. doi:10.1016/j.energy.2020.117924
- Kamranzad, B., Lin, P., and Iglesias, G. (2021). Combining methodologies on the impact of inter and intra-annual variation of wave energy on selection of suitable location and technology. *Renew. Energy* 172, 697–713. doi:10.1016/j.renene.2021.03.062
- Langlee Wave Power AS (2013). Langlee: Innovation for a better solution. [Online]. Available at: www.langleewp.com/?q=langlee-story (Accessed 07 15, 2022).
- Lavelle, J., and Kofoed, J. P. (2011). *Power production analysis of the OE buoy WEC for the cores project*. Department of Civil Engineering, Aalborg University. Technical reports No. 119.
- Lavidas, G., Agarwal, A., and Venugopal, V. (2018). Availability and accessibility for offshore operations in the mediterranean sea. *J. Waterw. Port. Coast. Ocean. Eng.* 144 (6), 05018006. doi:10.1061/(ASCE)WW.1943-5460.0000467
- Lavidas, G. (2019). Energy and socio-economic benefits from the development of wave energy in Greece. *Renew. Energy* 132, 1290–1300. doi:10.1016/j.renene.2018.09.007
- Marquis, L., Kramer, M., Kringelum, J., Chozas, J. F., and Helstrup, N. E. (2012). "Introduction of wavestar wave energy converters at the Danish offshore wind power plant horns rev 2," in *Paper presented at 4th international conference on Ocean Energy* Dublin, Ireland. Available at: http://www.icoe2012dublin.com/ICOE_2012/papers.html.
- Massel, S. R. (1996). "Ocean surface waves: their physics and prediction," in *Advanced Series on Ocean Engineering*. World Scientific 11, 491.
- Mørk, G., Barstow, S., Kabuth, A., and Pontes, M. T. (2010). "Assessing the global wave energy potential," in 29th International Conference on Ocean, Offshore Mechanics and Arctic Engineering, 447–454.
- Ocean Energy Ireland (2017). *Design – build – test: The Ocean Energy philosophy*. [Online]. Available at: www.oceanenergy.ie/oetechnology1/development (Accessed 07 15, 2022).
- Ojeda, E., Appendini, C. M., and Mendoza, E. T. (2017). Storm-wave trends in Mexican waters of the Gulf of Mexico and caribbean sea. *Nat. Hazards Earth Syst. Sci.* 17 (8), 1305–1317. doi:10.5194/nhess-17-1305-2017
- Patel, R. P., Nagababu, G., Arun Kumar, S. V. V., Seemanth, M., and Kachhwaha, S. S. (2020). Wave resource assessment and wave energy exploitation along the Indian coast. *Ocean. Eng.* 217, 107834. doi:10.1016/j.oceaneng.2020.107834

- Pérez, E. P., Magaña, V., Caetano, E., and Kusunoki, S. (2014). Cold surge activity over the Gulf of Mexico in a warmer climate. *Front. Earth Sci.* 2, 19. doi:10.3389/feart.2014.00019
- Pérez-Denicia, E., Fernández-Luqueño, F., Vilariño-Ayala, D., Manuel Montaña-Zetina, L., and Alfonso Maldonado-López, L. (2017). Renewable energy sources for electricity generation in Mexico: A review. *Renew. Sustain. Energy Rev.* 78, 597–613. doi:10.1016/j.rser.2017.05.009
- Piollé, J.-F., Dodet, G., and Quilfen, Y. (2020). ESA Sea State Climate Change Initiative (Sea_State_cci): Global remote sensing multi-mission along-track significant wave height, L2P product, version 1.1. *CEDA*. doi:10.5285/f91cd3ee7b6243d5b7d41b9beaf397e1
- Rosengaus, M., Jiménez, M., and Vázquez, M. (2014). “Atlas climatológico de ciclones tropicales en México,” in *México. Secretaría de Gobernación; México. Centro nacional de Prevención de Desastres (CENAPRED)* México. [Online]. Available at: https://www.acapulco.gob.mx/proteccioncivil/fasciculos/Atlas_climatologico.pdf.
- Rusu, L., and Rusu, E. (2021). Evaluation of the worldwide wave energy distribution based on ERA5 data and altimeter measurements. *Energies* 14 (2), 394. doi:10.3390/en14020394
- Salcedo, F., Ruiz-Minguela, P., Rodríguez, R., Ricci, P., and Santos, M. (2009). “Oceantec: Sea trials of a quarter scale prototype,” in *Proceedings of 8th European wave tidal energy conference*, 460–465.
- Sangalugeme, C., Luhunga, P., Kijazi, A., and Kabelwa, H. (2018). Validation of operational WAVEWATCH III wave model against satellite altimetry data over South West Indian Ocean off-coast of Tanzania. *Appl. Phys. Res.* 10 (4), 55. doi:10.5539/apr.v10n4p55
- SENER (2020). Balance nacional de Energía. [Online]. Available at: https://www.gob.mx/cms/uploads/attachment/file/707654/BALANCE_NACIONAL_ENERGIA_0403.pdf (Accessed February 17, 2022).
- Silva, D., Rusu, E., and Soares, C. G. (2013). Evaluation of various technologies for wave energy conversion in the Portuguese nearshore. *Energies* 6 (3), 1344–1364. doi:10.3390/en6031344
- Soerensen, H. C., and Weinstein, A. (2008). Ocean Energy: position paper for IPCC. *Hohmeyer Trittin*, 93–102.
- Stuhlmeier, R., and Xu, D. (2018). WEC design based on refined mean annual energy production for the Israeli Mediterranean coast. *J. Waterw. Port, Coast. Ocean Eng.* 14 (4), 06018002. doi:10.1061/(ASCE)WW.1943-5460.0000451
- Sun, Z., Zhang, H., Xu, D., Liu, X., and Ding, J. (2020). Assessment of wave power in the South China Sea based on 26-year high-resolution hindcast data. *Energy* 197, 117218. doi:10.1016/j.energy.2020.117218
- WaveStar (2019). The wavestar story. [Online]. Available at: wavestarenergy.com/projects (Accessed 07 15, 2022).
- WAVEWATCH III Development Group (WW3DG) (2019). *User manual and system documentation of WAVEWATCH III version 6.07*. College Park, MD, USA: NOAA/NWS/NCEP/MMAB, 465. Tech. Note 333Appendices [Online]. Available at: <https://raw.githubusercontent.com/wiki/NOAA-EMC/WW3/files/manual.pdf> (Accessed February 15, 2022).
- Wessel, P., and Smith, W. H. F. (1996). A global, self-consistent, hierarchical, high-resolution shoreline database. *J. Geophys. Res.* 101 (B4), 8741–8743. doi:10.1029/96JB00104
- Young, I. R., and Burchell, G. P. (1996). Hurricane generated waves as observed by satellite. *Ocean. Eng.* 23 (8), 761–776. doi:10.1016/0029-8018(96)00001-7
- Zheng, C.-w., Pan, J., and Li, J.-x. (2013). Assessing the China Sea wind energy and wave energy resources from 1988 to 2009. *Ocean. Eng.* 65, 39–48. doi:10.1016/j.oceaneng.2013.03.006



OPEN ACCESS

EDITED BY

Rahul R. Bhosale,
Qatar University, Qatar

REVIEWED BY

Ling Zhao,
China University of Geosciences Wuhan,
China
Liangdong Fan,
Shenzhen University, China

*CORRESPONDENCE

C. Herradon,
cherradon@mines.edu
N.P. Sullivan,
nsulliva@mines.edu

SPECIALTY SECTION

This article was submitted to Hydrogen
Storage and Production,
a section of the journal Frontiers in Energy
Research

RECEIVED 16 August 2022

ACCEPTED 05 September 2022

PUBLISHED 06 October 2022

CITATION

Herradon C, Le L, Meisel C, Huang J,
Chmura C, Kim YD, Cadigan C, O'Hayre R
and Sullivan NP (2022), Proton-conducting
ceramics for water electrolysis and
hydrogen production at elevated pressure.
Front. Energy Res. 10:1020960.
doi: 10.3389/fenrg.2022.1020960

COPYRIGHT

© 2022 Herradon, Le, Meisel, Huang,
Chmura, Kim, Cadigan, O'Hayre and
Sullivan. This is an open-access article
distributed under the terms of the [Creative
Commons Attribution License \(CC BY\)](#). The
use, distribution or reproduction in other
forums is permitted, provided the original
author(s) and the copyright owner(s) are
credited and that the original publication in
this journal is cited, in accordance with
accepted academic practice. No use,
distribution or reproduction is permitted
which does not comply with these terms.

Proton-conducting ceramics for water electrolysis and hydrogen production at elevated pressure

C. Herradon^{1*}, L. Le², C. Meisel³, J. Huang³, C. Chmura¹,
Y.D. Kim³, C. Cadigan¹, R. O'Hayre³ and N.P. Sullivan^{1*}¹Mechanical Engineering Department, Colorado Fuel Cell Center, Colorado School of Mines,
Golden, CO, United States, ²Pacific Northwest National Laboratory, Richland, WA, United States,
³Metallurgical and Materials Engineering Department, Colorado Center for Advanced Ceramics,
Colorado School of Mines, Golden, CO, United States

Pressurized operation is advantageous for many electrolysis and electrosynthesis technologies. The effects of pressure have been studied extensively in conventional oxygen-ion conducting solid-oxide electrochemical cells. In contrast, very few studies have examined pressurized operation in proton-conducting electroceramics. Protonic ceramics offer high proton conductivity at intermediate temperatures (~400–600°C) that are well-matched to many important thermochemical synthesis processes. Pressurized operation can bring significant additional benefits and/or provide access to synthetic pathways otherwise unavailable or thermodynamically disfavorable under ambient conditions and in higher- or lower-temperature electrochemical devices. Here we examine pressurized steam electrolysis in protonic-ceramic unit-cell stacks based on a BaCe_{0.4}Zr_{0.4}Y_{0.1}Yb_{0.1}O_{3-δ} (BCZYYb4411) electrolyte, a Ni-BZCYb4411 composite negatode (fuel electrode) and a BaCo_{0.4}Fe_{0.4}Zr_{0.1}Y_{0.1}O_{3-δ} (BCFZY) positrode (air-steam electrode). The cells are packaged within unit-cell stacks, including metallic interconnects, current collectors, sealing glasses and gaskets sealed by mechanical compression. The assembly is packaged within a stainless steel vessel for performance characterization at elevated pressure. Protonic-ceramic electrolyzer performance is analyzed at 550°C and pressures up to 12 bar_a. Increasing the operating pressure from 2.1 to 12.6 bar_a enables a 40% overall decrease in the over-potential required to drive electrolysis at 500 mA cm⁻², with a 33% decrease in the cell ohmic resistance and a 60% decrease in the cell polarization resistance. Faradaic efficiency is also found to increase with operating pressure. These performance improvements are attributed to faster electrode kinetics, improved gas transport, and beneficial changes to the defect equilibria in the protonic-ceramic electrolyte, which more than compensate for the slight increase in Nernst potential brought by pressurized operation. Electrochemical impedance spectroscopy (EIS) coupled with distribution of relaxation time (DRT) analysis provides greater insight into the fundamental processes altered by pressurized operation.

KEYWORDS

pressurized electrolysis, protonic ceramics, H₂ production, SOEC, SOFC

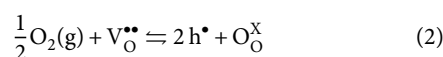
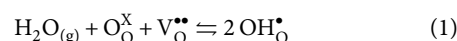
Introduction

Protonic ceramics represent an emergent class of materials that have potential utility in a number of intermediate-temperature electrochemical applications, including the production of “green” hydrogen. As shown in **Figure 1**, renewable-derived electricity can be used to drive steam electrolysis to form H₂ and O₂ products in a protonic ceramic electrolysis cell (PCEC). Typically operating in the 400–600°C temperature range, H₂O vapor carried by an air stream is fed into a gas channel adjacent to the air-steam electrode, or “positrode”. These gases diffuse through the porous positrode to the electrode-electrolyte interface, where H₂O is electrochemically split to form protons (OH[•]_O) and molecular oxygen (O₂). While the O₂ is swept out from the positrode, the OH[•]_O transports across the protonic-ceramic electrolyte to the fuel electrode or “negatrode”, where it recombines to form H₂. The molecular hydrogen diffuses through the porous negatrode into the adjacent fuel chamber and then exits the cell. Such devices have the potential to produce pure, dry, pressurized, carbon-free hydrogen from water and renewable electricity feedstocks.

Protonic ceramics boast a low activation energy for proton transport (Kreuer, 1996; Kreuer et al., 2004; Duan et al., 2015). This enables high proton conductivity at operating temperatures that may be 200–300°C lower than more-mature oxygen-ion conducting (O²⁻) solid-oxide electrolysis cells (SOECs). These lower temperatures reduce thermally driven degradation processes, such as nickel agglomeration and coarsening, chromium poisoning, and creep of metallic stack components. Further, while the electrochemically produced H₂ is diluted with water vapor in solid-oxide cells, necessitating downstream

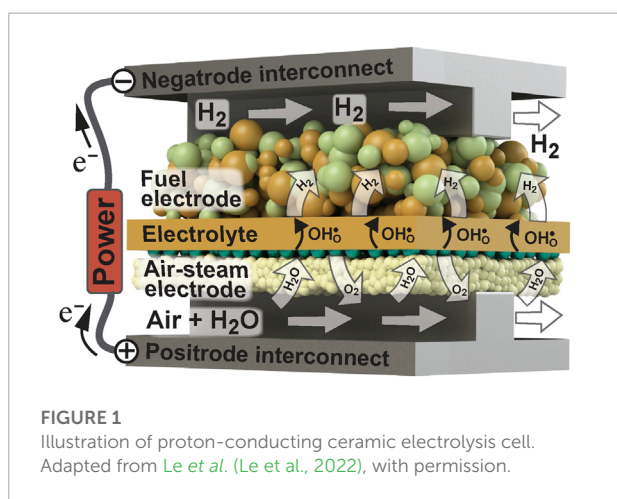
separation processes, PCECs provide a pure, dry hydrogen product stream. The 400–600°C operating temperatures is sufficiently high to promote facile chemical kinetics and thermal integration with high-value waste-heat sources, as well as significantly higher thermodynamic efficiency than low-temperature electrolysis technologies. Additionally, PCECs offer operational flexibility as they can potentially run effectively and efficiently across a range of steam concentrations. With these advantages, PCECs offer opportunities for large-scale hydrogen production.

Despite these benefits, reports of high-performance, high-efficiency PCECs are limited, and reports of pressurized operation are rarer still. Perhaps most significantly, PCECs can suffer from low Faradaic efficiency, usually attributed to electronic leakage across the electrolyte (Gan et al., 2012; Li and Licht, 2014; Gan et al., 2015; Li et al., 2015; Lei et al., 2017; Li et al., 2018; Zvonareva et al., 2022). Protonic ceramics are mixed proton, oxygen-ion and electron-hole conductors in which each charge carrier's transference number is determined by the specifics of the electrolyte composition, operating conditions and polarization current density (Zhu et al., 2018a; Zhu et al., 2018b). During electrolysis, water and oxygen compete for absorption onto surface sites and into the oxygen vacancies present in the protonic ceramic membrane lattice. When H₂O is incorporated to the membrane, the hydration reaction produces the desired charge defect and protons are transferred through the membrane (reaction 1). In parallel, molecular oxygen incorporation into a lattice vacancy generates electron holes via the membrane parasitic oxidation (reaction 2):



This reaction is associated with the observed p-type electronic leakage effect, thereby causing the lower Faradaic efficiencies commonly reported. High performance and stability have been observed with the chemically stable BaCe_{0.4}Zr_{0.4}Y_{0.1}Yb_{0.1}O_{3-δ} (BCZYYb4411) perovskite (Choi et al., 2019). Compared to earlier BaZr_{1-x}Y_xO_{3-δ} based materials, the BCZYYb compositional family leads to reduced electronic leakage and can enable Faradaic efficiencies exceeding 95% (Duan et al., 2019).

Most electrolysis reports analyze ambient-pressure operation, with hydrogen compression and storage subsequently executed in further downstream processes. Direct high-pressure electrolysis has the potential to bring cost reduction and plant simplification by reducing or avoiding the need of subsequent hydrogen compression (Onda et al., 2004;



Marangio et al., 2009). High-pressure operation can also in-part address the challenge posed by the electronic leakage issue in PCEC devices. As shown in Eq. 3 (Duan et al., 2020), the concentration of electron holes $[h^\bullet]$ is dependent upon oxygen and steam partial pressures. While high-pressure operation increases the oxygen partial pressure, this effect is more than offset by the higher order tied to the H_2O partial pressure. This leads to the potential for higher Faradaic efficiency with increasing pressure by decreasing the electron hole concentration in the electrolyte. Electrode activity can also be enhanced at higher pressures, enabling higher currents at lower driving voltages, and thus higher H_2 production rates and a lower overall energy demand per mole of H_2 produced.

$$[h^\bullet] = K_{ox} \cdot [OH^\bullet] \cdot P_{H_2O}^{-\frac{1}{2}} \cdot P_{O_2}^{\frac{1}{4}} \quad (3)$$

A variety of theoretical and experimental studies on pressurized operation in conventional oxygen-ion conducting solid oxide cells provide insight for pressurized PCECs. Henke et al. (Henke et al., 2011) applied a two-dimensional elementary kinetic model to study the influence of pressure on the thermodynamics, reaction kinetics, porous electrode diffusion, channel transport and efficiency to predict the performance of a single solid oxide-fuel cell (SOFC) in the pressure range of 1–20 bar. The results revealed higher power density and efficiency upon pressurization with the strongest increase in the range between 1 and 5 bar.

According to Henke et al. (Henke et al., 2012) the positive effect of pressurized operation in SOFCs is tied to three primary reasons:

- Increase in open-circuit voltage (OCV) associated with a small Nernst potential pressure dependence.
- Improvement in reactant adsorption rates at both electrodes. Increasing gas-phase partial pressures boost adsorption rates and electrode surface coverage, thereby improving surface reaction kinetics, significantly reducing activation overpotentials.
- Change in diffusion mechanism and an increase in starting (inlet) reactant concentrations. At low pressures, the molecular mean free path is much larger than the pore dimensions. Molecule-pore surface interactions are predominant, as governed by the Knudsen diffusion mechanism, where the gas density gradient and pressure govern transport. At higher pressures the controlling mechanism is ordinary diffusion; molecule-molecule collisions prevail leading to a higher net transport of molecules from the high to the low concentration region compared to the Knudsen diffusion regime. Concentration overpotentials can therefore be significantly reduced by increasing pressure.

All three effects show a logarithmic behavior, with effects being more pronounced at pressures up to 5 bar and leveling off at higher pressures. Pressure effects become less powerful above 5 bar as reactant surface coverage leans toward saturation at higher pressures. These theoretically predicted trends have been experimentally confirmed in later experimental studies by the same author (Henke et al., 2012).

Solid-oxide electrolysis cells can achieve near 100% energy efficiency through careful balancing of the exothermic cell losses with the endothermic water-splitting reaction. SOEC internal resistances lead to overvoltages and energy loss in the form of Joule heating. The SOEC operating voltage can be set so that this Joule heating is equal to the thermal-energy demand of the electrolysis reaction. This operating point is known as the thermoneutral voltage, and corresponds to 100% electrolysis efficiency (Henke et al., 2014; Yang et al., 2021).

Increasing pressure leads to a modest boost in the theoretical Nernst potential required for electrolysis:

$$E_{rev} = \frac{1}{nF} \times \left(\Delta g^0 + RT \sum_{k=1}^K v_k \ln p_k \right) \quad (4)$$

where n is the number of electrons, F is the Faraday constant (96500 C/mol), Δg^0 is the standard Gibbs energy, R is the ideal gas constant, v_k is the stoichiometric coefficient, and p_k is the partial pressure of each compound.

This increase brings a greater demand on the electric power required to drive the water-electrolysis reaction. In most oxygen-ion conducting cells, ohmic overvoltages are generally not influenced by pressure, as these are tied to the electrical and ionic resistances associated to the cell and stack components (e.g. electrolytes, electrodes, interconnects), and most oxygen-ion conducting electrolytes operate fully within the extrinsic electrolytic domain (i.e., pure ionic transport). In contrast, activation and concentration overvoltages are significantly reduced with increasing pressure. With the logarithmic pressure dependence shown in Eq. 4, the most-pronounced effects are found near ambient pressure for both SOFCs and SOECs.

Electrolysis at low current densities incurs relatively modest activation and concentration overvoltages. This enables high efficiency, but also means larger device sizes are needed to meet H_2 production targets. Because the activation and concentration overvoltages at low current density are small to begin with, the improvements brought by pressurized operation can be obscured by the increase in Nernst potential, leading to modest, or even negative performance-pressure dependencies at lower current density.

In contrast, overvoltages are more pronounced at higher current densities. In this case, the increase in power

requirements necessitated by the boost in Nernst potential due to pressurization is small in comparison to power required to overcome these higher overpotentials (Ni et al., 2007; Henke et al., 2014). Thus, the kinetic and mass-transport performance improvements brought by high-pressure operation are more impactful at these high-current-density conditions, as they can substantially decrease these large overvoltages. These phenomena have been theoretically and experimentally confirmed on anode-supported SOECs at 800°C (Ni et al., 2007; Henke et al., 2014; Bernadet et al., 2015; Sun et al., 2015).

Experimental performance analysis on a 16 cm² fuel-electrode-supported planar solid-oxide cell showed that pressurization brought stronger performance improvements in fuel-cell mode than in electrolysis mode. In this work, Jensen et al. (Jensen et al., 2010) found pressurization to have minimal influence on electrolyzer performance. Internal resistance decreased around 20% as operating pressure increased from 1 to 10 bar. O'Brien et al. (O'Brien, 2012) found a similar trend in a 10-cell planar SOEC stack operating at 800°C. The slope of the polarization curves in electrolysis mode decreased with increasing pressure, indicating lower area-specific resistance (ASR) as the pressure was increased from 1 to 17 bar (O'Brien, 2012). Kato et al. (Momma et al., 2013) found steam diffusion to be limiting in an anode-supported SOEC at operating pressures between 0.1 and 3 bar, with performance compromises most pronounced at lower pressures. Electrochemical impedance measurements have also confirmed that the individual processes expected to be dependent on gas partial pressures were all enhanced by increasing the operation pressure from 1 to 3 bar (Sun et al., 2015).

In contrast to conventional oxygen-ion conducting cells, there are few studies on the effect of pressurization on protonic-ceramic cells. Vøllestad et al. (Vøllestad et al., 2019) demonstrated the positive effect of higher steam and total pressure on tubular PCECs based on barium-zirconate. Increasing pressure from 1.5 to 4 bar at 600°C brought a ~10% increase in the current density for a driving voltage of ~1.9 V. In addition, they observed a decrease in the operating voltage of 30–50 mV and lower polarization resistance (R_p) as assessed by electrochemical impedance spectroscopy (EIS). Malerød-Fjeld et al. (2017) showed the viability of using a BaZrO₃-based proton-conducting electrolyte deposited as a dense film on a porous Ni-composite electrode as a protonic membrane reformer. The device achieved 99% conversion in steam methane reforming. Simultaneously, it produced high-purity hydrogen compressed electrochemically up to 50 bar.

In this paper, we expand on these limited high-pressure operation studies to further explore the electrochemical behavior of protonic-ceramic cells at elevated pressures. Fabrication and performance characterization protocols are subsequently described.

Experimental methods

Membrane electrode assembly fabrication

Materials compositions and stoichiometries for proton-conducting cells continue to be fine-tuned so that better electrochemical performance can be achieved during operation. Recently, low ohmic resistance and degradation rates have been observed using a highly conductive and chemically stable multi-doped perovskite BaCe_{0.4}Zr_{0.4}Y_{0.1}Yb_{0.1}O_{3-δ} (BCZYYb4411) as an electrolyte (Choi et al., 2015; Le et al., 2021). In this study we work with a composite of Ni-BCZYYb4411 as the fuel electrode (negatrode), BCZYYb4411 as the electrolyte and BaCo_{0.4}Fe_{0.4}Zr_{0.1}Y_{0.1}O_{3-δ} (BCFZY) as the air-steam electrode (positrode).

The negatrode and electrolyte layers of the membrane-electrode assemblies (MEA) used in this study are synthesized using the solid-state reactive sintering (SSRS) method. The SSRS method uses compacts comprised of multiphase oxide and carbonate precursors to form the negatrode and electrolyte layers, rather than starting from single-phase compacts. This approach combines phase formation, densification, and grain growth into a single high-temperature sintering step, simplifying the fabrication process (Nikodemski et al., 2013). SSRS provides a lower-cost alternative to cell fabrication in comparison to conventional methods (Duan et al., 2015; Dubois et al., 2017).

We use stoichiometric ratios of BaCO₃, CeO₂, ZrO₂, Y₂O₃ and Yb₂O₃ to form the electrolyte phase of the composite negatrode (Alfa Aesar 14341, 11328, 230693, 111328, and 11191, respectively). We then add NiO and potato starch as pore former (Alfa Aesar 45094 and 11961, respectively) in the proportion 60 wt% NiO: 40 wt% BCZYYb +20 wt% starch based on percentage of oxides. The mixture of precursors is ball milled in isopropanol for 72 h and then dried in a low-temperature furnace. Finally, we dry ball mill these powders for 24 h to form a homogeneous powder. Once formed, 20 g of this negatrode powder is well mixed with 2 g of binder (10% polyvinyl alcohol 20,000 M.W. dissolved in water) and dry pressed in a 57-mm-diameter stainless steel die with a compression pressure of 34 MPa for 10 s to form the negatrode support pellet.

The BCZYYb electrolyte is spray-coated onto this negatrode support. To form the electrolyte slurry, we first mix stoichiometric ratios of BaCO₃, CeO₂, ZrO₂, Y₂O₃ and Yb₂O₃, plus 1.0 wt% NiO following the same method as for the fuel electrode precursor powder. We mix the electrolyte powder with a homogeneous mixture of binder, plasticizer and dispersant (Heraeus V-006, Alfa Aesar PEG 400 B21992, and Alfa Aesar PVP 40000 J62417, respectively) to synthesize the electrolyte suspension. The mass fraction of the electrolyte solution is

13 wt% electrolyte precursor powder +1 wt% PEG +1 wt% PVP +2.5 wt% binder +2.5 wt% alpha terpineol (Alfa Aesar 16,285) + 80 wt% isopropanol. The suspension is suspended in a sonicator for 1.5 h before spraying.

This electrolyte slurry is spray-deposited onto the negatode support using a low-cost commercial airbrush (Master S68); 12 ml of the electrolyte solution produces a 20 μm -thick electrolyte layer across the 57-mm-diameter negatode disc. The distance between the air brush and the support during spray coating is held at approximately 20 cm. After spray-coating, the electrolyte-negatode assemblies are then co-sintered in an atmospheric furnace (Deltech) at temperatures between 1450 and 1550°C for 15 h. The firing process includes an intermediate 5 h dwell at 450 °C to burn out the binder; heating and cooling ramps are held at 3°C min⁻¹.

Following the high-temperature sintering, we apply the BCFZY air-steam positrode atop the electrolyte. The BCFZY material is prepared following the sol-gel method previously described by Duan et al. (2015). BCFZY powder is mixed with 20 wt% BCZYb4411 in order to improve the adherence and increase the electrochemically active region. This composite material is transformed into an ink by mixing with binder (Heraeus V006-A) and dispersant (Solsperse 28,000) to form a paste, adjusted to the desired viscosity. This paste is then brush-painted onto the sintered electrolyte.

Finally, the full cell (negatode-electrolyte assembly + brush-painted BCFZY positrode) is sintered at 900°C for 5 h. This positrode sintering temperature is sufficient to promote adherence between the air-steam electrode and the electrolyte while maintaining a nanoscale positrode structure with high surface area for maximum electrochemical activity. The result is an approximately 1 mm-thick, 39 mm-diameter membrane-electrode assembly with an active area of approximately 5 cm².

Stack design and fabrication

The unit-cell stack design and fabrication are similar to that described in Le et al. (Le et al., 2021). Figure 2A shows a schematic drawing of the unit-cell stack, along with a photograph of its assembly. The protonic-ceramic membrane-electrode assembly is first bonded to a composite ceramic frame. Glass sealing powder (Mo-Sci 1745p) is mixed with distilled water to create a viscous paste that is carefully applied on both sides of the cell circumference in contact with the frame internal edges. The applied glass sealing is later cured at 750°C for 2 hours at a heating rate of 1 °C/min to form a smooth, crack-free seal. The non-conductive ceramic frame helps to prevent electrical shorting within the stack.

The MEA-frame assembly is then packaged between 4-mm-thick ferritic steel endplates (Crofer 22H, ThyssenKrupp).

Thin sheet-steel interconnects are also placed between the MEA and the endplates. These interconnects have nano-scale cobalt and ceria coatings, as provided by the manufacturer (Sandvik SANERGY 441), to facilitate formation of the electrically conductive (Mn,Cr)₃O₄ scale (Le et al., 2021). The interconnects are pretreated through 30 h of continuous exposure to an air +10% H₂O environment at 900°C, an adaptation of the work by Goebel et al. (2018) and Talic et al. (2018). These 0.4-mm-thick interconnects are bonded to the thick end plates using silver paste.

Two 1-mm-thick chemically exfoliated vermiculated gaskets (Thermiculite 870, Flexitallic) provide sealing between the ceramic frame and the interconnects. These gaskets require compression for hermeticity. Metallic-mesh current collectors coated in silver paste are used to connect the cell electrodes with the interconnects. Current and voltage are drawn from the outside of the endplates, which are electrically insulated from the compression system and test stand using two alumina support plates (not shown).

The unit-cell stack assembly is placed within a compression system that promotes sealing of reactive gases from the surrounding environment as shown in Figure 2B. The compression force is transferred to the endplates through an Inconel rod secured within bulk compression plates that are pre-stressed to 4 MPa using a set of eight stainless-steel springs, nuts, and bolts (Hastelloy C276). Initial sealing is validated by gas analysis. This design enables the compression force to be transferred through the endplates and the ceramic frame instead of the comparatively delicate MEA.

The loaded electrochemical stack is assembled within a stainless-steel pressure vessel (Parr Series 4674) (Figure 2C). The pressure vessel includes ports for plumbing the reactant and product flows. The pressure vessel also includes four thermal wells in which resistive heaters are placed to achieve target operating temperatures. It is noteworthy that compression springs are located outside of the vessel hot zone to minimize creep and maintain compression.

High-pressure mass flow controllers (Alicat MCQ series) regulate the flow rates of reactants fed to the negatode and positrode. Additionally, an inert sweep gas flows through the pressure-vessel chamber into which the stack assembly is placed. A high-pressure isocratic pump (Teledyne, LS Class) accurately controls the water flow rate that is evaporated and carried with air to the positrode. Back-pressure regulators with feedback control (Equilibar ZF Zero Flow and QBS series) minimize pressure differentials between fuel, air and sweep gas to below 10 kPa. A data acquisition and control system (National Instruments) is used to operate the mass flow controllers and the electronic pressure regulator, while a PID unit powers the resistive heaters and controls the stack operating temperature (Parr 4838 Temperature Controller).

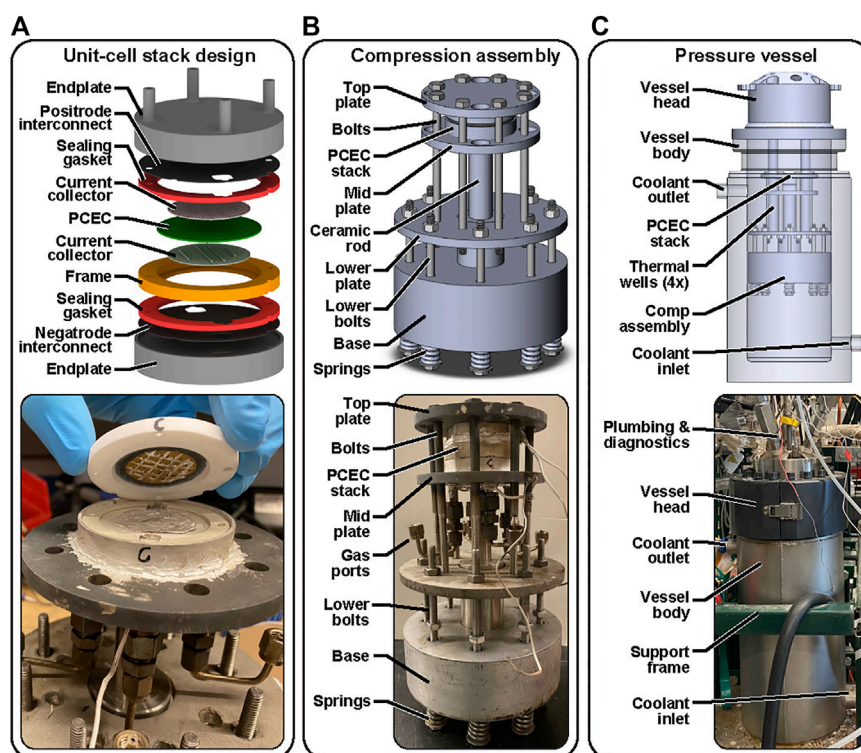


FIGURE 2

Designs and photographs of (A) unit-cell PCEC stack assembly; (B) stack-compression assembly; and (C) pressure vessel.

Stack electrochemical performance characterization

Electrolyzer performance is measured through polarization curves, electrochemical impedance spectroscopy, and galvanic operation at different pressures (Gamry, Reference 5000). Stack exhaust flow rates are continuously measured (DryCal Defender 530 Plus, Mesa Labs) and compared with inlet flow rates to confirm sealing, quantify hydrogen production, and calculate Faradaic efficiency.

The system is heated to 550°C at 1°C min⁻¹ with no gas flow at ambient pressure. Once the target temperature is reached, we start flowing 100 sccm of a H₂-N₂ mixture to the negatrode and 200 sccm of air +3% steam on the positrode. We also flow 200 sccm of argon as sweep gas. We gradually increase the H₂ concentration from 5 to 80% to reduce the NiO in the two-phase negatrode to metallic nickel; this process takes 3–4 h. Cell reduction is considered complete when the open-circuit voltage (OCV) is stable at around 1–1.1 V and EIS response is invariant with time. Then we set the standard gas compositions for experimental measurement: fuel side = 100 sccm (75% H₂ - 25% N₂), air side = 200 sccm of air (10–30% steam). The temperature is kept constant at 550°C. Operating pressure spans from 1 to 12 bar in 1-bar steps.

Results and discussion

Pressure effect on cell performance in electrolysis mode

The experiments in this work were conducted at a constant temperature of 550°C and fixed gas conditions of 75% H₂ + 25% N₂ fed to the negatrode and air +10%–30% H₂O fed to the positrode. Higher water-vapor concentrations have been shown to improve electrolyzer electrochemical performance, but have also been tied to increased degradation rates (Le et al., 2022).

The expected boost in open-circuit voltage (OCV) with high pressure is evident in Figure 3A, consistent with the Nernst equation (Eq. 4). This higher OCV can increase electrolysis power demand. However the improved kinetic and mass transport characteristics brought by pressurized operation more than offset the OCV increase, as evidenced in the polarization curves shown in Figure 3B. Focusing on the 1.6 V operating potential, current density increases from 375 to 600 mA cm⁻² as pressure rises from 2.1 to 12.6 bar, a 60% increase in performance (Figure 3C). However, at lower pressures (e.g., compare 2.1 bar vs 5.7 bar), the effect of pressure is far more modest.

As noted earlier, electrochemical performance studies at pressure from conventional oxygen-ion conducting solid-oxide

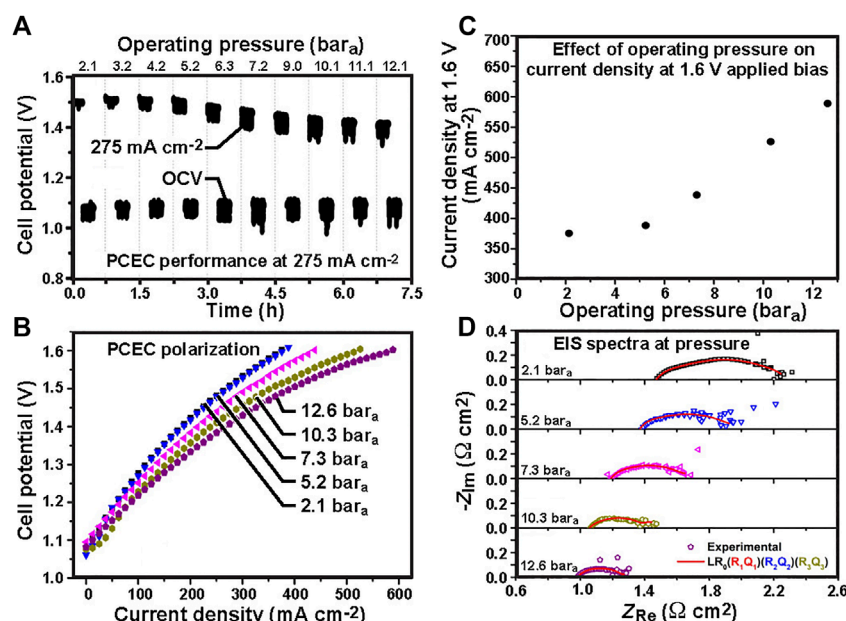


FIGURE 3

Protonic-ceramic electrolyzer performance from 2.1 to 12.1 bar_a: (A) open-circuit voltage and driving voltage at 275 mA cm⁻² over 7.5 h; (B) polarization behavior; (C) current density at 1.6 V driving voltage; and (D) electrochemical impedance spectra.

electrolyzers show similar trends. For example, at lower current densities (< 50 mA cm⁻²), and/or lower pressures, performance gains from pressurized operation often prove inadequate in offsetting the OCV increases, although improvements in pressurized cell performance at higher current density can lower overall electrical demand (Jensen et al., 2010; Momma et al., 2013; Bernadet et al., 2015; Sun et al., 2015).

Electrochemical impedance spectra in Figure 3D are consistent with the polarization behavior in Figure 3B. Ohmic and polarization resistance both decrease with increasing pressure, e.g. by as much as 33% and 60% respectively when the pressure increases from 2.1 to 12.6 bar_a. This result is in contrast to what is seen in SOECs, where polarization resistance decreases with pressure but ohmic resistance stays almost constant (Jensen et al., 2010; Momma et al., 2013). This notable PCEC ohmic pressure response is attributed to the mixed-conduction behavior of the protonic ceramic electrolyte, specifically the dependence of the proton and hole conductivities on gas composition and concentration. As noted by Henke et al. (Henke et al., 2014), ohmic heating at higher current densities can also bring modest temperature increases to the electrolysis cell that can additionally contribute to the observed drop in ohmic resistance.

As presented by Le et al. (Le et al., 2022), electrochemical impedance spectra acquired from PCECs can be fitted to an equivalent-circuit model (ECM) in which each element can be generally associated to characteristic phenomena taking place in the cell. We found that a four-component

ECM $LR_0(RQ)_1(RQ)_2(RQ)_3$ effectively captures the impedance responses from our cells. The typical processes associated to each of these elements are consistent with previous studies (Jensen et al., 2007; Lu et al., 2019; Wang et al., 2020):

- 1) L represents the inductance resistance;
- 2) R_0 represents the ohmic loss commonly associated with charge transport through the electrolyte;
- 3) R_1Q_1 represents charge transfer associated with a characteristic pseudo-capacitance of $\sim 10^{-4}$ – 10^{-3} (F cm²);
- 4) R_2Q_2 represents surface diffusion associated with a typical pseudo-capacitance of 10^{-3} – 10^{-2} (F cm²);
- 5) R_3Q_3 represents dissociative adsorption/dissociation of the gaseous species and/or mass transport processes within the electrode. The pseudo-capacitance of both phenomena is typically observed at 10^{-1} – 10^1 (F cm²).

Figure 4 quantify the influence of pressure on the elementary resistances. ASR_2 is associated with surface diffusion within the BCFZY electrode and appears to be the most pressure-dependent process. The charge transfer process (ASR_1) seems to be reduced as pressure increases up to 6 bar. After 6 bar the pressure effect on ASR_1 is negligible. Finally the surface adsorption-desorption process (ASR_3) is weakly affected by the operating pressure, specially after 5 bar.

Equivalent circuit modeling (ECM) of EIS is a valuable characterization tool to resolve transport and reaction pathways by their characteristic frequency dependencies. However,

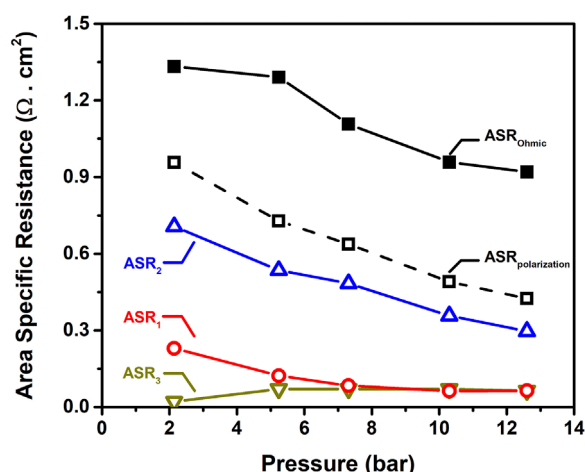


FIGURE 4
Effect of operating pressure on area-specific resistance.

electrode physical processes like charge transfer and transport often overlap in the frequency domain. This can challenge the traditional ECM interpretation of EIS data. Recently, distribution of relaxation time (DRT) analysis has risen to prominence as an important tool to further identify and separate distinct relaxations in an impedance response that may be associated with specific electrochemical processes. DRT can also assist in identification of the most appropriate equivalent-circuit model(s) for a system under study (Dierickx et al., 2020; Huang et al., 2021). That said, interpretation of the characteristic DRT response of protonic ceramic devices is at an early stage compared to other electrochemical systems; the authors know of no reports presenting the impact of operating pressure on DRT response from a protonic ceramic cell.

We utilize a robust DRT fitting package recently developed by Huang et al. (2021), which employs a hierarchical Bayesian model, to fit and analyze our impedance spectra across the range of pressures. The package applies Bayesian inference to eliminate manual tuning and automatically identify corrupted data points, enabling robust fitting of noisy impedance data.

Figure 5 shows the obtained cell DRT response at pressures ranging between 1 and 9 bar_a. EIS measurements were taken under OCV conditions at the featured pressures. At 1 bar_a, we can observe major DRT peaks at three time constants: 10⁻⁴, 10⁻² and 10⁻¹ s, broadly consistent with the three RQ circuit elements present in our ECM. While some additional minor peaks may be present in the DRT, the level of noise present in spectra obtained at elevated pressure makes resolution of these peaks very challenging; thus, we focus our analysis on the impact of operating pressure on these three primary peaks.

The DRT peak at 10⁻¹ s is quickly eliminated when pressure is increased from 2 to 4 bar_a. The peaks at 10⁻² and 10⁻⁴ s decrease with increasing pressure, especially the

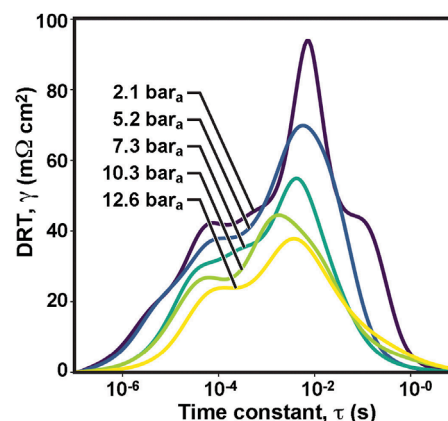


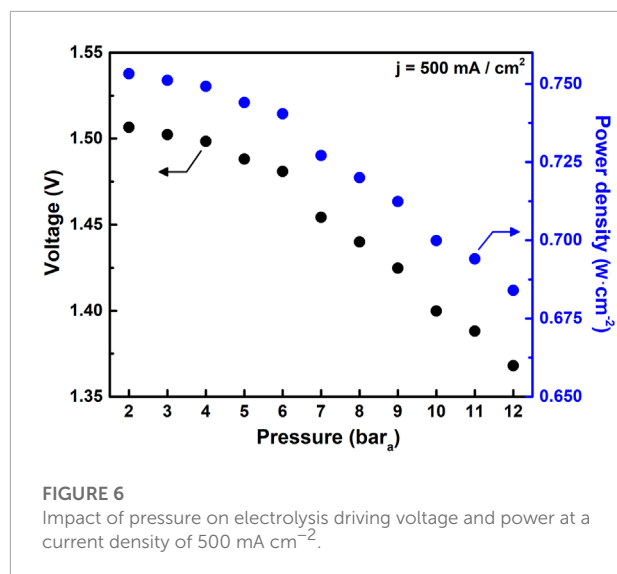
FIGURE 5
Effect of pressure on distribution of relaxation times in protonic-ceramic electrolyzer at open-circuit voltage.

peak at $\tau = 10^{-2}$ s. Gas diffusion is expected to be the most pressure-dependent process, typically manifesting at the lowest frequencies (Sumi et al., 2021). This suggests that the peak at 10⁻¹ s is likely tied to this physical process as proposed by Le et al. (Le et al., 2022). The peak at 10⁻² s seems more likely to be associated with the electrode surface diffusion which also improves at higher pressures; the resistance tied to this process decreases. Triple conductors oxides such as BCFZY are known to have large chemical capacitances which can push the time constants for electrode surface processes to longer timescales as observed in Figure 5.

It is noteworthy that pressure does not bring a significant shift in the magnitudes of the time constants, $\tau = RC$. Peak resistances decrease with pressure, while τ remains nearly constant. Therefore, we can conclude that higher operating pressures boost the capacitance C . This would be consistent with greater surface coverage of charged adsorbates, an increase in the accessible electrochemically active surface area, and/or greater concentration of charge carriers in the near-surface region of the electrode, all of which could reasonably be induced by higher-pressure operation.

Galvanic performance at elevated pressure

Figure 6 further reveals the encouraging gains in electrolysis performance that can be achieved with increasing pressure. In this series of experiments, the operating pressure is increased in 1-bar steps from 2.1 to 12.6 bar_a. Operating conditions are held for 20 min at each condition. Operating temperature is held constant at 550°C, while reactant gas composition is fixed at 75% H₂ + 25% N₂ fed to the negatode and 90% air + 10% H₂O fed to the positrode.



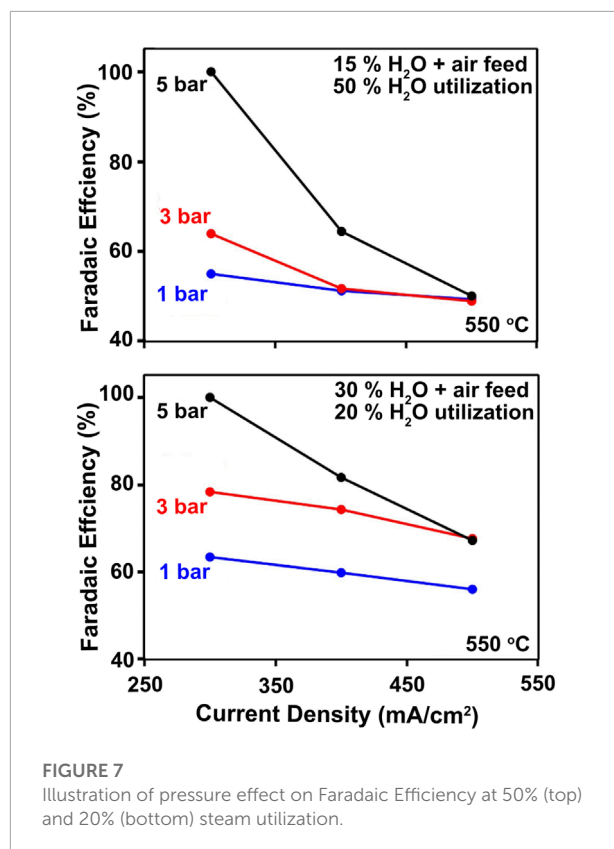
Over the course of the 6-h test, cell current density is alternated between 0 and 500 mA cm^{-2} . The driving voltage needed to maintain the 500 mA cm^{-2} current density decreases from 1.5 to 1.35 V as pressure increases from 2.1 to 12.6 bar_a. We also note that the electrochemical performance of the cell shown in **Figure 6** exceeds that of the cell shown in **Figure 3**. This is reflective of our challenges with process control and cell-to-cell repeatability in our academic laboratory setting.

Overall, pressurization reduces the power needed to drive electrolysis by 30% at 500 mA cm^{-2} . These gains are consistent with, or greater than, those generally observed in previous studies using solid oxide electrolysis cells, and as previously noted, the benefits of pressurized electrolysis can be even more pronounced at higher current densities (Ni et al., 2007; Henke et al., 2014; Sun et al., 2015).

Pressure effect on faradaic efficiency

Electronic leakage compromises the efficiency of protonic-ceramic electrolyzers for producing pure, dry, green H_2 , and presents one of the largest technical challenges facing the technology.

Pressurized operation can increase proton concentration in the membrane and suppress electronic charge carriers to boost Faradaic efficiency. High steam concentrations at the positrode promote OH^\bullet incorporation (Duan et al., 2020) through Reaction 1. **Figure 7** shows Faradaic efficiency results at varying steam-feed concentrations and steam utilizations. Several trends are evident. First, Faradaic efficiency is quite modest (50–60%) at 1 bar_a operating pressure over all current densities and steam-feed concentrations tested. Further, Faradaic efficiency decreases with increasing current density. This is consistent with a number of experimental studies involving



larger-area PCECs. Vollestad et al. (2019) suggests that when the cell resistance is high (over 2 ohm cm^2), the high electrode overpotentials increasingly favor the direct electronic pathway short-circuiting the electrolyte as opposed to the ionic pathway involving electrochemical reaction, charge transfer, and ionic conduction, leading to lower Faradaic efficiency with increasing current density. Higher current densities also increase the local oxygen concentration at the positrode. This promotes hole formation through reaction 2, increasing electronic conduction through the protonic-ceramic electrolyte, reducing Faradaic efficiency.

However, many button-cell and theoretical modeling studies show the opposite trend, where the internal short of electronic conduction is overwhelmed by the flux of driven protons at higher current densities, yielding higher efficiencies at higher loads (Zhu et al., 2022). Zhu et al. (2022) shows that Faradaic efficiency decreases drastically near open-circuit conditions, and can become negative at the lowest current densities. They found that at open circuit, the cell behaves as a concentration cell, driving protons from the negatrode to the positrode, resulting in a reverse proton flux. As the imposed current density increases the desired proton flux from the positrode to the negatrode eventually surpasses the reverse proton flux, increasing Faradaic efficiency. This model also suggests that unmeasured variations in operating conditions, such as local

temperature increases with high current density or local reactant depletion/product accumulation effects can be the reason of the diminished Faradaic efficiencies observed in some of the published experimental work on larger-area PCECs. This remains an active area of investigation in the protonic-ceramic community.

Figure 7 further shows that increases in operating pressure are found to boost Faradaic efficiency at current densities below 500 mA cm^{-2} , reaching nearly 100% at 5 bar_a and 300 mA cm^{-2} . Still, FE remains modest at lower pressures, particularly at the 15% steam feed condition and 50% utilization, where hole generation by Reaction 2 may be pronounced. The higher steam feed concentration of 30% and lower steam utilization shown in **Figure 7B** enables higher Faradaic efficiency. While yet-higher steam feeds could be even more beneficial, such conditions have proven to be deleterious to the air-steam electrode (Le et al., 2022). This motivates the development of more-advanced, stable PCEC electrode materials.

Similar to our findings, Vøllestad et al. (2019) reported the positive effect of higher steam and total pressures on the polarization behavior and Faradaic efficiency of a BZCY-based tubular electrolysis cell. They observed a 30–50 mV decrease in the operating voltage when the steam pressure was increased from 1.5 to 4 bar, reflecting the increased proton conductivity in the electrolyte as lower ohmic resistance was also observed from EIS. By increasing the steam partial pressure, or the total pressure at a given steam concentration, the water oxidation equilibrium shifts towards lower electron-hole concentration, higher proton concentration, and higher ionic transport to provide higher Faradaic efficiencies (Vøllestad et al., 2019).

In summary, our results show that pressurized electrolysis in protonic ceramic cells favors higher Faradaic efficiencies by decreasing the total resistance of the cell as well as the electron-hole concentration in the electrolyte. Electrode activity and mass transport are also enhanced at higher pressures, enabling higher current densities at lower driving voltages. These effects more than compensate for the slight increase in Nernst potential (and the corresponding OCV increase) and therefore enable significantly higher total electric-to-hydrogen energy efficiencies under pressurized operation.

Conclusion

This work summarizes our observations on pressurized operation of planar protonic-ceramic electrolyzers. High-temperature, high-pressure operation brings novel design challenges. Sealing of reactive gases is more challenging at high pressures; adequate sealing is central to achieving high Faradaic efficiency. Further, pressurized operation can magnify small differences in operating pressure between the anode and cathode chambers that can lead to fracture of fairly delicate electroceramic membrane-electrode assemblies. This paper

presents our approaches to meeting these challenges, and the benefits brought by pressurized electrolysis with protonic ceramics.

As pressure increased from 2.1 to 12.6 bar, we observed:

- The expected boost in OCV consistent with the Nernst equation.
- Ohmic and polarization resistances decreased by 33% and 60%, respectively, enabling higher current densities at lower driving voltages.
- A 60% performance increase confirmed at higher current densities; the improved kinetic and mass transport characteristics brought by pressurized operation more than offset the OCV increase.
- Faradaic efficiency increased, reaching 100% at 5 bar and 15% steam concentration.

These results confirm that pressurized electrolysis enhances electrode activity, improves the kinetic and mass-transport behavior, and lowers the power required for H₂O electrolysis. The higher Faradaic efficiencies suggest that pressurized operation decreases the electron-hole concentration in the electrolyte and can serve as a solution to mitigate deleterious electronic leakage in protonic ceramic devices.

Data availability statement

The raw data supporting the conclusion of this article will be made available by the authors, without undue reservation.

Author contributions

CH: Lead researcher, Formal analysis, Writing and editing manuscript, Investigation. LL: Formal analysis, Methodology, Investigation. CM: Methodology, Investigation. JH: Implement EIS/DRT data analysis, Data curation, Validation. Christopher Chmura: Methodology. YK: Methodology. CC: Methodology. RO: Conceptualization, Visualization, Writing—review and editing, Funding acquisition. NS: Supervision, Conceptualization, Writing—review and editing final draft, Funding acquisition.

Funding

The information, data, or work presented herein was funded in part by the Advanced Research Projects Agency-Energy (ARPA-E), U.S. Department of Energy, under Award Number DE-AR0000808. The views and opinions of authors expressed herein do not necessarily state or reflect those of the United States Government or any agency thereof.

Conflict of interest

The authors declare that the research was conducted in the absence of any commercial or financial relationships that could be construed as a potential conflict of interest.

Publisher's note

All claims expressed in this article are solely those of the authors and do not necessarily represent those of their affiliated

organizations, or those of the publisher, the editors and the reviewers. Any product that may be evaluated in this article, or claim that may be made by its manufacturer, is not guaranteed or endorsed by the publisher.

Author disclaimer

The views and opinions of authors expressed herein do not necessarily state or reflect those of the United States Government or any agency thereof.

References

- Bernadet, L., Gousseau, G., Chatroux, A., Laurencin, J., Mauvy, F., and Reytyer, M. (2015). Influence of pressure on solid oxide electrolysis cells investigated by experimental and modeling approach. *Int. J. Hydrogen Energy* 40 (38), 12918–12928. doi:10.1016/j.ijhydene.2015.07.099
- Choi, S., Davenport, T. C., and Haile, S. M. (2019). Protonic ceramic electrochemical cells for hydrogen production and electricity generation: exceptional reversibility, stability and demonstrated faradaic efficiency. *Energy Environ. Sci.* 12, 206–215. doi:10.1039/c8ee02865f
- Dierckx, S., Weber, A., and Ivers-Tiffée, E. (2020). How the distribution of relaxation times enhances complex equivalent circuit models for fuel cells. *Electrochim. Acta* 355, 136764. doi:10.1016/j.electacta.2020.136764
- Duan, C., Huang, J., Sullivan, N., and O'Hayre, R. (2020). Proton-conducting oxides for energy conversion and storage. *Appl. Phys. Rev.* 7 (1), 011314. doi:10.1063/1.5135319
- Duan, C., Kee, R., Zhu, H., Sullivan, N., Zhu, L., Bian, L., et al. (2019). Highly efficient reversible protonic ceramic electrochemical cells for power generation and fuel production. *Nat. Energy* 4 (3), 230–240. doi:10.1038/s41560-019-0333-2
- Duan, C., Tong, J., Shang, M., Nikodemski, S., Sanders, M., Ricote, S., et al. (2015). Readily processed protonic ceramic fuel cells with high performance at low temperatures. *Science* 349 (6254), 1321–1326. doi:10.1126/science.aab3987
- Dubois, A., Ricote, S., and Braun, R. J. (2017). Benchmarking the expected stack manufacturing cost of next generation, intermediate-temperature protonic ceramic fuel cells with solid oxide fuel cell technology. *J. Power Sources* 369, 65–77. doi:10.1016/j.jpowsour.2017.09.024
- Gan, L., Ye, L., Liu, M., Tao, S., and Xie, K. (2015). A scandium-doped manganate anode for a proton-conducting solid oxide steam electrolyzer. *RSC Adv.* 6 (1), 641–647. doi:10.1039/c5ra19844e
- Gan, Y., Zhang, J., Li, Y., Li, S., Xie, K., and Irvine, J. T. S. (2012). Composite oxygen electrode based on LSCM for steam electrolysis in a proton conducting solid oxide electrolyzer. *J. Electrochem. Soc.* 159 (11), F763–F767. doi:10.1149/2.018212jes
- Goebel, C., Alnegren, P., Faust, R., Svensson, J.-E., and Froitzheim, J. (2018). The effect of pre-oxidation parameters on the corrosion behavior of aisi 441 in dual atmosphere. *Int. J. Hydrogen Energy* 43 (31), 14665–14674. doi:10.1016/j.ijhydene.2018.05.165
- Henke, M., Kalló, J., Friedrich, K. A., and Bessler, W. G. (2011). Andreas friedrich and wolfgang G. Bessler. Influence of pressurization on SOFC performance and durability: A theoretical study. *Fuel Cells* 11 (4), 581–591. doi:10.1002/fuce.201000098
- Henke, M., Willich, C., Kalló, J., and Andreas Friedrich, K. (2014). Theoretical study on pressurized operation of solid oxide electrolysis cells. *Int. J. Hydrogen Energy* 39 (24), 12434–12439. doi:10.1016/j.ijhydene.2014.05.185
- Henke, M., Willich, C., Westner, C., Leucht, F., Leibinger, R., Kalló, J., et al. (2012). Effect of pressure variation on power density and efficiency of solid oxide fuel cells. *Electrochim. Acta* 66, 158–163. doi:10.1016/j.electacta.2012.01.075
- Huang, J., Papac, M., and O'Hayre, R. (2021). Towards robust autonomous impedance spectroscopy analysis: A calibrated hierarchical bayesian approach for electrochemical impedance spectroscopy (eis) inversion. *Electrochim. Acta* 367, 137493. doi:10.1016/j.electacta.2020.137493
- Kreuer, K. D., Paddison, S. J., Spohr, E., and Schuster, M. (2004). Transport in proton conductors for fuel-cell applications: Simulations, elementary reactions, and phenomenology. *Chem. Rev.* 104 (10), 4637–4678. doi:10.1021/cr020715f
- Kreuer, K. D. (1996). Proton conductivity: Materials and applications. *Chem. Mat.* 8 (3), 610–641. doi:10.1021/cm950192a
- Onda, K., Kyakuno, T., Hattori, K., and Ito, K. (2004). Prediction of production power for high-pressure hydrogen by high-pressure water electrolysis. *IEEE Trans. Pe.* 124 (4), 605–611. doi:10.1541/ieejpes.124.605
- Lei, L., Tao, Z., Wang, X., Lemmon, J. P., and Chen, F. (2017). Intermediate-temperature solid oxide electrolysis cells with thin proton-conducting electrolyte and a robust air electrode. *J. Mat. Chem. A* 5 (44), 22945–22951. doi:10.1039/c7ta05841a
- Li, F.-F., and Licht, S. (2014). Advances in understanding the mechanism and improved stability of the synthesis of ammonia from air and water in hydroxide suspensions of nanoscale Fe₂O₃. *Inorg. Chem.* 53 (19), 10042–10044. doi:10.1021/ic5020048
- Li, H., Chen, X., Chen, S., Wu, Y., and Xie, K. (2015). Composite manganate oxygen electrode enhanced with iron oxide nanocatalyst for high temperature steam electrolysis in a proton-conducting solid oxide electrolyzer. *Int. J. Hydrogen Energy* 40 (25), 7920–7931. doi:10.1016/j.ijhydene.2015.04.067
- Li, W., Guan, B., Liang, M., Hu, S., Zhang, N., and Liu, X. (2018). High performing triple-conductive Pr₂NiO_{4+δ} anode for proton-conducting steam solid oxide electrolysis cell. *J. Mat. Chem. A* 6 (37), 18057–18066. doi:10.1039/c8ta04018d
- Le, L. Q., Hernandez, C. H., Rodriguez, M. H., Zhu, L., Duan, C., Ding, H., et al. (2021). Proton-conducting ceramic fuel cells: Scale up and stack integration. *J. Power Sources* 482, 228868. doi:10.1016/j.jpowsour.2020.228868
- Le, L. Q., Meisel, C., Hernandez, C. H., Huang, J., Kim, Y., O'Hayre, R., et al. (2022). Performance degradation in proton-conducting ceramic fuel cell and electrolyzer stacks. *J. Power Sources* 537, 231356. doi:10.1016/j.jpowsour.2022.231356
- Lu, M. Y., Scipioni, R., Park, B.-K., Yang, T., Chart, Y. A., and Barnett, S. A. (2019). Mechanisms of prox performance enhancement of oxygen electrodes for low and intermediate temperature solid oxide fuel cells. *Mat. Today Energy* 14, 100362. doi:10.1016/j.mtener.2019.100362
- Malerød-Fjeld, H., Clark, D., Yuste-Tirados, I., Zanón, R., Catalán-Martínez, D., Beeaff, D., et al. (2017). Thermo-electrochemical production of compressed hydrogen from methane with near-zero energy loss. *Nat. Energy* 2 (12), 923–931. doi:10.1038/s41560-017-0029-4
- Marangio, F., Massimo, G. L. S., and Cali, M. (2009). Theoretical model and experimental analysis of a high pressure PEM water electrolyser for hydrogen production. *Int. J. Hydrogen Energy* 34 (3), 1143–1158. doi:10.1016/j.ijhydene.2008.11.083
- Momma, A., Takano, K., Tanaka, Y., Kato, T., and Yamamoto, A. (2013). Experimental investigation of the effect of operating pressure on the performance of SOFC and SOEC. *ECS Trans.* 57, 699–708. doi:10.1149/05701.0699ecst
- Ni, M., Michael, K., Leung, H., and Leung, D. Y. C. (2007). Parametric study of solid oxide steam electrolyzer for hydrogen production. *Int. J. Hydrogen Energy* 32 (13), 2305–2313. doi:10.1016/j.ijhydene.2007.03.001

Nikodemski, S., Tong, J., and O'Hayre, R. (2013). Solid-state reactive sintering mechanism for proton conducting ceramics. *Solid State Ion.* 253, 201–210. doi:10.1016/j.ssi.2013.09.025

O'Brien, (2012). High temperature electrolysis pressurized experiment design, operation, and results. Technical report.

Jensen, S. H., Hauch, A., Hendriksen, P. V., Mogensen, M., Bonanos, N., and Jacobsen, T. (2007). A method to separate process contributions in impedance spectra by variation of test conditions. *J. Electrochem. Soc.* 154, B1325. doi:10.1149/1.2790791

Jensen, S. H., Sun, X., Ebbesen, S. D., Knibbe, R., and Mogensen, M. (2010). Hydrogen and synthetic fuel production using pressurized solid oxide electrolysis cells. *Int. J. Hydrogen Energy* 35 (18), 9544–9549. doi:10.1016/j.ijhydene.2010.06.065

Sumi, H., Shimada, H., Yamaguchi, Y., Mizutani, Y., Okuyama, Y., and Amezawa, K. (2021). Comparison of electrochemical impedance spectra for electrolyte-supported solid oxide fuel cells (sofcs) and protonic ceramic fuel cells (pcfcs). *Sci. Rep.* 11, 10622. doi:10.1038/s41598-021-90211-9

Sun, X., Bonaccorso, A. D., Graves, C., Ebbesen, S. D., Jensen, S. H., Hagen, A., et al. (2015). Performance characterization of solid oxide cells under high pressure. *Fuel Cells* 15, 697–702. doi:10.1002/fuce.201500020

Talic, B., Molin, S., Hendriksen, P. V., and Lein, H. L. (2018). Effect of pre-oxidation on the oxidation resistance of crofer 22 apu. *Corros. Sci.* 138, 189–199. doi:10.1016/j.corsci.2018.04.016

Vøllestad, E., Strandbakke, R., Tarach, M., Catalan-Martinez, D., Fontaine, M.-L., Beeaff, D., et al. (2019). Mixed proton and electron conducting double perovskite anodes for stable and efficient tubular proton ceramic electrolyzers. *Nat. Mat.* 18, 752–759. doi:10.1038/s41563-019-0388-2

Wang, R., Sun, Z., Lu, Y., Gopalan, S., Basu, S. N., and Pal, U. B. (2020). Comparison of chromium poisoning between lanthanum strontium manganite and lanthanum strontium ferrite composite cathodes in solid oxide fuel cells. *J. Power Sources* 476, 228743. doi:10.1016/j.jpowsour.2020.228743

Yang, Y., Tong, X., Hauch, A., Sun, X., Yang, Z., Peng, S., et al. (2021). Study of solid oxide electrolysis cells operated in potentiostatic mode: Effect of operating temperature on durability. *Chem. Eng. J.* 417, 129260. doi:10.1016/j.cej.2021.129260

Zhu, H., Ricote, S., Duan, C., O'Hayre, R. P., and Kee, R. J. (2018). Defect chemistry and transport within dense $\text{BaCe}_{0.7}\text{Zr}_{0.1}\text{Yb}_{0.1}\text{O}_{3-\delta}$ (BCZYYb) proton-conducting membranes. *J. Electrochem. Soc.* 165 (10), F845–F853. doi:10.1149/2.1091810jes

Zhu, H., Ricote, S., Duan, C., O'Hayre, R. P., Tsvetkov, D. S., and Kee, R. J. (2018). Defect incorporation and transport within dense $\text{BaZr}_{0.8}\text{Y}_{0.2}\text{O}_{3-\delta}$ (BZY20) proton-conducting membranes. *J. Electrochem. Soc.* 165 (9), F581–F588. doi:10.1149/2.0161809jes

Zhu, H., Ricote, S., and Kee, R. J. (2022). Faradaic efficiency in protonic-ceramic electrolysis cells. *J. Phys. Energy* 4 (1), 014002. doi:10.1088/2515-7655/ac3729

Zvonareva, I., Fu, X.-Z., Medvedev, D., and Shao, Z. (2022). Electrochemistry and energy conversion features of protonic ceramic cells with mixed ionic-electronic electrolytes. *Energy Environ. Sci.* 15, 439–465. doi:10.1039/d1ee03109k



OPEN ACCESS

EDITED BY

Fabio Coral Fonseca,
Instituto de Pesquisas Energéticas e
Nucleares (IPEN), Brazil

REVIEWED BY

Xiaohui Yan,
Shanghai Jiao Tong University, China
Yu-Tong Mu,
Xi'an Jiaotong University, China

*CORRESPONDENCE

Pablo A. García-Salaberri,
pagsalab@ing.uc3m.es

SPECIALTY SECTION

This article was submitted to Fuel Cells,
Electrolyzers and Membrane Reactors, a
section of the journal Frontiers in Energy
Research

RECEIVED 30 September 2022

ACCEPTED 26 October 2022

PUBLISHED 06 December 2022

CITATION

García-Salaberri PA, Sánchez-Ramos A and
Das PK (2022), On the optimal cathode
catalyst layer for polymer electrolyte fuel
cells: Bimodal pore size distributions with
functionalized microstructures.
Front. Energy Res. 10:1058913.
doi: 10.3389/fenrg.2022.1058913

COPYRIGHT

© 2022 García-Salaberri, Sánchez-Ramos
and Das. This is an open-access article
distributed under the terms of the [Creative
Commons Attribution License \(CC BY\)](#). The
use, distribution or reproduction in other
forums is permitted, provided the original
author(s) and the copyright owner(s) are
credited and that the original publication in
this journal is cited, in accordance with
accepted academic practice. No use,
distribution or reproduction is permitted
which does not comply with these terms.

On the optimal cathode catalyst layer for polymer electrolyte fuel cells: Bimodal pore size distributions with functionalized microstructures

Pablo A. García-Salaberri^{1*}, Arturo Sánchez-Ramos¹ and
Prodip K. Das²

¹Department of Thermal and Fluids Engineering, University Carlos III of Madrid, Leganés, Spain,

²School of Engineering, Newcastle University, Newcastle, United Kingdom

A high advancement has been achieved in the design of proton exchange membrane fuel cells (PEMFCs) since the development of thin-film catalyst layers (CLs). However, the progress has slowed down in the last decade due to the difficulty in reducing Pt loading, especially at the cathode side, while preserving high stack performance. This situation poses a barrier to the widespread commercialization of fuel cell vehicles, where high performance and durability are needed at a reduced cost. Exploring the technology limits is necessary to adopt successful strategies that can allow the development of improved PEMFCs for the automotive industry. In this work, a numerical model of an optimized cathode CL is presented, which combines a multiscale formulation of mass and charge transport at the nanoscale (~ 10 nm) and at the layer scale (~ 1 μ m). The effect of exterior oxygen and ohmic transport resistances are incorporated through mixed boundary conditions. The optimized CL features a vertically aligned geometry of equally spaced ionomer pillars, which are covered by a thin nanoporous electron-conductive shell. The interior surface of cylindrical nanopores is catalyzed with a Pt skin (atomic thickness), so that triple phase points are provided by liquid water. The results show the need to develop thin CLs with bimodal pore size distributions and functionalized microstructures to maximize the utilization of water-filled nanopores in which oxygen transport is facilitated compared with ionomer thin films. Proton transport across the CL must be assisted by low-tortuosity ionomer regions, which provide highways for proton transport. Large secondary pores are beneficial to facilitate oxygen distribution and water removal. Ultimate targets set by the U.S. Department of Energy and other governments can be achieved by an optimization of the CL microstructure with a high electrochemical surface area, a reduction of the oxygen transport resistance from the channel to the CL, and an increase of the catalyst activity (or maintaining a similar activity with

Pt alloys). Carbon-free supports (e.g., polymer or metal) are preferred to avoid corrosion and enlarge durability.

KEYWORDS

catalyst layer, Pt loading, transport, optimization, performance, durability, proton exchange membrane fuel cell, fuel cell vehicle

1 Introduction

The development of thin-film catalyst layers (CLs) at Los Alamos National Laboratory (LANL) at the beginning of the 90s (thickness, $\delta_{cl} \approx 50\text{--}100\ \mu\text{m}$) was a breakthrough in proton exchange membrane fuel cells (PEMFCs). The replacement of microstructures that worked with liquid electrolytes based on Pt black catalyst and polytetrafluoroethylene (PTFE) binder by microstructures based on Pt/C catalyst and ionomer (Nafion) dramatically increased catalyst utilization, decreasing Pt loading from $L_{Pt} = 4\ \text{mg}_{Pt}\ \text{cm}^{-2}$ to $L_{Pt} = 0.4\ \text{mg}_{Pt}\ \text{cm}^{-2}$ (Wilson and Gottesfeld, 1992). However, Pt loadings around $L_{Pt} = 0.4\ \text{mg}_{Pt}\ \text{cm}^{-2}$ are still the commercial standard, since a further reduction of the Pt loading has been difficult since then due to performance and durability issues (Kongkanand and Mathias, 2016; Nguyen et al., 2021; Tellez-Cruz et al., 2021). Losses are more important at the cathode due to the sluggish kinetics of the oxygen reduction reaction (ORR) and lower diffusivity of oxygen compared with the fast kinetics of the hydrogen oxidation reaction (HOR) and high diffusivity of hydrogen (García-Salaberri, 2022). Concern about this situation has increased in the last decade as PEMFCs are reaching their commercialization stage, especially in the automotive sector, where they compete with other technologies (internal combustion engine and Li-ion battery) (Atanassov et al., 2021). Recent targets set by the U.S. Department of Energy (DOE) for fuel cell vehicles to make PEFC technology competitive have been hardly met (Wang et al., 2020a). The Toyota Mirai presented in 2018 showed limited durability of 3,000 h in a real-world driving test and failed largely in a DOE accelerated stress test (AST) protocol. The performance decreased significantly after 5,000 cycles with a cathode CL thickness reduction from approximately $10\ \mu\text{m}$ – $3\ \mu\text{m}$ (Borup et al., 2018). Recently, an assessment performed by a team of experts concluded that the median 2017 automotive cost of a PEMFC system is around $75\ \$\ \text{kW}^{-1}$ with a stack durability and power density of 4,000 h and $2.5\ \text{kW}\ \text{L}^{-1}$, whilst the DOE ultimate targets are $30\ \$\ \text{kW}^{-1}$, 8,000 h and $3\ \text{kW}\ \text{L}^{-1}$, respectively. The ultimate performance target is expected to be met by 2035 and the ultimate cost and durability targets by 2050 (Whiston et al., 2019). Despite the ongoing progress, other numbers are also still away of targets established for 2025 by the U.S. and other regions, such as the European Union (Yunzhe et al., 2020) (the status reported during 2015–2020 is indicated in brackets (DOE, 2015;

Wang et al., 2020a)): 1) total Pt group metal (PGM) content lower than $0.1\ \text{g}\ \text{kW}^{-1}$ ($0.16\ \text{g}\ \text{kW}^{-1}$); 2) rated power density of $1\ \text{W}\ \text{cm}^{-2}$ ($0.81\ \text{W}\ \text{cm}^{-2}$); 3) minimum electrical resistance of $1000\ \Omega\ \text{cm}^2$ ($1635\ \Omega\ \text{cm}^2$).

A key issue for decreasing Pt loading (mainly at the cathode) is caused by local mass transport resistance introduced by thin ionomer films surrounding Pt nanoparticles (Weber and Kusoglu, 2014; Sánchez-Ramos et al., 2021, 2022). The local oxygen transport resistance (per unit of geometric area) is inversely proportional to the roughness factor, the ratio between the electrochemically active surface area and the cell geometric area, $r_f = A_{Pt} A_{geo}^{-1}$. The detrimental effect of reducing r_f is a limitation of heterogeneous reactive systems, since the average oxygen flux at the surface of Pt nanoparticles, $N_{O_2}^{Pt}$, increases by a factor r_f^{-1} with respect to the oxygen flux per unit of geometric area, $N_{O_2}^{geo}$. In other words, $N_{O_2}^{Pt} = r_f^{-1} N_{O_2}^{geo}$ according to the species mass conservation equation (Greszler et al., 2012). For a vanishing Pt loading ($L_{Pt} \rightarrow 0$), the oxygen flux at a lonely catalytic site would become infinitely high, $N_{O_2}^{Pt} \rightarrow \infty$, thereby leading to strong mass transport losses to maintain a prescribed current density ($I^{avg} > 0$). Consequently, the cell performance will inevitably drop to the stable point provided by a null current density ($I^{avg} \rightarrow 0$ when $r_f \rightarrow 0$) regardless of the feed flow rate and the catalyst activity. A similar barrier would arise for other transported species, protons and electrons, even though the performance limitation is less severe than in the case of oxygen because charge transport resistances are lower, especially in the case of electrons. The performance loss at small r_f can be mitigated in three ways: 1) increasing the electrochemically active surface area per unit catalyst mass, ECSA, to increase A_{Pt} at a given Pt loading, L_{Pt} , 2) reducing any mass transport resistance in the path of oxygen from the channel (say, stack inlet) toward each catalyst site, and 3) increasing the catalyst mass activity, so that each Pt nanoparticle can potentially generate a higher current at a given overpotential (provided that other losses do not limit performance). If the design is not restricted to Pt, the fourth 4) available option is to use Pt alloys or PGM-free catalysts with an activity comparable to that of Pt (Sánchez-Ramos et al., 2022; Liu et al., 2019b,a).

A large effort has been devoted to improving performance at low Pt loading, including the increase of the ECSA, the development of more active catalysts with reduced Pt content, and the decrease of mass transport resistances in the membrane electrode assembly (MEA), flow field and

stack (Goshtasbi et al., 2019; Park et al., 2019; Chen et al., 2020; Cochet et al., 2020). Here, we shall focus mainly on the latter approach, since the other options can be incorporated into a previously optimized design in terms of mass transport. Reducing the oxygen transport resistance in a PEMFC can be addressed by: 1) a reduction of the internal mass transport resistance of the CL microstructure, 2) a reduction of the mass transport resistance of the backing layer (gas diffusion layer, GDL, and microporous layer, MPL) and at the GDL/channel/rib interface, 3) a decrease of the along-the channel and stack flow distributor resistance caused by difficulties in liquid water removal (especially at high current densities above $2\text{--}3\text{ A cm}^{-2}$), or a combination thereof (see, e.g. (Yi et al., 2012; Choi et al., 2014; García-Salaberri P. et al., 2017; Azarafza et al., 2019; Deng et al., 2021; Zhang et al., 2021; Zapardiel and García-Salaberri, 2022), among others). The ohmic loss in the proton exchange membrane (PEM) and CLs is less relevant at low Pt loading in state-of-the-art designs. **Figure 1A** shows the peak power density per unit mass of Pt achieved with some CL designs presented in the last years. To facilitate the presentation, two groups are distinguished: 1) conventional CLs (CONV and C-ENG in **Figure 1**) based on the original thin-film CL design without and with engineered or modified nanoporous supports (pore radius, $R_p \leq 10\text{ nm}$), and 2) innovative CLs (VA, NSTFC and I-ENG in **Figure 1**), which includes alternative CL designs aimed at reducing mass and ohmic transport losses across the CL thickness, at local Pt sites, or at both locations. Advances achieved in both groups are discussed below.

In terms of conventional CLs, two main approaches have been used to enhance performance at low Pt loading: 1) reduction of bulk transport losses considering alternative production techniques (e.g., catalyst deposition by electrospraying or freeze drying (Folgado et al., 2018; Talukdar et al., 2019)), and 2) the modification of nanoporous supports to optimize triple phase points at catalyst sites (CONV-ENG) (Yarlagadda et al., 2018; Ramaswamy et al., 2020; Kobayashi et al., 2021). The second strategy is more fundamental. Provided that a continuous electron pathway exists across a CL, there are two options to form triple phase points (allowing a simultaneous access of oxygen, protons and electrons): 1) active catalyst in contact with liquid water, and 2) active catalyst in contact with hydrated ionomer. Compared with transport in an ionomer film, oxygen diffusion in liquid water is easier while proton conduction in liquid water is more difficult (Zenyuk and Litster, 2014; Muzaffar et al., 2018). Since oxygen transport is typically the limiting process at low Pt loading, transport in liquid water at triple phase points is preferred (Yarlagadda et al., 2018). In addition, catalyst sites in contact with liquid water do not suffer from a reduction of the electrochemical activity due to adsorption of sulfonate groups at hydrophilic Pt surfaces (Takeshita et al., 2020). The General

Motors Company exploited this approach by engineering accessible nanopores already present in high surface area carbon (HSAC) supports, such as Ketjenblack, in contrast to low surface area carbon (LSCA) supports (e.g., Vulcan) (Yarlagadda et al., 2018). Van der Waals adsorption, capillary condensation and water generation ensured the presence of liquid water in nanopores. As a result, efficient oxygen and proton transport around catalyst sites was possible, while providing good proton transport at the layer scale through ionomer films (Zenyuk and Litster, 2014). The achieved Pt mass-specific performance was remarkably high (the largest reported so far to the authors' knowledge), $P_{Pt} \approx 20\text{ W mg}_{Pt}^{-1}$ ($I^{avg} = 2\text{ A cm}^{-2}$ at $V_{cell} \approx 0.65\text{ V}$ and $L_{Pt} = 0.06\text{ mg}_{Pt}\text{ cm}^{-2}$), similar to that reached in the Toyota Mirai with $L_{Pt} = 0.3\text{ mg}_{Pt}\text{ cm}^{-2}$ (five times higher). Generally speaking, for a given nanoporous support and CL preparation route, a fraction of Pt nanoparticles is deposited inside nanopores, while the remaining stays on the outer surface covered by ionomer. Consequently, there is an optimum ionomer-to-carbon ratio, I/C^{opt} , which maximizes the peak power density due to a proper balance between mass transport and ohmic losses. When most of the catalyst is inside nanopores, a higher I/C is desirable to facilitate proton transport along the outer surface if ionomer does not block the access to the interior of nanopores (Kobayashi et al., 2021).

In terms of innovative CLs, Toyota Motor Corporation developed vertically aligned (VA) microstructures based on the idealized design proposed by Middelmann (Middelmann, 2002; Murata et al., 2014). This idealized microstructure is composed of a structured array of electron-conductive pillars catalyzed with Pt and covered with a co-axial ionomer film for proton transport. This design provides the best theoretical solution to minimize bulk transport losses provided that water flooding is not an issue and the ionomer film is able to conduct protons efficiently with a negligible local mass transport resistance. However, this is not usually the case in practice, where the ionomer mass transport resistance significantly reduces the performance at low Pt loading, leading to a non-optimal ECSA utilization (Spingler et al., 2017; Schuler et al., 2019). Two worth noting designs have been proposed to overcome this issue: 1) ionomer-free nanostructured thin film catalyst (NSTFC) developed by The 3M Company (Debe et al., 2006; Debe, 2011; Debe et al., 2011; Debe, 2012; Ostroverkh et al., 2019), and 2) designs based on a combination of ionomer nanofibers (proton transport highways) and a conventional microstructure with reduced ionomer content (ION-ENG) examined by U.S. National Laboratories and Toyota Motor Corporation (Zhang and Pintauro, 2011; Borup and Weber, 2019; Sun et al., 2019; Yoshino et al., 2020). Ultra-thin NSTFC electrodes ($\delta_{cl} < 1\text{ }\mu\text{m}$) are solely composed of polymer whiskers catalyzed by a Pt monolayer, so that the Pt skin is used to conduct electrons and (generated) liquid water to conduct protons. Despite its simplicity, the main drawback of this design is caused by flooding of the cathode

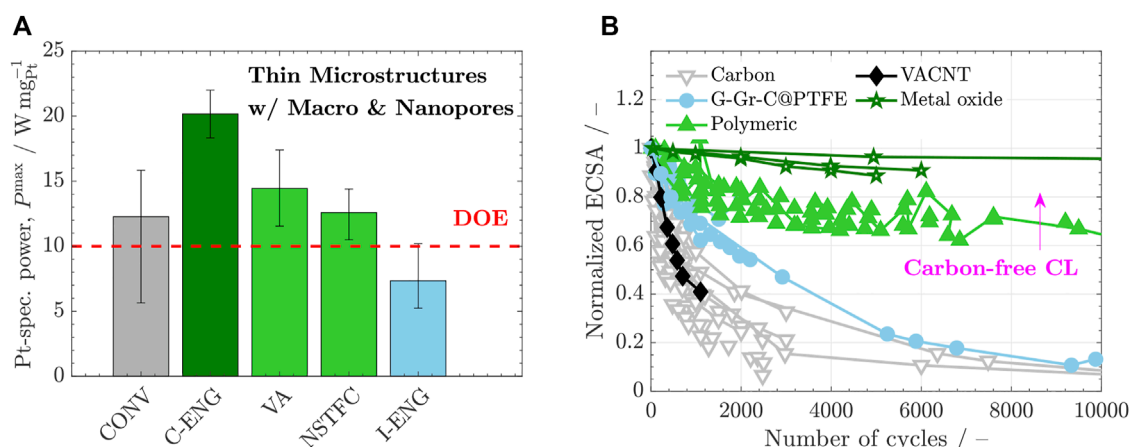


FIGURE 1

(A) Peak power per Pt milligram, P_{max} , achieved with different cathode CL designs: CONV, conventional CLs with solid (Vulcan) and nanoporous (e.g., KetjenBlack) carbon supports prepared by different techniques (e.g., airbrush or electro spraying) (Orfanidi et al., 2017; Garsany et al., 2018; Conde et al., 2019; Talukdar et al., 2019; Cui et al., 2021); CONV-ENG, conventional CLs with engineered or modified nanoporous supports (Yarlagadda et al., 2018; Ramaswamy et al., 2020); VA, CLs with vertically aligned supports covered by ionomer (i.e., based on Middelmann's ideal microstructure) (Murata et al., 2014; Xia et al., 2015; Meng et al., 2022); NSTFC, ionomer-free nanostructured thin film catalysts (Debe (2012); Debe et al. (2011); Debe (2011); Debe et al. (2006); Ostroverkh et al. (2019)); ION-ENG, CLs with engineered or modified ionomer distributions (e.g., a combination of ionomer nanofibers and conventional microstructures with reduced ionomer content) (Zhang and Pintauro, 2011; Borup and Weber, 2019; Sun et al., 2019; Yoshino et al., 2020). The 2020 DOE target, $P \approx 10\ W\ mg_{Pt}^{-1}$, is indicated by a red dashed line. Baseline operating conditions: air/ H_2 , temperature, $T = 70 - 80^\circ C$, relative humidity, $RH = 1$, cathode back pressure, $p_c = 150\ kPa(abs)$. (B) Normalized ECSA with respect to BOL as a function of the number of cycles in ASTs for different catalyst supports: Carbon, CLs supported on conventional carbon nanoparticles (Babu et al., 2021) and other references included herein); G-Gr-C@PTFE, CLs supported on either graphitized carbon, graphene or PTFE-doped carbon nanoparticles (Wang et al., 2019; Babu et al., 2021; Pushkareva et al., 2021); VACNT, CLs based on vertically aligned carbon nanotubes covered by ionomer (Murata et al., 2014; Meng et al., 2022); Polymer, CLs based on polymer whiskers without (e.g., NSTFC (Debe et al., 2006; Debe, 2011; Debe et al., 2011; Debe, 2012; Ostroverkh et al., 2019)) and with (Xia et al., 2015) ionomer films; Metal oxide, conventional CLs supported on metal oxide nanoparticles (e.g., titanium dioxide (TiO_2) powder) (Esfahani et al., 2018; Esfahani and Easton, 2020; Chen et al., 2021).

CL at low operating temperature, which can be ascribed to the hydrophilicity of the Pt skin and CL thinness (Debe, 2012; Zenyuk et al., 2016a). Moreover, oxygen diffusion and proton conduction across hundreds of nanometers of liquid water in NSTFC electrodes is a sub-optimal solution to increase the peak power density compared with the lower lengths that can be achieved in CON-ENG designs. ION-ENG electrodes are an interesting option toward the development of bi-functionalized microstructures that can combine facilitated domains for oxygen and proton transport. Currently, the main practical difficulty lies in producing composite microstructures with a good transition between ionomer nanofibers and ionomer thin films. The performance achieved with this variant is still below the 2020 DOE target, even though it has been shown to be a viable route to increase performance at reduced RH due to enhanced water uptake (Yoshino et al., 2020).

The ECSA reduction normalized with respect to the value at the beginning of life (BOL) achieved in ASTs with different catalyst supports is shown in Figure 1B. Although the high activity of Pt/C catalysts is desirable, carbon supports can suffer from limited durability mainly due to: 1) agglomeration of Pt nanoparticles ($R_{Pt} \sim 2\ nm$) caused by electrochemical

Ostwald ripening and/or migration-coalescence, and 2) an overlap between the operating voltage and the carbon corrosion potential, especially at cell voltages above $V_{cell} \approx 1\ V$ (Babu et al., 2021; Zhao et al., 2021). Catalyst agglomeration leads to a direct reduction of the ECSA, since larger Pt nanoparticles feature a lower specific surface area, $ECSA \propto R_{Pt}^{-1}$. An effective strategy to mitigate catalyst agglomeration is the use of stable catalyst skins, which behave as one being rather than as multiple independent entities (Debe et al., 2006; Mardle and Du, 2022). Carbon corrosion leads to a loss of support material due to carbon oxidation, which causes electrode thinning, porosity reduction, pore size increase (reduction of nanopore volume fraction) and ECSA reduction (Borup et al., 2020). The combined effect of material loss and nanopore clogging can be particularly problematic for HSAC supports that store a large part of their ECSA inside nanopores. Recent work has shown that the durability of carbon-based supports can be somewhat extended using graphitized carbon or graphene, as well as carbon supports doped with tailored amounts of PTFE, because of their higher oxidation resistance (Wang et al., 2019; Babu et al., 2021; Pushkareva et al., 2021). Vertically aligned carbon nanotubes (VACNTs) also seem

Bi – functionalized Bimodal Microstructure

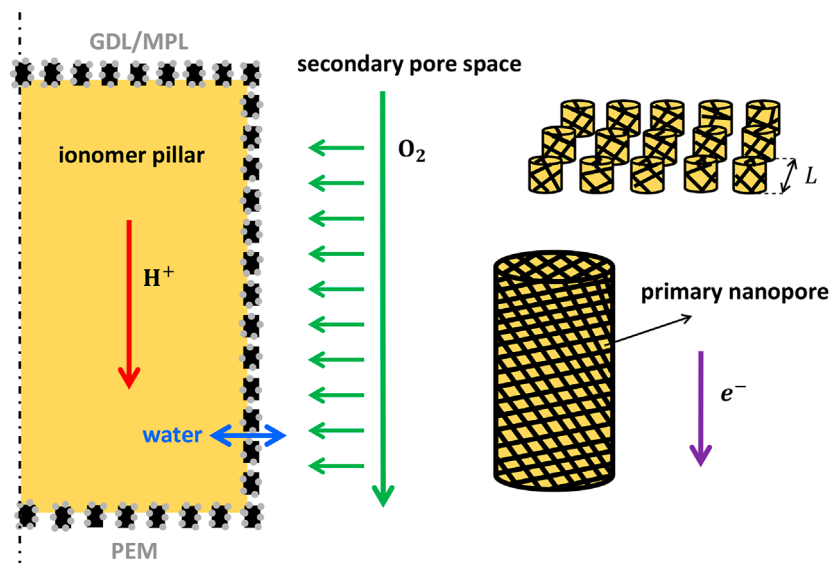


FIGURE 2

Schematic of a bi-functionalized bimodal cathode CL microstructure with targeted domains for proton and gas species transport, and a primary ($R \leq 10$ nm)/secondary ($R \geq 10$ nm) pore size distribution. ORR and electron transport take place in a nanoporous shell covering ionomer pillars, which is made of a highly electron-conductive material catalyzed with Pt. Liquid water can be transported both through ionomer pillars and released to secondary pores. The characteristic spacing between pillars is L .

to be an insufficient solution to solve the problem of carbon corrosion (Murata et al., 2014; Meng et al., 2022), even though improvement has been achieved with double-walled (DWCNTs) and multi-walled (MWCNTs) carbon nanotubes (Chen et al., 2007; MoghadamEsfahani et al., 2020). Carbon-free electrodes have shown significantly longer durability than carbon-based supports due to oxidation suppression (Antolini and Gonzalez, 2009; Lv and Mu, 2014). Among carbon-free supports, metal oxide supports are a robust option because of their high electrical conductivity and corrosion resistance. In particular, titanium dioxide (TiO_2) supports are very active with Pt and have provided an extraordinarily high corrosion resistance above DOE targets (Esfahani et al., 2018; Esfahani and Easton, 2020; Chen et al., 2021). Nevertheless, the widespread adoption of supports based on Ti requires an economic analysis. Polymeric and ceramic supports can be a cost-effective alternative but in general suffer from the problem of low electrical conductivity, being necessary a modification of the raw material (Xia et al., 2015). The issue of low electrical conductivity can be avoided if the support is not used for electron conduction, as in the case of NSTFC electrodes (Debe, 2012).

In this work, as shown in Figure 2, the performance of an idealized cathode CL which features a VA geometry with a bimodal pore size distribution is examined. The microstructure is fully bi-functionalized, so there is no interaction between the ionomer space devoted to proton transport and the secondary

space devoted to oxygen transport. The ORR takes place in water-filled primary nanopores grooved in an electron-conductive shell in contact with both domains, and catalyzed with an atomic Pt skin to maximize the ECSA. This microstructure provides an idealized version of the situation found in engineered HSAC supports (CONV-ENG) in which the solid volume fraction has been minimized with the aim of providing a continuous path for electron transport without a significant electrical loss (Wilson and Gottesfeld (1992)). The design further considers that all nanopores (i.e., Pt sites) are accessible and removes entirely any ionomer transport resistance at the entrance of nanopores. The proposed microstructure is to be optimized geometrically. The organization of the paper is as follows. In Section 2, the assumptions and the multiscale approach considered to model the idealized cathode CL and exterior mass and ohmic transport resistances are presented. A special focus is devoted in Subsection 2.1 to the assumptions made on water management, which has not been explicitly modeled here. The formulations of the macroscopic model at the layer scale and the microscopic model at the nanopore scale are presented in Sections 3 and 4, respectively. The case studies are described in Section 5, which considers an analysis of the optimized geometry of the idealized cathode CL, the effect of exterior transport resistances, and the effect of catalyst activity. The results are discussed in Section 6, where technological frontiers are analyzed. Finally, the conclusions are presented in Section 7.

2 Numerical model

2.1 Assumptions

The main simplifying assumptions adopted in the model formulation are as follows:

- 1) Steady state operation, isothermal conditions and ideal gases.
- 2) Full gas humidification ($RH_a^{in} = RH_c^{in} = 1$) and temperature operation at $T \approx 80^\circ\text{C}$.
- 3) The PEM is perfectly impermeable to gas species and convection is negligible in the CL.
- 4) Adsorption kinetics at catalyst sites for the examined voltage close to peak power density ($V_{\text{cell}} = 0.5\text{ V}$) is infinitely fast (Sánchez-Ramos et al., 2021).
- 5) The oxygen concentration drop from the channel to the CL/MPL interface and the voltage drop in other components different from the cathode CL are quantified by an overall mass transport resistance, $R_{\text{O}_2}^{\text{chl}}$, and an overall area-specific ohmic resistance, ASR_{pem} , respectively. Both resistances do not vary with current density.
- 6) Ohmic and thermal contact resistances are negligible.
- 7) The CL microstructure is macroscopically homogeneous, being composed of evenly spaced ionomer pillars covered by a nanoporous electron-conductive shell. The interior surface of nanopores is catalyzed with an atomic Pt skin, and the solid fraction of the shell is composed of a highly conductive material, such as graphite ($\sigma_e \sim 10^4\text{ S cm}^{-1}$), graphene ($\sigma_e \sim 10^5\text{ S cm}^{-1}$) or a metal (e.g., Ti, $\sigma_e \sim 10^4\text{ S cm}^{-1}$). The secondary pore space between ionomer pillars shows a uniform pore size distribution (rather than a heterogeneous pore size distribution as in conventional CLs (Sakai et al., 2009)).
- 8) Degradation is negligible and the stiffness of the CL is infinitely high (Jomori et al., 2012).
- 9) The CL temperature is high enough to avoid flooding due to electrochemical generation and net water transport from anode to cathode. The secondary pore space is partially saturated with a prescribed average saturation s_{avg} , which is used to correct the bulk effective diffusivity. Two-phase flow of water saturation and water vapor is not modeled (see below).
- 10) Primary nanopores grooved in the electron-conductive shell are filled with liquid water from the ORR due to Van der Waals adsorption, capillary condensation and Knudsen effect.

The last two assumptions deserve further attention. Unlike porous media with pore sizes larger than $1\text{ }\mu\text{m}$, two-phase transport in a CL is affected by two nanoscale aspects: 1) reduction of the vapor pressure of water by Van der Waals adsorption and Kelvin effect, and 2) reduction of the diffusivity coefficient of gas species by Knudsen effect.

According to the Kelvin equation, the actual saturation pressure of water in a nanometric concave meniscus, $p_{\text{H}_2\text{O}}^{\text{sat}}$, is reduced exponentially compared with the value of a flat interface, $p_{\text{H}_2\text{O}}^{\text{sat,flat}}$, according to

$$\ln\left(\frac{p_{\text{H}_2\text{O}}^{\text{sat}}}{p_{\text{H}_2\text{O}}^{\text{sat,flat}}}\right) = -\frac{2\sigma V_{m,\text{H}_2\text{O}}}{R^{\text{eff}} R^o T} \quad (1)$$

where R^o is the universal gas constant, $\sigma \approx 0.072\text{ Nm}^{-1}$ is the surface tension of the water-air fluid pair, $V_{m,\text{H}_2\text{O}} = M_{\text{H}_2\text{O}}/\rho_{\text{H}_2\text{O}}$ is the molar volume of water, $R^{\text{eff}} = R/\cos\theta$ is the (effective) meniscus radius, and θ is the contact angle. Water shows a hydrophilic or mixed-wettability character with conventional materials employed in CLs ($\theta \leq 90^\circ$). The contact angle is lower for metals, such as Pt, stainless steel and TiO_2 ($\theta_{\text{Pt}} \approx 40^\circ$, $\theta_{\text{ss}} \approx 65^\circ$, $\theta_{\text{TiO}_2} \approx 72^\circ$), and higher for carbon ($\theta_c \approx 80^\circ$) (Park and Aluru, 2009; Martinez-Urrutia et al., 2018; Liu et al., 2021). Hydrophobic contact angles can be achieved with graphene ($\theta_{\text{gr}} \approx 95^\circ - 100^\circ$) (Taherian et al., 2013).

The reduction of the diffusivity coefficient of species i due to Knudsen effect (i.e., the frequent collision of gas molecules with pore walls) depends on the pore radius, R , according to the expression

$$f^{\text{knud}} = \frac{D_i}{D_i^{\text{mol}}} = \left(1 + \frac{D_i^{\text{mol}}}{D_i^{\text{knud}}}\right)^{-1} \quad (2)$$

where D_i^{mol} is the molecular diffusivity coefficient, D_i is the apparent diffusivity coefficient, which can be approximated by the Bosanquet formula, and D_i^{knud} is the Knudsen diffusivity, given by the kinetic theory of gases

$$\frac{1}{D_i} = \frac{1}{D_i^{\text{mol}}} + \frac{1}{D_i^{\text{knud}}}; \quad D_i^{\text{knud}} = \frac{R}{3} \sqrt{\frac{8R^o T}{\pi M_i}} \quad (3)$$

with M_i the molecular mass of species i .

Four key characteristic times can be distinguished related with two-phase transport in the pore space of a CL: 1) capillary action estimated according to the Young–Laplace equation, t_c , 2) phase change of water from the Hertz–Knudsen equation (Jiao and Li, 2011; Attari Moghaddam et al., 2017), t_{pc} , 3) viscous transport of liquid water from the Navier–Stokes equations, t_v , and 4) diffusion of water vapor from Fick's law, $t_{\text{H}_2\text{O},d}$. For a pore radius $R \sim 50\text{ nm}$ and a characteristic velocity $v_c \sim (I^{\text{avg}}/2F)(M_{\text{H}_2\text{O}}/\rho_{\text{H}_2\text{O}}) \sim 10^{-6}\text{ s}$ at $I^{\text{avg}} \approx 1\text{ A cm}^{-2}$, the estimated times in increasing order are.

$$t_c = \frac{\rho v_c R^2}{\sigma} \sim 10^{-17}\text{ s} \quad (4a)$$

$$t_{pc} = \frac{1}{a_{lv} \sqrt{\frac{R^o T}{2\pi M_{\text{H}_2\text{O}}}}} \sim 10^{-12}\text{ s} \quad (4b)$$

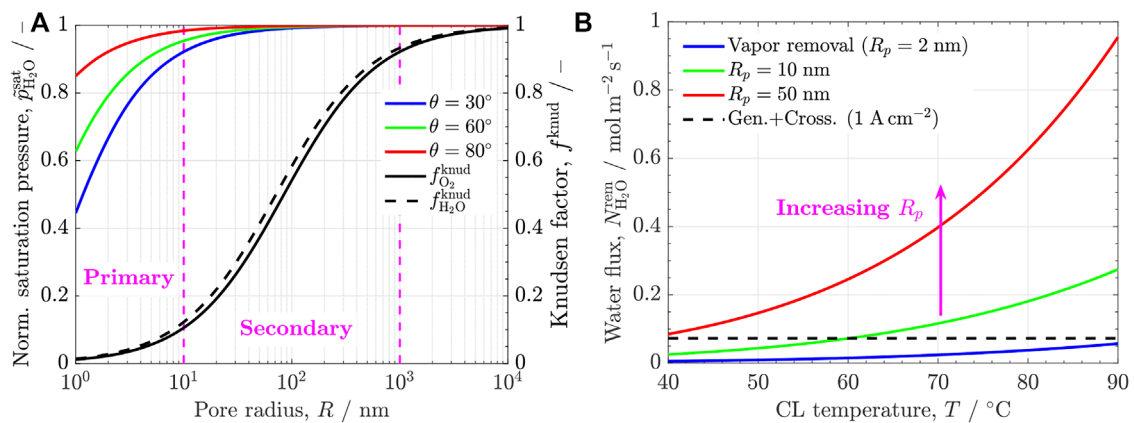


FIGURE 3

(A) Variation of the normalized saturation pressure, $\bar{p}_{\text{H}_2\text{O}}^{\text{sat}} = p_{\text{H}_2\text{O}} / p_{\text{H}_2\text{O}}^{\text{sat}}$, with the pore radius, R , for three different contact angles, $\theta = 30^\circ$ (\approx Pt), 60° , 80° (\approx C), corresponding to $T = 60^\circ\text{C}$. (B) Variation of the removal water vapor flux at the CL/MPL interface, $N_{\text{H}_2\text{O}}^{\text{out}}$, with the CL temperature, T , for three different pore radii, $R = 2, 10, 50$ nm, corresponding to $\theta = 80^\circ$. The water flux due to ORR generation and crossover from anode to cathode ($\beta = 0.2$) is also included for comparison (dashed line). Other parameters: $s^{\text{avg}} = 0.6$, $\varepsilon = 0.4$, $k^{\text{eff}}(s^{\text{avg}}) = 0.3 \text{ W m}^{-1}\text{K}^{-1}$, $\dot{Q} = 3 \text{ kW m}^{-2}$.

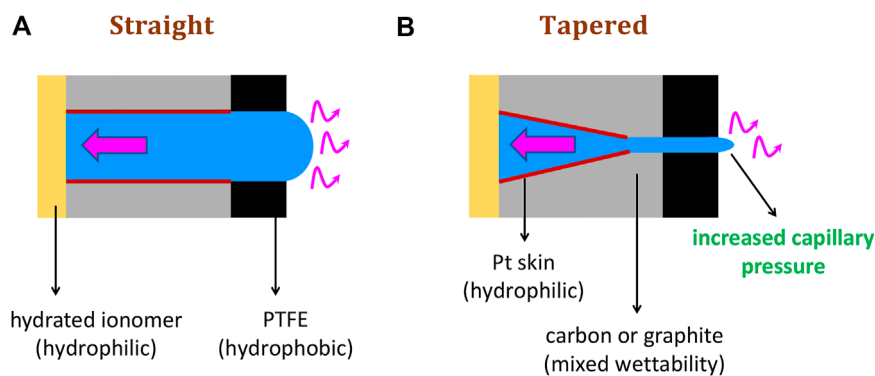


FIGURE 4

Schematic of tailored structures to mitigate cathode flooding in primary nanopores of the idealized bi-functional cathode CL examined in this work: (A) straight cylindrical nanopore with a PTFE coating added on the exterior surface of the nanoporous shell, and (B) tapered nanopore with increased Laplace pressure to enhance transport of liquid water from a hydrophobic PTFE coating toward hydrated ionomer (connected to the anode side through the PEM).

$$t_v = \frac{R^2}{\nu} \sim 10^{-9} \text{ s} \quad (4c)$$

$$t_{\text{H}_2\text{O},d} = \frac{R^2}{D_{\text{H}_2\text{O}}^{\text{eff}}} \sim 10^{-10} \text{ s} \quad (4d)$$

where a_{lv} is the liquid-water specific surface area, which is in the order of $a_{lv} \sim R^{-1} \sim 2 \times 10^7 \text{ m}^{-1}$ for $R = 50$ nm, and $\rho \approx 10^3 \text{ kg m}^{-3}$ and $\nu \approx 10^{-6} \text{ m}^2 \text{ s}^{-1}$ are the density and the kinematic viscosity of liquid water, respectively. The effective diffusivity of water vapor, $D_{\text{H}_2\text{O}}^{\text{eff}}$, for a conventional CL can be approximated as, $D_{\text{H}_2\text{O}}^{\text{eff}} = D_{\text{H}_2\text{O}}^{\text{mol}} f^{\text{knud}} f^{\text{obs}}$, with $f^{\text{obs}} = \varepsilon^2 (1 - s^{\text{avg}})^{2.5}$ ($\varepsilon \approx 0.4$, $s^{\text{avg}} \approx 0.4$) and $D_{\text{H}_2\text{O}}^{\text{mol}}(T) = 2.98 \times$

$10^{-5}(T/333)^{1.5}$ ($T = 80^\circ\text{C}$) (Sánchez-Ramos et al., 2021; García-Salaberri, 2022).

The liquid-phase pressure drop needed to drive the flow of liquid water across a CL can be estimated from Darcy's law. Considering a CL permeability, $K \sim 10^{-15} - 10^{-16} \text{ m}^2$, and a thickness, $\delta_{\text{cl}} \sim 5 \mu\text{m}$ (Zhao et al., 2018), we yield

$$\Delta p_l \sim \frac{\mu \nu_c \delta_{\text{cl}}}{K} \sim 1 - 10 \text{ Pa} \ll p_c \sim \frac{\sigma}{R^{\text{eff}}} \sim 10^4 \text{ Pa} \quad (5)$$

According to this result, the effect of the liquid water flow on the liquid pressure distribution established by capillarity is virtually negligible, which agrees with the numerical results of Liu et al. (2013) and previous experimental p_c - s curves reported for CLs without and with cracks Kusoglu et al. (2012).

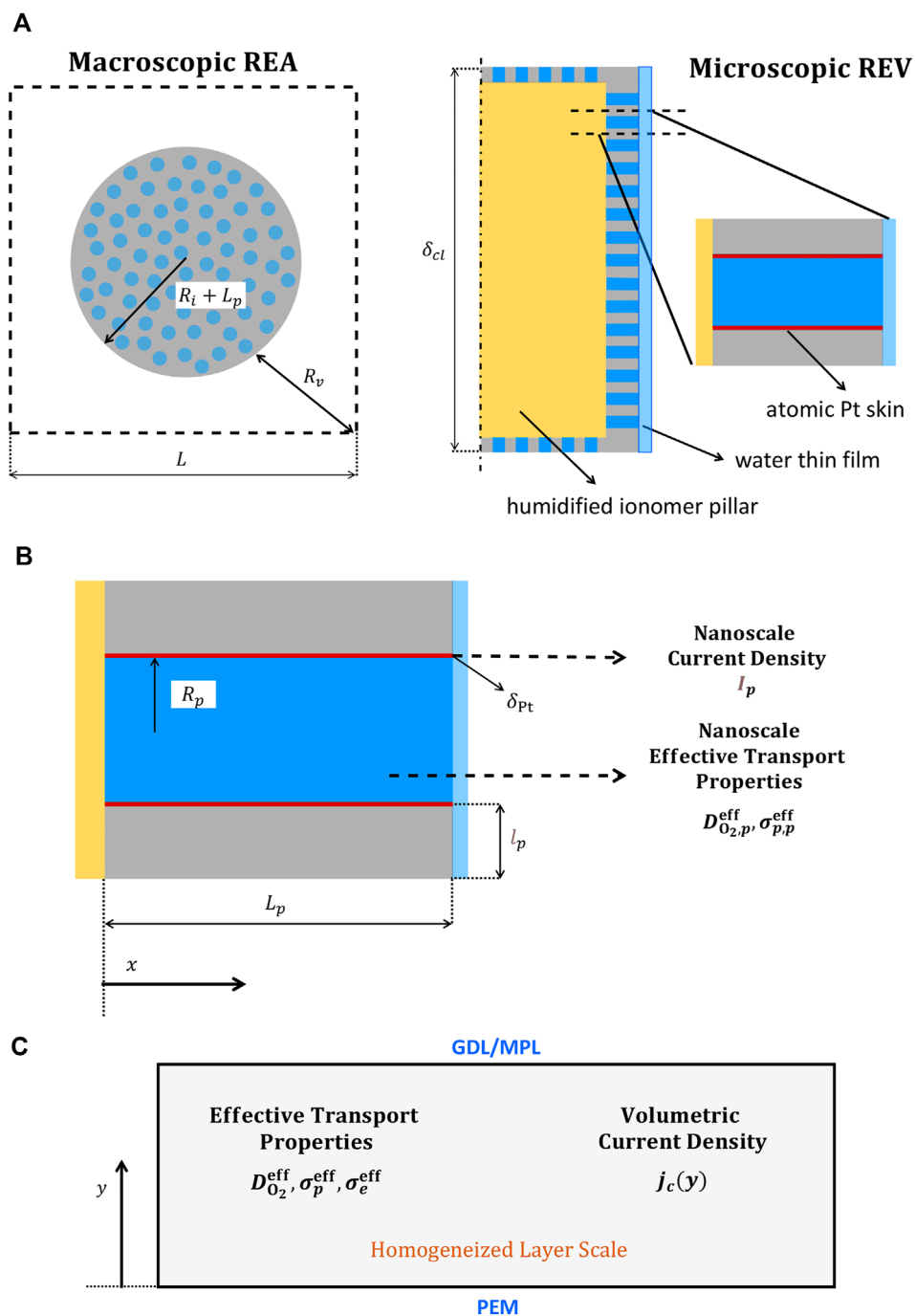


FIGURE 5

(A) REA of the examined bi-functionalized bimodal CL composed of cylindrical ionomer pillars surrounded by a nanoporous shell catalyzed with an atomic Pt skin. (B) Close-up view of the nanoscale geometry between an ionomer pillar and the secondary pore space. (C) Macro-homogenized representation of the CL at the layer scale with composition-dependent effective transport properties and volumetric current density determined from the microscopic model at the nanoscale.

Putting all together, the above estimations suggest that water transport in vapor and liquid forms take place on a time scale significantly slower than phase change phenomena and (virtually instantaneous) capillary action (i.e., $t_v, t_{H_2O,d} \gg t_{pc} \gg t_c$). Water transport is also expected to be slower compared with water desorption/sorption from/to ionomer, since ionomer and liquid-water specific surface areas are of a similar order of magnitude in conventional CLs ($a_{lv} \sim a_i \sim R^{-1}$). This scenario is comparable to that reported for GDLs, where evaporation/condensation of water is controlled by transport rather than interfacial kinetics (Gebel et al., 2011; Fumagalli et al., 2015; Zenyuk et al., 2016b). As shown in **Figure 3A**, the bimodal pore size distribution of CLs offers a good balance to simultaneously provide a high liquid-gas interfacial area in water-filled primary pores due to Van der Waals adsorption and capillary condensation ($R \sim 2\text{--}10\text{ nm}$), and an enhanced water vapor removal rate through secondary pores due to reduced Knudsen effect ($R \geq 50\text{ nm}$) (Zientara et al., 2013; Li et al., 2019; Huang et al., 2021). Neglecting phase-change resistances, the water vapor removal rate under partially-saturated conditions driven by a temperature gradient across a CL is given by (Kim and Mench, 2009)

$$N_{H_2O}^{out} = \frac{1}{R^0} \frac{d(D_{H_2O}^{eff} p_{H_2O}^{sat}/T)}{dT} \frac{dT}{dz} \quad (6)$$

where $p_{H_2O}^{sat}(T)$ is the saturation pressure of water (Sánchez-Ramos et al., 2021). This expression shows that although CLs are almost isotherms (temperature variation, $\Delta T \leq 10^{-3} - 10^{-2}\text{ K}$), the temperature gradient created by generated heat is similar to that found in GDLs and cannot be neglected. In a first approximation, neglecting the water vapor flux across the PEM, the temperature gradient at the CL/MPL interface increases with current density

$$\frac{dT}{dz} \sim \frac{\Delta T_d}{\delta_{cl}} \sim \frac{\dot{Q}}{k^{eff}(s^{avg})}; \quad \dot{Q} \sim \frac{1}{2} \left(\frac{h_{lv}}{2F} - V_{cell} \right) I^{avg} \quad (7)$$

where \dot{Q} is the heat flux removed through the cathode compartment due to electrochemical reaction at a current density I^{avg} , which can be reasonably assumed to be half of the total generated heat flux, $h_{lv} \approx 242\text{ kJ mol}^{-1}$ is the latent heat of vaporization/condensation of water, V_{cell} is the operating cell voltage and F is Faraday's constant (Thomas et al., 2014; Straubhaar et al., 2015).

Figure 3B shows the water vapor removal rate as a function of CL temperature for various pore radii, corresponding to an output current density $I^{avg} \approx 1\text{ A cm}^{-2}$ and a net water transport coefficient across the PEM from anode to cathode, $\beta = 0.2$ ($s^{avg} \approx 0.6$). For a small pore radius, $R \approx 2\text{ nm}$, the water removal flux in vapor form is not sufficient to transport the generation + crossover water flux in the temperature range $T = 40\text{--}90^\circ\text{C}$. The same situation is found at temperatures below $T \leq 60^\circ\text{C}$ for $R \approx 10\text{ nm}$. Consequently, excess water is

removed to the cathode MPL in liquid phase, condensed in the pore space, sorbed into the ionomer and/or pushed to the anode by a pressure difference (if a pressure difference between compartments exists). In contrast, when the pore radius is increased to tens of nanometers, $R \geq 50\text{ nm}$, removal in vapor form is possible in the full temperature range. As a result, liquid water is desorbed from the ionomer to the pore space, liquid water is evaporated and/or liquid water enters the cathode CL by a pressure difference. This result highlights the importance of maintaining the CL at as high a temperature as possible within operational constraints. For a given current density (i.e., heat flux, \dot{Q}), liquid water saturation in the cathode CL can be decreased in three (main) ways: 1) reducing the water crossover flux from anode to cathode (e.g., using a hydrophobic cathode CL and/or a thin PEM), 2) enhancing water removal in vapor form with a lower effective thermal conductivity under partially saturated conditions and/or increasing the CL temperature (regardless of the cell temperature), and 3) facilitating water removal in liquid form, so that water that cannot be vaporized or sorbed into the ionomer can be easily evacuated in liquid form (Avcioglu et al., 2016; Chi et al., 2018; Folgado et al., 2018; Steinbach et al., 2018; Wang et al., 2019; Lin et al., 2021). The second option is challenged by the dependency of the effective thermal conductivity on water saturation, so a proper design of the layers adjacent to the cathode CL (e.g., the cathode MPL) may be necessary. Solutions to improve water management by a modification of the cathode CL microstructure can be achieved through a tailored addition of PTFE to decrease hydrophilicity from the interior to the exterior of nanopores (see **Figure 4**). The generated Laplace pressure difference between cathode and anode can be used to push water toward the ionomer, water menisci pinned at PTFE edges to enhance evaporation (a similar approach to that used in PTFE membranes in separation processes (Lu et al., 2017; Wang et al., 2020b)), and the external hydrophobic surface outside nanopores to facilitate the transport of liquid water to the cathode MPL. A tapered geometry with a narrow tip at the PTFE surface could also be incorporated to increase the Laplace pressure difference and enhance water transport to ionomer (i.e., anode side)—a rather similar mechanism to that used by some varieties of cactus for water harvesting Malik et al. (2016). Given the variety of possibilities to improve water management, two-phase transport modeling was omitted here. The scope of this work is restricted to examining the technological limits of cathode CLs with optimal transport routes and extracting good design practices for improved performance. No flooding in the cathode CL is assumed due to cell operation at high temperature ($T = 80^\circ\text{C}$) and/or the incorporation of other strategies for water management. The cathode CL is partially saturated with a representative saturation, $s^{avg} \approx 0.4$, including an interfacial resistance caused by water films at the entrance of nanopores.

2.2 Multiscale approach

A multiscale across-the-membrane model is considered to describe oxygen, proton and electron transport in the idealized bi-functional cathode CL (Mu et al., 2022). As shown in Figure 5, the representative elementary area (REA) in the CL is composed of a square region of length L and thickness δ_{cl} with a central ionomer pillar of radius R_i . The average half-size of the secondary pore space surrounding an ionomer pillar is R_v . The ionomer pillar is covered by a nanoporous electron-conductive shell (see close-up view in Figures 5A,B). The microscopic representative elementary volume (REV) inside a shell is composed of a straight nanopore of radius R_p and length $L_p \ll R_i$ (negligible curvature), which is catalyzed with a Pt skin of thickness δ_{pt} . The nanoporosity of the shell is ε_p with an average spacing between pores l_p (hexagonal packing). The effect of the multicomponent microstructure and the nanoscale current generation rate are plugged into a volume-average formulation across the CL thickness by means of: 1) effective transport properties (effective diffusivity, and effective electrical and ionic conductivities), and 2) a volume-specific reaction rate (see the macro-homogeneous domain in Figure 5C). The information extracted before and during a simulation from the macroscopic REA and the microscopic REV is as follows:

- 1) Before a simulation, the bulk effective transport properties in the CL are expressed in terms of primary geometrical parameters. In the idealized geometry, the normalized dry effective molecular diffusivity, $D_{O_2, mol}^{eff, dry} D_{O_2}^{-1}$, is equal to the porosity of the secondary pore space, ε , to account for the reduction of the transport area with respect to the cell geometric area. The Knudsen effect, as presented before in Section 2.1, is introduced as a modification to $D_{O_2, mol}^{eff, dry} D_{O_2}^{-1}$. Similarly, the normalized effective ionic conductivity, $\sigma_p^{eff} \sigma_p^{-1}$, is given by the ionomer volume fraction, ε_i . The normalized effective electrical conductivity, $\sigma_e^{eff} \sigma_e^{-1}$, is modeled according to the expression for a conductive matrix embedded in a hexagonal array of non-conductive cylinders (i.e., nanopores). A hexagonal packing of nanopores provides an optimal solution to maximize the effective electrical conductivity at a given nanoporosity (Perrins et al., 1979; Tomadakis and Sotirchos, 1993). The oxygen diffusivity and the ionic conductivity in liquid water inside nanopores are $D_{O_2, w}$ and $\sigma_{p, w}$, respectively. These values are corrected by the nanoporosity of the shell, ε_p , to obtain the corresponding effective values, $D_{O_2, p}^{eff}$ and $\sigma_{p, p}^{eff}$. The decrease of the oxygen concentration caused by oxygen dissolution in liquid water is taken into account through Henry's constant, $k_{H, O_2, w}$, while the effect of the local curvature of the flux from the secondary pore space to each nanopore of radius R_p is modeled through the entry transport resistance derived by Newman (Newman, 1966).

- 2) During a simulation, oxygen and proton transport are solved in a single pore using a 1D along-the-pore model that includes a surface reaction term. The current density generated in a single pore per unit of platinized area, I_p , is determined, and then converted into a local volumetric current density, $j_c(y)$, through the roughness factor, r_f . The inlet boundary conditions for oxygen and protons in the microscopic model are provided by the local solution of the macroscopic model at each spatial coordinate across the thickness, y -coordinate. The local electronic potential, $\phi_e(y)$, used to evaluate the local overpotential, $\eta_c(y)$, is also provided by the macroscopic model.

The oxygen diffusive resistance from the channel to the CL and the ohmic resistance of the PEM and its interfaces are incorporated through integral mixed boundary conditions into the 1D cathode CL model. Further details of the implementation can be found in (Sánchez-Ramos et al., 2021). The formulations of the macroscopic and microscopic models are presented in the next two sections.

3 Macroscopic model (layer scale)

The macroscopic conservation equations of oxygen, protons and electrons across the CL thickness (y -coordinate) are given by

$$\frac{d}{dy} \left(-D_{O_2}^{eff} \frac{dC_{O_2}}{dy} \right) = -\frac{j_c}{4F} \quad (8a)$$

$$\frac{d}{dy} \left(-\sigma_p^{eff} \frac{d\phi_p}{dy} \right) = -j_c \quad (8b)$$

$$\frac{d}{dy} \left(\sigma_e^{eff} \frac{d\phi_e}{dy} \right) = -j_c \quad (8c)$$

where $D_{O_2}^{eff}$, σ_p^{eff} and σ_e^{eff} are the effective oxygen diffusivity, ionic conductivity and electronic conductivity in the bulk CL, respectively, and j_c is the volumetric current density (the negative sign accounts for consumption, i.e., $j_c > 0$).

3.1 Boundary conditions

Equations (8a)–(8c) are supplemented with the following boundary conditions at the CL/MPL ($y = \delta_{cl}$) and CL/PEM ($y = 0$) interfaces (see Figure 5).

$$C_{O_2} \Rightarrow \text{CL/MPL: } C_{O_2} = C_{O_2, cl}^in; \quad \text{CL/PEM: } \frac{dC_{O_2}}{dy} = 0 \quad (9a)$$

$$\phi_p \Rightarrow \text{CL/MPL: } \frac{d\phi_p}{dy} = 0; \quad \text{CL/PEM: } \phi_p = -\Delta\phi_p \quad (9b)$$

$$\phi_e \Rightarrow \text{CL/MPL: } \phi_e = V_{\text{cell}}; \quad \text{CL/PEM: } \frac{d\phi_e}{dy} = 0 \quad (9c)$$

where V_{cell} is the operating cell voltage, $C_{\text{O}_2}^{\text{in}}$ is the inlet oxygen concentration at the MPL/CL interface, and $\Delta\phi_p$ is the ionic potential drop across the PEM (and its interfaces). The last two quantities are related with the output current density, I^{avg} , through the following expressions.

$$C_{\text{O}_2, \text{cl}}^{\text{in}} = C_{\text{O}_2, \text{ch}}^{\text{in}} - R_{\text{O}_2}^{\text{chcl}} \frac{I^{\text{avg}}}{4F} \quad (10a)$$

$$\Delta\phi_p = \text{ASR}_{\text{pem}} I^{\text{avg}} \quad (10b)$$

where $R_{\text{O}_2}^{\text{chcl}}$ is the oxygen transport resistance from the channel to the MPL/CL interface, ASR_{pem} is the area-specific ionic resistance of the PEM, and $C_{\text{O}_2, \text{ch}}^{\text{in}}$ is the channel oxygen concentration. The output current density is given by

$$I^{\text{avg}} = \int_0^{\delta_{\text{cl}}} j_c(y) dy \quad (11)$$

According to the ideal gas law, the oxygen concentration in the air feed channel depends on the inlet cathode pressure, $p_{g, \text{c}}^{\text{in}}$, and relative humidity, RH_{c} , as

$$C_{\text{O}_2, \text{ch}}^{\text{in}} = \frac{p_{\text{O}_2}^{\text{in}}}{R^0 T}; \quad p_{\text{O}_2}^{\text{in}} = 0.21 (p_{g, \text{c}}^{\text{in}} - \text{RH}_{\text{c}} p_{\text{H}_2\text{O}}^{\text{sat}}) \quad (12)$$

3.2 Constitutive equations of the porous medium

Considering the representative geometry shown in **Figure 5**, the porosity of the secondary pore space, ε , the ionomer volume fraction, ε_i , the volume fraction of electron-conductive solid and Pt, $\varepsilon_{\text{c+Pt}}$, and the porosity of the primary pore space, $\varepsilon_{\text{prim}}$, are equal to.

$$\varepsilon \left(\tilde{R}_i, \frac{L_p}{L} \right) = 1 - \pi \left(\tilde{R}_i + \frac{L_p}{L} \right)^2 \quad (13a)$$

$$\varepsilon_i(\tilde{R}_i) = \pi \tilde{R}_i^2 \quad (13b)$$

$$\varepsilon_{\text{c+Pt}} \left(\tilde{R}_i, \frac{L_p}{L}, \varepsilon_p \right) = \pi \left[\left(\tilde{R}_i + \frac{L_p}{L} \right)^2 - \tilde{R}_i^2 \right] (1 - \varepsilon_p) \quad (13c)$$

$$\varepsilon_{\text{prim}} \left(\tilde{R}_i, \frac{L_p}{L}, \varepsilon_p \right) = \pi \left[\left(\tilde{R}_i + \frac{L_p}{L} \right)^2 - \tilde{R}_i^2 \right] \varepsilon_p \quad (13d)$$

where the ionomer radius ratio is equal to $\tilde{R}_i = R_i/L$. It can be verified that $\varepsilon + \varepsilon_i + \varepsilon_{\text{c+Pt}} + \varepsilon_{\text{prim}} = 1$.

The characteristic half-size of the secondary pore space, R_v , and the spacing between nanopores in the electron-conductive shell, l_p , are given by.

$$\frac{R_v}{L} \left(\tilde{R}_i, \frac{L_p}{L} \right) = \sqrt{1 - \pi \left(\tilde{R}_i + \frac{L_p}{L} \right)^2} \quad (14a)$$

$$\frac{l_p}{R_p} (\varepsilon_p) = \sqrt{\frac{2\pi}{\varepsilon_p}} \quad (\text{hexagonal packing}) \quad (14b)$$

Ideally, all nanopores are accessible and lined with active Pt. Hence, the roughness factor, r_f , and the catalyst specific surface area, a_{Pt} , are equal to.

$$r_f = \frac{2\pi N_p R_p L_p}{L^2} = \frac{L_{\text{Pt}}}{\delta_{\text{Pt}} \rho_{\text{Pt}}} \quad (15a)$$

$$a_{\text{Pt}} R_p \left(\tilde{R}_i, \frac{L_p}{L}, \varepsilon_p \right) = r_f \frac{R_p}{\delta_{\text{cl}}} = 2\pi \varepsilon_p \left[\left(\tilde{R}_i + \frac{L_p}{L} \right)^2 - \tilde{R}_i^2 \right] \quad (15b)$$

where N_p is the number of pores in a conductive shell. For a prescribed nanoporosity, N_p is given by

$$\varepsilon_p = \frac{N_p \pi R_p^2 L_p}{\pi \left[(R_i + L_p)^2 - R_i^2 \right] \delta_{\text{cl}}} \Rightarrow N_p = \frac{\varepsilon_p \delta_{\text{cl}} \left[(R_i + L_p)^2 - R_i^2 \right]}{R_p^2 L_p} \quad (16)$$

The CL thickness, δ_{cl} , is determined by the Pt loading, L_{Pt} , i.e.,

$$\begin{aligned} L_{\text{Pt}} &= \frac{r_f}{\text{ECSA}} = r_f \delta_{\text{Pt}} \rho_{\text{Pt}} \Rightarrow \frac{\delta_{\text{cl}}}{R_p} \left(\tilde{R}_i, \frac{L_p}{L}, \varepsilon_p \right) \\ &= \frac{L_{\text{Pt}}}{2\pi \varepsilon_p \delta_{\text{Pt}} \rho_{\text{Pt}} \left[\left(\tilde{R}_i + \frac{L_p}{L} \right)^2 - \tilde{R}_i^2 \right]} \end{aligned} \quad (17)$$

Here, $\rho_{\text{Pt}} = 21,450 \text{ kg m}^{-3}$ is the density of Pt. Note that the ECSA = $L_{\text{Pt}}(\delta_{\text{Pt}} \rho_{\text{Pt}})^{-1}$ is directly related to the thinness of the Pt skin. For a Pt atomic layer, $\delta_{\text{Pt}} \approx 0.2 \text{ nm}$, we yield ECSA $\approx 230 \text{ m}^2 \text{ g}_{\text{Pt}}^{-1}$ (Xie et al., 2014). The roughness factor is fixed for a given Pt loading and thickness of Pt skin.

3.3 Effective transport properties

The expressions of the bulk effective transport properties at the layer scale are presented below.

3.3.1 Effective oxygen diffusivity

The effective oxygen diffusivity is decomposed into a dry component due to the obstruction of the dry CL microstructure and the Knudsen effect, $f(\varepsilon, R_v)$, and the relative effective diffusivity due to the relative blockage of water saturation, $g(s^{\text{avg}})$

(Sánchez-Ramos et al., 2021; García-Salaberri et al., 2015b,a; García-Salaberri, 2021)

$$\frac{D_{O_2}^{\text{eff}}}{D_{O_2}^{\text{mol}}} = \frac{D_{O_2}^{\text{eff,dry}}}{D_{O_2}^{\text{mol}}} \frac{D_{O_2}^{\text{eff}}}{D_{O_2}^{\text{eff,dry}}} \quad (18)$$

$$\frac{D_{O_2}^{\text{eff}}}{D_{O_2}^{\text{mol}}} = \frac{D_{O_2}^{\text{eff,dry}}}{f(\epsilon, R_p)} \frac{D_{O_2}^{\text{eff}}}{g(s^{\text{avg}})}$$

where $D_{O_2}^{\text{mol}}(p_{g,c}, T)$ is the molecular diffusivity of oxygen in air (Ye and Van Nguyen, 2007)

$$D_{O_2}^{\text{mol}} = 2.65 \times 10^{-5} \left(\frac{T}{333} \right)^{1.5} \left(\frac{10^5}{p_{g,c}} \right) \quad [\text{m}^2 \text{s}^{-1}] \quad (19)$$

with T expressed in K and $p_{g,c}$ in Pa.

For a tortuosity factor $\tau \approx 1$, the normalized dry effective diffusivity is equal to

$$f(\epsilon, R_p) = \epsilon \left(1 + \frac{D_{O_2}^{\text{mol}}}{D_{O_2}^{\text{knud}}} \right)^{-1} \quad (20)$$

where $D_{O_2}^{\text{knud}}$ is the Knudsen diffusivity given by Eq. 3 with $R = R_p$ and $i = O_2$.

According to the data collected in Sánchez-Ramos et al. (2021), $g(s^{\text{avg}})$ in conventional CLs can be modeled as a power law of the form

$$g(s^{\text{avg}}) = (1 - s^{\text{avg}})^{2.5} \quad (21)$$

This expression was considered a reasonable first approximation to evaluate $g(s^{\text{avg}})$ in this work.

3.3.2 Effective proton conductivity

Proton conduction through hydrated ionomer pillars also features a tortuosity factor $\tau \approx 1$. Hence, we have that

$$\frac{\sigma_p^{\text{eff}}}{\sigma_p} = \epsilon_i \quad (22)$$

where σ_p is the bulk proton conductivity in ionomer. The value of σ_p in finite-sized ionomer domains depends on the size of the conductive medium and the confined morphology of protogenic groups (thin film vs. nanofiber). 2D thin ionomer films in conventional CLs show a lower conductivity than bulk PEMs (2–10 times lower) due to the more difficult percolation of protons through finite thickness domains (Siroma et al., 2009; Paul et al., 2014; Gostick and Weber, 2015; Chen et al., 2019), increasing with the film thickness—the bulk value of PEMs is reached when the film thickness is significantly larger than the size of protogenic nanodomains (around 10 nm) (Gomaa et al., 2022). However, ionomer nanofibers show an opposite behavior, reaching a higher ionic conductivity for small fiber diameters compared with bulk PEMs (up to 10 times higher) and a similar ionic conductivity to that of PEMs for significantly high fiber diameters (Pan et al., 2008; Sun et al., 2019). This opposite behavior can be explained by

the preferential alignment of protogenic nanodomains along nanofibers, which act as highways for proton conduction (Pan et al., 2008). Thin films and nanofibers reach a value comparable to that of bulk PEMs for thicknesses and diameters around 50–100 nm, which is similar to the mean diameter of ionomer pillars considered here. Therefore, the bulk proton conductivity at fully humidified conditions was assumed equal to that of Nafion PEMs as a first approximation (Kusoglu and Weber, 2017)

$$\sigma_p \approx 10 \text{ S m}^{-1} \quad (23)$$

3.3.3 Effective electrical conductivity

The effective electrical conductivity in the electron-conductive shell with a hexagonal packing of nanopores, $\sigma_{e,sh}^{\text{eff}}$, is modeled by the low-order analytical solution of Perrins et al. (Perrins et al., 1979)

$$\frac{\sigma_{e,sh}^{\text{eff}}}{\sigma_e} = 1 - \frac{2\epsilon_p}{1 + \epsilon_p - \frac{0.075422 \epsilon_p^6}{1 - 1.060283 \epsilon_p^{12}} - 0.000076 \epsilon_p^{12}} \quad (24)$$

where σ_e is the bulk electrical conductivity of the electron-conductive material. Here, the electrical conductivity of graphite was taken as a representative value, $\sigma_e \sim 10^6 \text{ S m}^{-1}$. A material with a high stiffness would also be necessary to provide mechanical integrity to the proposed core-shell microstructure for its fabrication.

At the layer scale, $\sigma_{e,sh}^{\text{eff}}$ is corrected by the volume fraction of the conductive shell, ϵ_{sh} , to account for the reduced area available for transport

$$\sigma_e^{\text{eff}} = \epsilon_{sh} \sigma_{e,sh}^{\text{eff}}; \quad \epsilon_{sh} = \frac{\epsilon_{c+Pt}}{1 - \epsilon_p} \quad (25)$$

4 Microscopic model (nanopore scale)

Oxygen and proton transport along a nanopore (local x -coordinate) is governed by a reaction-diffusion equation with a surface reactive term. Mass and charge balances in a pore segment of length dx and radius R_p yield.

$$\pi R_p^2 \frac{d}{dx} \left(-D_{O_2,p}^{\text{eff}} \frac{dC_{O_2,p}}{dx} \right) dx = -2\pi R_p dx \frac{I_p(x)}{4F} \quad (26a)$$

$$\pi R_p^2 \frac{d}{dx} \left(-\sigma_{p,p}^{\text{eff}} \frac{d\phi_{p,p}}{dx} \right) dx = -2\pi R_p dx I_p(x) \quad (26b)$$

The resulting differential conservation equations for the nanoscale oxygen concentration, $C_{O_2,p}$, and the ionic potential, $\phi_{p,p}$, are

$$\frac{d}{dx} \left(-D_{O_2,p}^{\text{eff}} \frac{dC_{O_2,p}}{dx} \right) = -\frac{2}{R_p} \frac{I_p(x)}{4F} \quad (27a)$$

$$\frac{d}{dx} \left(-\sigma_{p,p}^{\text{eff}} \frac{d\phi_{p,p}}{dx} \right) = -\frac{2}{R_p} I_p(x) \quad (27b)$$

where $I_p(x)$ is the current density generated in a single nanopore per unit of active surface area (i.e., internal nanopore surface). $I_p(x)$ is described by Tafel kinetics (Sánchez-Ramos et al., 2021)

$$I_p(x) = i_{o,c} \left(\frac{C_{O_2,p}}{C_{O_2}^{\text{ref}}} \right)^{\gamma} \exp \left[-\frac{\alpha_c F}{R^o T} \eta_c(x) \right] \quad (28)$$

Here, $i_{o,c} \approx 0.5 \text{ A m}_{\text{Pt}}^{-2}$ is the exchange current density, $\gamma = 0.7$ the reaction order, $\alpha_c = 0.5$ the symmetry coefficient, $C_{O_2}^{\text{ref}} \approx 40 \text{ mol m}^{-3}$ the reference oxygen concentration, and η_c the cathode overpotential. $i_{o,c}$ was set somewhat higher than the mean value reported in (Sánchez-Ramos et al., 2021) ($0.5 \text{ A m}_{\text{Pt}}^{-2}$ vs. $0.3 \text{ A m}_{\text{Pt}}^{-2}$ at $T = 80^\circ\text{C}$) due to improved catalyst activity in ultra-thin Pt skins not covered by ionomer ($\delta_{\text{Pt}} \leq 1 \text{ nm}$) (Debe, 2012; Xie et al., 2014; Yarlagadda et al., 2018). The cathode overpotential ($\eta_c \leq 0$) is defined as

$$\eta_c(x, y) = \phi_e(y) - \phi_{p,p}(x) - E_r \quad (29)$$

where $\phi_e(y)$ is the local electronic potential across the thickness (provided by the layer-scale model) and $E_r \approx 1.2 \text{ V}$ is the reversible cell voltage (Sánchez-Ramos et al., 2021).

The effective oxygen diffusivity, $D_{O_2,p}^{\text{eff}}$, and the effective ionic conductivity, $\sigma_{p,p}^{\text{eff}}$, in a water-filled nanopore are equal to

$$D_{O_2,p}^{\text{eff}} = \varepsilon_p D_{O_2,w}; \quad \sigma_{p,p}^{\text{eff}} = \varepsilon_p \sigma_{p,w} \quad (30)$$

where $D_{O_2,w}$ and $\sigma_{p,w}$ are the diffusivity coefficient of oxygen and the proton conductivity in liquid water, respectively. $D_{O_2,w}$ can be extracted from values measured in bulk water (Han and Bartels, 1996; Muzaffar et al., 2018), while $\sigma_{p,w}$ has been determined experimentally and numerically for pH values commonly found in operating PEMFCs (see (Zenyuk and Litster, 2014; Liu and Zenyuk, 2018) and references therein)

$$D_{O_2,w} \approx 5 \times 10^{-9} \text{ m}^2 \text{ s}^{-1}; \quad \sigma_{p,w} \approx 10^{-1} \text{ S m}^{-1} \quad (31)$$

Comparatively, $D_{O_2,w}$ is between one to three orders of magnitude higher than the oxygen diffusivity in ionomer films and PEMs (Kusoglu and Weber, 2017; Sánchez-Ramos et al., 2021), while $\sigma_{p,w}$ is one order of magnitude lower than the proton conductivity through thin films in conventional CLs (Sabarirajan et al., 2020). This favorable situation was

previously exploited in NSTFC electrodes with a relatively good performance (Debe et al., 2011; Debe, 2012).

At each y -coordinate, the surface current density drawn from one nanopore is equal to

$$I_p^{\text{avg}}(y) = \frac{1}{L_p} \int_0^{L_p} I_p(x) dx \quad (32)$$

The relationship between the nanoscale surface current density, I_p^{avg} , and the local volumetric current density at the layer scale, $j_c(y)$, is given by the active specific surface area (see Eq. 15b)

$$j_c(y) = I_p^{\text{avg}}(y) a_{\text{Pt}} \quad (33)$$

4.1 Boundary conditions

The boundary conditions at the nanopore inlet ($x = L_p$) and at the nanopore/ionomer interface ($x = 0$) are rather similar to those used at the layer scale due to the analogy between the arrangement of a nanopore inside the idealized bi-functional CL and a CL in a MEA

$$\begin{aligned} C_{O_2,p} \Rightarrow \text{Inlet: } C_{O_2} &= C_{O_2,p}^{\text{in}}(y) - D_{O_2,p}^{\text{eff}} \frac{dC_{O_2,p}}{dx} R_{O_2,p}^{\text{in}}; \\ \text{Ionomer: } \frac{dC_{O_2,p}}{dy} &= 0 \end{aligned} \quad (34a)$$

$$\phi_{p,p} \Rightarrow \text{Inlet: } \frac{d\phi_{p,p}}{dy} = 0; \quad \text{Ionomer: } \phi_{p,p} = \phi_p(y) + \sigma_{p,p}^{\text{eff}} \frac{d\phi_{p,p}}{dx} R_{p,p}^{\text{in}} \quad (34b)$$

where the dissolved oxygen concentration in liquid water at the nanopore inlet is given by Henry's law (Blunier et al., 2013) (rather than a Langmuir adsorption model as found for ionomers (Shen et al., 2017; Cheng et al., 2022))

$$C_{O_2,p}^{\text{in}}(y) = k_{\text{H},O_2,w} C_{O_2}(y); \quad \frac{R^o T}{k_{\text{H},O_2,w}} = 7.79 \times 10^4 \exp \left(5.7 - \frac{1700}{T} \right) \quad (35)$$

The entry resistances at the nanopore edges, $R_{O_2,p}^{\text{in}}$ and $R_{p,p}^{\text{in}}$, can be expressed as Newman (1966)

$$R_{O_2}^{\text{in}} = \frac{\pi R_p}{4 D_{O_2,w}}; \quad R_p^{\text{in}} = \frac{\pi R_p}{4 \sigma_{p,w}}, \quad (36)$$

leading to robin boundary conditions.

5 Case studies

The three case studies examined are schematized in Figure 6A: 1) baseline case devoted to the geometrical optimization of the CL microstructure (see optimization flow chart in Figure 6B) considering state-of-the-art channel-CL oxygen transport and area-specific ohmic resistances,

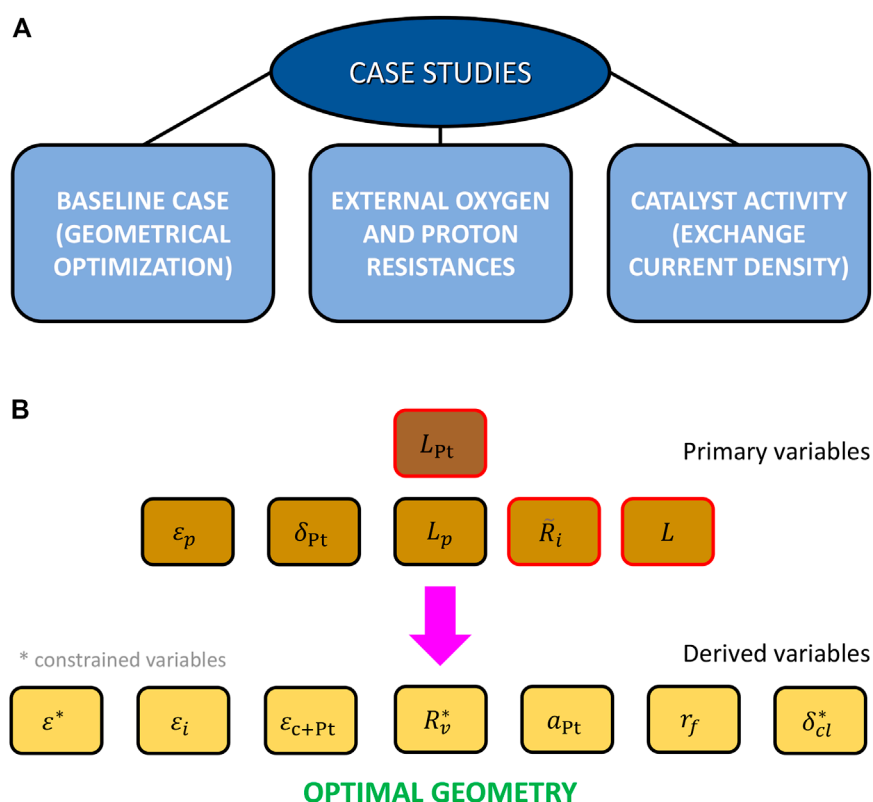


FIGURE 6

(A) Diagram of the case studies examined. The analysis of the baseline case with the geometrical optimization of the bi-functionalized cathode CL microstructure is presented in [Section 6.1](#), the effect of the external oxygen and proton transport resistances, $R_{O_2}^{chl}$ and ASR_{pem} , is presented in [Section 6.2](#), and the effect of the catalyst activity, $i_{o,c}$, is presented in [Section 6.3](#). (B) Flow chart of the optimization process to determine the optimal bi-functionalized cathode CL. Fixed and derived variables are indicated by boxes with black border and variables that were examined parametrically are indicated by boxes with red border. Constrained variables are marked with an asterisk.

$R_{O_2}^{chl} = 1 \text{ s cm}^{-1}$ and $ASR_{pem} = 0.02 \text{ cm}^2 \text{ S}^{-1}$, respectively (see, e.g. ([Owejan et al., 2013, 2014](#); [Ureña et al., 2021](#); [Gomaa et al., 2022](#))); 2) an analysis of the exterior mass and proton transport resistances, $R_{O_2}^{chl}$ and ASR_{pem} , where the baseline values are reduced to $R_{O_2}^{chl} = 0.5 - 0.1 \text{ s cm}^{-1}$ and $ASR_{pem} = 0.01 - 0.002 \text{ cm}^2 \text{ S}^{-1}$ (x0.5 and x0.1); 3) an analysis of the catalyst activity, i.e., the exchange current density, $i_{o,c}$, where the baseline value $i_{o,c} = 0.5 \text{ A m}_{Pt}^{-2}$ is increased up to $i_{o,c} = 1 - 5 \text{ A m}_{Pt}^{-2}$ (x2 and x10).

The parameters that were kept constant and examined parametrically for the geometrical optimization (presented in [Section 6.1](#)) are listed in [Table 1](#). The nanopore radius was fixed to $R_p = 2.5 \text{ nm}$ to ensure the presence of water in tiny nanopores and the average saturation in the secondary pore space was fixed to $s^{avg} = 0.4$, as previously discussed in [Section 2.1](#). The cell voltage was set to $V_{cell} = 0.5 \text{ V}$, close to maximum power density (see footnote in [Table 1](#) for other operating conditions). The Pt loading was varied in the range $L_{Pt} = 0.001 - 0.4 \text{ mg}_{Pt} \text{ cm}^{-2}$, which includes the loading needed to meet the ultimate target of a total PGM content below

$0.1 \text{ mg}_{Pt} \text{ cm}^{-2}$ ($L_{Pt} \sim 10^{-2} \text{ mg}_{Pt} \text{ cm}^{-2}$). For a given Pt loading, the CL microstructure is defined by five primary variables: ϵ_p , δ_{Pt} , L_p , L and \bar{R}_i . The nanoporosity of the shell was kept as high as possible, $\epsilon_p = 0.9$, below the percolation threshold given by $\epsilon_p^{max} = 1 - \pi/(2\sqrt{3}) \approx 0.906$, the thickness of the Pt skin was set to $\delta_{Pt} = 0.2 \text{ nm}$ to maximize the ECSA and the nanopore length was fixed to $L_p = 10 \text{ nm}$ to minimize the transport length in nanopores, while providing certain mechanical integrity. The ionomer radius ratio was varied between $\bar{R}_i = 0.1 - 0.4$ and the spacing between pillars between $L = L^{min} - 5000 \text{ nm}$, where L^{min} is the minimum spacing allowed to ensure a minimum half-size and porosity of the secondary pore space (see below). The remaining variables (ϵ , ϵ_i , ϵ_{c+Pt} , R_v , r_f , a_{Pt} and δ_{cl}) can be derived from the constitutive equations of the porous medium presented in [Section 3.2](#). The volume fractions (ϵ , ϵ_i , ϵ_{c+Pt}) can be determined from [Eqs. \(13a\)–\(13c\)](#), the half-size of the secondary pore space (R_v) from [Eq. 14a](#), the roughness factor and the specific surface area (r_f , a_{Pt}) from [Eqs. \(15a\)–\(15b\)](#), and the CL thickness from [Eq. 17](#). In addition, three geometrical constraints were imposed on the above variables: (1-2) $\epsilon \geq 0.15$ and $R_v \geq 0$

TABLE 1 Model parameters. The baseline case corresponds to $R_{O_2}^{chl} = 1 \text{ s cm}^{-1}$, $ASR_{pem} = 0.02 \text{ cm}^2 \text{ S}^{-1}$ and $i_{o,c} = 0.5 \text{ A mPt}^{-2}$. The constrained variables are indicated with an asterisk and the operating conditions are included in the footnote.

Parameter	Symbol	Value
Channel-CL O_2 transport resistance	$R_{O_2}^{chl}$	0.1, 0.5, 1 (baseline) s cm^{-1}
Area-specific ohmic resistance (\sim PEM)	ASR_{pem}	0.002, 0.01, 0.02 (baseline) $\text{cm}^2 \text{ S}^{-1}$
Exchange current density	$i_{o,c}$	0.5 (baseline), 1, 5 A mPt^{-2}
Pt skin thickness (\sim atomic layer)	δ_{Pt}	0.2 nm
Nanopore radius	R_p	2.5 nm
Nanopore length	L_p	10 nm
Shell nanoporosity	ϵ_p	0.9
Average water saturation	s^{avg}	0.4
Pt loading	L_{Pt}	0.001–0.3 $\text{mg}_{Pt} \text{ cm}^{-2}$
Pillar spacing	L	$L^{\min} - 5000 \text{ nm}$
Ionomer radius ratio	\tilde{R}_i	0.1–0.4
Porosity of secondary pore space*	ϵ	≥ 0.15
Half-size of secondary pore space*	R_v	≥ 0
CL thickness*	δ_{cl}	$\geq 1.5 \text{ }\mu\text{m}$

$P_{g,e} = 1.5 \text{ bar}$; $P_{g,a} = 1 \text{ bar}$; $T = 80^\circ\text{C}$; $RH_a = RH_c = 1$; $C_{O_2,chl}^{in} \approx 7.4 \text{ mol m}^{-3}$; $V_{cell} = 0.5 \text{ V}$.

to avoid an exceedingly low bulk oxygen effective diffusivity, and 3) $\delta_{cl} \geq 1.5 \text{ }\mu\text{m}$ to ensure a minimum mechanical integrity of the porous layer and avoid edge effects, such as capillary condensation at sharp angles (Mashio et al., 2014). The lower threshold used here for the thickness is similar to that considered in previous works with conventional CLs (Sun et al., 2020). The lowest pillar spacing imposed by constraints 1–2, L_ϵ^{\min} and $L_{R_v}^{\min}$, can be determined from Eq. 13a, Eq. 14a, leading to

$$L_\epsilon^{\min} = \frac{L_p}{\sqrt{\frac{1 - \epsilon^{\min}}{\pi}} - \tilde{R}_i} \quad (37a)$$

$$L_{R_v}^{\min} = \frac{L_p}{1 - \tilde{R}_i} \quad (37b)$$

Therefore, the smallest pillar spacing allowed is equal to $L^{\min} = \max\{L_\epsilon^{\min}, L_{R_v}^{\min}\}$.

6 Discussion of results

6.1 Baseline case (geometrical optimization)

The calculation of the optimal pillar spacing and ionomer radius ratio, L and \tilde{R} , was accomplished using physical considerations rather than a purely mathematical approach. Eqs. (27a)–(27b) are governed by two dimensionless parameters, which arise from the ratios of the characteristic times of oxygen and proton transport and the characteristic reaction time at both the nanoscale ($\Omega_{O_2}^p$, Ω_p^p) and the layer scale ($\Omega_{O_2}^{cl}$, Ω_p^{cl}) (Sánchez-Ramos et al., 2022). An alternative interpretation can be considered as the ratios of the diffusion/conduction

penetration depths and the characteristic length at a certain scale (Perry et al., 1998; Kulikovskiy, 2010). For a roughness factor in the range $r_f \sim 1$ –100 and a representative average current density needed for high performance, $I^{avg} \sim 2 \text{ A cm}^{-2}$, we yield the following estimations.

$$\Omega_{O_2}^p = \frac{t_{d,p}}{t_{r,p}} = \frac{L_p}{l_{O_2,p}} \sim \frac{L_p R_{O_2}^p I^{avg}}{C_{O_2,p}^{in} R_p F r_f} \sim 10^{-1} (r_f \sim 10^2) - 1 (r_f \sim 1) \propto r_f^{-1} \text{ (limiting at low } L_{Pt}) \quad (38a)$$

$$\Omega_{O_2}^{cl} = \frac{t_{d,cl}}{t_r} = \frac{\delta_{cl}}{l_{O_2,cl}} \sim \frac{R_{O_2}^{cl} I^{avg}}{C_{O_2,cl}^{in} F} \sim 10^{-2} - 10^{-1} \quad r_f - \text{independent} \quad (38b)$$

$$\Omega_p^p = \frac{t_{d,p}}{t_{r,p}} \frac{t_{p,p}}{t_{d,p}} = \frac{L_p}{l_{p,p}} \sim \frac{ASR_p^p L_p I^{avg}}{E_r R_p r_f} \sim 10^{-4} (r_f \sim 10^2) - 10^{-2} (r_f \sim 1) \propto r_f^{-1} \quad (38c)$$

$$\Omega_p^{cl} = \frac{t_{d,cl}}{t_r} \frac{t_{p,cl}}{t_{d,cl}} = \frac{\delta_{cl}}{l_{p,cl}} \sim \frac{ASR_p^{cl} I^{avg}}{E_r} \sim 10^{-3} - 10^{-2} \quad r_f - \text{independent} \quad (38d)$$

where the oxygen transport resistances at the layer scale and the nanoscale (under passive non-reactive conditions) are equal to $R_{O_2}^{cl} = \delta_{cl}/D_{O_2}^{eff}$ and $R_{O_2}^p = L_p/D_{O_2,p}^{eff}$, respectively, and the proton transport resistances at the layer scale and the nanoscale are equal to $ASR_p^{cl} = \delta_{cl}/\sigma_p^{eff}$ and $ASR_p^p = L_p/\sigma_{p,p}^{eff}$, respectively. (Note that the apparent bulk diffusive resistance under reactive conditions is proportional to that under passive conditions (see, e.g. (Schuler et al., 2019)), so the optimization problem at the layer scale can be reduced to minimizing $R_{O_2}^{cl}$ if other losses are not significant). The characteristic oxygen

concentration drops were estimated as $C_{O_2,p}^{in} \sim k_{H,O_2,w} C_{O_2,cl}^{in}$ and $C_{O_2,cl}^{in} \sim C_{O_2,cl}^{in}$, and the characteristic ionic potential drop as E_r . The dimensionless transport coefficients at the nanoscale depend on r_f because of the re-normalization between the cell current density and the current density per unit of active area, i.e., $I^{avg} = r_f I_p^{avg}$.

The most limiting transport process is oxygen transport at the nanoscale mainly due to the larger oxygen resistance at the nanoscale (compared with that of the bulk CL) and the dissolution of oxygen in liquid water to reach triple phase points unlike proton conduction. Ohmic losses at the layer scale can be lower or comparable to those found in water-filled nanopores depending on the value of the normalized ionic conductivity across the CL ($\sigma_p^{eff} \sigma_p^{-1} = \varepsilon_i$ in our case and dependent on bottlenecks created by thin films in conventional CLs (Sabarirajan et al., 2020)). For $r_f \approx 1$, regardless of I^{avg} , we yield

$$\frac{\Omega_{O_2}^p}{\Omega_{O_2}^{cl}} \sim \frac{L_p}{R_p} \times \frac{1}{k_{H,O_2,w}} \times \frac{R_{O_2}^p}{R_{O_2}^{cl}} \sim (1-10) \times 10 \times (1-10) \sim 10-10^3 \quad (39a)$$

$$\frac{\Omega_p^p}{\Omega_p^{cl}} \sim \frac{L_p}{R_p} \times \frac{ASR_p^p}{ASR_p^{cl}} \sim (1-10) \times (10^{-1}-1) \sim 10^{-1}-10 \quad (39b)$$

The maximum power density is achieved when all the dimensionless times (or penetration depths), Ω_i , are minimized (maximized), so that oxygen and proton transport are fast enough to maintain the reaction rate at the targeted current density, I^{avg} , with a low cathode overpotential. According to Eqs. (38a)–(38d), this condition is achieved when transport resistances, R_i , are minimized at all scales. The other option is to increase the oxygen concentration at the CL/MPL interface, something that can be done through a reduction of the exterior mass transport resistance to the cathode CL, $R_{O_2}^{ch,cl}$. Increasing Henry's constant of oxygen in liquid water is difficult, even though it is worth noting that the oxygen diffusivity in liquid water can be slightly increased using oxygen diffusion-enhancing compounds (usually used in medicine for the treatment of diseases, such as hypoxia and ischemia) (Stennett et al., 2006).

Figure 7A shows the variation of the bulk oxygen transport resistance, $R_{O_2}^{cl}$, as a function of L for various Pt loadings ($\tilde{R}_i = 0.3$). For a given Pt loading, there is a critical L for which $R_{O_2}^{cl}$ is minimized due to a trade-off between the increasing secondary pore size (lower $R_{O_2}^{cl}$) and the increasing thickness (higher $R_{O_2}^{cl}$) with L (see Eq. 14a and (17)). The optimal spacing is approximately reached when δ_{cl} is minimum, $\delta_{cl} = \Pi \delta_{cl}^{min}$; $\Pi = 1.2$ was taken here. The nearly minimum thickness also minimizes the bulk proton transport resistance, R_p^{cl} . Hence, the optimal design spacing, $L^{des}(\tilde{R}_i)$, can be determined from the

condition

$$\Pi \delta_{cl}^{min} = \frac{L_{Pt} R_p}{2\pi \varepsilon_p \delta_{Pt} \rho_{Pt} \left[\left(\tilde{R}_i^{des} + \frac{L_p}{L^{des}} \right)^2 - \left(\tilde{R}_i^{des} \right)^2 \right]}; \quad \Pi = 1.2 \quad (40a)$$

And the solid volume fraction, ε_{c+Pt} , can then be calculated from

$$\varepsilon_{c+Pt}^{des} = \pi \left[\left(\tilde{R}_i^{des} + \frac{L_p}{L^{des}} \right)^2 - \left(\tilde{R}_i^{des} \right)^2 \right] (1 - \varepsilon_p) \quad (40b)$$

As shown in Figure 7B, L^{des} increases with decreasing Pt loading, given that a smaller amount of Pt can be allocated in the same thickness but with larger secondary pores (where most of the pore space is present). This method of reducing L_{Pt} is theoretically optimal (compared with the addition of bare carbon to maintain a constant thickness), since it decreases $R_{O_2}^{cl}$ (lower Knudsen effect). The design spacing increases from around $R_v \approx 40$ nm at $L_{Pt} = 0.3$ mg_{Pt} cm⁻² (typical value found in CLs with the same loading (Wilson and Gottesfeld, 1992)) to $R_v \sim 1000$ nm for exceedingly small Pt loadings, $L_{Pt} \rightarrow 10^{-3}$ mg_{Pt} cm⁻². As a result, $R_{O_2}^{cl}$ is reduced by an order of magnitude from $\sim 10^{-2}$ s cm⁻¹ (similar to the resistance in water-filled nanopores, $R_{O_2}^p$) down to $\sim 10^{-3}$ s cm⁻¹ when the Pt loading is varied in the range $L_{Pt} = 0.3-10^{-3}$ mg_{Pt} cm⁻². $R_{O_2}^p$ and $R_{O_2}^{cl}$ are around 2-3 orders of magnitude lower than the channel-CL and local oxygen resistances, $R_{O_2}^{ch,cl}$ and $R_{O_2,p}^{ion}$, in conventional PEFCs with non-optimized CLs (Sánchez-Ramos et al., 2021). The volume fraction of electron-conductive material + Pt of the shell is small, growing from $\varepsilon_{c+Pt}^{des} \sim 10^{-3}$ at $L_{Pt} = 0.005$ mg_{Pt} cm⁻² up to $\varepsilon_{c+Pt}^{des} \approx 0.06$ at $L_{Pt} \approx 0.3$ mg_{Pt} cm⁻². The increase of ε_{c+Pt}^{des} with L_{Pt} goes hand in hand with the increase of L^{des} since the thickness of the shell is fixed to $L_p \ll L^{des}$. The above results suggest that there is room to improve performance by optimizing CLs together with a reduction of oxygen transport resistance in passive porous layers of the MEA, flow field and stack flow distributor.

The optimal \tilde{R}_i , which arises from a trade-off between ionomer and void volume fractions (ε_i vs. ε), is to be determined from numerical simulations. Figure 8A shows the power density, P , computed for the baseline case as a function of the ionomer volume fraction, $\varepsilon_i = 0.05-0.8$, and various Pt loadings, $L_{Pt} = 0.005-0.3$ mg_{Pt} cm⁻². P slightly varies with ε_i except for exceedingly small ionomer volume fractions when the area available for proton transport is strongly reduced, i.e., σ_p^{eff} is significantly decreased. A similar effect to that found in thin ionomer films. In a little more detail, it can be seen that the optimal ionomer volume fraction shifts to higher values as L_{Pt} is increased. This is explained by the larger secondary pore sizes reached with decreasing L_{Pt} , so the optimal design point is reached at a lower secondary porosity, ε . Nevertheless, the variations above $\varepsilon_i \geq 0.2$ are almost negligible, so the design point was fixed to $\tilde{R}_i = 0.3$ ($\varepsilon_i \approx 0.3$) for subsequent analyses.

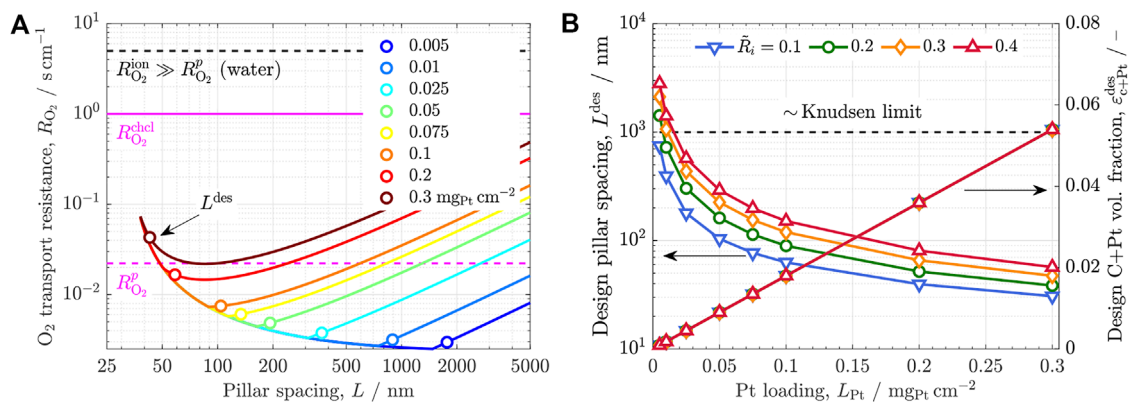


FIGURE 7

(A) Variation of the bulk O₂ transport resistance of the bi-functionalized bimodal cathode CL, $R_{O_2}^{cl}$, with the pillar spacing, L , corresponding to various Pt loadings, $L_{Pt} = 0.005, 0.01, 0.025, 0.05, 0.075, 0.1, 0.2, 0.3$ mgPt cm⁻², and $\bar{R}_i = 0.25$. The figure also includes the O₂ transport resistance in optimized water-filled nanopores, $R_{O_2}^p = L_p/D_{O_2,p}^{eff} \approx 0.02$ s cm⁻¹, the channel-CL O₂ transport resistance of state-of-the-art PEMFCs (Owejan et al., 2013, 2014; Sun et al., 2020), $R_{O_2}^{chcl} \sim 1$ s cm⁻¹, and the local O₂ transport resistance reported for non-optimized conventional CLs with ionomer thin films covering Pt nanoparticles at $r_f \approx 1$ (Sánchez-Ramos et al., 2021), $R_{O_2,p}^{ion} \sim 4.7$ s cm⁻¹ $\gg R_{O_2}^p$ (water). The design spacing is selected for $\delta_{cl} = \Pi \delta_{cl}^{min}$ ($\Pi = 1.2$), close to the optimal point of minimum bulk and local transport resistances. (B) Variation of the design spacing, L^{des} , and the design volume fraction of electron-conductive material + Pt, ε_{C+Pt} , Pt loading, L_{Pt} , corresponding to $\bar{R}_i = 0.1, 0.2, 0.3, 0.4$. The Knudsen limit for which species diffusion is not significantly reduced is around 1000 nm.

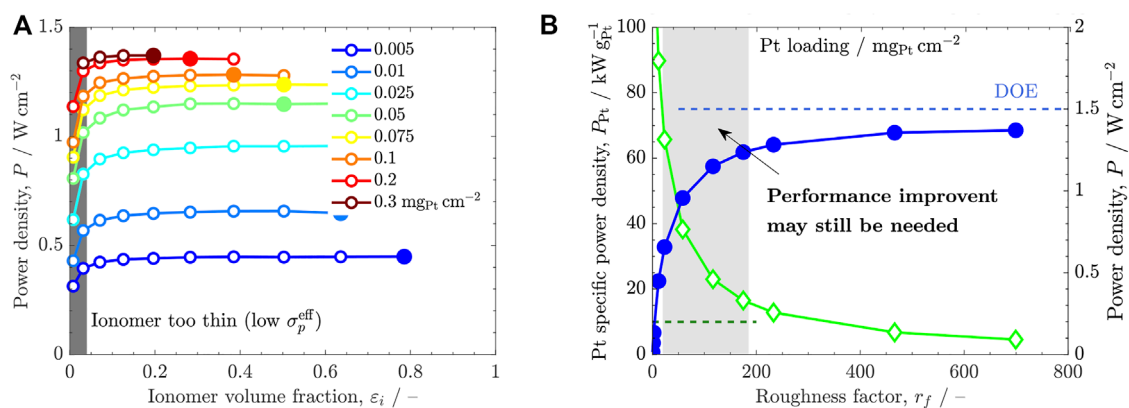


FIGURE 8

(A) Variation of the geometric power density, P , with the ionomer volume fraction, ε_i , at the design point of minimum transport resistance corresponding to several Pt loadings, $L_{Pt} = 0.005 - 0.3$ mgPt cm⁻². The power density is reduced when ε_i is small because of the drop of σ_p^{eff} (bottleneck effect caused by too thin ionomer pillars). The computed optimal ionomer volume fractions are highlighted by big solid dots. (B) Variation of the Pt mass-specific power density and geometric power density ($V_{cell} = 0.5$ V), P_{Pt} and P , respectively, with the roughness factor, r_f , at the optimal CL design point. The corresponding Pt loading is shown on the top axis, $L_{Pt} = r_f \delta_{Pt} \rho_{Pt}$; $\delta_{Pt} = 0.2$ nm. The DOE power density target at rated power (1 W cm⁻² @ 0.76 V, $T = 80^\circ$ C) has been extrapolated to the examined voltage (1.5 W cm⁻² @ 0.5 V) (DOE, 2015).

Figure 8B shows the variation of the Pt-specific and geometric power densities, P_{Pt} and P , with the roughness factor, r_f , at the optimal design point ($\bar{R}_i = 0.3$). The Pt loading corresponding to r_f in the optimized CL is indicated on the top axis (ECSA ≈ 200 m² gPt⁻¹). The Pt-specific power density increases abruptly with decreasing L_{Pt} because of the steep P - r_f relationship prevailing at low Pt loading. Although the limit $p = 0$ at $L_{Pt} = 0$ is inevitable (no reaction, no operation), the current density sharply increases when $r_f > 0$ if there are no huge

transport resistances and/or the ECSA is too small. The increase of P with r_f flattens for high roughness factors ($r_f \geq 100$) due to the effect of mass and ohmic resistances of the cathode CL and exterior components. Note that the limiting current density would be mainly controlled by $R_{O_2}^{chcl}$ if interior mass transport resistances in the CL are negligible and the roughness factor is extremely high ($r_f \rightarrow \infty$). Maximizing the performance in the range $L_{Pt} \approx 0.01-0.1$ mgPt cm⁻² to meet the ultimate DOE targets may require an integral optimization of oxygen transport

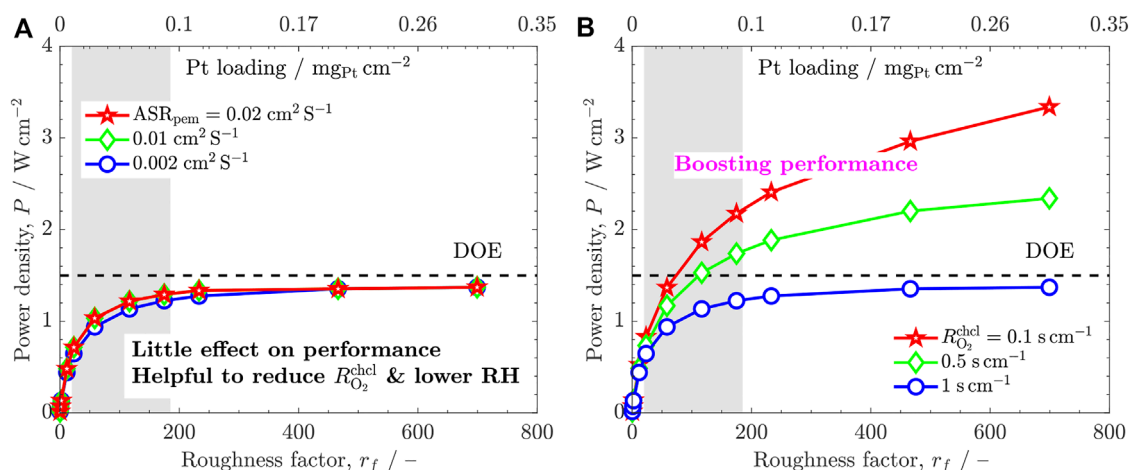


FIGURE 9

Variation of the geometric power density ($V_{\text{cell}} = 0.5 \text{ V}$), P , with the roughness factor, r_f , at the optimal design point, corresponding to: (A) three area-specific ohmic resistances, $\text{ASR}_{\text{pem}} = 0.02$ (baseline case), 0.01 , $0.002 \text{ cm}^2 \text{ S}^{-1}$, and (B) three channel-CL oxygen transport resistances, $R_{\text{O}_2}^{\text{chl}} = 1$ (baseline case), 0.5 , 0.1 s cm^{-1} . See caption to Figure 8 for further details.

resistances (see Section 6.2 below). In terms of the cathode CL, increasing the fraction of water-based triple phase points provides a viable route to reach Pt-specific power densities between $P_{\text{Pt}} \approx 10 - 40 \text{ kW g}_{\text{Pt}}^{-1}$ and surpass the DOE target of $10 \text{ kW g}_{\text{Pt}}^{-1}$, as recently demonstrated by The General Motors Company (Yarlagadda et al., 2018).

6.2 Effect of external transport resistances

The effect of the exterior ohmic and mass transport resistances, ASR_{pem} and $R_{\text{O}_2}^{\text{chl}}$, on the geometrical power density at the optimal design point is examined in Figures 9A,B, respectively. Improvement of P at low L_{Pt} by a direct reduction of ohmic losses is not feasible, since thin PEMs currently used in PEMFCs (e.g., reinforced Nafion) with small thickness ($\delta_{\text{pem}} \sim 10 - 30 \text{ }\mu\text{m}$) and high ionic conductivity ($\sigma_{\text{pem}} \approx 10 - 20 \text{ S m}^{-1}$ at $\text{RH} = 1$) have already been highly optimized and represent a rather small fraction of voltage losses, $\Delta V_{\text{ohm}} \approx 0.02 \text{ V}$ ($I^{\text{avg}} \approx 2 \text{ A cm}^{-2}$) $\ll E_r \approx 1.2 \text{ V}$. Moreover, thin PEMs can suffer from insufficient durability (e.g., ultra-thin GORE-SELECT PEMs (Kienitz et al., 2011)). As shown in Figure 9B, the power density is not significantly increased even when ASR_{pem} is decreased by an order of magnitude down to $0.002 \text{ cm}^2 \text{ S}^{-1}$, which is comparable to the resistance of an ultra-thin PEM $1 \text{ }\mu\text{m}$ thick without significant interfacial resistances. Nevertheless, a reduction of the PEM thickness can be useful to enhance water back diffusion to the anode and improve performance at low RH (Zhu et al., 2006; Steinbach et al., 2010). For instance, a thin reinforced PEM ($\delta_{\text{pem}} \approx 10 \text{ }\mu\text{m}$) was

incorporated in the Toyota Mirai in 2015, presumably to help alleviating cathode flooding at middle-to-high current density and making operation possible without external humidification (Yoshida and Kojima, 2015; Borup et al., 2018). By way of contrast, the impact of the channel-CL oxygen transport resistance is significantly larger, being crucial to reduce it to enhance performance at low L_{Pt} . A comparison of the external transport resistances against the layer-scale and nanoscale transport resistances in the CL leads to

$$\Gamma_{\text{O}_2, p}^{\text{chl}} = \frac{R_{\text{O}_2}^{\text{chl}}}{R_{\text{O}_2}^p} \sim \frac{10 - 10^2 \text{ s m}^{-1}}{1 - 10^2 \text{ s m}^{-1}} \sim 10^{-2} (r_f \sim 1) - 10^2 (r_f \sim 10^2) \quad (41a)$$

$$\Gamma_{\text{O}_2, cl}^{\text{chl}} = \frac{R_{\text{O}_2}^{\text{chl}}}{R_{\text{O}_2}^{\text{cl}}} \sim \frac{10 - 10^2 \text{ s m}^{-1}}{10^{-1} - 1 \text{ s m}^{-1}} \sim 10^2 - 10^3 \quad (41b)$$

$$\Gamma_{p, p}^{\text{pem}} = \frac{\text{ASR}_{\text{pem}}}{\text{ASR}_p^p} \sim \frac{10^{-7} - 10^{-6} \text{ m}^2 \text{ S}^{-1}}{10^{-7} - 10^{-5} \text{ m}^2 \text{ S}^{-1}} \sim 10^{-1} - 1 \quad (41c)$$

$$\Gamma_{p, cl}^{\text{pem}} = \frac{\text{ASR}_{\text{pem}}}{\text{ASR}_p^{\text{cl}}} \sim \frac{10^{-7} - 10^{-6} \text{ m}^2 \text{ S}^{-1}}{10^{-7} - 10^{-6} \text{ m}^2 \text{ S}^{-1}} \sim 1 \quad (41d)$$

From the above calculations, it turns out that the exterior and nanoscale oxygen transport resistances, $R_{\text{O}_2}^{\text{chl}}$ and $R_{\text{O}_2}^p$, are the most important ones. The bulk oxygen transport resistance of the CL, $R_{\text{O}_2}^{\text{cl}}$, can be more easily optimized to make its contribution negligible provided that there are no flooding-related issues (see Figure 7) (Conde et al., 2019; Talukdar et al., 2019). The contribution of $R_{\text{O}_2}^{\text{chl}}$ dominates the performance of the optimized CL when $r_f \geq 10$ ($R_{\text{O}_2}^p$ cannot be neglected at

$r_f \sim 1$ –10). The effect of ohmic losses in the CL is comparable to that of ASR_{pem} and can be neglected to optimize the performance at low L_{Pt} under normal conditions, as commented before.

Power densities above 1.5 W cm^{-2} are predicted with air feed at low Pt loading with a ten-fold reduction of the external oxygen resistance from $R_{O_2}^{chl} \approx 1 \text{ s cm}^{-1}$ to $R_{O_2}^{chl} \approx 0.1 \text{ s cm}^{-1}$. Decreasing $R_{O_2}^{chl}$ by one order of magnitude may require a highly optimized design of the cathode MEA/flow field/stack architecture. An example is the highly engineered 3D porous cathode flow field and thin GDLs ($\delta_{gdl} \approx 150 \text{ }\mu\text{m}$) incorporated in the Toyota Mirai to boost the performance of previously developed designs up to $3\text{--}4 \text{ A cm}^{-2}$ ($L_{Pt} \approx 0.3 \text{ mg}_{Pt} \text{ cm}^{-2}$) (Yoshida and Kojima, 2015). Water management at the cathode was also probably helped by the thin PEM and reduced humidification. The optimized component-architecture-operation design of the Toyota Mirai provides a good basis for subsequent reductions of the Pt loading via CL optimization. However, the fabrication of flow fields and stacks with complex 3D geometries using conventional methods is not desirable for large production. Work is still needed to develop alternative strategies for decreasing $R_{O_2}^{chl}$ at high current density using standard procedures, e.g., porous flow fields, flow fields with narrower channels and/or GDL-MPLs with tailored thickness and wettability (Jiao et al., 2021), or advanced manufacturing techniques, such as multiscale 3D printing of metal powders (e.g., Ti, stainless steel and Ni (Yi et al., 2012; Choi et al., 2014; Ercelik et al., 2022)) and alternative raw material powders (3D printing can also help in reducing electrical contact resistances and inhomogeneous assembly compression (García-Salaberri et al., 2011, 2018, 2019; García-Salaberri P. A. et al., 2017; Hack et al., 2020)). In particular, decreasing the thickness of GDLs and flow fields by integrating them into a single component can enable the production of more compact stacks, reducing weight and increasing volumetric current density, as recently demonstrated by Korean researchers (Park et al., 2019). Another option to improve cathode performance would be to use a more efficient compressor to increase the cathode pressure, while avoiding a reduction of the system efficiency (Sery and Leduc, 2022).

6.3 Effect of catalyst activity (exchange current density)

The last option to improve performance within DOE targets is catalyst modification by: 1) increasing the mass activity with the same amount of precious metals, and 2) maintaining the mass activity with a reduced amount of precious metals (or a combination of both). According to Tafel equation, for a given roughness factor and overpotential, a catalyst with a higher exchange current density can potentially increase the current

density in the same proportion (if transport losses are small)

$$I^{avg} = r_f I_p^{avg}, \quad \frac{I_{p,2}^{avg}}{I_{p,1}^{avg}} = \frac{i_{o,c,2}}{i_{o,c,1}} \quad C_{O_2}, \eta_c \approx \text{cte.} \quad (42)$$

Figure 10 shows the variation of P with r_f for three different exchange current densities, $i_{o,c} = 0.5, 1, 5 \text{ A m}_{Pt}^{-2}$, corresponding to high and low external oxygen transport resistances, 1) $R_{O_2}^{chl} = 1 \text{ s cm}^{-1}$ and 2) $R_{O_2}^{chl} = 0.01 \text{ s cm}^{-1}$. According to Eq. 42, increasing $i_{o,c}$ is useful to boost performance at middle-to-high current density when oxygen transport to the cathode CL is facilitated. In this case, the combination of a high average oxygen concentration and a high exchange current density can significantly raise the power density to around 2 W cm^{-2} at low L_{Pt} . The performance improvement in practice will largely depend on the increase of $i_{o,c}$ that can be achieved and the ability to keep $R_{O_2}^{chl}$ small at high water production rates (special attention is to be devoted to efficient water removal in vapor form with increasing heat generation). In contrast, when oxygen transport to the CL is hindered, the beneficial effect of increasing $i_{o,c}$ is strongly reduced since operation at high performance is no longer possible due to oxygen starvation. As shown in Figure 11A, the limiting current density remains the same regardless of the exchange current density for $R_{O_2}^{chl} = 1 \text{ s cm}^{-1}$, while no limiting current density is present in the voltage range examined for $R_{O_2}^{chl} = 0.01 \text{ s cm}^{-1}$. The average oxygen concentration in the cathode CL, $C_{O_2,cl}^{avg}$, closely follows the linear relationship given by $R_{O_2}^{chl}$ due to the reduced effect of other transport resistances in the optimized CL design (see Figure 11B).

As a final remark, it is relevant to examine the limit to which L_{Pt} might be reduced to ensure a certain minimum performance. The frontier is largely controlled by r_f . As shown in Figure 10B, the power density with a highly optimized PEMFC (i.e., CL based on water-filled triple phase points, $\times 0.1 R_{O_2}^{chl}$, $\times 10 i_{o,c}$ with respect to the state of the art and negligible losses at the anode) dramatically drops when $r_f \lesssim 10$, being impossible to meet DOE targets when $r_f \lesssim 1$ (similar electrochemical and geometrical areas). The positive effect of increasing $i_{o,c}$ and $C_{O_2,cl}^{avg}$ is dramatically reduced when $r_f \lesssim 1$ because I_p^{avg} becomes too small even if all transport resistances are minimized. Considering the Tafel equation again, the maximum possible current density at a given overpotential is equal to

$$I^{avg} \sim I_p^{avg} \sim i_{o,c} \left(\frac{C_{O_2,p}^{in}}{C_{O_2}^{ref}} \right)^{\gamma} \exp \left[-\frac{\alpha_c F}{R^0 T} \eta_c \right] \quad (43)$$

where $C_{O_2,p}^{in} \sim k_{H_2O_2,w} C_{O_2,chl}^{in}$ is the oxygen concentration at the entrance of nanopores. For $\eta_c \approx -(0.5\text{--}0.4) \text{ V}$ ($V_{cell} \approx 0.5 \text{ V}$), we yield $I^{avg} \sim I_p^{avg} \sim 10^{-2} \text{ A cm}^{-2}$ at $r_f \sim 1$. Interestingly, the region where operation at high performance is hardly complicated is adjacent to the ultimate DOE target corresponding to

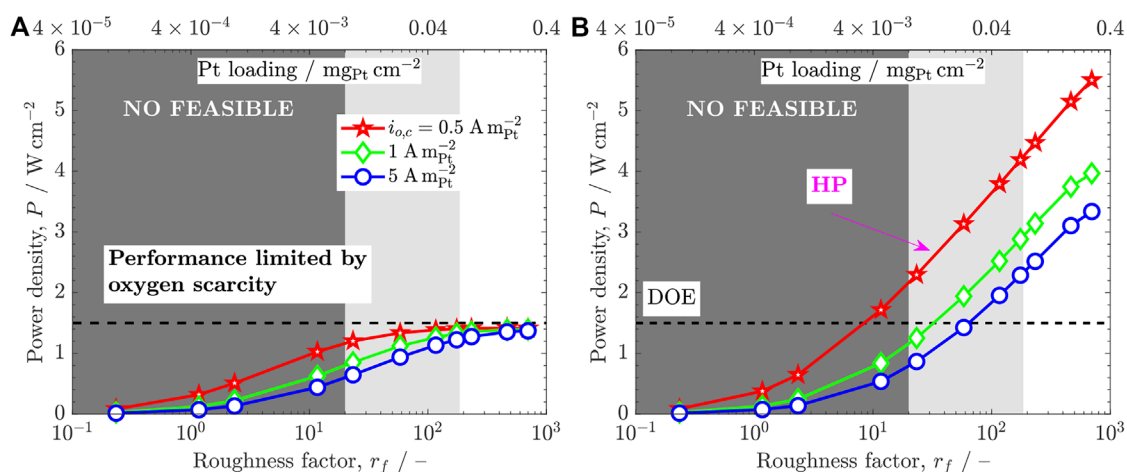


FIGURE 10

Variation of the geometric power density ($V_{\text{cell}} = 0.5 \text{ V}$), P , with the roughness factor, r_f , at the optimized design point for three exchange current densities, $i_{o,c} = 0.5, 1, 5 \text{ A mPt}^{-2}$, corresponding to: (A) state-of-the-art channel-CL oxygen transport resistance, $R_{\text{O}_2}^{\text{chl}} = 1 \text{ s cm}^{-1}$, and (B) optimized channel-CL oxygen transport resistance, $R_{\text{O}_2}^{\text{chl}} = 0.1 \text{ s cm}^{-1}$. See caption to Figure 8 for further details.

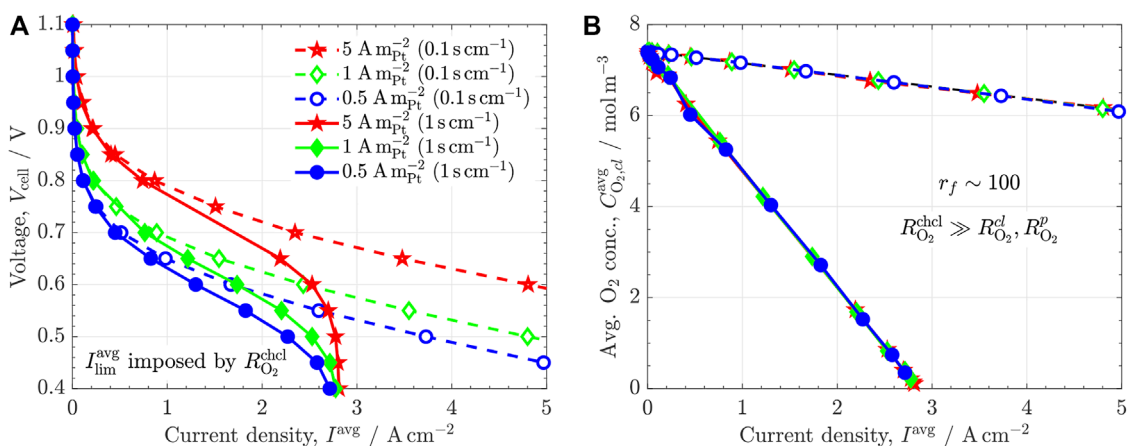


FIGURE 11

(A) Polarization curve, $V_{\text{cell}} - I^{\text{avg}}$, and (B) variation of the average oxygen concentration in the CL, $C_{\text{O}_2,\text{cl}}^{\text{avg}}$, with the average current density, I^{avg} , at $r_f \sim 100$ ($L_{\text{Pt}} = 0.05 \text{ mgPt cm}^{-2}$). The results for three exchange current densities, $i_{o,c} = 0.5, 1, 5 \text{ A mPt}^{-2}$, corresponding to both high and low channel-CL oxygen resistances, $R_{\text{O}_2}^{\text{chl}} = 1 \text{ s cm}^{-1}$ and $R_{\text{O}_2}^{\text{chl}} = 0.1 \text{ s cm}^{-1}$, are included.

the idealized high ECSA cathode CL examined here (weak $L_{\text{Pt}}-r_f$ relationship). This result highlights the importance of maximizing the ECSA and facilitating oxygen transport toward the cathode CL, while keeping $r_f \geq 10$ using highly active Pt-alloys with a reduced Pt content if needed.

7 Conclusion

The performance and durability of proton exchange fuel cells (PEFCs) is largely linked to an optimal design of the

cathode catalyst layer (CL), especially if a reduction of the Pt loading ($L_{\text{Pt}} \sim 10^{-2} \text{ mgPt cm}^{-2}$) is desired to meet industrial requirements in terms of design and cost (e.g., ultimate targets set by the U.S. Department of Energy to make PEFC technology competitive). Based on the analysis conducted in this work, good practices to enhance the performance and enlarge the durability of the cathode CL at low Pt loading are as follows:

- 1) To increase the electrochemical surface area, ECSA, as much as possible to decrease the Pt loading needed to achieve a specified roughness factor, r_f . Reaching high performance (say, beyond $P \approx 1.5 \text{ W cm}^{-2}$) at low Pt loading

with $r_f \leq 10$ can be difficult due to the sluggishness of the oxygen reduction reaction (ORR). An increase of the catalyst active area up to $\text{ECSA} \sim 100 \text{ m}^2 \text{ g}_{\text{Pt}}^{-1}$ (e.g., through a combination of small Pt nanoparticles or atomic skins and highly accessible nanoporous structures) can allow a reduction of the Pt loading down to $0.05 \text{ mg}_{\text{Pt}} \text{ cm}^{-2}$ ($r_f \sim 100$) and $0.005 \text{ mg}_{\text{Pt}} \text{ cm}^{-2}$ ($r_f \sim 10$). The decrease of r_f at low Pt loading can additionally be alleviated using active Pt-alloys (e.g., PtCo) if a further increase in ECSA is not feasible.

- 2) To increase the percentage of triple phase points based on water-filled nanopores with no entry mass transport losses caused by (thin) ionomer films. Modification of nanoporous supports with short transport lengths ($\sim 10 \text{ nm}$) can be a viable route to increase the Pt-specific power density above $P_{\text{Pt}} \sim 10 \text{ kW g}_{\text{Pt}}^{-1}$. Optimized CLs with bi-functionalized microstructures (i.e., with a (precise) separation of mass and proton transport domains) and bimodal pore size distributions (i.e., with tailored primary nanopores to promote water adsorption and capillary condensation, and secondary pores to facilitate water removal) is crucial. If a high degree of bi-functionalization of the CL is not possible, the development of ionomers with tailored mass and ionic transport resistances can be useful. Novel ionomers can reduce entry mass transport resistances at the nanoscale, while allowing good proton conduction at the layer scale.
- 3) To reduce the oxygen transport resistance from the channel to the CL (i.e., from the stack inlet(s) to the CL), $R_{\text{O}_2}^{\text{chdl}}$, especially at high current density. Optimization of the oxygen transport resistance in other components, such as the stack flow distributor, flow field, gas diffusion layer and microporous layer, can be necessary to reach power densities above $P = 1.5 \text{ W cm}^{-2}$ at low Pt loading. Although solving the problem of the local oxygen transport resistance of ionomer in conventional cathode CLs is mandatory ($R_{\text{O}_2,p}^{\text{ion}} \approx 0.4 - 4 \text{ s cm}^{-1}$ at $r_f \approx 10-1$), the performance can be limited by exterior oxygen transport resistances once $R_{\text{O}_2,p}^{\text{ion}}$ is significantly decreased or even removed using bi-functionalized bimodal microstructures ($R_{\text{O}_2,p} \approx 0.02 \text{ s cm}^{-1}$). A ten-fold decrease of the exterior oxygen transport resistance from $R_{\text{O}_2}^{\text{chdl}} \approx 1 \text{ s cm}^{-1}$ (conventional value) down to $R_{\text{O}_2}^{\text{chdl}} \approx 0.1 \text{ s cm}^{-1}$ (highly optimized cathode flow distributor) can allow power densities around $P \approx 2 \text{ W cm}^{-2}$ at $L_{\text{Pt}} \approx 0.05 \text{ mg}_{\text{Pt}} \text{ cm}^{-2}$. Ohmic losses play a secondary role to enhance performance at low Pt loading, but thin membranes can be used to promote back diffusion and improve water management.
- 4) Increasing the catalyst mass activity (exchange current density, $i_{o,c}$) can allow an improvement of the power density if other transport losses do not limit the cell performance. Increasing $i_{o,c}$ ($\times 10$) in combination with a reduction of $R_{\text{O}_2}^{\text{chdl}}$ ($\times 0.1$) and CL optimization can raise the power density

up to $P \approx 2-3 \text{ W cm}^{-2}$ at low Pt loading, even though this will require an optimized water management strategy to keep $R_{\text{O}_2}^{\text{chdl}}$ small. Increasing $i_{o,c}$ without reducing $R_{\text{O}_2}^{\text{chdl}}$ can significantly limit the performance gain.

- 5) Durability during dynamic operation can be increased if corrosion of the carbon support is avoided at the cathode. Polymer and metallic (e.g., T_1O_2) supports show a longer durability than carbon-based supports (e.g., carbon black, graphite or carbon nanotubes). However, an economic analysis is needed to quantify if a change of the support to more expensive materials (e.g., T_1O_2) is cost-effective.

Although commercialization of PEMFCs is underway for some applications, such as heavy-duty vehicles, trains, electric bicycles, etc., several aspects warrant future work to be addressed by a combination of experimental and numerical work. Research is expected to continue toward increasing performance and durability at low Pt loading, mainly for two reasons: 1) to examine the technology limits that could provide a more affordable and extended use in general purpose applications, and 2) to leverage the development of cheap, durable, high-performance PEMFCs for light-duty vehicles that can make the technology more competitive in the automotive sector. As exemplified in this work, research topics to be analyzed in more detail include: 1) reduction of Pt loading *via* optimization of the multiscale microstructure of CLs, 2) water management with a focus on CL design and interaction with other layers, 3) reduction of oxygen transport resistance in MEAs and stacks, 4) increasing durability of carbon-based supports through a reduction of carbon corrosion, and 5) simplification of balance of plant. An effort is to be made toward integrated, multidisciplinary work, since most of these topics are coupled with each other. This probably explains why most significant recent developments in PEMFC technology were accomplished by companies, while research in the field seems to be a scattered combination of chemical, electrical, electrochemical and mechanical engineering, among other disciplines. Modeling is an essential transversal tool for understanding and optimization.

Data availability statement

The raw data supporting the conclusion of this article will be made available by the authors, without undue reservation.

Author contributions

GS contributed to the conception and design of the study, the simulation campaign, and the writing of the first draft of the manuscript. All authors contributed to manuscript revision, read, and approved the submitted version.

Funding

This work was supported by projects PID2019-106740RB-I00 and EIN 2020-112247 of the Spanish Research Council.

Acknowledgments

GS acknowledges fruitful discussion with Dr. Adam Z. Weber at Lawrence Berkeley National Lab under the framework of the project “Multiphysics, Multiphase and Multiscale Modeling of Porous Media with Application to Energy Conversion and Storage Electrochemical Devices” granted by the Spanish Research Council.

References

- Antolini, E., and Gonzalez, E. (2009). Ceramic materials as supports for low-temperature fuel cell catalysts. *Solid State Ionics* 180, 746–763. doi:10.1016/j.ssi.2009.03.007
- Atanassov, P., Di Noto, V., and McPhail, S. (2021). From hydrogen manifesto, through green deal and just transition, to clean energy act. *Electrochem. Soc. Interface* 30, 57–60. doi:10.1149/2.f14214if
- Attari Moghaddam, A., Prat, M., Tsotsas, E., and Kharaghani, A. (2017). Evaporation in capillary porous media at the perfect piston-like invasion limit: Evidence of nonlocal equilibrium effects. *Water Resour. Res.* 53, 10433–10449. doi:10.1002/2017wr021162
- Avcioglu, G. S., Ficicilar, B., and Eroglu, I. (2016). Effect of ptfe nanoparticles in catalyst layer with high pt loading on pem fuel cell performance. *Int. J. hydrogen energy* 41, 10010–10020. doi:10.1016/j.ijhydene.2016.03.048
- Azarafza, A., Ismail, M. S., Rezakazemi, M., and Pourkashanian, M. (2019). Comparative study of conventional and unconventional designs of cathode flow fields in pem fuel cell. *Renew. Sustain. Energy Rev.* 116, 109420. doi:10.1016/j.rser.2019.109420
- Babu, S. K., Mukundan, R., Wang, C., Langlois, D., Cullen, D. A., Papadias, D., et al. (2021). Effect of catalyst and catalyst layer composition on catalyst support durability. *J. Electrochem. Soc.* 168, 044502. doi:10.1149/1945-7111/abf21f
- Blunier, B., Gao, F., and Miraoui, A. (2013). *Proton exchange membrane fuel cells modeling*. John Wiley & Sons.
- Borup, R. L., Kusoglu, A., Neyerlin, K. C., Mukundan, R., Ahluwalia, R. K., Cullen, D. A., et al. (2020). Recent developments in catalyst-related pem fuel cell durability. *Curr. Opin. Electrochem.* 21, 192–200. doi:10.1016/j.coelec.2020.02.007
- Borup, R. L., More, K. L., and Myers, D. J. (2018). Fc-pad: Fuel cell performance and durability consortium update to uscar analysis of toyota mirai components provided by uscar
- Borup, R., and Weber, A. (2019). *Fc135: Fc-pad: Fuel cell performance and durability consortium*. Washington DC: Annual Merit Review Proceedings.
- Chen, D., Kongkanand, A., and Jorne, J. (2019). Proton conduction and oxygen diffusion in ultra-thin nafion films in pem fuel cell: How thin? *J. Electrochem. Soc.* 166, F24–F33. doi:10.1149/2.0101902jes
- Chen, K., Deng, S., Lu, Y., Gong, M., Hu, Y., Zhao, T., et al. (2021). Molybdenum-doped titanium dioxide supported low-pt electrocatalyst for highly efficient and stable hydrogen evolution reaction. *Chin. Chem. Lett.* 32, 765–769. doi:10.1016/j.ccllet.2020.05.030
- Chen, M., Zhao, C., Sun, F., Fan, J., Li, H., and Wang, H. (2020). Research progress of catalyst layer and interlayer interface structures in membrane electrode assembly (mea) for proton exchange membrane fuel cell (pemfc) system. *ETransportation* 5, 100075. doi:10.1016/j.etrans.2020.100075
- Chen, Z., Deng, W., Wang, X., and Yan, Y. (2007). Durability and activity study of single-walled, double-walled and multi-walled carbon nanotubes supported pt catalyst for pemfcs. *ECS Trans.* 11, 1289–1299. doi:10.1149/1.2781042
- Cheng, X., Shen, S., Wei, G., Wang, C., Luo, L., and Zhang, J. (2022). Perspectives on challenges and achievements in local oxygen transport of low pt proton exchange membrane fuel cells. *Adv. Mat. Technol.* 7, 2200228. doi:10.1002/admt.202200228
- Chi, B., Hou, S., Liu, G., Deng, Y., Zeng, J., Song, H., et al. (2018). Tuning hydrophobic-hydrophilic balance of cathode catalyst layer to improve cell performance of proton exchange membrane fuel cell (pemfc) by mixing polytetrafluoroethylene (ptfe). *Electrochimica Acta* 277, 110–115. doi:10.1016/j.electacta.2018.04.213
- Choi, H., Kim, O.-H., Kim, M., Choe, H., Cho, Y.-H., and Sung, Y.-E. (2014). Next-generation polymer-electrolyte-membrane fuel cells using titanium foam as gas diffusion layer. *ACS Appl. Mat. Interfaces* 6, 7665–7671. doi:10.1021/am500962h
- Cochet, M., Forner-Cuenca, A., Manzi-Orezzoli, V., Siegwart, M., Scheuble, D., and Boillat, P. (2020). Enabling high power density fuel cells by evaporative cooling with advanced porous media. *J. Electrochem. Soc.* 167, 084518. doi:10.1149/1945-7111/ab8e82
- Conde, J. J., Foldgado, M. A., Ferreira-Aparicio, P., Chaparro, A. M., Chowdhury, A., Kusoglu, A., et al. (2019). Mass-transport properties of electrosprayed pt/c catalyst layers for polymer-electrolyte fuel cells. *J. Power Sources* 427, 250–259. doi:10.1016/j.jpowsour.2019.04.079
- Cui, L., Zhang, J., Wang, H., Lu, S., and Xiang, Y. (2021). The effects of different dimensional carbon additives on performance of pemfc with low-pt loading cathode catalytic layers. *Int. J. Hydrogen Energy* 46, 15887–15895. doi:10.1016/j.ijhydene.2021.02.032
- Debe, M. K., Atanasoski, R. T., and Steinbach, A. J. (2011). Nanostructured thin film electrocatalysts-current status and future potential. *ECS Trans.* 41, 937–954. doi:10.1149/1.3635628
- Debe, M. K. (2011). Effect of electrode surface area distribution on high current density performance of pem fuel cells. *J. Electrochem. Soc.* 159, B53–B66. doi:10.1149/2.032201jes
- Debe, M. K. (2012). Nanostructured thin film electrocatalysts for pem fuel cells-a tutorial on the fundamental characteristics and practical properties of nstf catalysts. *ECS Trans.* 45, 47–68. doi:10.1149/1.3701968
- Debe, M. K., Schmoekel, A. K., Vernstrom, G. D., and Atanasoski, R. (2006). High voltage stability of nanostructured thin film catalysts for pem fuel cells. *J. Power Sources* 161, 1002–1011. doi:10.1016/j.jpowsour.2006.05.033
- Deng, X., Huang, C., Pei, X., Hu, B., and Zhou, W. (2021). Recent progresses and remaining issues on the ultrathin catalyst layer design strategy for high-performance proton exchange membrane fuel cell with further reduced pt loadings: A review. *Int. J. Hydrogen Energy* 47, 1529–1542. doi:10.1016/j.ijhydene.2021.10.141

Conflict of interest

The authors declare that the research was conducted in the absence of any commercial or financial relationships that could be construed as a potential conflict of interest.

Publisher's note

All claims expressed in this article are solely those of the authors and do not necessarily represent those of their affiliated organizations, or those of the publisher, the editors and the reviewers. Any product that may be evaluated in this article, or claim that may be made by its manufacturer, is not guaranteed or endorsed by the publisher.

- DOE (2015). Hydrogen and fuel cell technologies office multi-year research, development, and demonstration plan. Available at: <https://www.energy.gov/eere/fuelcells/articles/hydrogen-and-fuel-cell-technologies-office-multi-year-research-development>.
- Ercelik, M., Ismail, M. S., Ingham, D. B., Hughes, K. J., Ma, L., and Pourkashanian, M. (2022). Efficient x-ray ct-based numerical computations of structural and mass transport properties of nickel foam-based gdl for pefcs. *Energy* 262, 125531. doi:10.1016/j.energy.2022.125531
- Esfahani, R. A. M., and Easton, E. B. (2020). Exceptionally durable pt/toms catalysts for fuel cells. *Appl. Catal. B Environ.* 268, 118743. doi:10.1016/j.apcatb.2020.118743
- Esfahani, R. A. M., Ebralizde, I. I., Specchia, S., and Easton, E. B. (2018). A fuel cell catalyst support based on doped titanium suboxides with enhanced conductivity, durability and fuel cell performance. *J. Mat. Chem. A Mat.* 6, 14805–14815. doi:10.1039/c8ta02470g
- Folgado, M., Conde, J., Ferreira-Aparicio, P., and Chaparro, A. (2018). Single cell study of water transport in pemfcs with electrosprayed catalyst layers. *Fuel Cells* 18, 602–612. doi:10.1002/fuce.201700217
- Fumagalli, M., Lyonard, S., Prajapati, G., Berrod, Q., Porcar, L., Guillermo, A., et al. (2015). Fast water diffusion and long-term polymer reorganization during nafion membrane hydration evidenced by time-resolved small-angle neutron scattering. *J. Phys. Chem. B* 119, 7068–7076. doi:10.1021/acs.jpcc.5b01220
- García-Salaberri, P. A. (2022). “General aspects in the modeling of fuel cells: From conventional fuel cells to nano fuel cells,” in *Nanotechnology in fuel cells* (Elsevier), 77
- García-Salaberri, P. A., Gostick, J. T., Hwang, G., Weber, A. Z., and Vera, M. (2015a). Effective diffusivity in partially-saturated carbon-fiber gas diffusion layers: Effect of local saturation and application to macroscopic continuum models. *J. Power Sources* 296, 440–453. doi:10.1016/j.jpowsour.2015.07.034
- García-Salaberri, P. A., Gostick, J. T., Zenyuk, I. V., Hwang, G., Vera, M., and Weber, A. Z. (2017b). On the limitations of volume-averaged descriptions of gas diffusion layers in the modeling of polymer electrolyte fuel cells. *ECS Trans.* 80, 133–143. doi:10.1149/08008.0133ecst
- García-Salaberri, P. A., Hwang, G., Vera, M., Weber, A. Z., and Gostick, J. T. (2015b). Effective diffusivity in partially-saturated carbon-fiber gas diffusion layers: Effect of through-plane saturation distribution. *Int. J. Heat Mass Transf.* 86, 319–333. doi:10.1016/j.ijheatmasstransfer.2015.02.073
- García-Salaberri, P. A., Vera, M., and Zaera, R. (2011). Nonlinear orthotropic model of the inhomogeneous assembly compression of pem fuel cell gas diffusion layers. *Int. J. Hydrogen Energy* 36, 11856–11870. doi:10.1016/j.ijhydene.2011.05.152
- García-Salaberri, P. A., Zenyuk, I. V., Hwang, G., Vera, M., Weber, A. Z., and Gostick, J. T. (2019). Implications of inherent inhomogeneities in thin carbon fiber-based gas diffusion layers: A comparative modeling study. *Electrochimica Acta* 295, 861–874. doi:10.1016/j.electacta.2018.09.089
- García-Salaberri, P. A., Zenyuk, I. V., Shum, A. D., Hwang, G., Vera, M., Weber, A. Z., et al. (2018). Analysis of representative elementary volume and through-plane regional characteristics of carbon-fiber papers: Diffusivity, permeability and electrical/thermal conductivity. *Int. J. Heat Mass Transf.* 127, 687–703. doi:10.1016/j.ijheatmasstransfer.2018.07.030
- García-Salaberri, P. (2021). Modeling diffusion and convection in thin porous transport layers using a composite continuum-network model: Application to gas diffusion layers in polymer electrolyte fuel cells. *Int. J. Heat Mass Transf.* 167, 120824. doi:10.1016/j.ijheatmasstransfer.2020.120824
- García-Salaberri, P., Sánchez, D., Boillat, P., Vera, M., and Friedrich, K. A. (2017a). Hydration and dehydration cycles in polymer electrolyte fuel cells operated with wet anode and dry cathode feed: A neutron imaging and modeling study. *J. power sources* 359, 634–655. doi:10.1016/j.jpowsour.2017.03.155
- Garsany, Y., Atkinson, R. W.III, Gould, B. D., and Swider-Lyons, K. E. (2018). High power, low-pt membrane electrode assemblies for proton exchange membrane fuel cells. *J. Power Sources* 408, 38–45. doi:10.1016/j.jpowsour.2018.10.073
- Gebel, G., Lyonard, S., Mendil-Jakani, H., and Morin, A. (2011). The kinetics of water sorption in nafion membranes: A small-angle neutron scattering study. *J. Phys. Condens. Matter* 23, 234107. doi:10.1088/0953-8984/23/23/234107
- Gomaa, M. M., Sánchez-Ramos, A., Ureña, N., Pérez-Prior, M. T., Levenfeld, B., García-Salaberri, P. A., et al. (2022). Characterization and modeling of free volume and ionic conduction in multiblock copolymer proton exchange membranes. *Polymers* 14, 1688. doi:10.3390/polym14091688
- Goshtasbi, A., García-Salaberri, P., Chen, J., Talukdar, K., Sanchez, D. G., and Ersal, T. (2019). Through-the-membrane transient phenomena in pem fuel cells: A modeling study. *J. Electrochem. Soc.* 166, F3154–F3179. doi:10.1149/2.0181907jes
- Gostick, J. T., and Weber, A. Z. (2015). Resistor-network modeling of ionic conduction in polymer electrolytes. *Electrochimica Acta* 179, 137–145. doi:10.1016/j.electacta.2015.03.126
- Greszler, T. A., Caulk, D., and Sinha, P. (2012). The impact of platinum loading on oxygen transport resistance. *J. Electrochem. Soc.* 159, F831–F840. doi:10.1149/2.061212jes
- Hack, J., García-Salaberri, P. A., Kok, M. D., Jervis, R., Shearing, P. R., Brandon, N., et al. (2020). X-Ray micro-computed tomography of polymer electrolyte fuel cells: What is the representative elementary area? *J. Electrochem. Soc.* 167, 013545. doi:10.1149/1945-7111/ab6983
- Han, P., and Bartels, D. M. (1996). Temperature dependence of oxygen diffusion in H₂O and D₂O. *J. Phys. Chem.* 100, 5597–5602. doi:10.1021/jp952903y
- Huang, Z., Chen, B., Mo, X., Yang, X., Yu, L., Hu, X., et al. (2021). Fast water evaporation from nanopores. *Adv. Mat. Interfaces* 8, 2100660. doi:10.1002/admi.202100660
- Jiao, K., and Li, X. (2011). Water transport in polymer electrolyte membrane fuel cells. *Prog. energy Combust. Sci.* 37, 221–291. doi:10.1016/j.pecs.2010.06.002
- Jiao, K., Xuan, J., Du, Q., Bao, Z., Xie, B., Wang, B., et al. (2021). Designing the next generation of proton-exchange membrane fuel cells. *Nature* 595, 361–369. doi:10.1038/s41586-021-03482-7
- Jomori, S., Nonoyama, N., and Yoshida, T. (2012). Analysis and modeling of pemfc degradation: Effect on oxygen transport. *J. Power Sources* 215, 18–27. doi:10.1016/j.jpowsour.2012.04.069
- Kienitz, B., Kolde, J., Priester, S., Baczowski, C., and Crum, M. (2011). Ultra-thin reinforced ionomer membranes to meet next generation fuel cell targets. *ECS Trans.* 41, 1521–1530. doi:10.1149/1.3635683
- Kim, S., and Mench, M. (2009). Investigation of temperature-driven water transport in polymer electrolyte fuel cell: Phase-change-induced flow. *J. Electrochem. Soc.* 156, B353. doi:10.1149/1.3046136
- Kobayashi, A., Fujii, T., Harada, C., Yasumoto, E., Takeda, K., Kakinuma, K., et al. (2021). Effect of pt and ionomer distribution on polymer electrolyte fuel cell performance and durability. *ACS Appl. Energy Mat.* 4, 2307–2317. doi:10.1021/acsaem.0c02841
- Kongkanand, A., and Mathias, M. F. (2016). The priority and challenge of high-power performance of low-platinum proton-exchange membrane fuel cells. *J. Phys. Chem. Lett.* 7, 1127–1137. doi:10.1021/acs.jpclett.6b00216
- Kulikovsky, A. (2010). The regimes of catalyst layer operation in a fuel cell. *Electrochimica Acta* 55, 6391–6401. doi:10.1016/j.electacta.2010.06.053
- Kusoglu, A., Kwong, A., Clark, K. T., Gunterman, H. P., and Weber, A. Z. (2012). Water uptake of fuel-cell catalyst layers. *J. Electrochem. Soc.* 159, F530–F535. doi:10.1149/2.031209jes
- Kusoglu, A., and Weber, A. Z. (2017). New insights into perfluorinated sulfonic-acid ionomers. *Chem. Rev.* 117, 987–1104. doi:10.1021/acs.chemrev.6b00159
- Li, Y., Chen, H., Xiao, S., Alibakhshi, M. A., Lo, C.-W., Lu, M.-C., et al. (2019). Ultrafast diameter-dependent water evaporation from nanopores. *ACS Nano* 13, 3363–3372. doi:10.1021/acsnano.8b09258
- Lin, R., Wang, H., and Zhu, Y. (2021). Optimizing the structural design of cathode catalyst layer for pem fuel cells for improving mass-specific power density. *Energy* 221, 119909. doi:10.1016/j.energy.2021.119909
- Liu, C. P., Saha, P., Huang, Y., Shimpalee, S., Satjaritanun, P., and Zenyuk, I. V. (2021). Measurement of contact angles at carbon fiber–water–air triple-phase boundaries inside gas diffusion layers using x-ray computed tomography. *ACS Appl. Mat. Interfaces* 13, 20002–20013. doi:10.1021/acsmi.1c00849
- Liu, J., García-Salaberri, P. A., and Zenyuk, I. V. (2019a). Bridging scales to model reactive diffusive transport in porous media. *J. Electrochem. Soc.* 167, 013524. doi:10.1149/2.0242001jes
- Liu, J., García-Salaberri, P. A., and Zenyuk, I. V. (2019b). The impact of reaction on the effective properties of multiscale catalytic porous media: A case of polymer electrolyte fuel cells. *Transp. Porous Media* 128, 363–384. doi:10.1007/s11242-019-01252-8
- Liu, J., Gazzarri, J., and Eikerling, M. (2013). Model-based *ex situ* diagnostics of water fluxes in catalyst layers of polymer electrolyte fuel cells. *Fuel Cells* 13, 134–142. doi:10.1002/fuce.201200072
- Liu, J., and Zenyuk, I. V. (2018). Proton transport in ionomer-free regions of polymer electrolyte fuel cells and implications for oxygen reduction reaction. *Curr. Opin. Electrochem.* 12, 202–208. doi:10.1016/j.coelec.2018.11.015
- Lu, Z., Wilke, K. L., Preston, D. J., Kinefuchi, I., Chang-Davidson, E., and Wang, E. N. (2017). An ultrathin nanoporous membrane evaporator. *Nano Lett.* 17, 6217–6220. doi:10.1021/acs.nanolett.7b02889
- Lv, H., and Mu, S. (2014). Nano-ceramic support materials for low temperature fuel cell catalysts. *Nanoscale* 6, 5063–5074. doi:10.1039/c4nr00402g
- Malik, F., Clement, R., Gethin, D., Kiernan, M., Goral, T., Griffiths, P., et al. (2016). Hierarchical structures of cactus spines that aid in the directional movement of dew droplets. *Phil. Trans. R. Soc. A* 374, 20160110. doi:10.1098/rsta.2016.0110

- Mardle, P., and Du, S. (2022). Introduction to materials for pemfc electrodes. *J. Encycl. Smart Mater.* 242–255.
- Martinez-Urrutia, A., de Arroiabe, P. F., Ramirez, M., Martinez-Agirre, M., and Bou-Ali, M. M. (2018). Contact angle measurement for libr aqueous solutions on different surface materials used in absorption systems. *Int. J. Refrig.* 95, 182–188. doi:10.1016/j.jrefrig.2018.05.041
- Mashio, T., Sato, K., and Ohma, A. (2014). Analysis of water adsorption and condensation in catalyst layers for polymer electrolyte fuel cells. *Electrochimica Acta* 140, 238–249. doi:10.1016/j.electacta.2014.07.058
- Meng, Q. H., Hao, C., Yan, B., Yang, B., Liu, J., Shen, P. K., et al. (2022). High-performance proton exchange membrane fuel cell with ultra-low loading pt on vertically aligned carbon nanotubes as integrated catalyst layer. *J. Energy Chem.* 71, 497–506. doi:10.1016/j.jechem.2022.03.018
- Middelmann, E. (2002). Improved pem fuel cell electrodes by controlled self-assembly. *Fuel Cells Bull.* 9–12, 9–12. doi:10.1016/s1464-2859(02)11028-5
- MoghadamEsfahani, R. A., Vankova, S. K., Easton, E. B., Ebralidze, I. I., and Specchia, S. (2020). A hybrid pt/nbo/cnts catalyst with high activity and durability for oxygen reduction reaction in pemfc. *Renew. Energy* 154, 913–924. doi:10.1016/j.renene.2020.03.029
- Mu, Y.-T., He, P., Gu, Z.-L., Qu, Z.-G., and Tao, W.-Q. (2022). Modelling the reactive transport processes in different reconstructed agglomerates of a pefc catalyst layer. *Electrochimica Acta* 404, 139721. doi:10.1016/j.electacta.2021.139721
- Murata, S., Imanishi, M., Hasegawa, S., and Namba, R. (2014). Vertically aligned carbon nanotube electrodes for high current density operating proton exchange membrane fuel cells. *J. Power Sources* 253, 104–113. doi:10.1016/j.jpowsour.2013.11.073
- Muzaffar, T., Kadyk, T., and Eikerling, M. (2018). Tipping water balance and the pt loading effect in polymer electrolyte fuel cells: A model-based analysis. *Sustain. Energy Fuels* 2, 1189–1196. doi:10.1039/c8se00026c
- Newman, J. (1966). Resistance for flow of current to a disk. *J. Electrochem. Soc.* 113, 501–502. doi:10.1149/1.2424003
- Nguyen, H. L., Han, J., Nguyen, X. L., Yu, S., Goo, Y.-M., and Le, D. D. (2021). Review of the durability of polymer electrolyte membrane fuel cell in long-term operation: Main influencing parameters and testing protocols. *Energies* 14, 4048. doi:10.3390/en14134048
- Orfanidi, A., Madkikar, P., El-Sayed, H. A., Harzer, G. S., Kratky, T., and Gasteiger, H. (2017). The key to high performance low pt loaded electrodes. *J. Electrochem. Soc.* 164, F418–F426. doi:10.1149/2.1621704jes
- Ostrovkerkh, A., Johánek, V., Dubau, M., Kúš, P., Khalakhan, I., Šmíd, B., et al. (2019). Optimization of ionomer-free ultra-low loading pt catalyst for anode/cathode of pemfc via magnetron sputtering. *Int. J. Hydrogen Energy* 44, 19344–19356. doi:10.1016/j.ijhydene.2018.12.206
- Owejan, J. P., Owejan, J. E., and Gu, W. (2013). Impact of platinum loading and catalyst layer structure on pemfc performance. *J. Electrochem. Soc.* 160, F824–F833. doi:10.1149/2.072308jes
- Owejan, J. P., Trabold, T. A., and Mench, M. M. (2014). Oxygen transport resistance correlated to liquid water saturation in the gas diffusion layer of pem fuel cells. *Int. J. Heat Mass Transf.* 71, 585–592. doi:10.1016/j.jheatmasstransfer.2013.12.059
- Pan, C., Wu, H., Wang, C., Wang, B., Zhang, L., Cheng, Z., et al. (2008). Nanowire-based high-performance “micro fuel cells”: One nanowire, one fuel cell. *Adv. Mat.* 20, 1644–1648. doi:10.1002/adma.200700515
- Park, J. E., Lim, J., Lim, M. S., Kim, S., Kim, O.-H., Lee, D. W., et al. (2019). Gas diffusion layer/flow-field unified membrane-electrode assembly in fuel cell using graphene foam. *Electrochimica Acta* 323, 134808. doi:10.1016/j.electacta.2019.134808
- Park, J. H., and Aluru, N. (2009). Temperature-dependent wettability on a titanium dioxide surface. *Mol. Simul.* 35, 31–37. doi:10.1080/08927020802398884
- Paul, D. K., McCreery, R., and Karan, K. (2014). Proton transport property in supported nafion nanothin films by electrochemical impedance spectroscopy. *J. Electrochem. Soc.* 161, F1395–F1402. doi:10.1149/2.0571414jes
- Perrins, W., McKenzie, D. R., and McPhedran, R. (1979). Transport properties of regular arrays of cylinders. *Proc. R. Soc. Lond. A. Math. Phys. Sci.* 369, 207–225.
- Perry, M. L., Newman, J., and Cairns, E. J. (1998). Mass transport in gas-diffusion electrodes: A diagnostic tool for fuel-cell cathodes. *J. Electrochem. Soc.* 145, 5–15. doi:10.1149/1.1838202
- Pushkareva, I. V., Pushkarev, A. S., Kalinichenko, V. N., Chumakov, R. G., Soloviev, M. A., Liang, Y., et al. (2021). Reduced graphene oxide-supported pt-based catalysts for pem fuel cells with enhanced activity and stability. *Catalysts* 11, 256. doi:10.3390/catal11020256
- Ramaswamy, N., Gu, W., Ziegelbauer, J. M., and Kumaraguru, S. (2020). Carbon support microstructure impact on high current density transport resistances in pemfc cathode. *J. Electrochem. Soc.* 167, 064515. doi:10.1149/1945-7111/ab819c
- Sabarirajan, D. C., Liu, J., Qi, Y., Perego, A., Haug, A. T., and Zenyuk, I. V. (2020). Determining proton transport in pseudo catalyst layers using hydrogen pump dc and ac techniques. *J. Electrochem. Soc.* 167, 084521. doi:10.1149/1945-7111/ab927d
- Sakai, K., Sato, K., Mashio, T., Ohma, A., Yamaguchi, K., and Shinohara, K. (2009). Analysis of reactant gas transport in catalyst layers; effect of pt-loadings. *ECS Trans.* 25, 1193–1201. doi:10.1149/1.3210674
- Sánchez-Monreal, J., Vera, M., and García-Salaberri, P. A. (2018). Fundamentals of electrochemistry with application to direct alcohol fuel cell modeling ” in. *Proton exchange membrane fuel cell*. Rijeka: Intech, 121
- Sánchez-Ramos, A., Gostick, J., and García-Salaberri, P. (2022). Modeling the effect of low pt loading cathode catalyst layer in polymer electrolyte fuel cells. Part ii: Parametric analysis. *J. Electrochem. Soc.* 169, 074503. doi:10.1149/1945-7111/ac811d
- Sánchez-Ramos, A., Gostick, J. T., and García-Salaberri, P. A. (2021). Modeling the effect of low pt loading cathode catalyst layer in polymer electrolyte fuel cells: Part i. model formulation and validation. *J. Electrochem. Soc.* 168, 124514. doi:10.1149/1945-7111/ac4456
- Schuler, T., Chowdhury, A., Freiberg, A. T., Sneed, B., Spingler, F. B., Tucker, M. C., et al. (2019). Fuel-cell catalyst-layer resistance via hydrogen limiting-current measurements. *J. Electrochem. Soc.* 166, F3020–F3031. doi:10.1149/2.0031907jes
- Sery, J., and Leduc, P. (2022). Fuel cell behavior and energy balance on board a hyundai nexu. *Int. J. Engine Res.* 23, 709–720. doi:10.1177/14680874211059046
- Shen, S., Cheng, X., Wang, C., Yan, X., Ke, C., Yin, J., et al. (2017). Exploration of significant influences of the operating conditions on the local o₂ transport in proton exchange membrane fuel cells (pemfcs). *Phys. Chem. Chem. Phys.* 19, 26221–26229. doi:10.1039/c7cp04837h
- Siroma, Z., Kakitsubo, R., Fujiwara, N., Ioroi, T., Yamazaki, S.-i., and Yasuda, K. (2009). Depression of proton conductivity in recast nafion® film measured on flat substrate. *J. Power Sources* 189, 994–998. doi:10.1016/j.jpowsour.2008.12.141
- Spingler, F. B., Phillips, A., Schuler, T., Tucker, M. C., and Weber, A. Z. (2017). Investigating fuel-cell transport limitations using hydrogen limiting current. *Int. J. Hydrogen Energy* 42, 13960–13969. doi:10.1016/j.ijhydene.2017.01.036
- Steinbach, A. J., Allen, J. S., Borup, R. L., Hussey, D. S., Jacobson, D. L., Komlev, A., et al. (2018). Anode-design strategies for improved performance of polymer-electrolyte fuel cells with ultra-thin electrodes. *Joule* 2, 1297–1312. doi:10.1016/j.joule.2018.03.022
- Steinbach, A. J., Debe, M. K., Wong, J., Kurkowsky, M. J., Haug, A. T., Peppin, D. M., et al. (2010). A new paradigm for pemfc ultra-thin electrode water management at low temperatures. *ECS Trans.* 33, 1179–1188. doi:10.1149/1.3484611
- Stennett, A. K., Dempsey, G. L., and Gainer, J. L. (2006). trans-sodium crocetinate and diffusion enhancement. *J. Phys. Chem. B* 110, 18078–18080. doi:10.1021/jp064308+
- Straubhaar, B., Pauchet, J., and Prat, M. (2015). Water transport in gas diffusion layer of a polymer electrolyte fuel cell in the presence of a temperature gradient: phase change effect. *Int. J. hydrogen energy* 40, 11668–11675. doi:10.1016/j.ijhydene.2015.04.027
- Sun, X., Yu, H., Zhou, L., Gao, X., Zeng, Y., Yao, D., et al. (2020). Influence of platinum dispersity on oxygen transport resistance and performance in pemfc. *Electrochimica Acta* 332, 135474. doi:10.1016/j.electacta.2019.135474
- Sun, Y., Cui, L., Gong, J., Zhang, J., Xiang, Y., and Lu, S. (2019). Design of a catalytic layer with hierarchical proton transport structure: The role of nafion nanofiber. *ACS Sustain. Chem. Eng.* 7, 2955–2963. doi:10.1021/acssuschemeng.8b03910
- Taberian, F., Marcon, V., van der Vegt, N. F., and Leroy, F. (2013). What is the contact angle of water on graphene? *Langmuir* 29, 1457–1465. doi:10.1021/la304645w
- Takeshita, T., Kamitaka, Y., Shinozaki, K., Kodama, K., and Morimoto, Y. (2020). Evaluation of ionomer coverage on pt catalysts in polymer electrolyte membrane fuel cells by co stripping voltammetry and its effect on oxygen reduction reaction activity. *J. Electroanal. Chem.* 871, 114250. doi:10.1016/j.jelechem.2020.114250
- Talukdar, K., Delgado, S., Lagarteira, T., Gazdzicki, P., and Friedrich, K. A. (2019). Minimizing mass-transport loss in proton exchange membrane fuel cell by freeze-drying of cathode catalyst layers. *J. Power Sources* 427, 309–317. doi:10.1016/j.jpowsour.2019.04.094
- Tellez-Cruz, M. M., Escorihuela, J., Solorza-Feria, O., and Compañ, V. (2021). Proton exchange membrane fuel cells (pemfcs): Advances and challenges. *Polymers* 13, 3064. doi:10.3390/polym13183064

- Thomas, A., Maranzana, G., Didierjean, S., Dillet, J., and Lottin, O. (2014). Thermal and water transfer in pemfcs: Investigating the role of the microporous layer. *Int. J. Hydrogen Energy* 39, 2649–2658. doi:10.1016/j.ijhydene.2013.11.105
- Tomadakis, M. M., and Sotirchos, S. V. (1993). Effective diffusivities and conductivities of random dispersions of nonoverlapping and partially overlapping unidirectional fibers. *J. Chem. Phys.* 99, 9820–9827. doi:10.1063/1.465464
- Ureña, N., Pérez-Prior, M. T., Levenfeld, B., and García-Salaberri, P. A. (2021). On the conductivity of proton-exchange membranes based on multiblock copolymers of sulfonated polysulfone and polyphenylsulfone: An experimental and modeling study. *Polymers* 13, 363. doi:10.3390/polym13030363
- Wang, M., Chen, M., Yang, Z., Liu, G., Lee, J. K., Yang, W., et al. (2019). High-performance and durable cathode catalyst layer with hydrophobic c@ ptfe particles for low-pt loading membrane assembly electrode of pemfc. *Energy Convers. Manag.* 191, 132–140. doi:10.1016/j.enconman.2019.04.014
- Wang, Y., Diaz, D. F. R., Chen, K. S., Wang, Z., and Adroher, X. C. (2020a). Materials, technological status, and fundamentals of pem fuel cells—a review. *Mater. today* 32, 178–203. doi:10.1016/j.mattod.2019.06.005
- Wang, Y., Qiu, B., Fan, S., Liu, J., Qin, Y., Jian, S., et al. (2020b). Membrane distillation of butanol from aqueous solution with polytetrafluoroethylene membrane. *Chem. Eng. Technol.* 43, 1160–1166. doi:10.1002/ceat.201900484
- Weber, A. Z., and Kusoglu, A. (2014). Unexplained transport resistances for low-loaded fuel-cell catalyst layers. *J. Mat. Chem. A* 2, 17207–17211. doi:10.1039/c4ta02952f
- Whiston, M. M., Azevedo, I. L., Litster, S., Whitefoot, K. S., Samaras, C., and Whitacre, J. F. (2019). Expert assessments of the cost and expected future performance of proton exchange membrane fuel cells for vehicles. *Proc. Natl. Acad. Sci. U. S. A.* 116, 4899–4904. doi:10.1073/pnas.1804221116
- Wilson, M. S., and Gottesfeld, S. (1992). Thin-film catalyst layers for polymer electrolyte fuel cell electrodes. *J. Appl. Electrochem.* 22, 1–7. doi:10.1007/bf01093004
- Xia, Z., Wang, S., Jiang, L., Sun, H., Liu, S., Fu, X., et al. (2015). Bio-inspired construction of advanced fuel cell cathode with pt anchored in ordered hybrid polymer matrix. *Sci. Rep.* 5, 16100–16111. doi:10.1038/srep16100
- Xie, S., Choi, S.-I., Lu, N., Roling, L. T., Herron, J. A., Zhang, L., et al. (2014). Atomic layer-by-layer deposition of pt on pd nanocubes for catalysts with enhanced activity and durability toward oxygen reduction. *Nano Lett.* 14, 3570–3576. doi:10.1021/nl501205j
- Yarlagadda, V., Carpenter, M. K., Moylan, T. E., Kukreja, R. S., Koestner, R., Gu, W., et al. (2018). Boosting fuel cell performance with accessible carbon mesopores. *ACS Energy Lett.* 3, 618–621. doi:10.1021/acsenrgylett.8b00186
- Ye, Q., and Van Nguyen, T. (2007). Three-dimensional simulation of liquid water distribution in a pemfc with experimentally measured capillary functions. *J. Electrochem. Soc.* 154, B1242. doi:10.1149/1.2783775
- Yi, P., Peng, L., Lai, X., Li, M., and Ni, J. (2012). Investigation of sintered stainless steel fiber felt as gas diffusion layer in proton exchange membrane fuel cells. *Int. J. hydrogen energy* 37, 11334–11344. doi:10.1016/j.ijhydene.2012.04.161
- Yoshida, T., and Kojima, K. (2015). Toyota mirai fuel cell vehicle and progress toward a future hydrogen society. *Interface Mag.* 24, 45–49. doi:10.1149/2.f03152if
- Yoshino, S., Shinohara, A., Kodama, K., and Morimoto, Y. (2020). Fabrication of catalyst layer with ionomer nanofiber scaffolding for polymer electrolyte fuel cells. *J. Power Sources* 476, 228584. doi:10.1016/j.jpowsour.2020.228584
- Yunzhe, J., Bowei, Z., Feifei, W., and Mengmeng, L. (2020). “Research on hydrogen energy and fuel cell vehicle roadmap in various countries” in IOP Conference Series: Earth and Environmental Science, 512. IOP Publishing, 012136.
- Zapardiel, D., and García-Salaberri, P. A. (2022). Modeling the interplay between water capillary transport and species diffusion in gas diffusion layers of proton exchange fuel cells using a hybrid computational fluid dynamics formulation. *J. Power Sources* 520, 230735. doi:10.1016/j.jpowsour.2021.230735
- Zenyuk, I. V., Das, P. K., and Weber, A. Z. (2016a). Understanding impacts of catalyst-layer thickness on fuel-cell performance via mathematical modeling. *J. Electrochem. Soc.* 163, F691–F703. doi:10.1149/2.1161607jes
- Zenyuk, I. V., Lamibrac, A., Eller, J., Parkinson, D. Y., Marone, F., Buchi, F. N., et al. (2016b). Investigating evaporation in gas diffusion layers for fuel cells with x-ray computed tomography. *J. Phys. Chem. C* 120, 28701–28711. doi:10.1021/acs.jpcc.6b10658
- Zenyuk, I. V., and Litster, S. (2014). Modeling ion conduction and electrochemical reactions in water films on thin-film metal electrodes with application to low temperature fuel cells. *Electrochimica Acta* 146, 194–206. doi:10.1016/j.electacta.2014.08.070
- Zhang, W., and Pintauro, P. N. (2011). High-performance nanofiber fuel cell electrodes. *ChemSusChem* 4, 1753–1757. doi:10.1002/cssc.201100245
- Zhang, Y., Tao, Y., and Shao, J. (2021). Application of porous materials for the flow field in polymer electrolyte membrane fuel cells. *J. Power Sources* 492, 229664. doi:10.1016/j.jpowsour.2021.229664
- Zhao, J., Shahgaldi, S., Alaefour, I., Xu, Q., and Li, X. (2018). Gas permeability of catalyzed electrodes in polymer electrolyte membrane fuel cells. *Appl. Energy* 209, 203–210. doi:10.1016/j.apenergy.2017.10.087
- Zhao, J., Tu, Z., and Chan, S. H. (2021). Carbon corrosion mechanism and mitigation strategies in a proton exchange membrane fuel cell (pemfc): A review. *J. Power Sources* 488, 229434. doi:10.1016/j.jpowsour.2020.229434
- Zhu, X., Zhang, H., Zhang, Y., Liang, Y., Wang, X., and Yi, B. (2006). An ultrathin self-humidifying membrane for pem fuel cell application: Fabrication, characterization, and experimental analysis. *J. Phys. Chem. B* 110, 14240–14248. doi:10.1021/jp061955s
- Zientara, M., Jakubczyk, D., Litniewski, M., and Holyst, R. (2013). Transport of mass at the nanoscale during evaporation of droplets: The hertz–knudsen equation at the nanoscale. *J. Phys. Chem. C* 117, 1146–1150. doi:10.1021/jp3091478

Nomenclature

A_{Pt}	Active Pt surface area/m ²
A_{geo}	ell geometric surface area/m ²
ASR	area-specific ohmic resistance/m ² S ⁻¹
a	active specific surface area/m ⁻¹
a_{lv}	liquid-vapor specific surface area/m ⁻¹
$C_{\text{O}_{\{2\}}}$	oxygen concentration/mol m ⁻³
$D_{\text{O}_{\{2\}}}$	oxygen diffusivity in air/m ² s ⁻¹
E_r	reversible cell voltage/V
$ECSA$	electrochemical surface area/m ² kg ⁻¹
F	Faraday's constant/C mol ⁻¹
f	normalized diffusivity/-
g	relative diffusivity/-
h	specific enthalpy/J mol ⁻¹
I	surface current density/A m ⁻²
I/C	ionomer-to-carbon weight ratio/-
$i_{o,c}$	exchange current density of oxygen reduction reaction/A m _{Pt} ⁻²
j	volumetric current density/A m ⁻³
K	permeability/m ²
k	thermal conductivity/W m ⁻¹ K ⁻¹
k_H	dimensionless Henry's constant/-
L	pillar spacing/m
L_{Pt}	Pt loading/kg _{Pt} m ⁻²
l_p	nanopore spacing/m
M_i	molecular mass of species i /kg mol ⁻¹
$N_{\text{O}_{\{2\}}}$	oxygen molar flux/mol m ⁻² s ⁻¹
N_p	number of nanopores per ionomer pillar/-
P	(geometric) power density/W m ⁻²
P_{Pt}	Pt-specific power density/W kg _{Pt} ⁻¹
p	pressure/Pa
\tilde{p}	normalized pressure/-
\dot{Q}	heat flux/W m ⁻²
R	radius/m
$R_{\text{O}_{\{2\}}}$	oxygen transport resistance/s m ⁻¹
R_{Pt}	radius of Pt nanoparticle/m
R	nanopore radius/m
R_v	secondary pore radius/m
R^o	universal gas constant/J mol ⁻¹ K ⁻¹
\tilde{R}_i	ionomer radius ratio/-
RH	relative humidity/-
r_f	roughness factor/-
s	water saturation/-

T	temperature/K
t	time/s
V_m	molar volume/m ³ mol ⁻¹
V_{cell}	cell voltage/V
v_c	characteristic velocity/m s ⁻¹
x	local coordinate through the nanoporous shell/m
y	through-plane coordinate across the CL thickness/m

Greek letters

α_c	transfer coefficient of oxygen reduction reaction/-
β	dimensionless net transport coefficient of water from anode to cathode/-
Γ	dimensionless ratio of transport resistances/-
γ	reaction order of oxygen reduction reaction/-
δ	thickness/m
ϵ	porosity or volume fraction/-
η_c	cathode overpotential/V
θ	contact angle/-
ν	kinematic viscosity/m ² s ⁻¹
Π	dimensionless factor related to the optimal design point/-
ρ	density/kg m ⁻³
σ	conductivity/S m ⁻¹ or surface tension/N m ⁻¹
τ	tortuosity factor/-
ϕ	potential/V
Ω	dimensionless ratio of characteristic times or penetration depths/-

Subscripts and superscripts

avg	average
c	cathode or capillary
ch	channel
chcl	channel-CL
cl	catalyst layer
c + Pt	electron-conductive material + Pt
d	diffusion
des	design
dry	dry conditions
e	electric
eff	effective
flat	flat surface
g	gas

geo geometric

i ionomer

in inlet

knud Knudsen

l liquid

max maximum

min minimum

mol molecular

obs obstruction

ohm ohmic

opt optimum

p primary nanopore or proton

pc phase change

pem polymer electrolyte membrane

prim primary

sat saturation

sh shell

v viscous

w water

wet wet conditions



OPEN ACCESS

EDITED BY

Wilfried G. J. H. M. Van Sark,
Utrecht University, Netherlands

REVIEWED BY

Miguel Centeno Brito,
University of Lisbon, Portugal
Imane Sebari,
School of Geomatics and Surveying
Engineering, Morocco

*CORRESPONDENCE

Mattia Manni,
✉ mattia.manni@ntnu.no

SPECIALTY SECTION

This article was submitted
to Solar Energy,
a section of the journal
Frontiers in Energy Research

RECEIVED 27 October 2022

ACCEPTED 05 December 2022

PUBLISHED 22 December 2022

CITATION

Manni M, Nocente A, Kong G, Skeie K,
Fan H and Lobaccaro G (2022), Solar
energy digitalization at high latitudes: A
model chain combining solar irradiation
models, a LiDAR scanner, and high-
detail 3D building model.
Front. Energy Res. 10:1082092.
doi: 10.3389/fenrg.2022.1082092

COPYRIGHT

© 2022 Manni, Nocente, Kong, Skeie,
Fan and Lobaccaro. This is an open-
access article distributed under the
terms of the [Creative Commons
Attribution License \(CC BY\)](https://creativecommons.org/licenses/by/4.0/). The use,
distribution or reproduction in other
forums is permitted, provided the
original author(s) and the copyright
owner(s) are credited and that the
original publication in this journal is
cited, in accordance with accepted
academic practice. No use, distribution
or reproduction is permitted which does
not comply with these terms.

Solar energy digitalization at high latitudes: A model chain combining solar irradiation models, a LiDAR scanner, and high-detail 3D building model

Mattia Manni^{1*}, Alessandro Nocente², Gefei Kong¹,
Kristian Skeie³, Hongchao Fan¹ and Gabriele Lobaccaro¹

¹Department of Civil and Environmental Engineer, Faculty of Engineering, Norwegian University of Science and Technology (NTNU), Trondheim, Norway, ²SINTEF AS, Trondheim, Norway, ³Department of Architecture and Technology, Faculty of Architecture, Norwegian University of Science and Technology (NTNU), Trondheim, Norway

Solar mapping can contribute to exploiting more efficiently the solar energy potential in cities. Solar maps and 3D solar cadasters consist of visualization tools for solar irradiation analysis on urban surfaces (i.e., orography, roofs, and façades). Recent advancements in solar decomposition and transposition modeling and Light Detection and Ranging (LiDAR) scanning enable high levels of detail in 3D solar cadasters, in which the façade domain is considered beside the roof. In this study, a model chain to estimate solar irradiation impinging on surfaces with different orientations at high latitudes is developed and validated against experimental data. The case study is the Zero Emission Building Laboratory in Trondheim (Norway). The main stages of the workflow concern (1) data acquisition, (2) geometry detection, (3) solar radiation modeling, (4) data quality check, and (5) experimental validation. Data are recorded from seven pyranometers installed on the façades (4), roof (2), and pergola (1) and used to validate the Radiance-based numerical model over the period between June 21st and September 21st. This study investigates to which extent high-resolution data sources for both solar radiation and geometry are suitable to estimate global tilted irradiation at high latitudes. In general, the Radiance-based model is found to overestimate solar irradiation. Nonetheless, the hourly solar irradiation modeled for the two pyranometers installed on the roof has been experimentally validated in accordance with ASHRAE Guideline 14. When monthly outcomes are considered for validation, the east and the south pyranometers are validated as well. The achieved results build the ground for the further development of the 3D solar cadaster of Trondheim.

KEYWORDS

solar mapping, 3D solar cadaster, global tilted irradiation, solar radiation model, LiDAR

1 Introduction

Solar mapping represents a commonly used visualization technique to support urban planners, authorities, and architects in addressing onsite energy generation while enhancing daylight and sunlight accessibility in buildings (Good et al., 2014; Lobaccaro et al., 2017). The solar potential of urban surfaces (i.e., orography, roofs, and façades) permits providing inputs to the predesign of solar installations in order to develop optimal exploitation of solar energy through generalized planning recommendations, guidelines, and best practices. The efficacy of these models varies considerably due to the following modeling strategy: the accuracy depends on the spatial information available and generated (e.g., satellite data and data from a Light Detection and Ranging (LiDAR) scanner) and the associated level of detail (LoD) of three-dimensional (3D) models (Behar et al., 2015). A popular modeling assumption is that building façades are vertical and that 3D building models can be extruded from 2D roof planes (i.e., 2.5D building models). Current developments in these research fields aim to create more precise information layers to estimate solar system integration not only on roofs (Brito et al., 2012; Desthieux et al., 2018), which are mostly devoid of building infrastructure (e.g., chimneys, elevator lift engines, technical installations, terraces, and balconies) that are common constraints for optimal solar system installation, but also on the non-negligible vertical surfaces (i.e., façades) (Carneiro et al., 2010). In fact, the total surface of the building's envelope is usually strongly reduced by the shading of architectural elements and obstructions and by the presence of glazed surfaces, which can only be partially replaced with PV systems. In Lobaccaro et al. (2019), a reduction factor, which is related to architectural and geometrical building features, is applied to account for transparent surfaces and obstructions, reducing the solar energy potential of roofs and façades. Although limited to the roof spatial domain, an advanced approach for detecting buildings' superstructures, which is based on deep learning for the semantic 3D city model, is proposed by Krapf et al. (2022). Estimating solar irradiation on façades including transparent surfaces and obstructions is therefore challenging, and it represents a significant limitation when it comes to high latitude locations where the façades are characterized by a solar potential similar to the roofs in the intermediate seasons (Manni et al., 2018).

In a reliable solar map, an accurate solar radiation model is coupled to a 3D urban geometry with a high LoD. Numerous solar radiation models have been implemented to enable assessing solar energy accessibility at multiple scales, ranging from building components to neighborhoods and cities (Peronato et al., 2018; Boccalatte et al., 2022; De Luca et al., 2022). The solar potential of buildings is analyzed by considering dynamic shadowing, solar inter-building reflections, and other related complex urban phenomena (e.g., high surface temperature and air flow) (Jakica, 2018; Manni et al., 2020).

Moreover, high-resolution solar data can be exploited to evaluate instantaneous events, e.g., cloud and albedo enhancement effects (Gueymard, 2017). Advanced solar radiation models allow to identify the most irradiated building surfaces for solar system installations or to evaluate the integration of solar systems in a heritage-constrained environment. Nonetheless, the application of such accurate numerical models to solar mapping at the city scale is still challenging due to the significant computational time.

Several studies have presented procedures to evaluate the solar energy potential in urban areas based on different techniques that have been developed in the last few decades together with the advancement of digital technologies and innovative approaches, methods, and tools. In Brito et al. (2012), the LiDAR technique was coupled to the Solar Analyst tool to estimate the photovoltaic (PV) potential of the Lisbon urban region. Thebault et al. (2022) proposed a multicriteria approach based on a geographic information system (GIS) to evaluate the suitability of a building to be equipped with PV systems. Similarly, a statistical model based on 2D-GIS and multiple linear regression has been developed by Nouvel et al. (2015) to predict heat demand and energy saving potential of building stock at several scales within the city of Rotterdam.

With the development of remote sensing technology and the increase of the available computational capacity, many new methods and technologies were proposed to enable the automatic collection of 3D information about buildings and other target objects (e.g., urban infrastructures and terrain morphology) (Bonczak and Kontokosta, 2019). Geometrical models characterized by a high LoD can be generated through an unmanned aerial vehicle (UAV) and terrestrial laser scanning (TLS) for data collection. The LiDAR technology integrates a laser scanner, the Global Positioning System (GPS), and inertial navigation systems (INS) to produce point clouds for buildings (Zhou and Gong, 2018; Yastikli and Cetin, 2021). The point clouds can provide high-resolution and accurate geometry information for the whole building, including windows, balconies, and other façade architectural elements. Laser scanning can bring 3D point clouds with very high density (with ca. < 1 cm point distance) that are usually post-processed to reduce noise and outliers applying probabilistic approaches such as the one proposed by Min and Meng (2019). The point clouds can significantly contribute to the reconstruction of high-LoD 3D models at multiple scales. Several studies investigate methods to build the 3D model from LiDAR's outputs, proposing reliable automatic or semi-automatic workflows, even if limited to LoD1 and LoD2 3D models (Sajadian and Arefi, 2014; Yastikli and Cetin, 2017; Jayaraj and Anandakumar, 2018). In fact, automatic reconstruction methods for models with LoD3 or LoD4, including windows and other façade semantic information, are still in the preliminary development phase (Wen et al., 2019; Cao and Scaioni, 2021).

2 Motivation and goals

Within this framework, the present study aims at investigating the application of advanced solar mapping techniques to high latitude locations. The research core concerns both 3D geometry construction workflows and approaches to solar radiation modeling, with a specific focus on input solar datasets. In fact, the study allows one to determine whether satellite-based solar irradiance data and the LiDAR scan technique are suitable to estimate the global tilted irradiation (GTI) for different orientations of solar sensors (i.e., pyranometers) at high latitudes. The results from the numerical model will be validated against measurement data from the Zero Emission Building (ZEB) Laboratory (Nocente et al., 2021) in Trondheim, Norway, presented in section 3.2.

The motivation of this work states the fact that solar maps that have been implemented for low latitudes (e.g., southern Europe and continental Europe) need to be further developed before being efficiently exploited at high latitudes. For instance, the proper spatial domain of solar maps which is usually limited to rooftop surfaces must be extended to façade surfaces as well. In that regard, the sun geometry in the Nordics (i.e., low sun elevation angles) is favorable for such vertical surfaces, which have higher solar potential than roofs (Manni et al., 2018). To model the solar energy potential of building façades in an articulated urban environment, it is necessary to accurately simulate inter-building optical interactions (i.e., mutual reflections and complex shading phenomena) by increasing the LoD of the 3D model and defining the optical properties of the materials applied to urban surfaces.

The novelty of the hereby presented study is grounded around the exploitation of a LoD3 3D model as a geometry base layer for solar irradiation mapping and the validation of the numerical model for multiple orientations at high latitudes. The vertical scanning of the building envelope enables a more precise construction of both the footprint and the façade's morphology. On the other hand, the extensive monitoring apparatus of solar irradiation that is installed in the ZEB Laboratory permits to perform an experimental validation of the numerical model for the main orientations of the building surfaces. A similar availability of observation data is not present in similar studies carried out for high latitude locations.

The present study is structured as follows: the Introduction (Section 1) outlines a theoretical framework for solar mapping techniques; the Motivation and goals section identifies the reasons for conducting such a study (Section 2); the Methodology section (Section 3) defines the research workflow, the tools for solar analysis and their settings, the information about the case study, the solar data sources, the quality check scheme, the geometry definition process, and the statistical indicators and validation criteria; the Results and Discussion section (Section 4) provides an overview of the capability of the numerical model to simulate the GTI for

various orientations, followed by the validation test and the limitations of the study. The article concludes by considering future developments and summarizing the most relevant findings and the implications for future advancements in the implementation of solar maps at high latitudes (Section 5).

3 Methodology

3.1 Workflow

The workflow (Figure 1) proposed and followed in this study is built around five main stages, which are 1) data acquisition, 2) geometry detection, 3) solar radiation modeling, 4) data quality check, and 5) experimental validation (Figure 1). The first stage (stage 1) concerns the acquisition of data about urban geometry, solar irradiation, and weather variables from different online databases, e.g., the Trondheim municipality's database, solar radiation service from the Copernicus Atmosphere Monitoring Service (CAMS), and climate.onebuilding.org database¹. The user-defined inputs of this stage are the case study's location and the time interval to investigate. The 3D model of Trondheim contains information about both buildings and terrain. Rhinoceros and Grasshopper tools are used, respectively, to edit the geometry model and select the spatial domain for the solar analysis. A circular area of radius 100 m with the center located in the ZEB Laboratory is selected. Regarding the solar irradiance and weather variables, a Python script is implemented to retrieve such data from the respective databases and combine them into a new EnergyPlus weather file (.epw). In particular, the new .epw file combines solar irradiation values, e.g., direct normal irradiation (DNI), diffuse horizontal irradiation (DHI), and Global Horizontal Irradiation (GHI), from CAMS solar radiation, with the weather variables, e.g., dew point temperature, relative humidity, and cloud cover, from the typical meteorological year (TMY) of Trondheim. The TMY of Trondheim is defined according to the measurements taken at the weather station in Voll (Trondheim) over the 2007–2021 period. The solar irradiation values from CAMS solar radiation are preferred to the values from the TMY since they are based on satellite observations performed during the specific time interval and for the exact location of the case study.

The geometry detection stage (stage 2) moves from the LiDAR scanning campaign of the ZEB Laboratory. Point cloud data are generated as output of the scanning activity, and it is regarded as the reference to detect and reconstruct the geometry of the building and its components (e.g., windows, doors, pergola, and the pattern of building-integrated PV (BIPV) panels). The 3D model is then re-meshed to provide more refined

¹ climate.onebuilding.org

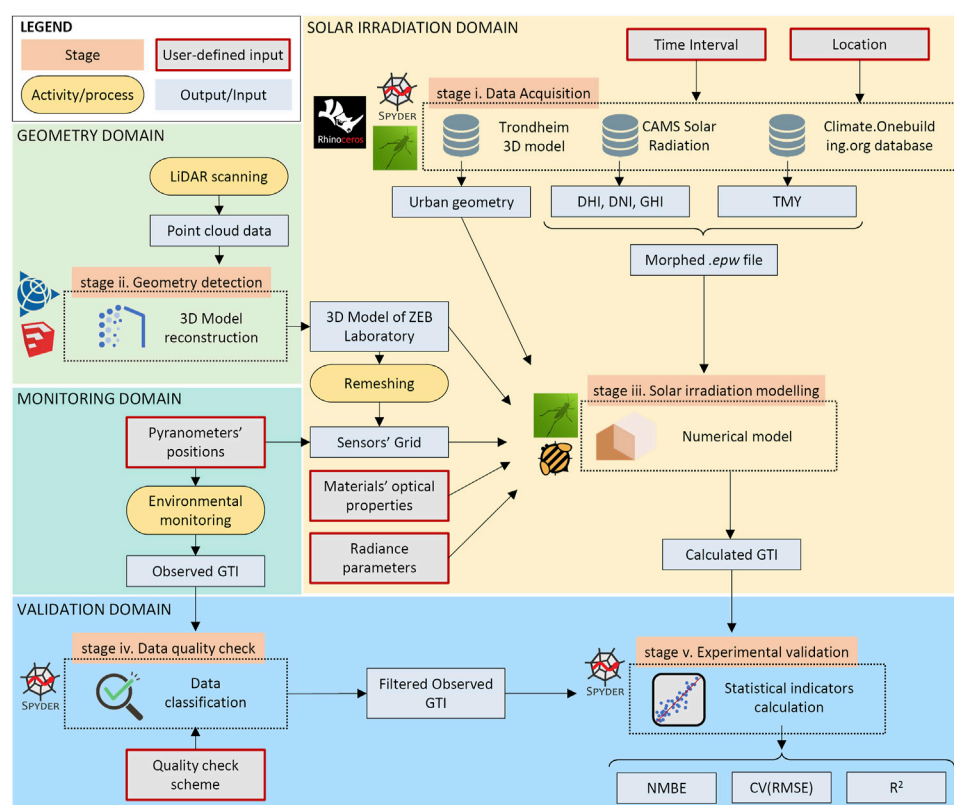


FIGURE 1

Overview of the workflow followed in this study. The main domains (e.g., solar irradiation domain, geometry domain, monitoring domain, and validation domain) are highlighted with different colors, while in the left corner, the four block typologies (e.g., stage, user-defined input, activity/process, and output/input) are reported.

bases for the simulation sensors' grid. Sensors' position is also determined according to the location of the pyranometers, whose measurements are used in the experimental validation of the numerical model.

The urban geometry, the 3D model of the ZEB Laboratory, the sensors' grid, and the morphed .epw file are among the inputs of the numerical model for solar analyses (stage 3). In addition to these, the optical properties of each surface and the Radiance parameters (e.g., ambient accuracy (aa), ambient bounces (ab), ambient division (ad), and ambient resolution (ar)) must be defined. The output from the solar irradiation modeling consists of a time series of simulated GTI values for each sensor (i.e., pyranometer).

In stage 4, the solar irradiation data from measurements in the ZEB Laboratory are classified according to the quality check scheme described in section 3.5. A quality flag is associated with each datapoint and then used to filter the observed GTI quantities to exclude the erroneous measurements from the validation process.

Finally, the simulated GTI was validated against observations (stage 5). The two datasets are visually compared in scatter plots;

one graph is created for each pyranometer. Moreover, three statistical indicators, namely, the normalized mean bias error (NMBE), the coefficient of variation of the root mean square error CV(RMSE), and the coefficient of determination (R^2), are calculated to evaluate the model's accuracy.

3.2 Case study

The ZEB Laboratory² is used as a case study for this research. Located in Trondheim, Norway (63.41 N, 10.4 E), the ZEB Laboratory is a four-story high office building (Nocente et al., 2021), designed and realized as a pilot building to facilitate the diffusion of innovative components, solutions, and energy strategies in the building industry. The load-bearing structure consists of glued laminated timber (gluelam) columns, cross-laminated timber (CLT) floors, some stiffening inner walls, and

² www.zeblab.no



FIGURE 2
ZEB Laboratory: southern and western façade (© Photo: M. Herzog).

traditional insulated wooden framework in the outer walls. The whole building is constructed according to the ZEB-COM ambition (Lobaccaro et al., 2018), which means that the local production of renewable energy must compensate, in terms of equivalent CO₂, the materials, the construction process, and the operation for 60 years, which is the programmed life of the building. To achieve this ambition, most of the building envelope is covered in BIPV, PV being the main source of renewable energy. A total of 701 mono-Si BIPV panels are installed for a rated power of 184 kW_p. According to simulations, the system can deliver over 150 MWh/y of renewable energy, partly used on the spot, while the rest is delivered to the grid.

The presence of such an extensive installation, together with the advanced monitoring and control system, allows the building to produce a high quantity of data, making the ZEB Laboratory a valuable source for studying BIPV operation in a Nordic climate and over a long period of time (i.e., the life of the PV installation). To have a reference for the outdoor weather and the available solar radiation, the laboratory is equipped with many outdoor sensors. A weather station is installed on the roof, continuously registering the main meteorological parameters. Another weather station is installed on the ground toward the south. The measurement of the available solar resources is performed by second-class pyranometers. One pyranometer registers the radiation on the horizontal plane, while five others evaluate the radiation on the planes of each façade and the roof. As shown in Figure 2, a pergola is mounted outside of the building, and it is entirely constituted by PV panels in a chessboard distribution of opaque and semi-transparent modules. Both surfaces of the pergola, the external and the internal ones, are equipped with pyranometers. The panels of the whole building (i.e., BIPV and the pergola's PV) are connected in strings, and the solar power production can be monitored and registered at any time.

3.3 Tools and settings

Solar analyses are performed within the Grasshopper environment. The Honeybee (HB) environmental plugin is exploited to connect Grasshopper to the Radiance-based engine, coupling the features of such a daylighting and solar simulation tool to the parametric modeling principles implemented in Grasshopper. The “HB annual irradiance” component enables computing broadband solar irradiance considering multiple and mutual inter-building reflections. Input parameters are the weather data, the geometry and optical properties of the model's surfaces, the grid of sensors, and the Radiance parameters. The weather data are retrieved for the Trondheim location (see section 3.4 for the weather input data).

When it comes to geometry modeling, the 3D model of the ZEB Laboratory is implemented starting from the data provided by the LiDAR scanner. The geometry configuration of the surrounding area is provided by the 3D model from the municipality of Trondheim³. All the materials applied to the urban surfaces are considered opaque and clustered into four groups; each group is characterized by a unique combination of reflection and specular coefficients. A reflection coefficient of 0.10 and a specular coefficient of 0.6 are associated with the BIPV and installed on the pergola (see section 3.2) and the glazed surfaces. The charred timber coating covering the other part of the building's façade is defined as completely diffusive, with a reflection coefficient of 0.25. The same reflection coefficient is defined for the building surrounding the ZEB Laboratory. Finally, the ground is fully diffusive, and it is characterized by a reflection coefficient of 0.10.

The grid of sensors is applied to the geometry moving from the triangular and quadrangular meshes composing the 3D model of the ZEB Laboratory. The centers and the normal vectors of the meshes are considered inputs for the locations and directions (i.e., orientations) of the sensors. The density of the resulting virtual sensors' point cloud is averagely equal to two points per square meter, but higher density values are observed in complex building areas (i.e., windows and frames). Once the solar analysis is performed, only the points of the grid that are near to the location of the pyranometers are considered for the validation.

Radiance parameters are determined according to the best practices identified in the literature to achieve a high quality of outcomes. An overview of the selected Radiance parameters is reported in Table 1.

The outputs are average and peak global irradiation and the cumulative radiation in the year. These data are processed with the “HB annual results to data” and “LB deconstruct data” components to extract hourly amounts of global irradiance, which will be later validated against experimental data.

³ www.trondheim.kommune.no

TABLE 1 Radiance parameters defined in this study.

ab	ad	as	c	dc	dp	dr	ds	dt	lr	lw	ss	st
6	25,000	4,096	1	0.75	512	3	0.05	0.15	8	4e-07	1.0	0.15

ab, number of ambient bounces; ad, number of ambient divisions; as, number of ambient super-samples; c, sampling; dc, direct certainty; dp, direct pretest density; dr, direct relays; ds, source substructuring; dt, direct thresholding; lr, limit reflection; lw, limit weight; ss, specular sampling; st, specular threshold.

3.4 Solar data sources

Weather datasets used in this work refer to Trondheim, Norway (lat. 63°25'49.76"N). The climate of Trondheim is classified as continental subarctic climate (Dfc) in the Köppen Geiger classification (Figure 3), and it is moderately continental, with cold winters and mild summers (Beck et al., 2018). The analyses are carried out for the period between June 21st and September 21st. The datasets are characterized by a time resolution of 1 hour. This period of the year was selected to validate the model's outputs in summer conditions, during days characterized by clear or overcast sky conditions.

The EnergyPlus weather file of Trondheim, created considering monitored values over the years between 2007 and 2021, was retrieved from the repository of free climate data for building performance simulation (climate.onebuilding.org). Then, the irradiation parameters (GHI, DNI, and DHI) are replaced with values retrieved from the CAMS. The CAMS solar radiation service combines output from the CAMS global forecast system on aerosol and ozone with detailed cloud information directly from geostationary satellites. The CAMS solar radiation service provides, among others, historical values (from 2004 to present) of GHI, DHI, and DNI (both overcast and clear sky conditions) with a time resolution of 1 min. Such irradiance parameters are retrieved for the time interval investigated in this study and resampled hourly.

The GTI is measured by sensors that are either integrated in the building envelope of the ZEB Laboratory or installed on a mast on the roof at a short distance from the surfaces and with accurately measured angles. Installed sensors are second-class pyranometers. The orientation is described in Figure 4 and Table 2. The tilt is reported in degrees from the horizontal surface. Quantities of GTI are recorded with 1-min time resolution and then resampled to calculate average hourly values.

3.5 Quality check scheme for monitored data

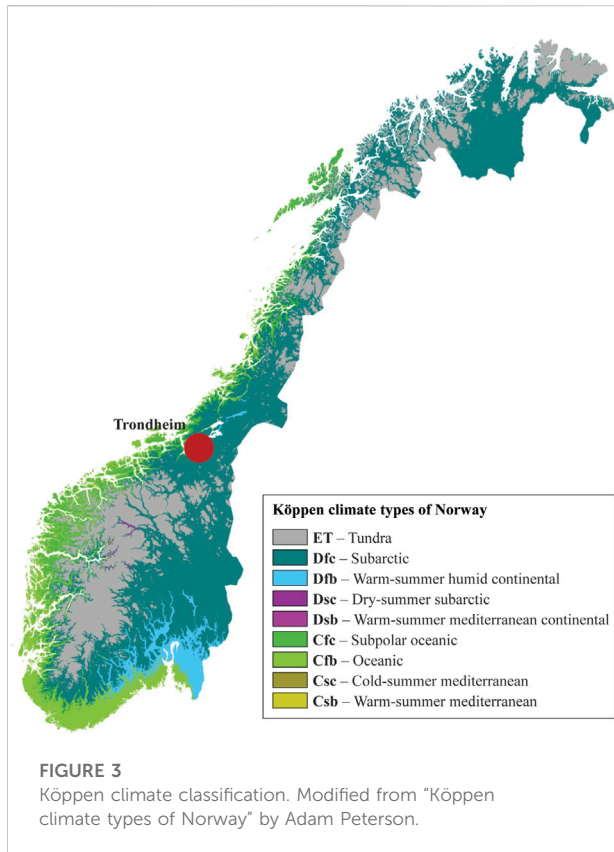
The outcomes from the numerical analyses are experimentally validated against quantities measured in the ZEB Laboratory. In order to ensure a good data quality, the quality control scheme described in Lorenz et al. (2022) is applied. Lorenz et al. (2022) implemented a quality control scheme for sensors with different orientations. Their measurement stations consist of a pyranometer for measuring

GHI and three silicon cells oriented east, south, and west with tilt angles of 25 for measuring GTI. Such a configuration is similar to the sensors' layout in the ZEB Laboratory, except that there are pyranometers instead of silicon cells and different orientations are considered (see Table 2). Therefore, only the quality checks for irradiation measurements are considered. Temperature monitoring can in fact be neglected when using pyranometers instead of silicon cells.

Different quality tests are performed for each variable in order to associate a quality flag (QF) to each measure. QFs are later used to filter erroneous measurements. The executed tests consist of the comparison to range limits and the evaluation of sensor consistency. The thresholds identified by Lorenz et al. (2022) are specifically adjusted for our location and sensors, that is, high latitude location and vertically mounted sensors.

A single QF is associated with each value measured; a high number corresponds to a low quality. QFs range between 0 (the test is passed) and 3 (the measurement is most likely erroneous). A value of 1 (QF = 1) indicates that the test cannot be performed, while a value of 2 (QF = 2) stands for a measurement that is likely to be erroneous. The range and consistency limits for all measurement variables are reported in Table 3.

For GHI upper limits, the upper envelope function proposed by Espinar et al. (2011) is applied to determine rare (QF = 2) and extreme (QF = 3) values. The function to define QF = 3 for GTI in the range limit test is adapted from the one proposed for GHI by using angle of incidence instead of solar zenith angle as an input parameter. In regards to consistency check, the GTI is compared to the modeled GTI (GTI_{mod}): monitored hourly values that differ from the modeled quantity by more than 200 W/m² are classified as QF = 3. The modeled GTI for each pyranometer is calculated from the measured GHI which is considered as input in the model chain described in the following lines. The Engerer2 model (Bright and Engerer, 2019) is applied to decompose the measured GHI into direct and diffuse fractions, and then, the Perez model (Perez et al., 1990) is exploited to transpose them according to the surface azimuth and tilt angle. The model chain applied in the consistency test differs from the one that is validated in this study (e.g., based on HB), although the output parameters are the same. Consistency quality flags for GHI values are determined by the QFs of GTI data. A detailed description of how the range and the consistency limits are determined can be found in Lorenz et al. (2022).



3.6 Geometry detection

Existing fully automatic methods for geometry detection cannot fit the requirements in terms of LoD that are necessary for the 3D model to be implemented in this study, e.g., the depth of windows, the layout of solar panels, material patterns, architecture element detection/recognition, and reconstruction. Hence, the high-LoD 3D model of the ZEB Laboratory is detected and reconstructed based on point cloud data, with the support of a vertical survey of façades conducted with LiDAR laser scanning techniques. The reconstruction of the high-LoD 3D building model and the further geometry detection need the support of accurate geometry information. To obtain the related geometry and geographic information, the high-density 3D scan data were collected by the Trimble SX10 3D scanning device on June 17, 2022. A total of six scan stations are set up to position the scanning device (Figure 5).

The set point spacing is 2–3 mm, while the average distance between the station points and the building is around 15 m. The multi-station scan data are registered by using Trimble Business Center (TBC) software to generate the 3D point cloud information describing the geometry configuration of the ZEB Laboratory. Following this, the point cloud data are converted into the high-LoD 3D model of the building case study in the SketchUp environment. At the same time, the geometry information

for façade elements, e.g., windows, doors, and photovoltaic panels, is also identified.

3.7 Measuring uncertainty and validation criteria

The American Society of Heating, Refrigerating and Air-Conditioning Engineers (ASHRAE) Guideline 14 is (ASHRAE, 2002) considered here as the reference source in the determination of the uncertainty associated with the numerical model (Ruiz and Bandera, 2017). The recommended uncertainty indices are the NMBE, the CV(RMSE), and R^2 .

The NMBE is expressed as a percentage and consists of a normalization of the mean bias error (MBE) index, which is, in turn, the average of the errors in a sample space. Normalizing the MBE enables comparing different outcomes. The general formula to calculate the NMBE is (Eq. 1).

$$NMBE = \frac{1}{\bar{o}} \frac{\sum_{i=1}^n (o_i - s_i)}{n-1} \cdot 100\%, \quad (1)$$

where \bar{o} is the mean of the observed values, o_i is the i th observed value, s_i is the i th simulated value, and n is the number of measured data points. Positive values mean that the numerical model tends to under-predict the measured parameter. On the contrary, negative values indicate an overestimation of the measured parameter. However, the NMBE is also subject to cancellation errors; consequently, the use of this index alone is not recommended.

The CV(RMSE) measures the variability of the errors between observed and simulated values, and it is determined according to (Eq. 2).

$$CV(RMSE) = \frac{1}{\bar{o}} \sqrt{\frac{\sum_{i=1}^n (o_i - s_i)^2}{n-1}} \cdot 100\% \quad (2)$$

It is not subject to cancellation errors; thus, the ASHRAE Guidelines couple it with the NMBE index to verify the models' accuracy.

The R^2 index provides information on how close the simulated values are to the regression line of the observed values. It ranges from 0 to 1, where the former indicates a complete mismatch between observed and simulated values and the latter means a perfect match between them. It is calculated as follows:

$$R^2 = \left(\frac{n \sum_{i=1}^n o_i s_i - \sum_{i=1}^n o_i \sum_{i=1}^n s_i}{\sqrt{(n \sum_{i=1}^n o_i^2 - (\sum_{i=1}^n o_i)^2) (n \sum_{i=1}^n s_i^2 - (\sum_{i=1}^n s_i)^2)}} \right)^2. \quad (3)$$

When it comes to the calibration of the numerical model, the criteria provided by the ASHRAE Guideline 14 are adopted (Table 4). The document presents different thresholds depending on the time resolution of the outcomes, ranging from hourly to monthly quantities. On the one hand, the NMBE index should be within

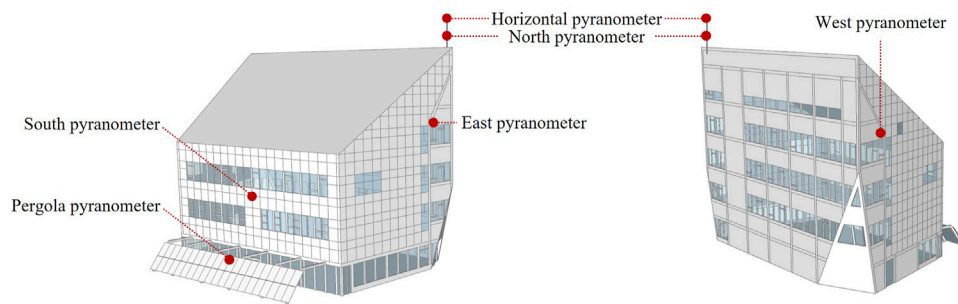


FIGURE 4
Location of the pyranometer in the ZEB Laboratory.

TABLE 2 Orientation of the pyranometers installed in the ZEB Laboratory.

	East	South	West	North	Roof	Pergola	Horizontal
Surface tilt	90	90	90	90	40	60	0
Surface azimuth	90	180	240	0	180	180	-

TABLE 3 Upper a) and lower limits b), acceptable max step amount c), and consistency check d) for the measurement of GHI and GTI (Lorenz et al., 2022).

	GHI	GTI
(a)	$QF_{range} = 2: 1.2 I_0 \cos(SZA) + 50 \text{ W/m}^2$	$QF_{range} = 3: 0.9 I_0 \cos(AOI)^{1.2} + 300 \text{ W/m}^2$
	$QF_{range} = 3: \min \left\{ \begin{array}{l} 1.2 I_0 \\ 1.5 I_0 \cos(SZA)^{1.2} + 100 \text{ W/m}^2 \end{array} \right.$	
(b)	$QF_{range} = 3: \begin{cases} 0.01 I_0 \cos(SZA) & \text{for } SZA < 75^\circ \\ 0 & \text{for } SZA > 75^\circ \end{cases}$	
(c)	1,000 W/m ²	
(d)	-	$QF_{range} = 3: GTI - GTI_{mod} > 200 \text{ W/m}^2$

the interval from -5% to 5% for monthly outcomes and within the interval from -10% to 10% for hourly outcomes. On the other hand, an upper limit of 15 is associated with the CV(RMSE) when monthly analyses are performed. This upper limit is doubled (up to 30) if hourly analyses are carried out. Finally, although the R^2 is not a prescriptive value for calibrated models, the ASHRAE Handbook recommends that the value be higher than 0.75 for calibrated models.

4 Results and discussion

4.1 Geometry detection

The output point cloud data of the ZEB Laboratory and the corresponding high-LoD 3D model are shown in Figure 6 and Figure 7. Data points collected by the scanner during the

campaign are later post-processed by filtering noise and elements from the background and surrounding environment. In total, around 18,600,000 data points are used to build the 3D model.

In general, the LoD3 is preferred to the lower levels (e.g., LoD1 and LoD2) because it allows including all architectural features on the façades (e.g., balconies, frames, doors, windows, and other façade details). In the case of the ZEB Laboratory, the PV pergola and other façades' elements (e.g., windows and frames) are modeled in high detail. Such elements influence the solar irradiation collected by the south pyranometer and the pyranometer installed on the pergola. In addition to this, the implementation of a LoD3 model in the ZEB Laboratory lays the groundwork for advanced solar energy analyses, where the details of architectural elements are relevant to have more accurate

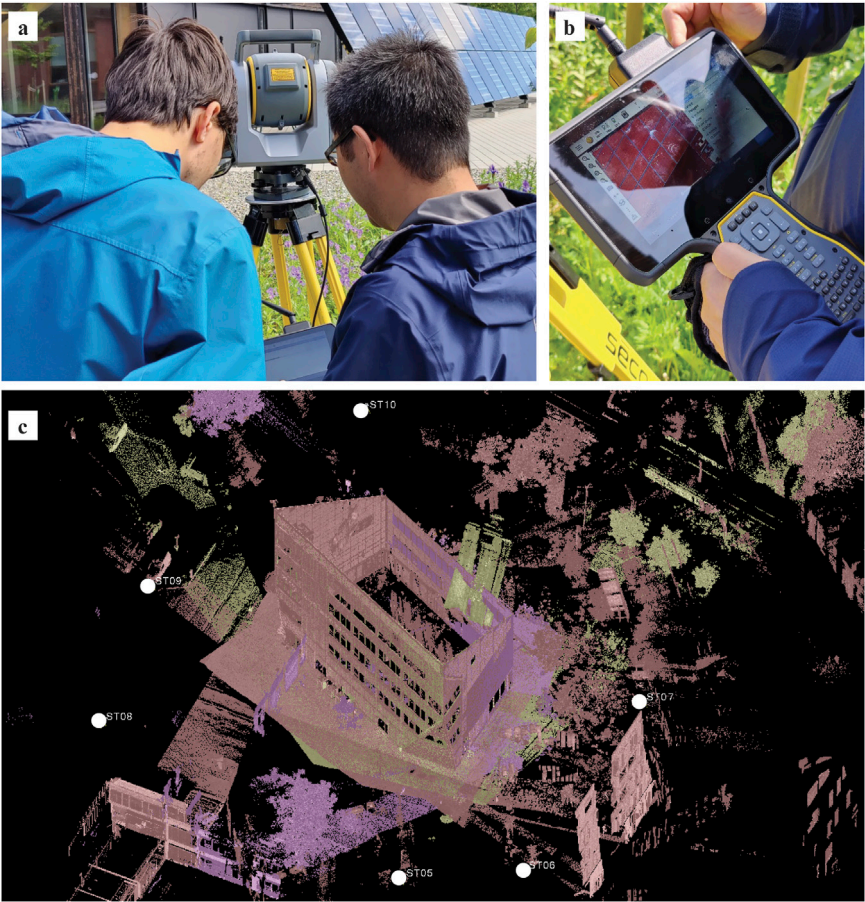


FIGURE 5
From the top: (A) scanning operations, (B) view of the point cloud during the scanning operations, and (C) positions of scanning stations around the ZEB Laboratory.

results and for the development of high-LoD solar cadaster. The latter can be coupled to other numerical models to perform energy analyses, visual and thermal comfort assessments, and PV energy simulations.

4.2 Solar analysis

The outcomes from solar analyses performed through the HB plugin and Radiance simulation engine are reported in this section. The solar irradiation impinging on the seven sensors extracted from the grid and representative of the seven pyranometers installed in the ZEB Laboratory is reported in Table 5 and Figure 8.

The three pyranometers facing south with different tilt angles together with the horizontal pyranometer are the most irradiated throughout the year. The pyranometers integrated in the roof, the pergola, and the south façade collect up to 934.57 kWh/m² per year, 836.70 kWh/m² per year, and 659.53 kWh/m² per year, respectively.

The solar irradiation impinging on the one horizontally mounted achieves 745.33 kWh/m² per year. Conversely, the pyranometer facing the north is the least irradiated (261.82 kWh/m² per year). Although the west façade is partially shaded by the nearby building, it is still reached and receives almost the same amount of irradiance

TABLE 4 Validation criteria provided by the ASHRAE Guideline 14.

Data type	Index	ASHRAE Guideline 14
Calibration criteria		
Monthly criteria	NMBE	±5%
	CV(RMSE)	15%
Hourly criteria	NMBE	±10%
	CV(RMSE)	30%
Model recommendation		
	R ²	>0.75

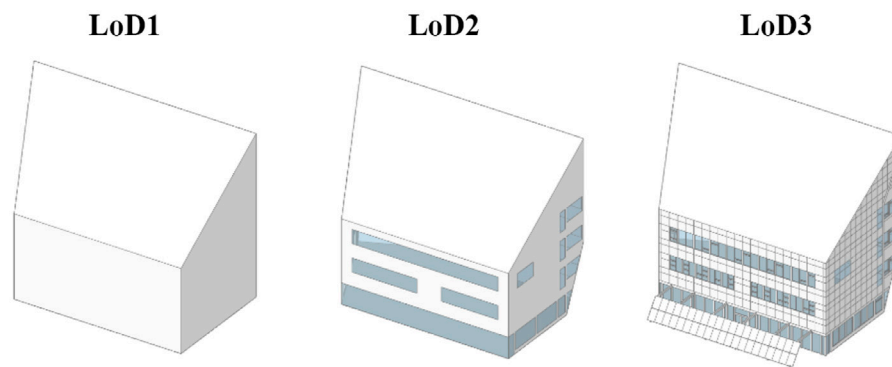


FIGURE 6

Different levels of detail associated with the 3D model of the ZEB Laboratory. The LoD3 is the one achieved in this study.

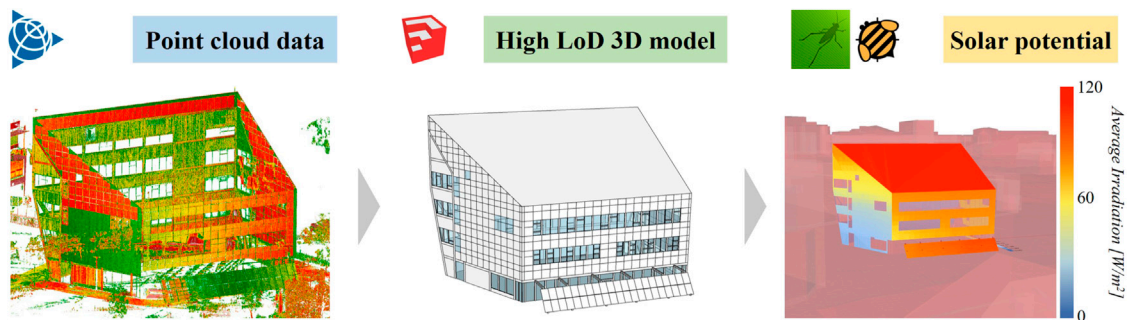


FIGURE 7

Changes in the geometry model from the point cloud data to the high-LoD 3D model of the ZEB Laboratory and to the solar potential analysis.

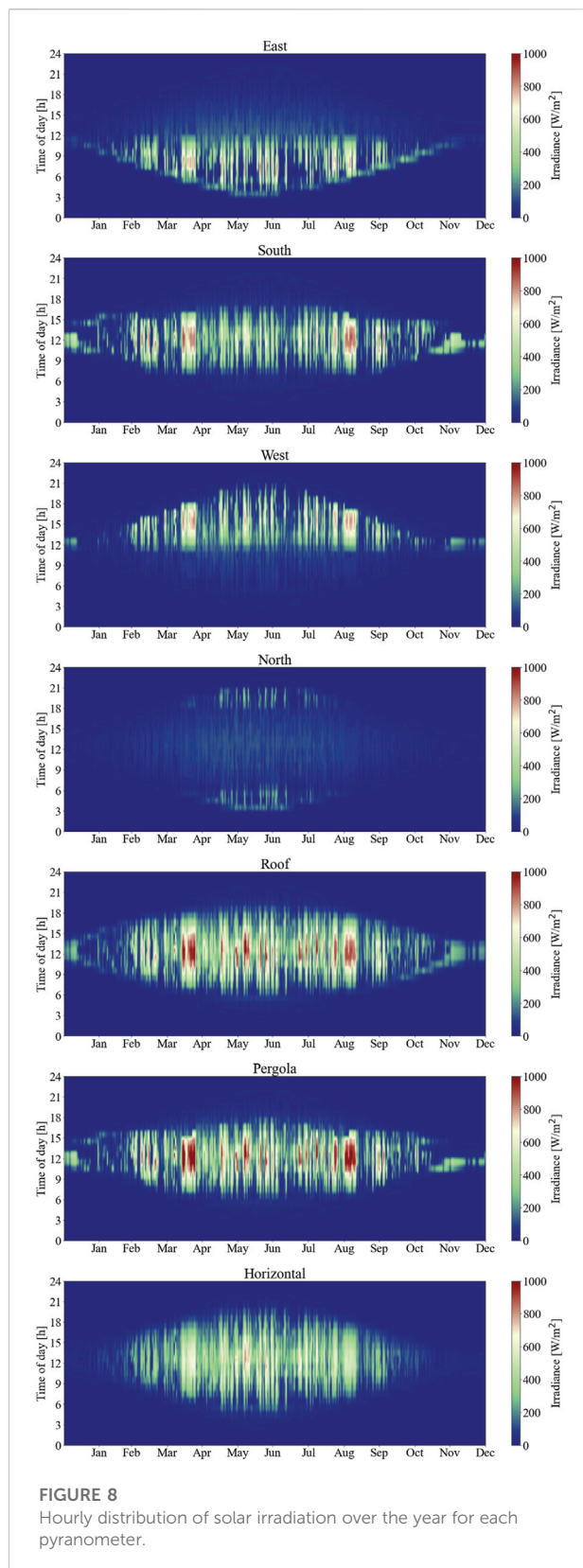
TABLE 5 Hourly mean and yearly global irradiation over the year for each pyranometer.

Pyranometer	Hourly mean global irradiation [W/m^2]	Yearly global irradiation [kW/m^2]
East	57.94	507.52
South	75.29	659.53
West	56.79	497.47
North	29.89	261.82
Roof	106.69	934.57
Pergola	95.52	836.70
Horizontal	85.08	745.33

as the east façade, which is mostly unobstructed (around 500 kWh/m^2 per year). This is mostly due to the fact that the west façade is not perfectly facing west, that is, the azimuth angle is 240° . The irradiation patterns of the west and east façades (Figure 8) highlight this aspect.

4.3 Data quality check

The quality check of the solar irradiation data recorded by the pyranometers integrated in the ZEB Laboratory between June 21st and September 21st is performed by assigning a quality flag



to each observation. An overview of these quality flags is presented in Figure 9. The visual inspection of the diagrams suggests that a low level of reliability ($QF = 3$) is mostly associated either with low solar irradiation amounts or with those values that have been measured during particularly overcast sky conditions.

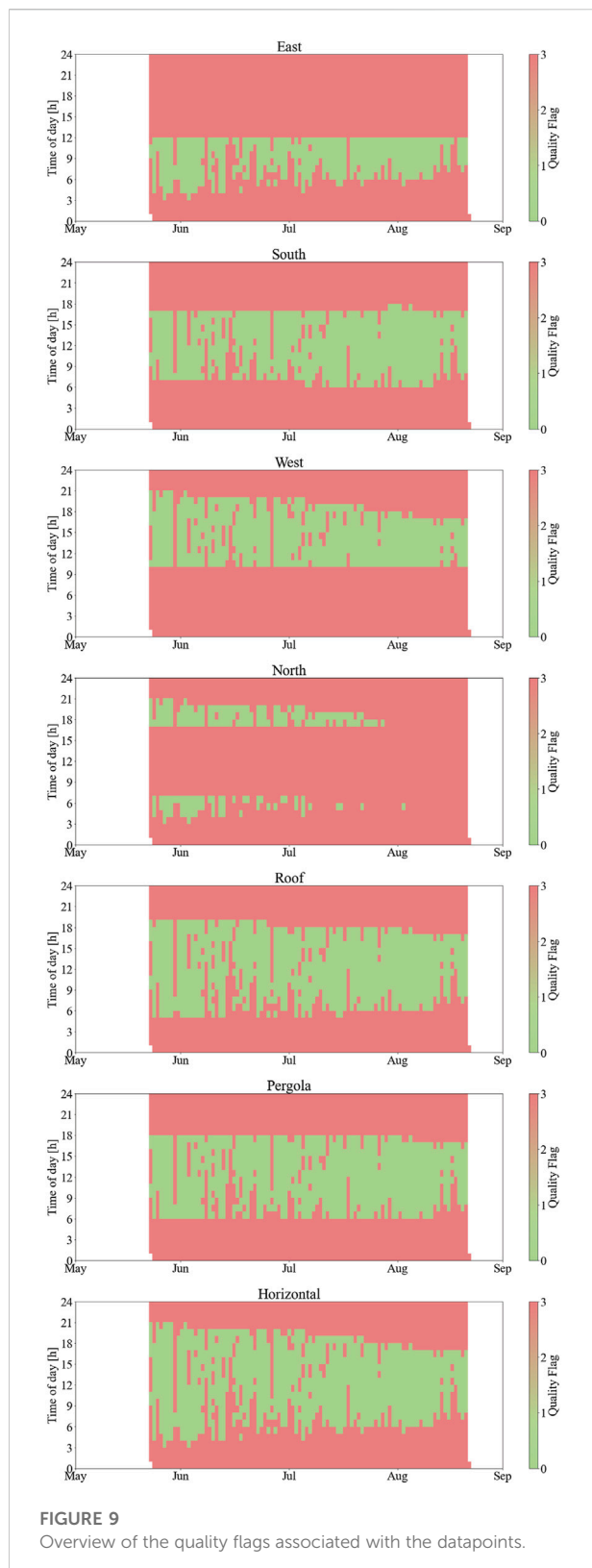
Following this, the datapoints that are suitable to be used in the validation process ($QF = 0$) are filtered out for each pyranometer. The applied quality check scheme allowed excluding more than 10,000 data points including, among the others, values measured during the night. The resulting datasets differ for the number of values; the dataset affected the most by this reduction is the one from the north-facing pyranometer, which is reduced to around one-tenth (from 2,208 to 212 data points). Among the others, the horizontally mounted pyranometer is the sensor collecting the most reliable data since it shows the highest amount of data with $QF = 0$ (1,018 data points). This is probably due to the fact that the sensor is exposed to direct sunlight for most of the time during the investigated period, and solar irradiation is usually measured with high accuracy by the pyranometer in this condition. A complete overview of the filtered data for each pyranometer is provided in Figure 9.

4.4 Experimental validation

The solar irradiation outcomes from the numerical model are reported against the experimental observations in the scatter plots in Figure 10. It is worth highlighting that only the values satisfying the requirements of the quality check scheme are included in these graphs. Hence, the length of the datasets changes depending on the considered pyranometer (Table 6).

The visual comparison of the observed and calculated values shows that the numerical model can calculate in a more accurate way the solar irradiation impinging on the horizontal pyranometer and on the roof surface compared to the others. However, the general tendency of the numerical model to overestimate the solar irradiation amounts is clear, as shown by the significant presence of data points above the red line.

The experimental validation is performed according to the ASHRAE Guideline 14 (section 3.7). The statistical indicators and their respective thresholds are considered on both an hourly and monthly basis. When it comes to the hourly solar irradiation amounts, the statistical indicators, e.g., NMBE, CV(RMSE), and R^2 , are estimated for the seven pyranometers (Table 7). The NMBE values are always lower than the threshold identified by the ASHRAE Guideline 14 (i.e., $NMBE < \pm 10\%$). The negative NMBE values indicate that the numerical model tends to



overestimate the solar irradiation quantities, confirming the deductions from the graphs' observations. The R^2 amounts always fit ASHRAE's requirements (i.e., $R^2 > 0.75$). However, it

TABLE 6 Datapoints after the application of the quality check scheme.

Pyranometer	Quality-checked datapoints
East	467
South	806
West	712
North	212
Roof	939
Pergola	888
Horizontal	1,018

is just a recommendation and not a calibration criterion. On the contrary, only the CV(RMSE) values calculated for the roof and horizontal pyranometers are acceptable (i.e., $CV(RMSE) < \pm 30\%$); therefore, these are the only hourly outcomes from the numerical model that can be validated.

The east, south, west, and pergola sensors showed CV(RMSE) values that are slightly above the upper limit (30%). In this regard, the exploitation of ground measurements of DNI and DHI as model input in place of the solar radiation data from satellite observation can enhance the result's accuracy. Finally, the sensor installed in the north façade is the one characterized by the lowest level of accuracy probably because it is the sensor that receives the least radiation, and the main irradiation contribution is usually from the diffuse fraction.

When the statistical indicators are calculated for data aggregated on a monthly basis, the simulated amounts for the east- and south-oriented pyranometers, in addition to the roof and horizontal pyranometers, are labeled as validated (Table 7). In fact, both the NMBE and the CV(RMSE) indicators of these two sensors are within the thresholds from the ASHRAE Guideline 14 (i.e., $NMBE < \pm 5\%$ and $CV(RMSE) < \pm 15\%$).

In this case, the sensor that is farthest to be validated is the one installed on the pergola. In fact, the pergola is located near the ground; therefore, it is the one mostly affected by human activities happening around the buildings, e.g., the presence of vehicles, and by the optical properties of the ground, e.g., changes in ground reflectivity due to weather conditions.

4.5 Limitations of the study

The main limitations of this study are presented and discussed in the following section. First, data on solar radiation from satellite observations may contain an incorrect estimation of direct and diffuse fractions and systematic errors within the evaluation of the GTI. Ground measurements of solar radiation are more reliable and can overcome this issue. However, satellite observations are available for every location

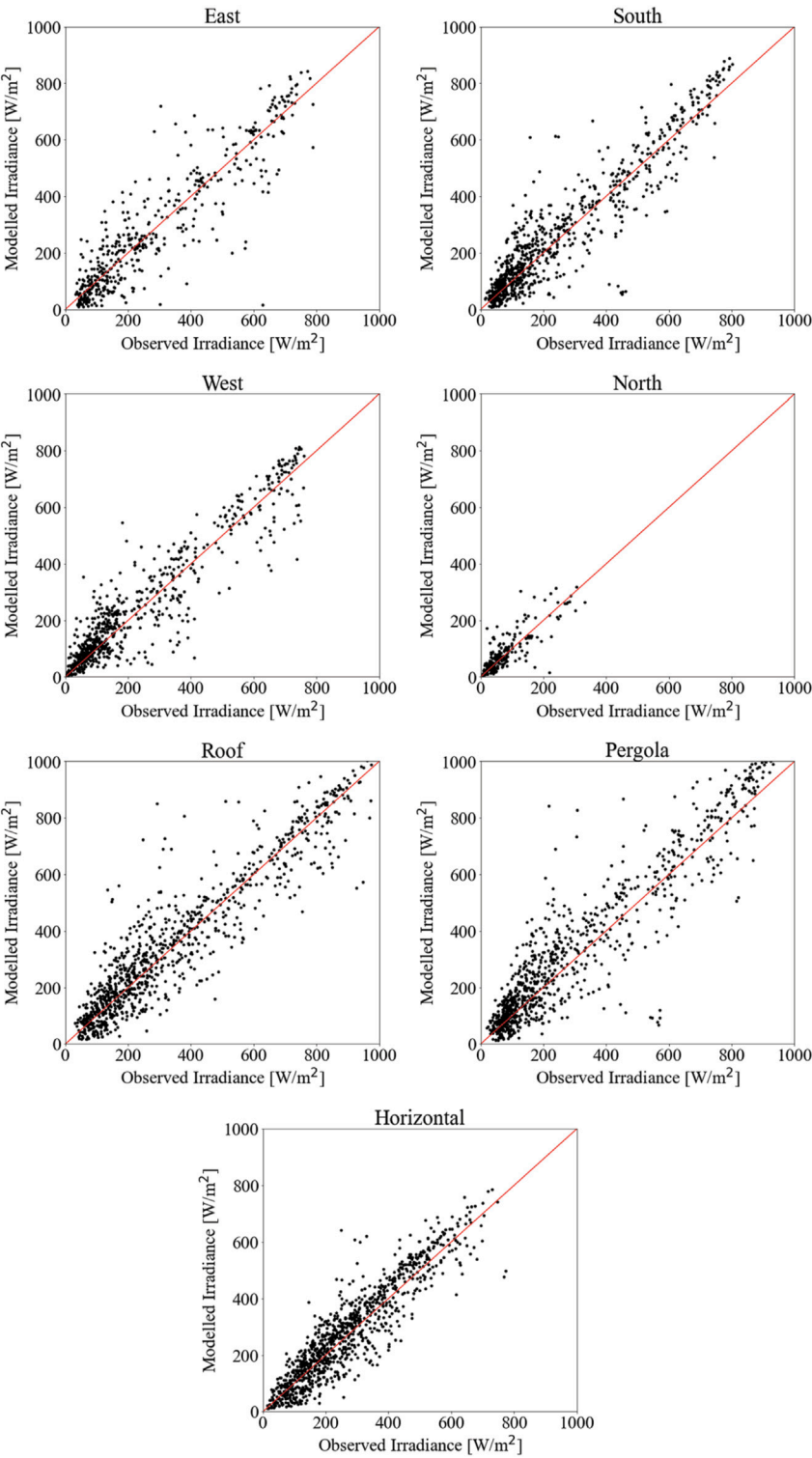


FIGURE 10
Scatter plots with solar irradiation outcomes from the numerical model against the experimental observations.

TABLE 7 Statistical indicators estimated for the observed and calculated hourly solar irradiation amounts for each pyranometer.

		East	South	West	North	Roof	Pergola	Horizontal
Hourly	NMBE [%]	−0.78	−5.73	−5.38	−7.95	−2.65	−9.42	−4.06
	CV(RMSE) [%]	33.14	33.35	34.09	51.68	27.98	34.89	25.76
	R^2 [0–1]	0.81	0.85	0.87	0.64	0.85	0.83	0.82
Monthly	NMBE [%]	0.13	−5.17	−5.20	−6.37	−1.81	−9.50	−4.14
	CV(RMSE) [%]	3.00	6.16	7.47	10.11	3.99	11.49	5.53
	R^2 [0–1]	0.98	0.89	0.88	0.96	0.93	0.59	0.81

within the spatial domain of CAMS solar radiation, providing up-to-date information. This aspect, together with the possibility of retrieving direct and diffuse solar irradiation data that are not calculated by decomposition models, makes CAMS solar radiation one of the most used and most accepted sources of solar radiation data inputs in solar mapping.

Concerning the 3D model, the optical properties of the materials applied to the urban surfaces are not experimentally determined but retrieved from the literature. This might lead to an incorrect assessment of mutual reflections between the building case study and either the surrounding buildings or the ground surface. Nonetheless, none of the sensors except the ones installed on the pergola and the one facing east have nearby surfaces that can reflect solar radiation toward them, that is, these sensors are installed far from the ground and other buildings.

Finally, the experimental validation is carried out only in summer conditions and for a limited time interval (i.e., 3 months). However, this is the period of the year when the solar irradiation is maximum at high latitudes; hence, it is the one determining the most the solar energy potential of a building. However, further validation studies are planned to be performed to validate the numerical model during intermediate seasons (i.e., spring and fall) when the solar energy potential of façades is significant at high latitudes.

5 Conclusion and future outlooks

A workflow integrating the geometry definition of high-LoD 3D models and the mapping of the solar irradiation is proposed for application at high latitudes. The 3D model of the building case study is reconstructed with the help of laser scanning techniques. The outcomes from the solar radiation model are experimentally validated against data collected from seven pyranometers installed in the ZEB Laboratory in Trondheim. A quality check scheme is applied to reduce the influence of potentially erroneous observations on the statistical indicators.

The findings of this study can be summarized in the following points:

- 1) The applied quality check scheme allowed excluding more than 10,000 data points that would have decreased the reliability of the experimental validation process.
- 2) The Radiance-based numerical model tends to overestimate the solar irradiation quantities for all the sensors compared to real measured data recorded with pyranometers.
- 3) The hourly solar irradiation outcomes of the roof and the horizontal pyranometers are experimentally validated in accordance with the ASHRAE Guideline 14.
- 4) The monthly solar irradiation outcomes of the east, the south, the roof, and the horizontal pyranometers are validated in accordance with the ASHRAE Guideline 14.

Such results represent a first and significant step toward the implementation of a solar cadaster in Trondheim that will help to enhance the predesign of solar systems and estimation of their solar potential and the social acceptability of solar energy and promote the involvement of stakeholders through the visualization of energy production data and accurate performance predictions. The solar irradiation collected by the façades, which is neglected in the existing 2D solar maps, is experimentally validated against data collected by vertically mounted pyranometers with multiple orientations. Including building façade in solar cadaster is challenging since it requires to accurately model inter-building effects (e.g., mutual shading and reflections). Also, high-detail 3D models like the one implemented in this study are necessary to trace the path covered by sunrays within the investigated spatial domain.

The future developments of this work will be focused on

- 1) Performing the experimental validation of the numerical model over a longer period, e.g., 1 year.
- 2) Experimentally validate the south, east, west, and north sensors and the one installed on the pergola by considering ground measurements of direct and diffuse irradiation and integrating decomposition and transposition modeling into the workflow.
- 3) Enhance the numerical model to perform 1-min solar analyses that enable simulating instantaneous phenomena, e.g., cloud enhancement events.

- 4) Implement the algorithm to fully automatically detect building geometry and materials applied to surfaces.

Data availability statement

Publicly available datasets were analyzed in this study. This data can be found here: ads.atmosphere.copernicus.eu (CAMS solar radiation service), climate.onebuilding.org (Climate. OneBuilding.Org).

Ethics statement

Written informed consent was obtained from the individual(s) for the publication of any potentially identifiable images or data included in this article.

Author contributions

All authors listed have made a substantial, direct, and intellectual contribution to the work and approved it for publication.

References

- Ashrae (2002). *Measurement of energy and demand savings*. Atlanta, Georgia: American Society of Heating, Ventilating and Air Conditioning Engineers.
- Beck, H. E., Zimmermann, N. E., McVicar, T. R., Vergopolan, N., Berg, A., and Wood, E. F. (2018). Present and future Köppen-Geiger climate classification maps at 1-km resolution. *Sci. Data* 5, 180214. doi:10.1038/sdata.2018.214
- Behar, O., Khellaf, A., and Mohammedi, K. (2015). Comparison of solar radiation models and their validation under Algerian climate – the case of direct irradiance. *Energy Convers. Manag.* 98, 236–251. doi:10.1016/j.enconman.2015.03.067
- Boccalatte, A., Thebault, M., Ménéz, C., Ramousse, J., and Fossa, M. (2022). Evaluating the impact of urban morphology on rooftop solar radiation: A new city-scale approach based on geneva GIS data. *Energy Build.* 260, 111919. doi:10.1016/j.enbuild.2022.111919
- Bonczak, B., and Kontokosta, C. E. (2019). Large-scale parameterization of 3D building morphology in complex urban landscapes using aerial LiDAR and city administrative data. *Comput. Environ. Urban Syst.* 73, 126–142. doi:10.1016/j.compenvurbsys.2018.09.004
- Bright, J. M., and Engerer, N. A. (2019). Engerer2: Global re-parameterisation, update, and validation of an irradiance separation model at different temporal resolutions. *J. Renew. Sustain. Energy* 11, 033701. doi:10.1063/1.5097014
- Brito, M. C., Gomes, N., Santos, T., and Tenedório, J. A. (2012). Photovoltaic potential in a Lisbon suburb using LiDAR data. *Sol. Energy* 86, 283–288. doi:10.1016/j.solener.2011.09.031
- Cao, Y., and Scaioni, M. (2021). 3DLEB-Net: Label-Efficient deep learning-based semantic segmentation of building point clouds at LoD3 level. *Appl. Sci.* 11, 8996. doi:10.3390/app11198996
- Carneiro, C., Morello, E., Desthieux, G., and Golay, F. (2010). VIS '10. World Scientific and Engineering Academy and Society (WSEAS), Stevens Point, 141–148. Urban environment quality indicators: Application to solar radiation and morphological analysis on built area, Proceedings of the 3rd WSEAS International Conference on Visualization, Imaging and Simulation, Wisconsin, USA.
- De Luca, F., Sepúlveda, A., and Varjas, T. (2022). Multi-performance optimization of static shading devices for glare, daylight, view and energy consideration. *Build. Environ.* 217, 109110. doi:10.1016/j.buildenv.2022.109110
- Desthieux, G., Carneiro, C., Camponovo, R., Ineichen, P., Morello, E., Boulmier, A., Abdennadher, N., Derve, S., and Ellert, C. (2018). Solar energy potential assessment on rooftops and facades in large built environments based on LiDAR data, image processing, and cloud computing. Methodological background, application, and validation in geneva (solar cadaster). *Front. Built Environ.* 4. doi:10.3389/fbuil.2018.00014
- Espinar, B., Wald, L., Blanc, P., Hoyer-Klick, C., Schroedter Homscheidt, M., and Wanderer, T. (2011). *Project ENDORSE - excerpt of the report on the harmonization and qualification of meteorological data: Procedures for quality check of meteorological data*. Paris, France, Europe: Mines ParisTech.
- Good, C. S., Lobaccaro, G., and Härklau, S. (2014). 58. Elsevier, 166–171. doi:10.1016/j.egypro.2014.10.424 Optimization of solar energy potential for buildings in urban areas - a Norwegian case study *Energy Procedia*
- Gueymard, C. A. (2017). Cloud and albedo enhancement impacts on solar irradiance using high-frequency measurements from thermopile and photodiode radiometers. Part 2: Performance of separation and transposition models for global tilted irradiance. *Sol. Energy* 153, 766–779. doi:10.1016/j.solener.2017.04.068
- Jakica, N. (2018). State-of-the-art review of solar design tools and methods for assessing daylighting and solar potential for building-integrated photovoltaics. *Renew. Sustain. Energy Rev.* 81, 1296–1328. doi:10.1016/j.rser.2017.05.080
- Jayaraj, P., and Anandakumar, R. (2018). 3D citygml building modelling from LIDAR point cloud data. *Int. Arch. Photogramm. Remote Sens. Spat. Inf. Sci.* 5, 175–180. doi:10.5194/isprs-archives-XLII-5-175-2018
- Krapf, S., Willenborg, B., Knoll, K., Bruhse, M., and Kolbe, T. H. (2022). Deep learning for semantic 3D city model extension: Modeling roof superstructures using aerial images for solar potential analysis. *ISPRS Ann. Photogramm. Remote Sens. Spat. Inf. Sci.* 4/W2-202, 161–168. doi:10.5194/isprs-annals-X-4-W2-2022-161-2022
- Lobaccaro, G., Carlucci, S., Croce, S., Paparella, R., and Finocchiaro, L. (2017). Boosting solar accessibility and potential of urban districts in the nordic climate: A case study in Trondheim. *Sol. Energy* 149, 347–369. doi:10.1016/j.solener.2017.04.015
- Lobaccaro, G., Lisowska, M. M., Saretta, E., Bonomo, P., and Frontini, F. (2019). A methodological analysis approach to assess solar energy potential at the neighborhood scale. *Energies* 12, 3554. doi:10.3390/en12183554

Funding

This research was supported by the Research Council of Norway through the research projects “Enhancing Optimal Exploitation of Solar Energy in Nordic Cities through the Digitalization of the Built Environment” (Helios, project no. 324243) and from NTNU Digital project (project no. 81771593).

Conflict of interest

The authors declare that the research was conducted in the absence of any commercial or financial relationships that could be construed as a potential conflict of interest.

Publisher's note

All claims expressed in this article are solely those of the authors and do not necessarily represent those of their affiliated organizations, or those of the publisher, the editors, and the reviewers. Any product that may be evaluated in this article, or claim that may be made by its manufacturer, is not guaranteed or endorsed by the publisher.

- Lobaccaro, G., Wiberg, A. H., Ceci, G., Manni, M., Lolli, N., and Berardi, U. (2018). Parametric design to minimize the embodied GHG emissions in a ZEB. *Energy Build.* 167, 106–123. doi:10.1016/j.enbuild.2018.02.025
- Lorenz, E., Guthke, P., Dittmann, A., Holland, N., Herzberg, W., Karalus, S., Müller, B., Braun, C., Heydenreich, W., and Saint-Drenan, Y. M. (2022). High resolution measurement network of global horizontal and tilted solar irradiance in southern Germany with a new quality control scheme. *Sol. Energy* 231, 593–606. doi:10.1016/J.SOLENER.2021.11.023
- Manni, M., Bonamente, E., Lobaccaro, G., Goia, F., Nicolini, A., Bozonnet, E., and Rossi, F. (2020). Development and validation of a Monte Carlo-based numerical model for solar analyses in urban canyon configurations. *Build. Environ.* 170, 106638. doi:10.1016/J.BUILDENV.2019.106638
- Manni, M., Lobaccaro, G., Goia, F., and Nicolini, A. (2018). An inverse approach to identify selective angular properties of retro-reflective materials for urban heat island mitigation. *Sol. Energy* 176, 194–210. doi:10.1016/J.SOLENER.2018.10.003
- Min, Z., and Meng, M. Q.-H., 2019. Robust generalized point set registration using inhomogeneous hybrid mixture models via expectation maximization, in Proceedings of the 2019 International Conference on Robotics and Automation (ICRA). 8733–8739. Montreal, QC, Canada, doi:10.1109/ICRA.2019.8794135
- Nocente, A., Time, B., Mathisen, H. M., Kvande, T., and Gustavsen, A. (2021). The ZEB laboratory: The development of a research tool for future climate adapted zero emission buildings. *J. Phys. Conf. Ser.* 2069, 012109. doi:10.1088/1742-6596/2069/1/012109
- Nouvel, R., Mastrucci, A., Leopold, U., Baume, O., Coors, V., and Eicker, U. (2015). Combining GIS-based statistical and engineering urban heat consumption models: Towards a new framework for multi-scale policy support. *Energy Build.* 107, 204–212. doi:10.1016/j.enbuild.2015.08.021
- Perez, R., Ineichen, P., Seals, R., Michalsky, J., and Stewart, R. (1990). Modeling daylight availability and irradiance components from direct and global irradiance. *Sol. Energy* 44, 271–289. doi:10.1016/0038-092X(90)90055-H
- Peronato, G., Rastogi, P., Rey, E., and Andersen, M. (2018). A toolkit for multi-scale mapping of the solar energy-generation potential of buildings in urban environments under uncertainty. *Sol. Energy* 173, 861–874. doi:10.1016/j.solener.2018.08.017
- Sajadian, M., and Arefi, H. (2014). A data driven method for building reconstruction from LiDAR point clouds. *Int. Arch. Photogramm. Remote Sens. Spat. Inf. Sci.* XL-2/W3, 225–230. doi:10.5194/isprsarchives-XL-2-W3-225-2014
- Thebault, M., Desthieux, G., Castello, R., and Berrah, L. (2022). Large-scale evaluation of the suitability of buildings for photovoltaic integration: Case study in Greater Geneva. *Appl. Energy* 316, 119127. doi:10.1016/j.apenergy.2022.119127
- Wen, X., Xie, H., Liu, H., and Yan, L. (2019). Accurate reconstruction of the LoD3 building model by integrating multi-source point clouds and oblique remote sensing imagery. *ISPRS Int. J. Geo-Information* 8, 135. doi:10.3390/ijgi8030135
- Yastikli, N., and Cetin, Z. (2017). Automatic 3D building model generations with airborne LiDAR data. *ISPRS Ann. Photogramm. Remote Sens. Spat. Inf. Sci.* IV-4/W4, 411–414. doi:10.5194/isprs-annals-IV-4-W4-411-2017
- Yastikli, N., and Cetin, Z. (2021). Classification of raw LiDAR point cloud using point-based methods with spatial features for 3D building reconstruction. *Arab. J. Geosci.* 14, 146. doi:10.1007/s12517-020-06377-5
- Zhou, Z., and Gong, J. (2018). Automated residential building detection from airborne LiDAR data with deep neural networks. *Adv. Eng. Inf.* 36, 229–241. doi:10.1016/J.AEI.2018.04.002
- Ruiz, G. R., and Bandera, C. F. (2017). Validation of calibrated energy models: Common errors. *Energies* 10, 1587. doi:10.3390/en10101587

Glossary

3D three dimensional

aa ambient accuracy

ab ambient bounces

ad ambient division

ar ambient resolution

ASHRAE American Society of Heating, Refrigerating and Air-Conditioning Engineers

BIPV building-integrated photovoltaic

CAMS Copernicus Atmosphere Monitoring Service

CLT cross laminated timber

CV(RMSE) coefficient of variation of the root mean square error

Dfc continental subarctic climate

DHI diffuse horizontal irradiation

DNI direct normal irradiation

GHI Global Horizontal Irradiation

GIS geographic information system

GPS Global Positioning System

GTI global tilted irradiation

HB Honeybee

INS inertial navigation system

LiDAR Light Detection and Ranging

LoD level of detail

MBE mean bias error

NMBE normalized mean bias error

PV photovoltaic

QF quality flag

R² coefficient of determination

TBC Trimble Business Center

TLS terrestrial laser scanning

TMY typical meteorological year

UAV unmanned aerial vehicle

ZEB zero emission building.



OPEN ACCESS

EDITED BY

Wilfried G. J. H. M. Van Sark,
Utrecht University, Netherlands

REVIEWED BY

Terry Chien-Jen Yang,
University of Cambridge, United Kingdom
Gabriele Lobaccaro,
Norwegian University of Science
and Technology, Norway

*CORRESPONDENCE

Mark Khenkin,
✉ mark.khenkin@helmholtz-berlin.de

SPECIALTY SECTION

This article was submitted
to Solar Energy,
a section of the journal
Frontiers in Energy Research

RECEIVED 07 December 2022

ACCEPTED 21 March 2023

PUBLISHED 03 April 2023

CITATION

Graniero P, Khenkin M, Köbler H,
Hartono NTP, Schlattmann R, Abate A,
Unger E, Jacobsson TJ and Ulbrich C
(2023), The challenge of studying
perovskite solar cells' stability with
machine learning.
Front. Energy Res. 11:1118654.
doi: 10.3389/fenrg.2023.1118654

COPYRIGHT

© 2023 Graniero, Khenkin, Köbler,
Hartono, Schlattmann, Abate, Unger,
Jacobsson and Ulbrich. This is an open-
access article distributed under the terms
of the [Creative Commons Attribution
License \(CC BY\)](#). The use, distribution or
reproduction in other forums is
permitted, provided the original author(s)
and the copyright owner(s) are credited
and that the original publication in this
journal is cited, in accordance with
accepted academic practice. No use,
distribution or reproduction is permitted
which does not comply with these terms.

The challenge of studying perovskite solar cells' stability with machine learning

Paolo Graniero^{1,2}, Mark Khenkin^{1*}, Hans Köbler³,
Noor Titan Putri Hartono³, Rutger Schlattmann¹, Antonio Abate³,
Eva Unger⁴, T. Jesper Jacobsson⁵ and Carolin Ulbrich¹

¹PVcomB, Helmholtz-Zentrum-Berlin, Berlin, Germany, ²Department of Business Informatics, Freie Universität Berlin, Berlin, Germany, ³Department Active Materials and Interfaces for Stable Perovskite Solar Cells, Helmholtz-Zentrum-Berlin, Berlin, Germany, ⁴Department of Solution-Processing of Hybrid Materials and Devices, Helmholtz-Zentrum-Berlin, Berlin, Germany, ⁵Institute of Photoelectronic Thin Film Devices and Technology, Key Laboratory of Photoelectronic Thin Film Devices and Technology of Tianjin, College of Electronic Information and Optical Engineering, Nankai University, Tianjin, China

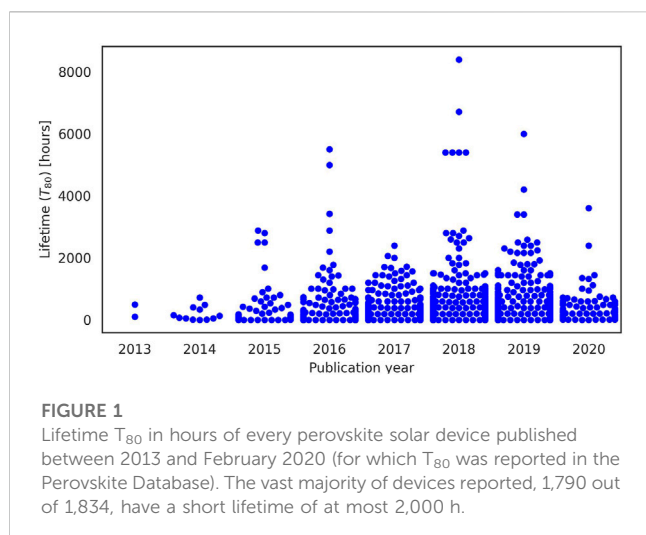
Perovskite solar cells are the most dynamic emerging photovoltaic technology and attracts the attention of thousands of researchers worldwide. Recently, many of them are targeting device stability issues—the key challenge for this technology—which has resulted in the accumulation of a significant amount of data. The best example is the “Perovskite Database Project,” which also includes stability-related metrics. From this database, we use data on 1,800 perovskite solar cells where device stability is reported and use Random Forest to identify and study the most important factors for cell stability. By applying the concept of learning curves, we find that the potential for improving the models' performance by adding more data of the same quality is limited. However, a significant improvement can be made by increasing data quality by reporting more complete information on the performed experiments. Furthermore, we study an in-house database with data on more than 1,000 solar cells, where the entire aging curve for each cell is available as opposed to stability metrics based on a single number. We show that the interpretation of aging experiments can strongly depend on the chosen stability metric, unnaturally favoring some cells over others. Therefore, choosing universal stability metrics is a critical question for future databases targeting this promising technology.

KEYWORDS

perovskite solar cell, stability, machine learning, figures of merit, learning curves, database, feature importance analysis, halide perovskite

1 Introduction

New photovoltaic technologies are urgently needed to accelerate the adoption of affordable renewable energy sources and combat climate change. Perovskite solar cells (PSCs) represent a prime candidate technology, which has become the most dynamic research area in photovoltaics. Researchers have obtained power conversion efficiency (PCE) values of over 25% in a single junction device (Green et al., 2022) and over 32.5% in tandems with silicon (“Best Research-Cell Efficiency Chart” n.d.) thanks to perovskite compositional engineering, deposition techniques optimization, and device architecture adjustments. Despite this highly competitive efficiency compared to silicon and the low manufacturing costs, there are still barriers to the commercialization of halide



perovskites. Operational stability is the most prominent and, therefore, the focus of the data analysis in this work.

Currently, the lifetime of perovskite solar devices remains well below the target value of 25–30 years (i.e., more than 200,000 h); **Figure 1** shows the average lifetime of perovskite solar devices published in scientific papers over the period 2013 to February 2020 (i.e., the period considered in the Perovskite Database project, see below), clearly showing the need to improve the operational stability of these devices. The factors that have contributed so far to improvements in PSCs stability from hours to months are, for example, perovskite compositional engineering (**Chi and Banerjee, 2021; Mazumdar, Zhao, and Zhang, 2021**), the introduction of passivation (**Chen et al., 2019**) and blocking (**Brinkmann, Gahlmann, and Riedl, 2020**) layers, optimization of transport (**Foo et al., 2017; Xinxing Yin et al., 2020; Dipta and Uddin, 2021**) and contact (**Nath et al., 2022**) layers, and device encapsulation (**Lu et al., 2021**).

With thousands of researchers worldwide dedicating their efforts to studying PSCs, an individual researcher has no chance of keeping track of all these results. Combining the device data produced during the experiments in shared databases offers significant benefits. The abundance of data allows the application of statistical techniques, most notably machine learning (ML), to empower data-driven research activities and for gaining new insights that would be otherwise impossible to obtain by analyzing data from individual studies only. Several authors have already pointed at ML as one important tool in overcoming challenges (**Myung et al., 2022**) in perovskite research, for example, screening of suitable candidate materials for photovoltaic applications (**Chen et al., 2022**), or to use data extracted from scientific publications to characterize the performance of PSCs (**Liu et al., 2022**). Thus far, few authors have attempted to use shared data to examine the stability of perovskite solar cells (**Beyza Yılmaz and Ramazan Yıldırım, 2021**). Even fewer authors used shared experimental data: **Tiihonen et al. (2018)** studied a set of 261 aging tests to assess the quality of published stability data, finding several issues in how the authors reported the results of their studies at the time; **Çağla Odabaşı and Ramazan Yıldırım (2020)** applied ML to a data

collection of 404 aging tests data to derive the effects of perovskite composition and transport layers on the PSCs stability, concluding that the analysis of data collected from the literature can be beneficial to better understand the overall state of the literature and for gaining insights about high stability devices.

Collecting the data from publications represents a tremendous effort which explains the lack of studies in this direction. Notably, the “Perovskite Database Project” was recently released (**Jacobsson et al., 2022**) (www.perovskitedatabase.com). This publicly open database contains manually extracted data from more than 15,000 publications with keywords “perovskite solar” from the Web of Science until February 2020. It holds information about more than 42,400 devices, 1,834 of which contain measured T_{80} (i.e., the time it takes for a device to lose 20% of its initial efficiency). The Perovskite Database is not only a much larger dataset than any other previously put together, but it also attempts to collect the most detailed information: the authors collected more than 400 parameters in the database, which include information about the cells’ design, the functional layers of the device stack, the details of device synthesis and key metrics about efficiency, stability, and outdoor performance.

Even though this dataset is the largest so far, the quality of stability-related data is a concern. Some aspects of particular relevance are the number of missing values due to incomplete reporting in the source publications, the low statistical relevance of data entries which report only the best-performing devices and an incomplete set of experimental results, and the need to stick to standardized guidelines for the aging conditions to improve comparability. This work is a first attempt at applying ML to the stability data in the Perovskite Database to identify relevant factors affecting device stability. However, the performance of the models turns out to be unsatisfactory. To understand if this low performance is due to the small database size or data quality issues introduced above, we perform computational experiments using the concept of learning curves. This tool allows us to extrapolate the performance of the ML models to more extensive databases that we expect will be available in the future. We want to show how data quality, specifically regarding the number of missing values, impacts the performance of ML models used to study perovskite stability. We further use the concept of learning curves to estimate how much the performance of an ML model would increase by collecting more data, as a function of data quality.

Importantly, even with a much larger dataset, there is another potentially critical issue with tabular data where a single number represents device stability. Aging experiments typically record the evolution of power conversion efficiency (PCE) or other device parameters under different stress conditions. Unlike PCE, a highly standardized figure of merit (FOM) of device performance, there is no generally accepted figure of device stability that would reduce the time series from aging experiments to a single number in a tabular database. T_{80} is one of the most common stability metrics, working sufficiently well for solar technologies that show uniform degradation curves. T_{80} is reported in the Perovskite Database and was used in this work as the target variable for ML modeling. To study the adequacy of this metric, we use an in-house dataset that includes complete time series from more than 1,000 aging experiments, which were recorded in a custom-built setup (**Köbler et al., 2022**) in the years 2019–2022. We show that

there are diverse aging behaviors resulting in a variety of time-series shapes. We computed different FOMs used in the PSCs literature (Khenkin et al., 2020; Almora et al., 2021) to all these curves, showing that they poorly correlate with each other, given the variety of degradation behaviors. This lack of correlation shows the urgent need to define a “fair” FOM for device stability. This fair FOM would then empower data-driven research activities on the stability of PSCs, providing a meaningful, universal, accurate, and precise stability measure. The definition of this fair FOM of stability and the production of more complete data regarding aging experiments can significantly accelerate the development of commercially viable perovskite solar devices through ML methods.

2 Data and methods

2.1 Data

We used two large datasets in the analyses presented in this work. The first one is the Perovskite Database, based on the data extracted from the literature. It contains information on a wide variety of device architectures and aging conditions. The other dataset originates from in-house aging experiments and contains fewer details but provides full aging curves. The latter is only used to discuss the issue of selecting a FOM to characterize device stability.

2.1.1 The Perovskite Database

The Perovskite Database Project contains data manually collected from more than 15,000 papers about perovskite solar cells. The manual scraping of the publications resulted in collecting information about more than 42,400 perovskite solar devices.

The data categories, or features, contained in the Perovskite Database include reference data about the source publication, properties of the cell (e.g., area, architecture), data for every functional layer in the device stack, about the synthesis of the cell, and key metrics (e.g., stability, JV metrics, outdoor performance). The database's total number of features (i.e., the number of columns) is 409.

This dataset represents the most extensive collection of published experimental data about perovskite solar devices. Out of more than 42,400 devices reported in the database, only 1,834 include measured T_{80} values. In principle, we could use the PCE at the end of the stability experiments and the length of such experiments to extrapolate the value of T_{80} for instances in which it has not been reported. We refrain from doing this because, as we show in this work using the in-house dataset, the wide variety of aging behaviors would make such extrapolation highly uncertain.

Note that, in this study, we selected a subset of 67 out of the 409 features in the database based on expert knowledge about the factors most likely to affect the stability of the devices.

2.1.2 In-house dataset

The in-house dataset (collected in the Department “Active Materials and Interfaces for Stable Perovskite Solar Cells” at Helmholtz-Zentrum Berlin) contains time-series data of aging experiments performed on over 1,000 perovskite solar cells of

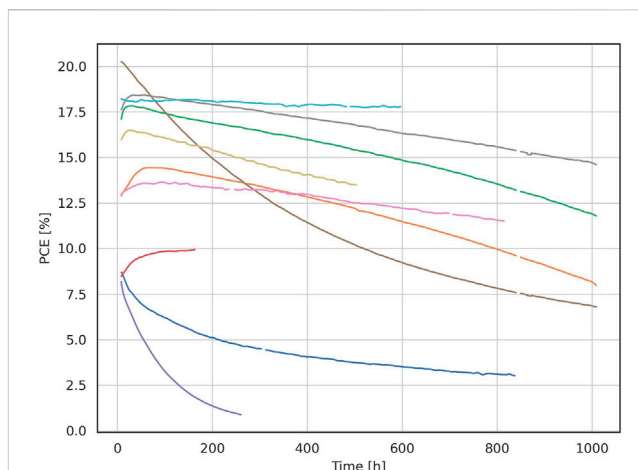


FIGURE 2

Example of time series data from the in-house aging experiments dataset. Each curve represents the aging of a different PSC (PCE evolution over time), showing the variety of behaviors in the aging of PSCs.

various types in the years 2019–2022. This dataset is the largest of this type used in a publication. Cells were aged in a custom-built high-throughput aging system (Köbler et al., 2022) under continuous illumination of a metal-halide lamp. Special electronics are employed to MPP-track every solar cell individually. Experiments are performed under nitrogen atmosphere at room temperature or at elevated temperatures according to ISOS-L1I or ISOS-L2I (Khenkin et al., 2020). The time exposure of experiments ranges between 150 and 2,060 h. The exact experimental conditions are less relevant to our goals since we want to compare how different FOMs for stability correlate with each other for the same curve when computed automatically. Figure 2 shows an example of aging curves.

2.2 Methods

In the following subsections, we briefly describe how we prepared the data for analysis and the methods and concepts used to perform the analysis. More detailed information could be found in the [Supplementary Material](#). The overall structure of the experiments is depicted schematically in [Figure 3](#).

Since the data in the Perovskite Database Project was collected by manually extracting information from scientific publications and manually writing the information to the database, some errors can be present. For example, there might be spelling errors in the names of chemical compounds and manufacturing techniques, or numerical values might be incorrect. We have not attempted to identify potential input errors in the numerical values of the features (i.e., we did not perform outlier detection or additional checks for numerical features), but we attempted to correct spelling and text formatting errors.

We have prepared the data in the Perovskite Database encoding every column of the dataset in numerical format, splitting columns that contained multiple simple features (e.g., device stack containing several layers), converting categorical values into dummy binary

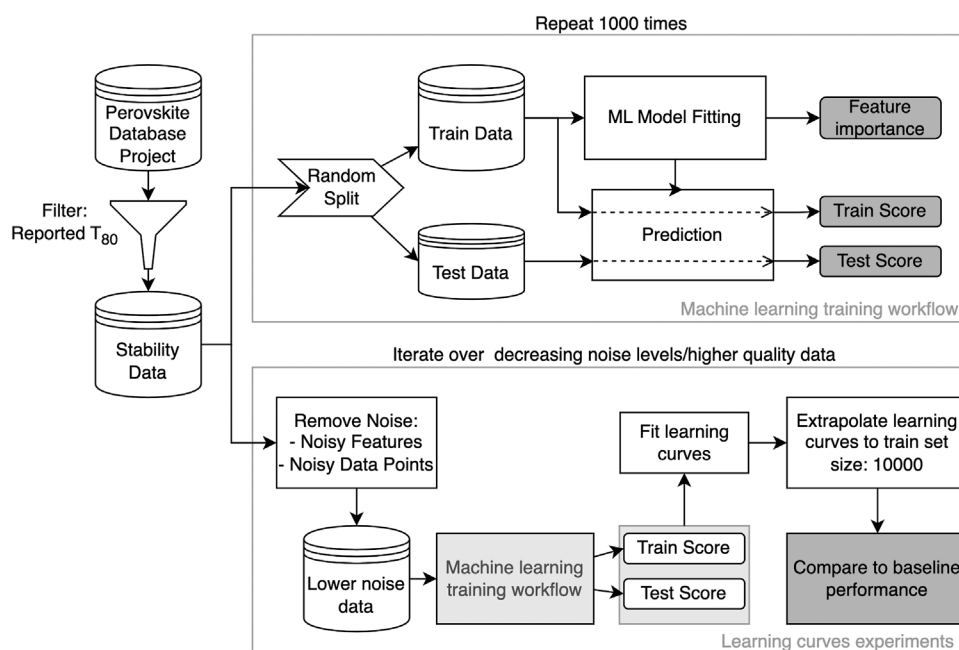


FIGURE 3
Schematic representation of the experiments performed.

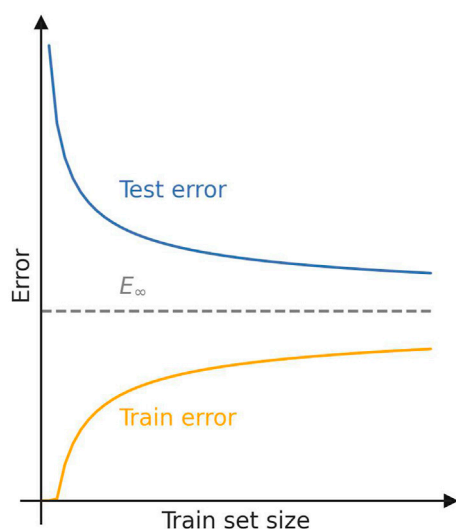


FIGURE 4
Schematic of the general behavior of learning curves for a given ML model.

variables, and flagging missing values (NaNs) into additional columns.

2.2.1 Feature importance through machine learning modeling

Machine learning can be used with different goals in mind based on what knowledge we try to extract from the data: patterns,

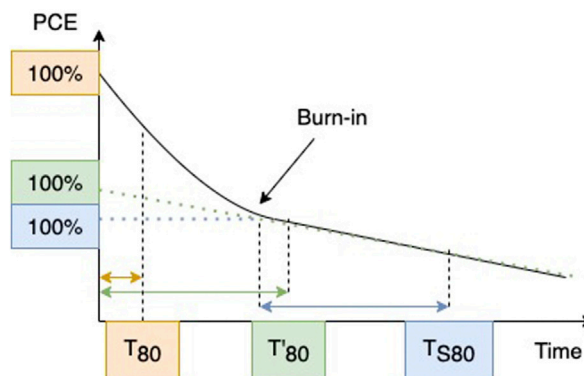
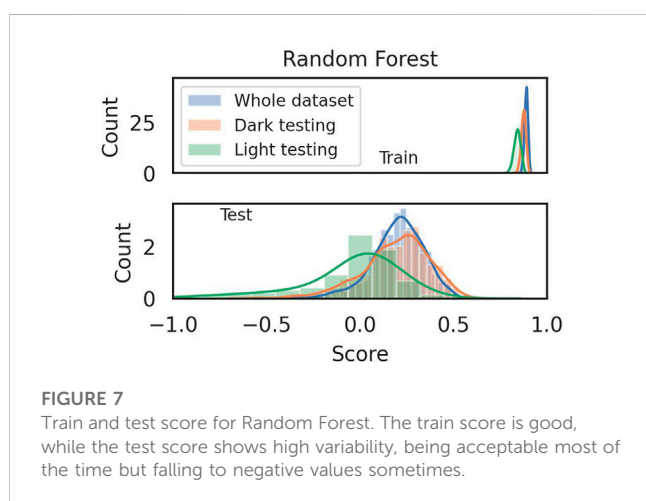
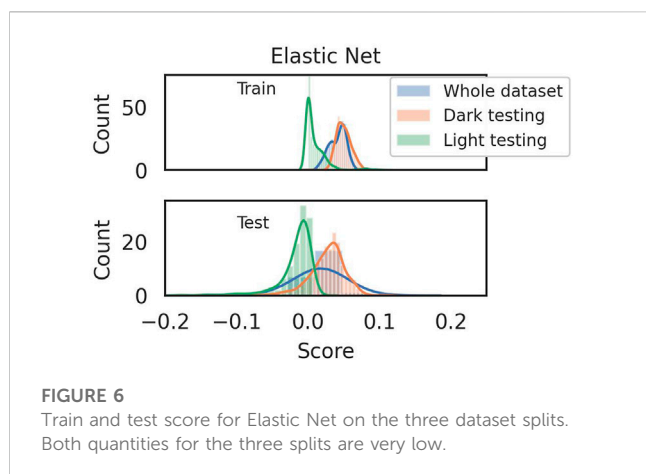


FIGURE 5
Three different definitions of T_{80} for an aging time series. The reported T_{80} varies depending on the chosen definition. Adapted from (Khenkin et al., 2020).

explanations, and predictors. Studies like (Odabasi and Yildirim, 2020) for PSC and (David et al., 2020) for organic PV try to find explanations, that is, explain how a given variable, like lifetime, is affected by properties of the devices. In the ML literature, the properties are generally referred to as features. Feature importance analysis refers to identifying a group of features with a significant impact on the target variable, in our case, T_{80} .

There are different ways to study feature importance. In this work, we use the embedded method: we fit an ML model to the dataset and use measures of feature importance embedded in the



model to study which factors affect stability the most. We explored several models (see [Supplementary Material](#) and [Supplementary Figure S3](#)) and selected two of them: Elastic Net (eNet), which is a linear model, and Random Forest (RF), which is a non-linear model. These represent the two broadest classes of ML models we can consider: they assume a linear or a non-linear relationship between the input features and the target variable, respectively.

Feature importance in eNet can be derived from the coefficients of the fitted model: the larger the magnitude of the coefficient of a feature, the higher the importance of that feature. For RF, a feature importance measure can be obtained during the training process by looking at the decrease in impurity in the trees that form the forest. Details about this can be found in ([James et al., 2013](#)).

When performing a feature importance analysis, it is necessary to consider how well the model can capture the patterns in the data, i.e., the goodness of fit. This is done by analyzing the model's coefficient of determination, also called R^2 -score. The closer this coefficient is to 1, the better the goodness of fit of the model (the [Supplementary Material](#) contains the mathematical definition of the coefficient of determination).

Repeating the computation of the R^2 score and feature importance value for multiple possible realizations of train and test set returns probability distributions instead of single values. We perform 1,000 draws of the train and test sets, keeping 75% of the

data in the train set. We have considered both the whole dataset and two relevant subsets of the data: aging in the dark most of the time results in much longer lifetimes compared to photo-stability experiments; we, therefore, split the dataset into “Dark testing” and “Light testing” (refer to aging tests in the dark and under illumination). We also removed features related to the performance of the PSCs, like the initial PCE. While there is a statistical correlation between device efficiency and stability, it might reflect, for example, that simultaneous progress was made in these two critical aspects of the technology. In this work, we focused on the analysis of the impact of the device structure and parameters of ageing experiments.

2.2.2 Learning curves

Fundamental quantities in ML analysis are train and test errors. The train error measures the discrepancy between the values estimated by the ML model and the actual values of the target variable for the data in the train set, while the test error measures the same type of discrepancy but for the data in the test dataset. Since the train set is used to optimize the parameters of the models while the test set contains unseen data, the test error gives a reasonable estimation of the actual performance of the ML model. Additional details can be found in the [Supplementary Material](#).

Following the definition in ([Cortes et al., 1993](#)), by learning curves, we mean the expected values of the test and training error as a function of the size of the training set; the expected value is taken over all the possible ways of choosing a training set of a given size.

[Figure 4](#) schematically shows typical learning curves for a given model on a given dataset. If the model is sufficiently flexible (i.e., can learn a large number of functions) and the train set is relatively small, the training error will be very low, even zero: the model can perfectly fit the train set. In this case, the test error will be very high since it is highly likely that the model perfectly fitting the train set has learned not to model the data-generating process but the random noise present in the train set. As the size of the train set increases, the training error grows: the model learns more about the data-generating process from the available data, while the random noise is disregarded; at the same time, the test error decreases since the model becomes better at modeling the data and not the noise. In the limit of infinite train set size, training and test error converge to a common value E_{∞} , called limiting performance.

From theoretical arguments ([Seung, Sompolinsky, and Tishby, 1992](#)), the learning curves can be modeled as power-law decays to the asymptotic error E_{∞} . We can extract the parameters of these power laws and use them to extrapolate the values of train and test errors for larger train set sizes.

We use learning curves to estimate the performance of our ML model in the hypothetical case in which a larger train set size becomes available. The learning curves (and the limiting performance) depend on the quality of the data. To simulate different data quality levels, we perform the learning curves experiments in three different settings:

- using the complete dataset in its original form;
- removing noisy features from the dataset;
- removing noisy data points from the dataset.

We start removing features or data points with the most missing values, therefore containing more noise, and iteratively less noisy

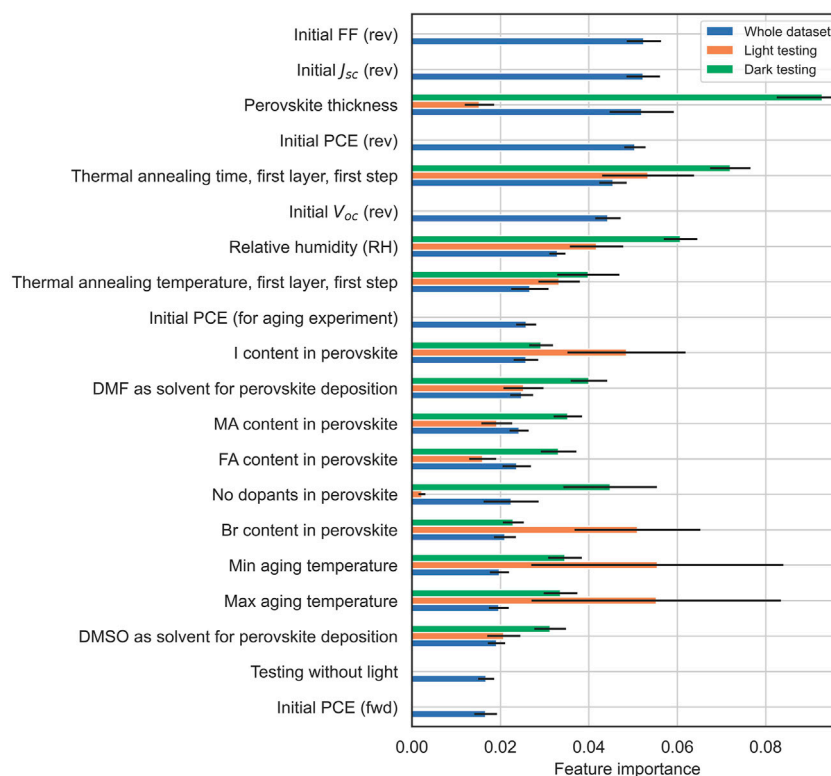


FIGURE 8

Feature importance for the Random Forest model. The different colors identify the possible dataset splits. We show the 20 most important features when modeling the complete dataset.

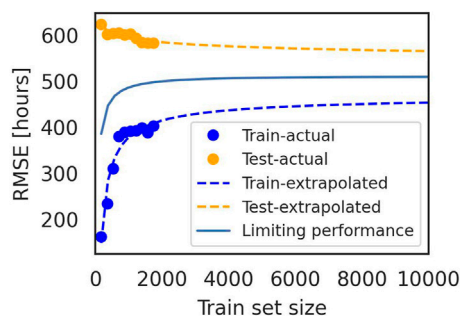


FIGURE 9

Learning curves as derived for the complete dataset. Extrapolation to size 10,000 of the train set.

ones, one at a time for the features, or allowing only a certain amount of missing values per data point in the third setting.

We perform the learning curves experiments for the complete dataset and data quality levels. We compute the learning curves for every dataset at ten different, increasing values of the training set size. To obtain the interpolation points, we average the results of a 20-fold cross-validation (sampling each train set 20 times) for each train set size. We then extract the parameters of the underlying power law function and extrapolate up to a train set size of 10,000 data points. The last step compares the estimated error

values on such a hypothetical dataset with the extrapolated value obtained using the complete dataset.

In all learning curves experiments, we use Gradient Boosting as model, which performs similarly to Random Forest in modeling the dataset but has resulted in more stability during the training process; that is, the power law approximation is more accurate.

2.2.3 Figures of merit for stability

Figures of merit for perovskite stability are numerical values used to quantify the stability of the perovskite solar cells. Several different FOMs exist in the field. The most commonly used is T_{80} , which represents the time it takes for the cell to lose 20% of its initial PCE. T_{80} has been successfully used with silicon-based photovoltaic technology since the aging behavior of such devices is relatively simple (in many cases, close to linear), and the aging behavior is well captured by T_{80} . This is not necessarily the case for emerging PV technologies. For example, for organic photovoltaics typical shape has a fast initial decay (“burn-in”) followed by a linear decrease in efficiency, and an adapted metric called “stabilized T_{80} ” is more common (Roesch et al., 2015).

In contrast, PSCs show a variety of aging behaviors. This variety is reflected in the lack of a universally accepted FOM for their stability. For example, T_{80} alone has at least three different definitions based on the type of aging behavior and authors’ preferences (Khenkin et al., 2020), as illustrated in Figure 5.

Since all the FOMs are used to quantify the same concept, e.g., stability, ideally, we want all of them to, at least qualitatively, agree: if a given device is more stable than another according to one FOM, it

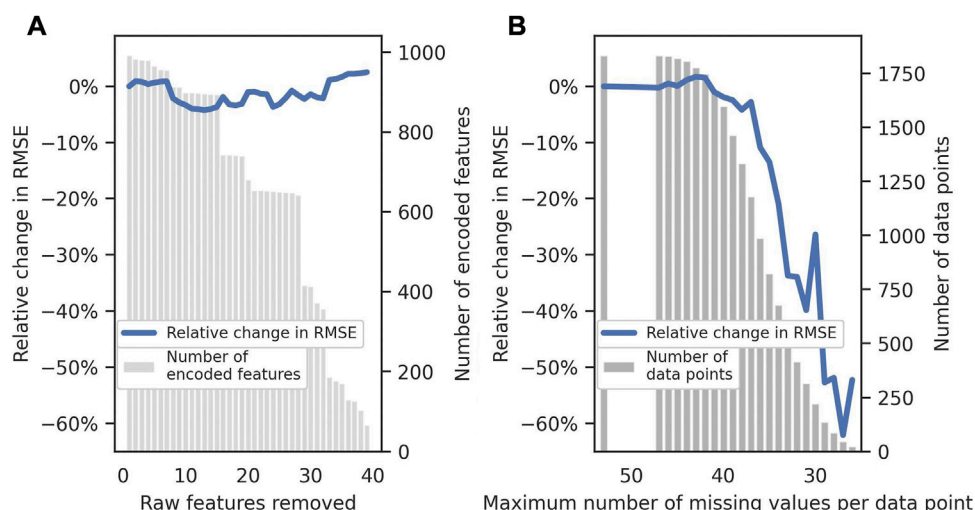


FIGURE 10

(A) Relative change in the extrapolated test RMSE when removing noisy features (the abscissa indicates the number of raw features removed from the 67 initial features; each raw feature might correspond to multiple encoded features). The baseline is taken as the extrapolated RMSE computed on the complete dataset. The grey bars indicate how many encoded features are left in the dataset after removing the noisy ones. (B) Percent change in the extrapolated test RMSE when removing noisy data points. The baseline is taken as the extrapolated RMSE computed on the complete dataset. The grey bars indicate how many data points are left in the dataset after removing the noisy ones.

should also be more stable according to other FOMs. In order to confirm whether different FOMs for perovskite stability agree, we have used our in-house dataset of time-series data produced during aging experiments. We have defined different FOMs:

- T_{80} : The time it takes for the PCE to drop 20% from the value at the beginning of the experiment.
- T'_{80} : The time it takes for the PCE to drop 20% from the back-extrapolated value at the beginning of the experiment; back-extrapolation performed with a linear function, starting after the burn-in point.
- T_{S80} : The time it takes for the PCE to drop 20% from the value at the burn-in point
- % PCE after X hours: Fraction of the initial PCE measured after X hours.
- Degradation rate: Slope of the linear interpolation of the data after the burn-in.

We then applied these FOMs to the in-house time-series data to get a list of stability measures for every examined cell. Finally, we have examined the pairs of FOMs and computed the Pearson correlation coefficient between them to check how well they agree in quantifying the stability of the cells.

3 Results and discussion

3.1 Feature importance

As previously described, each experiment randomly samples 75% of the data points in the given dataset to train the model. The sampling is repeated 1,000 times, and for each run, we obtain the feature importance values alongside train and test scores.

Figure 6 shows the train and test scores of the eNet model, while Figure 7 shows the performance of the RF model. As stated above, we have considered the whole dataset and two relevant subsets of the data: “Dark testing” and “Light testing” considering, respectively, aging tests in the dark and under illumination. The scores in Figures 6, 7 are represented by the R^2 -scores. A score of 1 indicates perfect agreement between estimated and actual values; a value of 0 corresponds to the performance of a random guessing model, and negative values reflect even worse performance than this.

The performances of the two models are very different: looking at train and test scores for the eNet, we see that the model cannot describe this dataset. A score close to zero indicates that we cannot do better than random guessing, which indicates the model’s complete inability to capture patterns in the data (we nonetheless show the results in the Supplementary Figures S7–S9). On the other hand, RF performs better than eNet and can better describe the data. The test score is much lower than the train score, indicating poor generalization capabilities. Still, the performance is acceptable for such a complicated task, at least with the available data and all the data quality issues we discussed. The significant difference in performance between eNet and RF lets us conclude that a non-linear model, such as RF and Gradient Boosting, can satisfactorily model the dataset. A linear model, even an advanced one like eNet, cannot capture the patterns in the data that relate the device properties to its stability.

Figure 8 shows the 20 most important features that the RF model identified for the complete dataset while also showing the importance of such features for the other two dataset splits. RF model captured many features known to influence the thermal, moisture, or photo-stability of perovskite solar cells. The magnitudes of stresses (temperature, relative humidity) applied are predictably among the top influencing factors. And so is the perovskite composition, particularly the presence of MA or FA organic

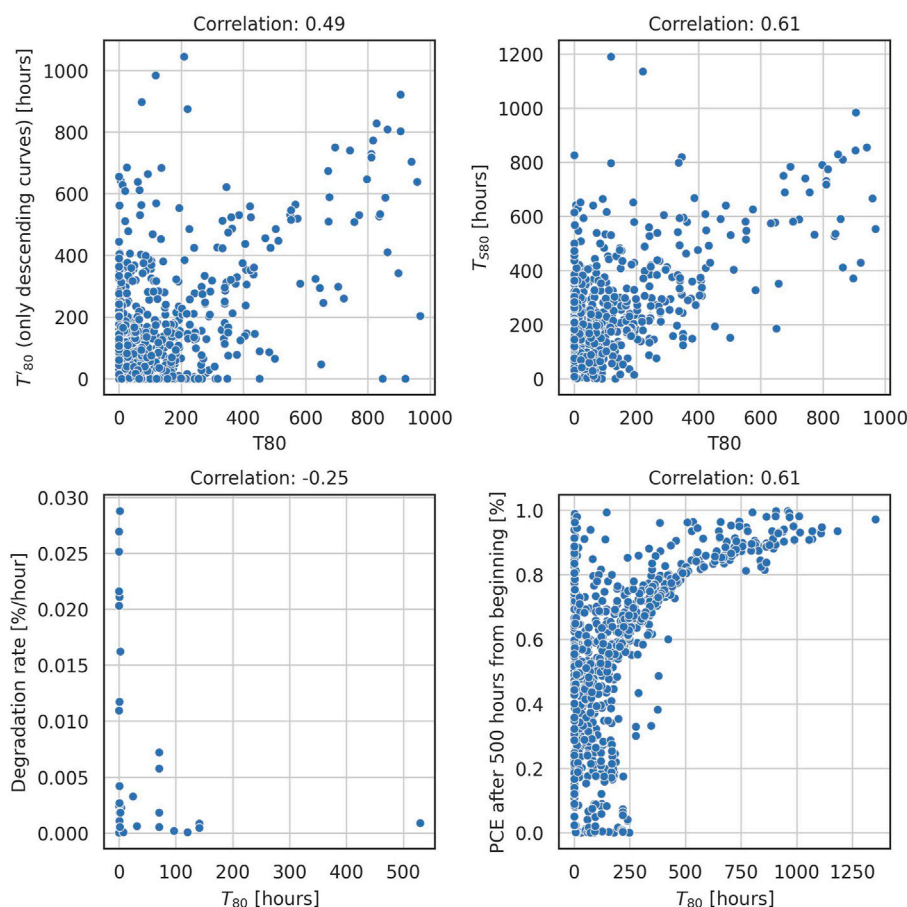


FIGURE 11

Scatter plot of T_{80} against four other stability figures of merit. Above every plot, the corresponding Pearson correlation coefficient is shown.

species as a monovalent cation or iodine as anion will generally result in less resilient perovskite materials. Multiple transport materials investigated as options for electron or hole transport layers significantly influence the device stability, and RF predictions agree on this point too. See an extended list of features and their impacts on stability in [Supplementary Figures S4–S6](#).

Some predictions are less straightforward to verify, such as the significance of solvents, quenching, and annealing procedures. Though they influence perovskite crystallization and, therefore, device stability, it is hard to tell at the moment whether their role is as defining for the final device stability as predicted by the RF results. While it is interesting to investigate these factors' importance on the PSC stability experimentally, we believe we need to improve our data-driven predictions to provide confident guidance for the experimental research.

Splitting the dataset into light and dark testing conditions while removing performance-related features shows that different features are selected as the most important. This is in accordance with different degradation mechanisms present with and without illumination. Given the low performance of the models, the numbers come with high uncertainty. However, we believe it is a good starting point for demonstrating the potential

of ML methods to dramatically accelerate the learning process with a reduced number of (extremely time-consuming!) aging experiments.

3.2 Data quality and dataset size: Learning curves experiments

As previously mentioned, we ran the learning curves experiments in three different settings. In the first setting, we use the database in its original form to check how good the power law approximation for the learning process is. As shown in [Figure 9](#), the approximation seems appropriate, hence we extrapolate the learning curves to a dataset size of 10,000 data points to simulate the performance we could obtain when more data is added to the database. The second and third settings simulate an increase in data quality in two different ways: dropping noisy features and dropping noisy data points. By noisy, we mean features and data points with the highest number of missing values. If we consider the tabular representation of data that is usually adopted when applying machine learning to this type of data, in the first case, we are dropping columns, while in the second, we are dropping rows.

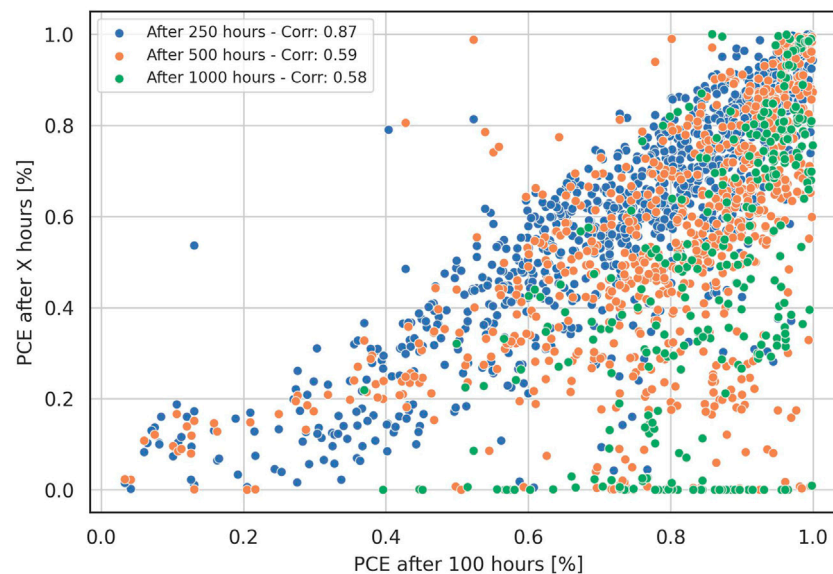


FIGURE 12

Scatter plot and correlation of the PCE normalized with the PCE at time 0, after 100 h, and the PCE at 250, 500, and 1,000 h.

3.2.1 Whole dataset

Figure 9 shows the interpolation points for computing the learning curves and the extrapolation to a larger train set size when modeling the complete dataset. The limiting performance represents the average between train and test errors at each train set size. This experiment shows that the performance we can obtain from a much larger dataset than the one used in this study (10,000 points compared to the current 1,800) is not much better in terms of the test error. The performance looks already saturated and adding more data with the same quality and statistical properties is not expected to improve the model's performance.

3.2.2 Removing noisy features

In this second experiment, we simulate higher-quality datasets by iteratively removing noisy features from the training set according to the number of missing values they contain. We remove the feature with the most missing values and then the less noisy ones, one at a time. We define the baseline performance of the ML model as the value of the test error extrapolated to 10,000 when using the complete train set, with no features removed. This baseline performance will also be used in the following experiment, where we remove noisy data points. Figure 10A shows the percentage change in extrapolated root mean squared error (RMSE) for each dataset compared to the baseline performance. It is clear from the figure that the extrapolated performance does not significantly change when removing noisy features. This might indicate that the benefit of having fewer missing values is canceled out by having less information about the devices, compared to when the parameters are reported.

3.2.3 Removing noisy data points

The third experiment simulates higher-quality datasets by iteratively removing noisy data points, i.e., data points with a higher number of missing values (or devices with the least reported information). We remove the noisiest data points and then remove points with a lower noise level. Figure 10B shows the percentage change in extrapolated RMSE for each dataset compared to the baseline performance. The bars in the figure represent the number of data points left after removing the noisy ones, while the horizontal axis shows the maximum number of missing data values allowed for each dataset.

In contrast with the previous experiment, we observed pronounced improvement in the test score with higher quality data. However, we have to treat these results carefully. Removing data points lowers the statistical significance of the results and might also make the learning task easier, improving performance. Nevertheless, the trend is evident even for a reasonably sized dataset, around 1,000 data points, that are still larger than all similar datasets used in the literature.

Better conclusions can be drawn by comparing what happens when we remove features or data points: the first scenario corresponds to considering fewer properties of a device for an ML task, and the second corresponds to having only entries with a given quality in terms of the number of missing values. The difference in the evolution of the expected performance suggests how the features are relevant, and we need to collect them if we want to significantly improve the performance of machine learning models used for applications similar to the one explored in this study.

3.3 Figures of merit

Machine learning techniques are optimized to predict a target variable; in our case, the lifetime is defined as T_{80} . In this last section, we want to discuss how representative this metric is for describing perovskite solar cell stability. In the context of projects involving “Big Data,” the large number of aging curves available demands the programmatic extraction of stability metrics, which requires exact definitions, contrary to manually extracting FOMs from the aging curves. We have programmatically extracted different stability FOMs for PSCs, defined above, and compared them pairwise to assess their agreement. For this, we used the in-house data set with complete time series for aging experiments available. Figure 11 shows how T_{80} correlates to four other FOMs; the actual value of the Pearson correlation coefficient is shown on the upper edge of every sub-figure.

Figure 12 focuses only on examining the normalized PCE after a given time has passed during the experiment. We have compared the PCE value after 100 h of aging against those after 250, 500, and 1,000 h following the suggestion that it might be possible to reasonably extrapolate shorter aging experiments (Almora et al., 2021).

From Figures 11, 12, it is clear how even FOMs with very similar definitions can result in very different values for PSCs aging curves. More importantly, they do not always agree regarding which devices are more stable. This is due to the wide variety of PSCs' aging behaviors, which makes identifying a universal FOM for stability a non-trivial task. An agreement on the FOM to use that best describes what we mean by stability of PSCs will surely help in improving the performance of ML models. The low correlation between FOMs shows that the single number fed to ML algorithms might not represent the task we are trying to solve. This increases the difficulty of the task, which is already high due to other quality issues and the relatively small size of the available datasets compared to the number of parameters to consider.

4 Conclusion

Machine learning methods have a great potential to accelerate the development of more stable perovskite devices, potentially avoiding the extremely time-consuming aging experiments. Using the perovskite database project that summarizes available literature, we have demonstrated the possibility of applying ML for PSC stability data, although only non-linear methods (such as random forest) show promising results. Even in this case, however, data quality remains a significant challenge. Learning curves experiments indicate that just increasing the amount of data (i.e., collecting more aging experiments) has a limited positive effect on boosting the confidence of ML forecast. Instead, we show that it is critical to improve the data quality by reporting as complete information on the device manufacturing and aging conditions as possible. More accurate data leads to higher statistical relevance of the results, better ability of the ML algorithms to capture patterns in the data, and increased prediction performance.

Another, perhaps more significant, challenge is defining the FOMs for stability used as target variables for the ML analysis. With in-house data, we show that the variety of behaviors observed in the aging curves of perovskite devices leads to the dependence of the results on the choice of the metric. A single number (e.g., T_{80}) cannot capture the complexity of such curves and, therefore, is unlikely to be an optimal choice. Sharing the complete aging curves would be vital to solving this problem. These

shared data would facilitate the discussion on universal FOMs that describe stability for perovskite solar devices in a meaningful and precise way.

We encourage perovskite researchers to report more complete data regarding the experiments and full aging curves since we believe this can significantly accelerate the development of commercially viable perovskite solar devices through machine learning.

Data availability statement

The original contributions presented in the study are included in the article/Supplementary Material, further inquiries can be directed to the corresponding author.

Author contributions

PG has performed the data preparation and machine learning analysis. PG and MK wrote the first draft of the manuscript. HK, NH, and AA provided the in-house database of aging experiments. PG, MK, HK, EU, TJ, and CU contributed to the conception of the study. MK, RS, and CU contributed to the supervision of the project. All authors contributed to the manuscript revision.

Funding

PG acknowledges the support of the Helmholtz Einstein International Berlin Research School in Data Science (HEIBriDS). MK, RS, and CU acknowledge the support of the European partnering project TAPAS (PIE-0015). HK acknowledges the support from the HyPerCells graduate school. HK acknowledges the VIPERLAB project funded by the European Union's Horizon 2020 research and innovation programme under grant agreement N°101006715

Conflict of interest

The authors declare that the research was conducted in the absence of any commercial or financial relationships that could be construed as a potential conflict of interest.

Publisher's note

All claims expressed in this article are solely those of the authors and do not necessarily represent those of their affiliated organizations, or those of the publisher, the editors and the reviewers. Any product that may be evaluated in this article, or claim that may be made by its manufacturer, is not guaranteed or endorsed by the publisher.

Supplementary material

The Supplementary Material for this article can be found online at: <https://www.frontiersin.org/articles/10.3389/fenrg.2023.1118654/full#supplementary-material>

References

- Almora, O., Baran, D., Bazan, G. C., Berger, C., Cabrera, C. I., Catchpole, K. R., et al. (2021). Device performance of emerging photovoltaic materials (version 2). *Adv. Energy Mater.* 11 (48), 2102526. doi:10.1002/aenm.202102526
- Best Research-Cell Efficiency Chart (2023). *Best research-cell efficiency Chart*. n.d. <https://www.nrel.gov/pv/cell-efficiency.html> (Accessed February 17 2023).
- Brinkmann, K. O., Gahlmann, T., and Riedl, T. (2020). Atomic layer deposition of functional layers in planar perovskite solar cells. *Sol. RRL* 4 (1), 1900332. doi:10.1002/solr.201900332
- Chen, J., Feng, M., Zha, C., Shao, C., Zhang, L., and Wang, L. (2022). Machine learning-driven design of promising perovskites for photovoltaic applications: A review. *Surfaces Interfaces* 35 (December), 102470. doi:10.1016/j.surfin.2022.102470
- Chen, M., Ju, M. G., Garces, H. F., Carl, A. D., Ono, L. K., Hawash, Z., et al. (2019). Highly stable and efficient all-inorganic lead-free perovskite solar cells with native-oxide passivation. *Nat. Commun.* 10 (1), 16. doi:10.1038/s41467-018-07951-y
- Chi, W., and Banerjee, S. K. (2021). Stability improvement of perovskite solar cells by compositional and interfacial engineering. *Chem. Mater.* 33 (5), 1540–1570. doi:10.1021/acs.chemmater.0c04931
- Cortes, C., Jackel, L. D., Solla, S. A., Vapnik, V., and Denker, J. S. (1993). Learning curves. *Asymptot. Values Rate Convergence* 6 (November), 327–334.
- David, T. W., Helder Anizelli, T., Jacobsson, T. J., Gray, C., Teahan, W., Kettle, J., et al. (2020). Enhancing the stability of organic photovoltaics through machine learning. *Nano Energy* 78 (December), 105342. doi:10.1016/j.nanoen.2020.105342
- Dipta, S. S., and Uddin, A. (2021). Stability issues of perovskite solar cells: A critical review. *Energy Technol.* 9 (11), 2100560. doi:10.1002/ente.202100560
- Foo, G. S., Polo-Garzon, F., Fung, V., Jiang, D., Overbury, S. H., and Wu, Z. (2017). Acid–base reactivity of perovskite catalysts probed via conversion of 2-propanol over titanates and zirconates. *ACS Catal.* 7 (7), 4423–4434. doi:10.1021/acscatal.7b00783
- Green, M. A., Dunlop, E. D., Hohl-Ebinger, J., Yoshita, M., Kopidakis, N., Bothe, K., et al. (2022). Solar cell efficiency tables (version 60). *Prog. Photovoltaics Res. Appl.* 30 (7), 687–701. doi:10.1002/pip.3595
- Jacobsson, T. J., Adam, H., García-Fernández, A., Anand, A., Al-Ashouri, A., Anders, H., et al. (2022). An open-access database and analysis tool for perovskite solar cells based on the FAIR data principles. *Nat. Energy* 7 (1), 107–115. doi:10.1038/s41560-021-00941-3
- James, G., Witten, D., Hastie, T., and Tibshirani, R. (2013). *An introduction to statistical learning*, 103. New York, NY: Springer Texts in Statistics. doi:10.1007/978-1-4614-7138-7Springer New York
- Khenkin, M. V., Katz, E. A., Abate, A., Brabec, C., Abate, A., Bardizza, G., et al. (2020). Consensus statement for stability assessment and reporting for perovskite photovoltaics based on ISOS procedures. *Nat. Energy* 5 (1), 35–49. doi:10.1038/s41560-019-0529-5
- Köbler, H., Neubert, S., Jankovec, M., Glazar, B., Haase, M., Hilbert, C., et al. (2022). High-throughput aging system for parallel maximum power point tracking of perovskite solar cells. *Energy Technol.* 10 (6), 2200234. doi:10.1002/ente.202200234
- Liu, Y., Yan, W., Han, S., Zhu, H., Tu, Y., Guan, L., et al. (2022). How machine learning predicts and explains the performance of perovskite solar cells. *Sol. RRL* 6 (6), 2101100. doi:10.1002/solr.202101100
- Lu, Q., Yang, Z., Meng, X., Yue, Y., Ahmad, M. A., Zhang, W., et al. (2021). A review on encapsulation technology from organic light emitting diodes to organic and perovskite solar cells. *Adv. Funct. Mater.* 31 (23), 2100151. doi:10.1002/adfm.202100151
- Mazumdar, S., Zhao, Y., and Zhang, X. (2021). Stability of perovskite solar cells: Degradation mechanisms and remedies. *Front. Electron.* 2. doi:10.3389/felec.2021.712785
- Myung, C. W., Hajibabaei, A., Cha, J., Ha, M., Kim, J., and Kwang, S. (2022). Challenges, opportunities, and prospects in metal halide perovskites from theoretical and machine learning perspectives. *Adv. Energy Mater.* 12 (45), 2202279. doi:10.1002/aenm.202202279
- Nath, B., Ramamurthy, P. C., Mahapatra, D. R., and Hegde, G. (2022). Electrode transport layer–metal electrode interface morphology tailoring for enhancing the performance of perovskite solar cells. *ACS Appl. Electron. Mater.* 4 (2), 689–697. doi:10.1021/acsaem.1c01100
- Odabasi, C., and Yildirim, R. (2020). Machine learning analysis on stability of perovskite solar cells. *Sol. ENERGY Mater. Sol. CELLS* 205 (February). doi:10.1016/j.solmat.2019.110284
- Roesch, R., Faber, T., von Hauff, E., Thomas, M., Brown, M., Hoppe, H., et al. (2015). Procedures and practices for evaluating thin-film solar cell stability. *Adv. Energy Mater.* 5 (20), 1501407. doi:10.1002/aenm.201501407
- Seung, H. S., Sompolinsky, H., and Tishby, N. (1992). Statistical mechanics of learning from examples. *Phys. Rev. A* 45 (8), 6056–6091. doi:10.1103/PhysRevA.45.6056
- Tiihonen, A., Miettinen, K., Halme, J., Lepikko, S., Poskela, A., and Peter, D. (2018). Critical analysis on the quality of stability studies of perovskite and dye solar cells. *Energy and Environ. Sci.* 11 (4), 730–738. doi:10.1039/C7EE02670F
- Yilmaz, B., and Yildirim, R. (2021). Critical review of machine learning applications in perovskite solar research. *Nano Energy* 80, 105546. doi:10.1016/j.nanoen.2020.105546
- Yin, X., Yin, X., Song, Z., Li, Z., Li, Z., Li, Z., et al. (2020). Toward ideal hole transport materials: A review on recent progress in dopant-free hole transport materials for fabricating efficient and stable perovskite solar cells. *Energy Environ. Sci.* 13, 4057–4086. doi:10.1039/d0ee02337j



OPEN ACCESS

EDITED BY

John S. Hardy,
Pacific Northwest National Laboratory
(DOE), United States

REVIEWED BY

Jie Bao,
Pacific Northwest National Laboratory
(DOE), United States
Alexander Kozlov,
Omsk State Technical University, Russia

*CORRESPONDENCE

L. Mastropasqua,
✉ lm1@aep.uci.edu

RECEIVED 09 December 2022

ACCEPTED 07 April 2023

PUBLISHED 09 May 2023

CITATION

Cammarata A and Mastropasqua L (2023),
Theoretical analysis of mixed open-
circuit potential for high temperature
electrochemical cells electrodes.
Front. Energy Res. 11:1120343.
doi: 10.3389/fenrg.2023.1120343

COPYRIGHT

© 2023 Cammarata and Mastropasqua.
This is an open-access article distributed
under the terms of the [Creative
Commons Attribution License \(CC BY\)](#).
The use, distribution or reproduction in
other forums is permitted, provided the
original author(s) and the copyright
owner(s) are credited and that the original
publication in this journal is cited, in
accordance with accepted academic
practice. No use, distribution or
reproduction is permitted which does not
comply with these terms.

Theoretical analysis of mixed open-circuit potential for high temperature electrochemical cells electrodes

A. Cammarata^{1,2} and L. Mastropasqua^{2*}

¹Department of Energy, Politecnico di Milano, Milan, Italy, ²National Fuel Cell Research Center, University of California, Irvine, Irvine, CA, United States

The Nernst equilibrium potential calculates the theoretical OCV, which estimates the best performance achievable by an electrochemical cell. When multiple semi-reactions (or multiple ionic species) are active in one of the electrodes, the calculation of the theoretical OCV is not straightforward, since different Nernst potentials are associated to each semi-reaction. In this paper, analytical equations for calculation of the theoretical OCV are developed, using the mixed potential theory. The case of H₂ and CO co-oxidation (or H₂O and CO₂ co-reduction) in solid oxide cells is used as a reference case, but similar conclusions can be drawn for other equivalent cases. OCV data from literature are used to calibrate and validate the model. The relative reaction rate of H₂ and CO semi-reactions is estimated within the calibration process, and the result is in line with assumptions and suggestions given by other authors. The validation procedure shows predicted OCV values in line with experimental literature data, except for mixtures with relatively large CH₄ concentration (e.g., 8%), for which the OCV is significantly underestimated. This is expected when thermochemical reactions, in parallel to electrochemical reactions occur, since the additional H₂ produced by internal steam methane reforming is not accounted within the local mixed potential model. A fuel cell polarization model is developed based on the results from the calibration procedure, and it is used to predict the polarization behavior of an SOFC fed with a H₂-H₂O-CO-CO₂ fuel mixture. It is found that either H₂ or CO may be reduced rather than oxidized via an equivalent electrochemical water-gas-shift reaction.

KEYWORDS

mixed open circuit potential, electrochemical cells, solid oxide fuel cells (SOFC), electrode potential, co-oxidation, co-electrolysis

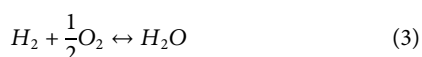
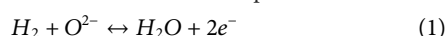
1 Introduction

Solid Oxide Fuel Cell (SOFC) and Solid Oxide Electrolyzer Cell (SOEC) are innovative technologies used for energy conversion purposes. SOFCs are used to efficiently produce electricity using a fuel such as hydrogen (H₂). The high operating temperature of SOFCs (500°C–1,000°C) allows them to operate using a variety of fuels, such as carbon monoxide (CO), methane (CH₄), methanol (CH₃OH), and ammonia (NH₃) (Donazzi et al., 2016; Kishimoto et al., 2020; Fan et al., 2022; Sang et al., 2022). Conversely, SOECs are used to produce fuels like H₂ and CO, starting from water (H₂O), carbon dioxide (CO₂), and an electricity supply. In the framework of energy transition, SOFCs may be used for the design of efficient and fuel-flexible energy systems (Ishak et al., 2012; Campanari et al., 2016;

Mastropasqua et al., 2020; Duong et al., 2022), while SOECs could be a key technology for the synthesis of e-fuels, since CO and H₂ are precursors for the production of high-value hydrocarbons via the Fischer-Tropsch process (Wang et al., 2017). Therefore, it is necessary to develop SOFC and SOEC models able to predict the performance in presence of different chemical species, interacting with each other through chemical and electrochemical reactions.

The open circuit voltage (OCV) of an electrochemical cell is the voltage established in the electrical circuit at zero current, and it is closely related to its thermodynamic and kinetic performance. The meaning of the OCV measured for an electrochemical cell is twofold. In fuel cell mode, the OCV represents the maximum producible electric power per unit current. Conversely, the OCV represents the minimum electric power required per unit current to perform the electrolysis reaction at a certain temperature, pressure, and composition. When a finite current is flowing through an electrochemical cell, the cell voltage is different from the OCV due to electrochemical losses (i.e., overpotentials or polarization losses). For fuel cell operation the cell voltage is lower compared to the OCV, while the opposite is true for electrolyzers. This concept forms the basis for the development of numerical models, which require the precise theoretical estimation of the OCV. For the above reasons, it is important to correctly estimate the OCV of electrochemical cells. When multiple electrochemical reactions (or multiple ionic species) are active at one electrode, the estimation of the OCV is not a simple task due to the formation of the so-called mixed potential. Therefore, the primary goal of this paper is to develop a model suitable for the estimation of the mixed OCV of electrochemical cells, analyzing the case of H₂ and CO half-reactions in solid oxide cells as an example.

Considering the half-reactions in a conventional SOFC, (Eq. 1) and (Eq. 2) are the only active electrochemical reactions at the fuel and air electrode respectively, and reaction (Eq. 3) is the global reaction. The Nernst potential (Eq. 4) is generally used to calculate the theoretical OCV, where p_i is the partial pressure of species i in the gas phase. Note that in this analysis, we do not account for mass transport or gas mixture composition variation along the thickness of the porous fuel electrode. Therefore, one might use the bulk gas composition for the calculation of the Nernst potential.

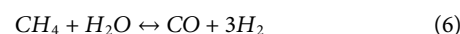


$$E_{\text{H}_2} = E_{\text{H}_2}^\circ + \frac{RT}{2F} \ln \left(\frac{p_{\text{H}_2} p_{\text{O}_2}^{0.5}}{p_{\text{H}_2\text{O}}} \right) \quad (4)$$

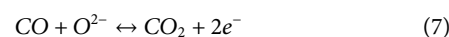
The Nernst equation is strictly valid when all steps required for reaction (Eq. 3) to occur are in equilibrium or in partial equilibrium (Kee et al., 2005). Therefore, the presence of chemical reactions like water-gas-shift (WGS) and steam methane reforming (SMR), expressed by reactions (Eq. 5) and (Eq. 6) respectively, could invalidate Eq. 4 since the elementary steps of reaction (Eq. 1) might not be in equilibrium. As an example, the hydrogen adsorption reaction is expected to be non-equilibrated if SMR is active, since the rate of hydrogen desorption from the electrode is larger than the rate of its adsorption. Therefore, the Gibbs free energy variation of the hydrogen adsorption reaction is different

from zero, invalidating the demonstration shown in ref. (Kee et al., 2005). Following the demonstrations shown in the reference, it can also be inferred that the larger the reaction rate of the global oxidation reaction (Eq. 3) compared to that of the chemical reactions, the better is the accuracy of the Nernst equation.

Eq. 4 is expected to be particularly accurate when a mixture of H₂ and H₂O is used at the fuel electrode, since chemical equilibrium is guaranteed at open circuit. However, the Nernst equation has been extensively used to model non-equilibrium cell operation; for instance, when either WGS or SMR are active at the fuel electrode (Campanari and Iora, 2005; Spallina et al., 2015; Corigliano and Fragiaco, 2020). In this case, it is implicitly assumed that WGS and SMR are relatively slow reactions, they do not prevent reactions (Eq. 1) and (Eq. 2) to reach partial equilibrium, and they do not significantly alter the partial pressures of gases within the porous electrode compared to the ones in the bulk gas mixture.



Conversely, assuming that WGS and SMR are fast reactions, some authors estimate the OCV by substituting the equilibrium partial pressures in Eq. 4 (Stoots et al., 2009; Lee et al., 2015; Jin et al., 2018; Vágner et al., 2019), calculated assuming that both WGS and SMR go to equilibrium at local temperature and pressure, starting from the bulk gas composition. Therefore, using the equilibrium partial pressures allows to indirectly include species like CO and CH₄ in the estimation of the OCV. Moreover, the equilibrium model allows to easily estimate the OCV in presence of several electrochemical semi-reactions occurring at one electrode. For instance, if both half-reactions (Eq. 1) and (Eq. 7) are active at the fuel electrode, a second Nernst voltage could be defined as in Eq. 8.



$$E_{\text{CO}} = E_{\text{CO}}^\circ + \frac{RT}{2F} \ln \left(\frac{p_{\text{CO}} p_{\text{O}_2}^{0.5}}{p_{\text{CO}_2}} \right) \quad (8)$$

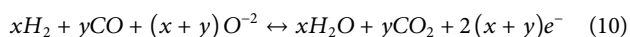
If the equilibrium partial pressures are used, E_{H_2} and E_{CO} are equal (Spallina et al., 2015), and there is no ambiguity in the estimation of the OCV. However, if the partial pressures in the non-equilibrated bulk gas mixture are used, E_{H_2} and E_{CO} are different, and the estimation of the OCV should account for the mixed potential that is originated at the fuel electrode.

The first method to estimate the cell OCV in a non-equilibrated mixture considering two active electrochemical semi-reactions at one electrode was introduced by Fleming (Fleming, 1977). Fleming defined an equivalent electric circuit representing the electrochemical cell, with as many parallel branches as the number of covered active sites (see Supplementary Appendix SB), for both H₂ and CO (however, Fleming assumed that O₂ and CO are electrochemically active at the fuel electrode). Assuming each branch includes both a voltage generator with value equal to either E_{H_2} or E_{CO} , and a resistance with a constant value for each branch, the OCV can be computed by applying Norton's theorem to the equivalent electric circuit. The mixed OCV results to be equal to the average of E_{H_2} and E_{CO} , weighted on the surface coverage, as expressed in Eq. 9.

$$V_{OC} = \theta_{H_2} E_{H_2} + \theta_{CO} E_{CO} \quad (9)$$

However, Norton's theorem is only applicable for linear electric circuits, and the resistances in H_2 and CO branches are not equal in general. For instance, the activation overpotentials are generally modeled using a Butler-Volmer relationship which is not linear and it can lead to different activation overpotentials for H_2 and CO charge transfer processes (Petruzzi et al., 2003; Suwanwarangkul et al., 2006; Andreassi et al., 2009; Iwai et al., 2011; Ni, 2012; Park et al., 2012; Andersson et al., 2013a; Razbani et al., 2013; De Lorenzo and Fragiaco, 2015; Bao et al., 2016).

Other authors (Zhu and Kee, 2003; Aloui and Halouani, 2007; Stempien et al., 2012; Andersson et al., 2013b; Stempien et al., 2013; Baldinelli et al., 2015a) attempt to estimate the OCV by assuming a fictitious electrochemical semi-reaction (Eq. 10) occurring at the fuel electrode, which is a function of two parameters x and y . It can be demonstrated that the OCV resulting from this assumption is the average between E_{H_2} or E_{CO} , weighted on the parameters x and y , as expressed by Eq. 11 (see Supplementary Appendix SA for demonstration).



$$V_{OC} = \frac{x E_{H_2} + y E_{CO}}{x + y} \quad (11)$$

The stoichiometric coefficients x and y can be assumed to be equal to unity (Penchini et al., 2013), which corresponds to calculating the arithmetic average of E_{H_2} or E_{CO} . More frequently, x and y are replaced by the molar fractions of H_2 and CO, respectively (Aloui and Halouani, 2007; Stempien et al., 2012; Andersson et al., 2013b; Stempien et al., 2013; Baldinelli et al., 2015a). However, since the elementary steps of the global H_2 semi-reaction (Eq. 2) are relatively fast, this semi-reaction is likely to be close to partial equilibrium, even if the H_2 concentration in the fuel is relatively low (Kee et al., 2005). In other words, the OCV is likely to be close to E_{H_2} even if H_2 molar fraction is low.

In Section 2, a simple model is developed to estimate the mixed OCV, where two (or more) electrochemical semi-reaction are considered at one of the electrodes. The relative reaction rate of the semi-reactions, which affects the OCV, is considered using Butler-Volmer equations and exchange current densities. This approach is derived from the theory available for corrosion processes, in which two semi-reactions occur in presence of an electrolyte and an equipotential electrode, to calculate parameters such as the corrosion potential, which is a mixed potential, and the corrosion current (Bockris and Reddy, 2000). The case of H_2 and CO co-oxidation in SOFC (or, equivalently, H_2O and CO_2 co-reduction in SOEC) is considered as an example. In Section 3 the model is calibrated and validated using experimental OCV data from the literature, which allowed to retrieve information regarding the relative reaction rate of H_2 and CO semi-reactions. Finally, a simple polarization model is developed in Section 4 using the results from the calibration procedure. The model is used to calculate the polarization curve of an SOFC fed with a H_2 - H_2O -CO- CO_2 mixture.

2 Mixed potential model

The approach followed hereafter is similar to that followed to develop corrosion theory, due to analogies between a corrosion

process, and a fuel electrode at OCV where both reactions (Eq. 1) and (Eq. 7) are active (Bockris and Reddy, 2000). During a corrosion process, two semi-reactions occur in presence of an electrolyte (water) and an equipotential electrode (the corroded metal), as shown in Figure 1 (left).

In corrosion, a species is oxidized (e.g., a metal), and a species is reduced (e.g., oxygen), and the process is driven by the different equilibrium potential (i.e., equilibrium electric potential difference between electrode and electrolyte) of the two semi-reactions at the specific operating conditions. Similarly, for the electrochemical cell at OCV shown in Figure 1 (right), it is expected that either H_2 is oxidized to H_2O and CO_2 is reduced to CO, or CO is oxidized to CO_2 and H_2O is reduced to H_2 . The process is driven by the different equilibrium potentials of semi-reactions (Eq. 1) and (Eq. 7) at the specific operating conditions, which can be identified as the difference between E_{H_2} and E_{CO} , since the equilibrium potential of reaction (Eq. 2) is equally accounted for in the calculation of E_{H_2} and E_{CO} . The overall process may be regarded as an electrochemical WGS reaction. Note that it is expected that the electrochemical WGS is not only active at OCV, but also in a condition of mild cell polarization.

The kinetics of the semi-reactions is modeled using Butler-Volmer Eqs 12, 13. The parameters α and β are the charge transfer coefficients, n^e is the number of electrons involved in the charge transfer process, i_0 is the exchange current density, and η is the activation overpotential. The reference area for both i and i_0 is the geometrical electrolyte surface.

$$i_{H_2} = i_{0,H_2} \left[\exp\left(\alpha \frac{n_{H_2}^e F \eta_{H_2}}{RT}\right) - \exp\left(-(1 - \alpha) \frac{n_{H_2}^e F \eta_{H_2}}{RT}\right) \right] \quad (12)$$

$$i_{CO} = i_{0,CO} \left[\exp\left(\beta \frac{n_{CO}^e F \eta_{CO}}{RT}\right) - \exp\left(-(1 - \beta) \frac{n_{CO}^e F \eta_{CO}}{RT}\right) \right] \quad (13)$$

Similarly to a corrosion process, it is assumed that the current produced by one of the two semi-reaction is completely absorbed by the other semi-reaction, which for a complete cell is equivalent to assuming a vanishing net current flowing in the external circuit, as expressed by Eq. 14.

$$i_{H_2} + i_{CO} = 0 \quad (14)$$

Finally, the activation overpotentials can be written as functions of the OCV as in Eqs 15, 16.

$$\eta_{H_2} = E_{H_2} - V_{OC} \quad (15)$$

$$\eta_{CO} = E_{CO} - V_{OC} \quad (16)$$

Eqs 12–16 allow calculating V_{OC} once the kinetic parameters in the Butler-Volmer equations are known. Note that if Eq. 14 is satisfied, then i_{H_2} and i_{CO} have opposite signs, and the same is true for η_{H_2} and η_{CO} , which stems from the functional form of Butler-Volmer equations (i.e., i has the same sign of η). If η_{H_2} and η_{CO} have opposite signs, it is easy to see from Eqs 15, 16 that the value of V_{OC} must be in the range defined by E_{H_2} and E_{CO} .

Using the procedure outline above, and introducing Tafel's approximation (i.e., activation overpotentials are low), it is possible to find a simple analytical solution for V_{OC} , as expressed in Eq. 17, similar to Eq. 9 proposed by Fleming (Fleming, 1977). Assuming that electric resistances in H_2 and CO branches are different and not equal, it is possible to derive Eq. 17 using

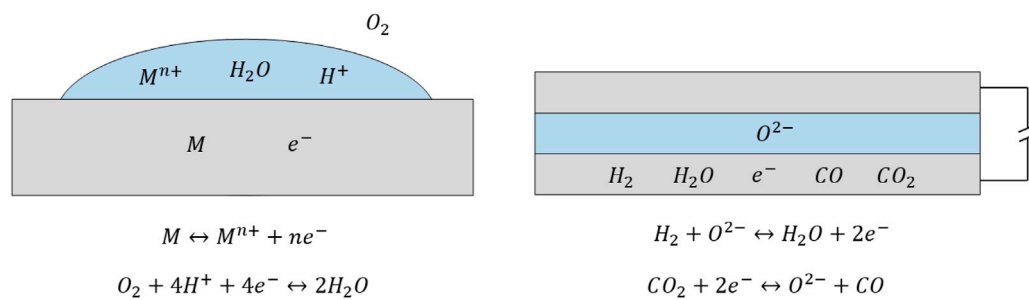


FIGURE 1

Analogy between a corrosion process (left) and the fuel electrode in an electrochemical cell at OCV, exposed to a H_2 - H_2O - CO - CO_2 mixture (right). In both cases there is an equipotential electrode, either the corroded metal or the porous fuel electrode, an electrolyte, either water or a solid electrolyte, and two competing electrochemical semi-reactions.

Fleming's approach (see [Supplementary Appendix SB](#)), which stems from the electric circuit linearity requirement for the application of the Norton's theorem, and the actual linear relationship between current and voltage provided by Tafel's approximation. Therefore, Eq. 9 provides a less accurate estimation of the OCV compared to solving Eqs 12–16 by assuming Tafel's approximation and same kinetics of H_2 and CO electrochemical reactions. By assuming that $n_{H_2}^e$ is equal to n_{CO}^e , the open circuit voltage results to be the average between E_{H_2} and E_{CO} , weighted on exchange current densities. This is a sound result, as it is expected that the measured voltage is close to the Nernst voltage of the faster semi-reaction.

$$V_{OC} = \frac{i_{0,H_2} n_{H_2}^e E_{H_2} + i_{0,CO} n_{CO}^e E_{CO}}{i_{0,H_2} n_{H_2}^e + i_{0,CO} n_{CO}^e} \quad (17)$$

Removing Tafel's approximation, and assuming that α is equal to β , and $n_{H_2}^e$ is equal to n_{CO}^e , it is still possible to find an analytical solution for the OCV, as shown in Eq. 18.

$$V_{OC} = \frac{RT}{Fn^e} \ln \left[\frac{i_{0,H_2} \exp\left(\alpha \frac{n^e FE_{H_2}}{RT}\right) + i_{0,CO} \exp\left(\alpha \frac{n^e FE_{CO}}{RT}\right)}{i_{0,H_2} \exp\left(-(1-\alpha) \frac{n^e FE_{H_2}}{RT}\right) + i_{0,CO} \exp\left(-(1-\alpha) \frac{n^e FE_{CO}}{RT}\right)} \right] \quad (18)$$

The form of this equation is similar to that used to calculate the electrode mixed potential in a corrosion process ([Bockris and Reddy, 2000](#)). Note that by collecting either i_{0,H_2} or $i_{0,CO}$, it can be seen that V_{OC} is only a function of the ratio of current densities, hence it is not necessary to provide exact values for i_{0,H_2} and $i_{0,CO}$.

Eq. 18 is slightly modified assuming n^e equal to 1 (i.e., single-electron charge transfer process), and α equal to 0.5. Moreover, assuming that i_{0,H_2} and $i_{0,CO}$ are computed using relations (Eq. 19) and (Eq. 20) ([Razbani et al., 2013](#)), the OCV can be calculated using Eq. 21, which is used for the numerical calculations shown in the next section.

$$i_{0,H_2} = \gamma_{H_2} \left(\frac{p_{H_2}}{p_{ref}} \right) \left(\frac{p_{H_2O}}{p_{ref}} \right) \exp\left(-\frac{E_{act}}{RT}\right) \quad (19)$$

$$i_{0,CO} = \gamma_{CO} \left(\frac{p_{CO}}{p_{ref}} \right) \left(\frac{p_{CO_2}}{p_{ref}} \right) \exp\left(-\frac{E_{act}}{RT}\right) \quad (20)$$

$$V_{OC} = \frac{RT}{F} \ln \left[\frac{\gamma_{H_2} \frac{p_{H_2} p_{H_2O}}{p_{CO} p_{CO_2}} \exp\left(0.5 \frac{FE_{H_2}}{RT}\right) + \exp\left(0.5 \frac{FE_{CO}}{RT}\right)}{\gamma_{H_2} \frac{p_{H_2} p_{H_2O}}{p_{CO} p_{CO_2}} \exp\left(-0.5 \frac{FE_{H_2}}{RT}\right) + \exp\left(-0.5 \frac{FE_{CO}}{RT}\right)} \right] \quad (21)$$

Note that the functional form of i_{0,H_2} and $i_{0,CO}$ is commonly assumed to be the same, since the rate-determining step of H_2 and CO semi-reactions is similar ([Suwanwarangkul et al., 2006](#); [Andreassi et al., 2009](#)). However, the pre-exponential factor for H_2 exchange current density is usually assumed to be 2–3 times larger than that of CO for Ni-YSZ cermet electrodes, following the work of [Matsuzaki and Yasuda \(2000\)](#).

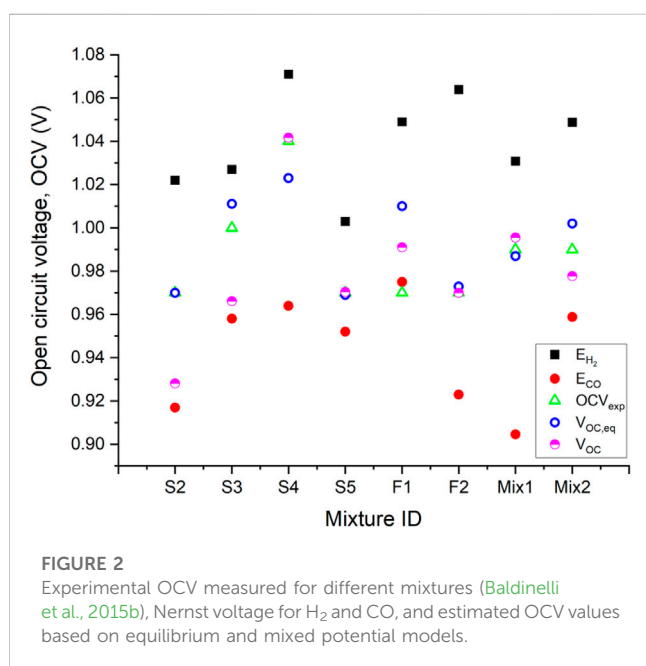
3 Model calibration and validation

Eq. 21 can be used to estimate the OCV, but the reverse process can be useful to predict the ratio of pre-exponential factors of H_2 and CO exchange current densities, if OCV experimental data are available. In order to calibrate and validate the model, literature OCV data on H_2 - H_2O - CO - CO_2 mixtures are used to estimate the ratio of pre-exponential factors, which is then compared with literature estimations. In principle, one could calibrate more parameters, like the difference between activation energies (here assumed null), or the species activity exponents in Eqs 19, 20. However, the scarce amount of reliable experimental data prevents this.

Ideally, the mixture used to produce experimental OCV data should not contain CH_4 , since the effective concentrations of H_2 , H_2O , CO , and CO_2 may be modified by the onset of the SMR reaction. Note that also the WGS reaction may modify the effective species concentrations, however here it is assumed that this effect is negligible. Moreover, the N_2 concentration in the mixture should be minimized since it could lead to an increase in the OCV despite not directly appearing in the Nernst equation ([Cinti et al., 2016](#)), which is an effect that cannot be captured by Eq. 21. Finally, electrolytes having significant electronic conduction (e.g., Ceria-based) cannot be accurately modelled, because the estimation of the OCV would also depend on the short-circuit electronic current. To the best of the author's knowledge, the literature does not provide experimental OCV data that respect all the above experimental operating conditions. However, the OCV data from [Baldinelli et al. \(2015b\)](#) are produced under operating conditions close to those described above, hence it is used as a reference for the model calibration and validation. A Ni-YSZ|8YSZ|LSCF button cell was used to produce

TABLE 1 Percentage molar composition of the mixtures used for model calibration and validation (Baldinelli et al., 2015b).

Mixture ID	H ₂	H ₂ O	CO	CO ₂	CH ₄	N ₂	Measured OCV [V]
S2	17.4	3.0	25.2	46.6	7.8	0.0	0.97
S3	19.4	3.0	38.8	29.1	9.7	0.0	1.00
S4	50.4	3.0	14.6	9.7	1.0	21.3	1.04
S5	11.6	3.0	13.6	11.6	0.0	60.2	0.97
F1	31.0	3.0	40.8	21.3	3.9	0.0	0.97
F2	42.6	3.0	20.4	33.0	1.0	0.0	0.97
Mix1	21.0	3.0	5.0	12.0	2.0	57.0	0.99
Mix2	31.0	3.0	35.0	26.0	5.0	0.0	0.99



experimental results, the oven temperature is 800°C, and the cathode is exposed to air (21% O₂ molar fraction is assumed). Note that the adoption of a button cell configuration is preferred for the validation purpose, since the mixture composition may change if the fuel is blown through a channel, mainly due to WGS reaction. The mixture compositions used for calculation are shown in Table 1, and they are named as in reference (Baldinelli et al., 2015b). The measured OCV values are estimated from the figures shown in the reference.

The mixture F2 is used to calibrate the ratio of pre-exponential factors appearing in Eq. 21, since it is free of N₂, and the CH₄ concentration is very low. The result is 2.54, which is in line with the range 2–3 suggested for a Ni-YSZ electrode working in a similar temperature range (Stoots et al., 2009; Razbani et al., 2013; Wang et al., 2017; Duong et al., 2022). After calibration, Eq. 21 is used to predict the OCV values for the mixtures in Table 1. The results are also compared to the OCV calculated assuming that the mixtures reach chemical equilibrium before giving rise to the cell potential, following the conventional

method discussed in the introduction section. The results of the analysis are shown in Figure 2.

Figure 2 shows the experimental OCV data from (Baldinelli et al., 2015b), E_{H_2} and E_{CO} calculated with Eqs 4, 8 respectively, the OCV calculated assuming that the mixture is at equilibrium, and V_{OC} computed with Eq. 21, using the calibrated value for the ratio of pre-exponential factors. In general, it is expected that the experimental and estimated OCVs are located within the range defined by E_{H_2} and E_{CO} . This is true for all the data analyzed, except for the mixture F1, for which the experimental OCV falls below E_{CO} . The reason for that is unknown and must be associated to the specific experimental setup of the reported test data. For all other mixtures, either one or both models for OCV estimation are close to the experimental value. For mixtures S4 and S5, which only contain 1% and 0% CH₄, Eq. 21 predicts the OCV with very good accuracy. For S4 the accuracy is significantly better compared to the equilibrium OCV model. The equilibrium model gives a good prediction also for F2, which is the mixture used for calibration.

The prediction accuracy of the mixed potential model seems to decrease with increasing CH₄ concentration. The model underpredicts the OCV for Mix2, S2, and S3, which have 5%, 8%, and 10% CH₄ concentration respectively. This is ascribed to the onset of SMR, which increases the effective H₂ and CO partial pressures near the active sites, with a positive effect on both E_{H_2} and E_{CO} . However, in the mixed potential model proposed, the mixture composition near the active sites is assumed equal to that in the bulk gas mixture for simplicity, and the effect of SMR is not accounted for. Therefore, the inaccuracy is more evident for S2 and S3, which contain a larger CH₄ concentration compared to Mix2. For Mix1, which contains 2% CH₄, the mixed potential model overpredicts the OCV, which suggests that the CH₄ concentration is too low to significantly increase the effective H₂ and CO partial pressures. For mixtures S2 and S3, which contain a significant amount of CH₄, the equilibrium model predicts the OCV more accurately compared to the mixed potential model, which is expected.

Overall, the equilibrium model always provides a reasonable estimation of the cell voltage, if mixture F1 is not considered. The mixed potential model predicts the OCV with either equal or better accuracy for the mixtures containing a relatively low CH₄ concentration in the range 0%–5% (S4, S5, F2, Mix1, Mix2), i.e., scenarios without heterogeneous catalytic reactions in parallel to electrochemical reactions. For the mixtures with higher CH₄ concentration (S2, S3),

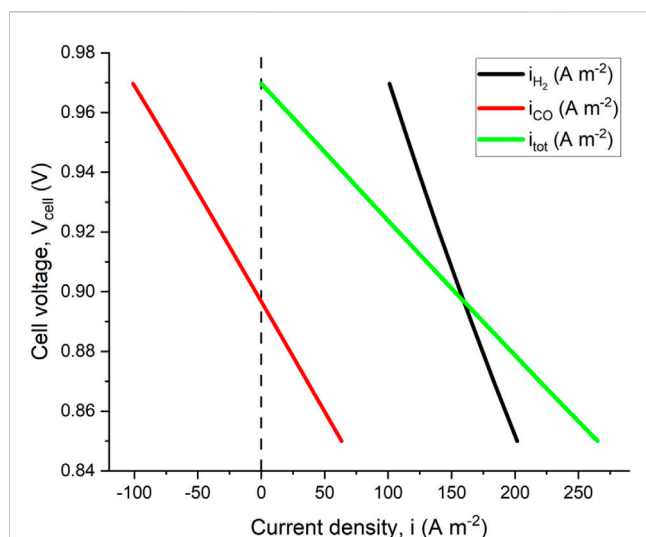


FIGURE 3

Polarization curve relative to mixture F2 at 800°C. Both H₂ and CO contributions to total current density are shown. The model predicts a negative current density for CO semi-reaction at high voltage, which means that CO is electrochemically produced rather than consumed.

the equilibrium model is more accurate, which is expected. These preliminary results indicate that the model developed is suitable to estimate the OCV of an electrochemical cell, or to retrieve data regarding the relative velocity of competing semi-reactions occurring on the same electrode. However, dedicated and detailed experimentation is required to further validate the model developed, following the guidelines outlined above.

4 Development of a polarization model

The calibration process shown in Section 3 is not only useful to predict the OCV of an electrochemical cell, but it can also be used to develop a polarization model. Referring to the example shown in Section 3, the ratio between pre-exponential factors appearing in Eqs 19, 20 can be used to calculate γ_{CO} , if a value for γ_{H_2} is fixed. Therefore, a polarization model may be developed, accounting for both H₂ and CO semi-reactions. The numerical model described in this section has already been used by several authors to model the polarization behavior of electrochemical cells (Petruzzini et al., 2003; Suwanwarangkul et al., 2006; Andreassi et al., 2009; Iwai et al., 2011; Ni, 2012; Park et al., 2012; Andersson et al., 2013a; Razbani et al., 2013; De Lorenzo and Fragiaco, 2015; Bao et al., 2016). However, here the focus of the analysis is the region of mild polarization close to the OCV. The model developed is used to predict the i - V relation near the OCV in fuel cell mode, relative to mixture F2 (see Table 1), assuming a uniform temperature equal to 800°C.

The voltage balance equations for both H₂ and CO are represented by Eqs 22, 23. Note that concentration losses are neglected in this model for the sake of simplicity, which may be justified by the fact that only the polarization behavior near the OCV is of interest for the purpose of this paper, and concentration losses are usually relatively more important at large values of current density. Moreover, an electrolyte supported

configuration is assumed, which is expected to make concentration losses even less important.

$$V_{cell} = E_{H_2} - \eta_{O_2} - \eta_{ohm} - \eta_{H_2} \quad (22)$$

$$V_{cell} = E_{CO} - \eta_{O_2} - \eta_{ohm} - \eta_{CO} \quad (23)$$

Exchange current densities (Eq. 19) and (Eq. 20), and Butler-Volmer Eqs 12, 13 are used for the polarization model developed. A similar Butler-Volmer equation is used to model the reaction rate of O₂ semi-reaction. For all Butler-Volmer equations, a single-electron charge transfer, with charge transfer coefficient equal to 0.5 is assumed. The kinetic parameters and the functional form of H₂ and O₂ exchange current densities are the same as in reference (Campanari and Iora, 2005). As already mentioned, γ_{CO} is assumed equal to γ_{H_2} divided by 2.54, which stems from the calibration procedure shown in Section 3. The ohmic polarization is calculated with Eq. 24, and it only accounts for the ionic resistance within the electrolyte, whose thickness and conductivity are also assumed equal to the values shown in reference (Campanari and Iora, 2005). This assumption may be justified by the relatively large electrolyte thickness considered (150 μ m), which arguably allows to neglect other contributions to the overall ohmic resistance.

$$\eta_{ohm} = \frac{i_{tot} L_{ely}}{\sigma_{ely}} \quad (24)$$

The total current density, i_{tot} is the sum of H₂ and CO current densities, as expressed in Eq. 25. The total current density is also equal to the cathodic current density (i.e., oxygen net reduction).

$$i_{tot} = i_{H_2} + i_{CO} \quad (25)$$

Figure 3 shows the polarization curve near the OCV predicted by the model developed. Note that the contributions of both i_{H_2} and i_{CO} to the overall current density is also shown.

The model predicted OCV is 0.97 V, which is the same value calculated using Eq. 21. This can be explained by noticing that when the overall current equals zero, Eqs 22, 23, 25 become equivalent to Eqs 14-16, respectively. Moreover, the model predicts a negative CO current density when the cell voltage is very close to the OCV, meaning that reaction (Eq. 7) is reversed, and CO₂ is reduced to CO. This is also expected since either i_{H_2} or i_{CO} must be negative at OCV to satisfy Eq. 25. This means that CO may be produced rather than consumed for cell voltages slightly lower than the OCV, which is counterintuitive for fuel cell operation, where reduced species are expected to always be electrochemically oxidized. Therefore, the potential difference between E_{H_2} and E_{CO} drives an electrochemical WGS reaction, which is directed towards the establishment of chemical equilibrium in the gas mixture. However, when the cell voltage is below a certain threshold (about 0.9 V in this case), the CO oxidation reaction overcomes CO₂ reduction, positively contributing to the overall current density.

5 Conclusion

In this work, the mixed potential theory is applied to derive analytical equations for the estimation of the OCV in a fuel cell or electrolyzer, when two electrochemical semi-reactions are active on one of the electrodes. The case of H₂ and CO co-oxidation (or H₂O and CO₂

co-reduction) is used as an example throughout the work. The equation found is calibrated and validated using OCV data from literature. The calibration process was used to estimate the ratio of pre-exponential factors of H_2 and CO current densities. The resulting value of 2.54 is in line with values suggested and used by other authors for similar operating conditions. Very good matching between experimental and estimated OCV was obtained during model validation for mixtures with low CH_4 content (0%–5%). The prediction accuracy was either comparable or better compared to using the equilibrium mixture composition to estimate the OCV. For mixtures with relatively large CH_4 concentration (more than 8%), the mixed potential model significantly underestimates the OCV, due to additional H_2 produced by SMR, which is not accounted for by the model developed. Conversely, the equilibrium potential model predicts with reasonable accuracy also the OCV generated by mixtures with relatively large CH_4 concentration. The results from the calibration procedure are used to develop a polarization model of an SOFC fed with a H_2 - H_2O -CO- CO_2 fuel mixture. It is found that a fuel such as CO or H_2 may be electrochemically produced rather than consumed when the cell voltage is close to or equal to the OCV.

Data availability statement

The raw data supporting the conclusion of this article will be made available by the authors, without undue reservation.

References

- Aloui, T., and Halouani, K. (2007). Analytical modeling of polarizations in a solid oxide fuel cell using biomass syngas product as fuel. *Appl. Therm. Eng.* 27, 731–737. doi:10.1016/j.applthermaleng.2006.10.011
- Andersson, M., Yuan, J., and Sundén, B. (2013). Grading the amount of electrochemical active sites along the main flow direction of an SOFC. *J. Electrochem. Soc.* 160, F1–F12. doi:10.1149/2.026301jes
- Andersson, M., Yuan, J., and Sundén, B. (2013). SOFC modeling considering hydrogen and carbon monoxide as electrochemical reactants. *J. Power Sources* 232, 42–54. doi:10.1016/j.jpowsour.2012.12.122
- Andreassi, L., Toro, C., and Ubertini, S. (2009). Modeling carbon monoxide direct oxidation in solid oxide fuel cells. *J. Fuel Cell Sci. Technol.* 6, 0213071–02130715. doi:10.1115/1.3080552
- Baldinelli, A., Barelli, L., and Bidini, G. (2015). Performance characterization and modelling of syngas-fed SOFCs (solid oxide fuel cells) varying fuel composition. *Energy* 90, 2070–2084. doi:10.1016/j.energy.2015.07.126
- Baldinelli, A., Barelli, L., and Bidini, G. (2015). Syngas-fed SOFCs: Analysis of performance sensitivity to fuel composition. *ECS Trans.* 68, 2763–2774. doi:10.1149/06801.2763ecst
- Bao, C., Jiang, Z., and Zhang, X. (2016). Modeling mass transfer in solid oxide fuel cell anode: II. H_2 /CO co-oxidation and surface diffusion in synthesis-gas operation. *J. Power Sources* 324, 261–271. doi:10.1016/j.jpowsour.2016.05.088
- Bockris, J. O., and Reddy, A. K. N. (2000). *Modern electrochemistry 2B. Electrochemistry, engineering, biology, and environmental science*. Second Edition. London: Kluwer Academic Publishers.
- Campanari, S., and Iora, P. (2005). Comparison of finite volume SOFC models for the simulation of a planar cell geometry. *Fuel Cells* 5, 34–51. doi:10.1002/fuce.200400057
- Campanari, S., Mastropasqua, L., Gazzani, M., Chiesa, P., and Romano, M. C. (2016). Predicting the ultimate potential of natural gas SOFC power cycles with CO_2 capture – Part A: Methodology and reference cases. *J. Power Sources* 324, 598–614. doi:10.1016/j.jpowsour.2016.05.104
- Cinti, G., Discepoli, G., Sisani, E., and Desideri, U. (2016). SOFC operating with ammonia: Stack test and system analysis. *Int. J. Hydrogen Energy* 41, 13583–13590. doi:10.1016/j.ijhydene.2016.06.070
- Corigliano, O., and Fragiaco, P. (2020). Extensive analysis of SOFC fed by direct syngas at different anodic compositions by using two numerical approaches. *Energy Convers. Manag.* 209, 112664. doi:10.1016/j.enconman.2020.112664
- De Lorenzo, G., and Fragiaco, P. (2015). Energy analysis of an SOFC system fed by syngas. *Energy Convers. Manag.* 93, 175–186. doi:10.1016/j.enconman.2014.12.086
- Donazzi, A., Rahmanipour, M., Maestri, M., Groppi, G., Bordini, L., Pappacena, A., et al. (2016). Experimental and model analysis of the co-oxidative behavior of syngas feed in an intermediate temperature solid oxide fuel cell. *J. Power Sources* 306, 467–480. doi:10.1016/j.jpowsour.2015.12.038
- Duong, P. A., Ryu, B., Jung, J., and Kang, H. (2022). Thermal evaluation of a novel integrated system based on solid oxide fuel cells and combined heat and power production using ammonia as fuel. *Appl. Sci.* 12, 6287. doi:10.3390/app12126287
- Fan, L., Li, C., van Biert, L., Zhou, S. H., Tabish, A. N., Mokhov, A., et al. (2022). Advances on methane reforming in solid oxide fuel cells. *Renew. Sustain. Energy Rev.* 166, 112646. doi:10.1016/j.rser.2022.112646
- Fleming, W. J. (1977). Physical principles governing nonideal behavior of the zirconia oxygen sensor. *J. Electrochem. Soc.* 124, 21–28. doi:10.1149/1.2133235
- Ishak, F., Dincer, I., and Zamfirescu, C. (2012). Energy and exergy analyses of direct ammonia solid oxide fuel cell integrated with gas turbine power cycle. *J. Power Sources* 212, 73–85. doi:10.1016/j.jpowsour.2012.03.083
- Iwai, H., Yamamoto, Y., Saito, M., and Yoshida, H. (2011). Numerical simulation of intermediate-temperature direct-internal-reforming planar solid oxide fuel cell. *Energy* 36, 2225–2234. doi:10.1016/j.energy.2010.03.058
- Jin, X., Ku, A., Verma, A., Ohara, B., Huang, K., and Singh, S. (2018). The performance of syngas-fueled SOFCs predicted by a reduced order model (ROM): Temperature and fuel composition effects. *J. Electrochem. Soc.* 165, F786–F798. doi:10.1149/2.0511810jes
- Kee, R. J., Zhu, H., and Goodwin, D. G. (2005). Solid-oxide fuel cells with hydrocarbon fuels. *Proc. Combust. Inst.* 30 II, 2379–2404. doi:10.1016/j.proci.2004.08.277
- Kishimoto, M., Muroyama, H., Suzuki, S., Saito, M., Koide, T., Takahashi, Y., et al. (2020). Development of 1 kW-class ammonia-fueled solid oxide fuel cell stack. *Fuel Cells* 20, 80–88. doi:10.1002/fuce.201900131

Author contributions

AC: formal analysis, writing original draft; LM: manuscript review and editing, image processing.

Conflict of interest

The authors declare that the research was conducted in the absence of any commercial or financial relationships that could be construed as a potential conflict of interest.

Publisher's note

All claims expressed in this article are solely those of the authors and do not necessarily represent those of their affiliated organizations, or those of the publisher, the editors and the reviewers. Any product that may be evaluated in this article, or claim that may be made by its manufacturer, is not guaranteed or endorsed by the publisher.

Supplementary material

The Supplementary Material for this article can be found online at: <https://www.frontiersin.org/articles/10.3389/fenrg.2023.1120343/full#supplementary-material>

- Lee, W. Y., Ong, K. M., and Ghoniem, A. F. (2015). Detailed H₂ and CO electrochemistry for a MEA model fueled by syngas. *Syngas* 68, 3059–3074. doi:10.1149/06801.3059ecst
- Mastropasqua, L., Pegorin, A., and Campanari, S. (2020). Low fuel utilisation solid oxide fuel cell system for CO₂-free hydrogen production in oil refineries. *J. Power Sources* 448, 227461. doi:10.1016/j.jpowsour.2019.227461
- Matsuzaki, Y., and Yasuda, I. (2000). Electrochemical oxidation of H₂ and CO in a H₂-H₂O-CO-CO₂ system at the interface of a Ni-YSZ cermet electrode and YSZ electrolyte. *J. Electrochem Soc.* 147, 1630. doi:10.1149/1.1393409
- Ni, M. (2012). An electrochemical model for syngas production by co-electrolysis of H₂O and CO₂. *J. Power Sources* 202, 209–216. doi:10.1016/j.jpowsour.2011.11.080
- Park, J., Li, P., and Bae, J. (2012). Analysis of chemical, electrochemical reactions and thermo-fluid flow in methane-feed internal reforming SOFCs: Part i - modeling and effect of gas concentrations. *Int. J. Hydrogen Energy* 37, 8512–8531. doi:10.1016/j.ijhydene.2012.02.110
- Penchini, D., Cinti, G., Discepoli, G., Sisani, E., and Desideri, U. (2013). Characterization of a 100 W SOFC stack fed by carbon monoxide rich fuels. *Int. J. Hydrogen Energy* 38, 525–531. doi:10.1016/j.ijhydene.2012.09.060
- Petruzzi, L., Cocchi, S., and Fineschi, F. (2003). A global thermo-electrochemical model for SOFC systems design and engineering. *J. Power Sources* 118, 96–107. doi:10.1016/S0378-7753(03)00067-3
- Razbani, O., Assadi, M., and Andersson, M. (2013). Three dimensional CFD modeling and experimental validation of an electrolyte supported solid oxide fuel cell fed with methane-free biogas. *Int. J. Hydrogen Energy* 38, 10068–10080. doi:10.1016/j.ijhydene.2013.05.153
- Sang, J., Li, Y., Yang, J., Wu, T., Luo, X., Chi, B., et al. (2022). Power generation by flat-tube solid oxide fuel cells with enhanced internal reforming of methanol. *ACS Sustain Chem. Eng.* 10, 6276–6288. doi:10.1021/acssuschemeng.2c00518
- Spallina, V., Mastropasqua, L., Iora, P., Romano, M. C., and Campanari, S. (2015). Assessment of finite volume modeling approaches for intermediate temperature Solid Oxide Fuel Cells working with CO-rich syngas fuels. *Int. J. Hydrogen Energy* 40, 15012–15031. doi:10.1016/j.ijhydene.2015.08.101
- Stempien, J. P., Ding, O. L., Sun, Q., and Chan, S. H. (2012). Energy and exergy analysis of Solid Oxide Electrolyser Cell (SOEC) working as a CO₂ mitigation device. *Int. J. Hydrogen Energy* 37, 14518–14527. doi:10.1016/j.ijhydene.2012.07.065
- Stempien, J. P., Sun, Q., and Chan, S. H. (2013). Performance of power generation extension system based on solid-oxide electrolyzer cells under various design conditions. *Energy* 55, 647–657. doi:10.1016/j.energy.2013.03.031
- Stoots, C. M., O'Brien, J. E., Herring, J. S., and Hartvigsen, J. J. (2009). Syngas production via high-temperature coelectrolysis of steam and carbon dioxide. *J. Fuel Cell Sci. Technol.* 6, 0110141–0110142. doi:10.1115/1.2971061
- Suwanwarangkul, R., Croiset, E., Entchev, E., Charojrochkul, S., Pritzker, M. D., Fowler, M. W., et al. (2006). Experimental and modeling study of solid oxide fuel cell operating with syngas fuel. *J. Power Sources* 161, 308–322. doi:10.1016/j.jpowsour.2006.03.080
- Vágner, P., Kodým, R., and Bouzek, K. (2019). Thermodynamic analysis of high temperature steam and carbon dioxide systems in solid oxide cells. *Sustain Energy Fuels* 3, 2076–2086. doi:10.1039/c9se00030e
- Wang, Y., Liu, T., Lei, L., and Chen, F. (2017). High temperature solid oxide H₂O/CO₂ co-electrolysis for syngas production. *Fuel Process Technol.* 161, 248–258. doi:10.1016/j.fuproc.2016.08.009
- Zhu, H., and Kee, R. J. (2003). A general mathematical model for analyzing the performance of fuel-cell membrane-electrode assemblies. *J. Power Sources* 117, 61–74. doi:10.1016/S0378-7753(03)00358-6



OPEN ACCESS

EDITED BY

Mohammadreza Aghaei,
Norwegian University of Science and
Technology, Norway

REVIEWED BY

Atse Louwen,
Eurac Research, Italy
Aref Eskandari,
Amirkabir University of Technology, Iran

*CORRESPONDENCE

Dorian Esteban Guzman Razo,
✉ dorianeguzman@gmail.com

RECEIVED 03 October 2022

ACCEPTED 15 May 2023

PUBLISHED 01 June 2023

CITATION

Guzman Razo DE, Madsen H and
Wittwer C (2023), Genetic algorithm
optimization for parametrization, digital
twinning, and now-casting of unknown
small- and medium-scale PV systems
based only on on-site measured data.
Front. Energy Res. 11:1060215.
doi: 10.3389/fenrg.2023.1060215

COPYRIGHT

© 2023 Guzman Razo, Madsen and
Wittwer. This is an open-access article
distributed under the terms of the
[Creative Commons Attribution License
\(CC BY\)](#). The use, distribution or
reproduction in other forums is
permitted, provided the original author(s)
and the copyright owner(s) are credited
and that the original publication in this
journal is cited, in accordance with
accepted academic practice. No use,
distribution or reproduction is permitted
which does not comply with these terms.

Genetic algorithm optimization for parametrization, digital twinning, and now-casting of unknown small- and medium-scale PV systems based only on on-site measured data

Dorian Esteban Guzman Razo^{1*}, Henrik Madsen² and
Christof Wittwer¹

¹Fraunhofer ISE, Fraunhofer Institute for Solar Energy Systems, Freiburg, Germany, ²Department of Applied Mathematics and Computer Science (DTU Compute), Technical University of Denmark, Kongens Lyngby, Denmark

Accurately predicting and balancing energy generation and consumption are crucial for grid operators and asset managers in a market where renewable energy is increasing. To speed up the process, these predictions should ideally be performed based only on on-site measured data and data available within the monitoring platforms, data which are scarce for small- and medium-scale PV systems. In this study, we propose an algorithm that can now-cast the power output of a photovoltaic (PV) system with high accuracy. Additionally, it offers physical information related to the configuration of such a PV system. We adapted a genetic algorithm-based optimization approach to parametrize a digital twin of unknown PV systems, using only on-site measured PV power and irradiance in the plane of array. We compared several training datasets under various sky conditions. A mean deviation of -1.14 W/kW_p and a mean absolute percentage deviation of 1.81% were obtained when we analyzed the accuracy of the PV power now-casting for the year 2020 of the 16 unknown PV systems used for this analysis. This level of accuracy is significant for ensuring the efficient now-casting and operation of PV assets.

KEYWORDS

machine learning, genetic algorithms, auto-calibrated algorithms, photovoltaic systems, parameter estimation, digital twin, PV power forecasting, PV system modeling

1 Introduction

Photovoltaic (PV) system installed capacity has doubled globally in the past 3 years, hitting a terawatt in April 2022, and is projected to reach 2.3 TW by 2025 ([SolarPower Europe, 2022](#)). The surge in PV capacity is being driven by a variety of factors, including favorable laws and growing public knowledge of solar energy's advantages, which are causing this remarkable increase. According to predictions by the International Energy Agency (IEA) in 2022, PV electricity will generate an extra 180 TW-hours by 2030, making up 60% of all renewable energy production ([International Energy Agency, 2022](#)). An additional important factor contributing to the success of PV systems is their rapidly declining cost. The average

global weighted levelized cost of electricity (LCOE) for the utility-scale PV has dropped by 13% per year since 2010, reaching around 4.8 cents per kilowatt-hour in 2021 (IRENA, 2021). This trend is expected to continue as technology improves and economies of scale are reached, making solar energy an increasingly attractive and cost-effective option for energy generation.

Simulating and forecasting the PV power output of a utility-scale PV plant is very important for both plant managers and electricity network operators. Indeed, an accurate PV yield study is one of the most crucial elements for a successful bankability and feasible study of a PV power plant (Müller et al, 2016). Reliable irradiance data and an effective PV power simulation tool are crucial for correctly forecasting the power output of a PV system. Although the irradiance data should be approximated with high accuracy and temporal resolution, the simulation tool should mimic the behavior of a PV system under various weather and operating conditions. These two elements can be used to produce an accurate and reliable PV yield study (Müller et al, 2007). Achieving an accurate PV power simulation often requires specific physical and technical data for the PV system or subsystem being modeled, according to Müller et al (2007). Yet, these data are not always available or may be incomplete for certain PV systems or subsystems in a larger PV portfolio. As a result, accurate power prediction for such systems may be challenging. Moreover, irradiance data used for PV power simulation can be derived from satellite observations or measured on-site. However, inconsistencies between the on-site and satellite-derived irradiance data can propagate proportionally up to the simulated PV power output. Furthermore, inaccuracies in the different models used within the PV power modeling process can amplify these errors (Urraca et al, 2018a).

As suggested in IEC 61850-7-420 (IEC, 2009), PV systems are expected to have basic meteorological measurement devices for ambient temperature and solar irradiation. Considering this, our work focuses on developing an optimization algorithm that learns the basic parameters of an unknown small- or medium-scale PV system or subsystem. Thereby, an accurate PV power simulation is implemented based on only the on-site measured PV power and on-site measured meteorological data.

This work is a continuation of a previous publication (Guzman Razo et al, 2020), in which we used a genetic algorithm (GA) approach to parametrize and create a digital twin of an unknown PV system based on the measured PV power and data provided by SolarGIS s.r.o., including air temperature and satellite-derived irradiation. Next, we created a digital twin and accurately simulated the behavior of that specific PV power plant under different outdoor conditions. This publication will be referred to as *Guzman1* in the following sections of this work.

GA optimization offers a deterministic and time-efficient alternative for curve fitting. Additionally, GA optimization characteristically offers an alternative (crossover and mutation) to avoid solving for local minima. In contrast with *Guzman1*, in this work, we created a digital twin of an unknown small- or medium-scale PV system without exogenous information. In other words, the current GA optimization approach is based on only the on-site measured PV power and on-site measured meteorological data, specifically, module temperature (T_{mod}) and irradiance in the

plane of array (G) data (considered to be the most accurate source of irradiance data for PV power simulations (Urraca et al, 2018b)).

This work aims to

- Show an accurate method to create a digital twin of a PV system based on the GA optimization;
- Learn and optimize basic parameters of an unknown PV system or subsystem without the need for external data, including the PV module temperature coefficient, Heydenreich a , b , and c , DC-to-AC ratio, and nominal power;
- Evaluate the accuracy of the digital twin created with different lengths of training data;
- Evaluate the now-cast precision of a digital twin trained with either all-sky or clear-sky conditions;
- Propose potential accuracy improvement for the GA optimization approach proposed in this study.

This article is structured as follows: We present a summary of previous publications for PV simulation and forecasting using exclusively monitoring data and metrics to evaluate the results (Section 2). In Section 3, we show how we adapted the methodology from *Guzman1* and present a description of the data to be used within this study. In Section 4, we offer a discussion regarding the results of the GA optimization, namely, digital twin parameters and the now-casting results using these parameters. In addition, we validate the methodology proposed in the current study and propose an example to improve the now-casting accuracy considering additional weather information. Finally, in Section 5, we present the main conclusion of this work and future improvements.

2 Literature overview and evaluation metrics

Short-term PV power forecasting is key for achieving a balance between energy consumption and production in a grid with high PV penetration, applications for storage management, and reliability of the bidding markets. This work focuses on creating an accurate tool that can be applied for PV parameter extraction and short-term PV power forecasting.

In this section, we present methods suggested in the literature to create a model of a PV system and the use of that model for short-term forecasting with no additional data to those collected on-site by the data acquisition systems. Moreover, in this section, we show the accuracy metrics used to evaluate the method proposed in this publication.

2.1 PV system modeling methods for short-term power forecasting without external inputs

At present, several machine-learning approaches have been studied to develop models for PV power forecasting. These models use on-site power-measured data in combination with numerical weather prediction or satellite-derived data. These

methods commonly minimize data used while increasing the overall accuracy of the solution. However, these approaches rarely provide a physical description of the PV system's components and configuration. In this study, we focus on methods without exogenous data, in other words, methods that include exclusively on-site PV power-measured data and on-site measured weather data.

Mandal et al (2012) offered a solution with a mix of wavelet transform (WT) and different machine learning techniques. A PV system model is created by dividing the PV power time-series data between the ill-mode and non-linear fluctuations (spikes in power). After that, four components are extracted by downsampling and then filtered using low-pass filters. Finally, the PV system model is obtained after a wavelet reconstruction, including some upsampling after feeding each one of the individual components from the TW into different neural networks. A mean absolute percentage deviation (MAPD) of 2.38% can be achieved for clear-sky periods of PV power forecasting. This method has a horizon of 12 h, and its performance decreases considerably when cloudy or rainy days are forecasted (Mandal et al, 2012).

Almeida et al (2015) proposed an alternative model for PV power output forecasting that includes on-site weather data. They applied a random forest (RF) model to create a PV model and then used numerical weather prediction data to forecast the PV power output. The results suggested an MAPD of 9.5% between the forecasted and the on-site measured data (Almeida et al, 2015).

This contribution proposed a data-driven approach based on the use of artificial neural networks (ANNs) trained with measured PV power to create day-ahead forecasts of PV power. Unlike other methods, this solution does not require any weather data and offers an MAPD of 6.64% for the best-case scenario.

The suggestions from González Ordiano et al (2017) on using weather-free approaches based on machine learning techniques are particularly relevant. This contribution proposed a data-driven approach based on the use of ANNs trained with measured PV power to create day-ahead forecasts of PV power. Unlike other methods, this solution does not require any weather data and offers an MAPD of 6.64%, for the best-case scenario (González Ordiano et al, 2017).

In contrast to the various machine learning solutions, there are only a few physics-based or hybrid methods in the literature that provide a description of a specific PV system or subsystem's configuration.

The article by Ogliari et al (2017) presents a model for next-day PV power forecasting based on the well-known single-diode model, which can consider either three or five parameters. In addition, the authors propose two other approaches, an ANN model and a hybrid model combining both physical and ANN models, for next-day forecasting. The ANN and hybrid models use historical weather data for training, with two different training approaches. However, it is important to note that the physical parameters required for the single-diode model need to be determined from the PV module's datasheet or from previous experiments (Ogliari et al, 2017).

It is important to mention that the physical model used in Ogliari et al can only describe the behavior of a PV module under outdoor conditions without considering the losses from the rest of the components of a PV system or subsystem, i.e., cabling losses and inverter efficiency (DC-to-AC ratio). Ogliari et al reported achieving

mean absolute deviations (MADs) of 19.1 W and 20.2 W for the three- and five-parameter physical models, respectively. In the case of the hybrid method, the MAD is 12.46 W for the best case of the first training approach and 12.5 W for the best case of the second training approach.

2.1.1 Evaluation metrics

Similar to *Guzman1*, we used four values to evaluate the accuracy of the digital twin created by the GA optimization method offered here, i.e., root mean square deviation (RMSD), MAPD, mean bias deviation (MBD), and MAD. Eqs. 1–4, respectively, show how we calculate the values.

$$RMSD = \sqrt{\frac{1}{n} \sum_{i=1}^n (y_i - x_i)^2}, \quad (1)$$

$$MAPD = \frac{100}{n} \sum_{i=1}^n \frac{|y_i - x_i|}{|y_i|}, \quad (2)$$

$$MBD = \frac{1}{n} \sum_{i=1}^n (x_i - y_i), \quad (3)$$

$$MAD = \frac{1}{n} \sum_{i=1}^n |y_i - x_i|, \quad (4)$$

where y_i is the actual value, x_i is the estimated value, and the number of observations is n . Estimated values and actual values exclude nighttime.

3 Methodology and data

In this work, we adapted some steps of a PV power simulation tool developed in-house by Fraunhofer ISE and suggested by Dirnberger et al (2015) and Müller et al (2016). We optimized the parameters required by the PV system simulation tool using the GA and created a digital twin of an unknown PV system or subsystem.

Figure 1 shows the overall methodology used to parameterize an unknown PV system or subsystem, with the GA optimization process, the PV system simulation tool (and its main models), the inputs (i.e., initial parameters, and on-site measured meteorological and PV power), and the optimized parameters as an output, which are later used as a digital twin. The green dotted rectangle represents the GA optimization process, while the orange dotted rectangle represents the PV system simulation process and its corresponding steps.

3.1 PV system simulation

As shown in the orange rectangle in Figure 1, the adapted PV system simulation tool can simulate AC PV power with only on-site measured T_{mod} and G as inputs. Comparable to *Guzman1*, the simulation tool proposed here neglects some PV power performance losses, such as soiling, degradation, snow, and inter-row shading. However, surrounding shading loss effects (horizon line) can be included in the G on-site measurements, in addition to specific objects projecting shadow to a particular part of the PV system or subsystem. The PV system simulation model proposed here comprises two main steps, DC PV power and AC PV power:

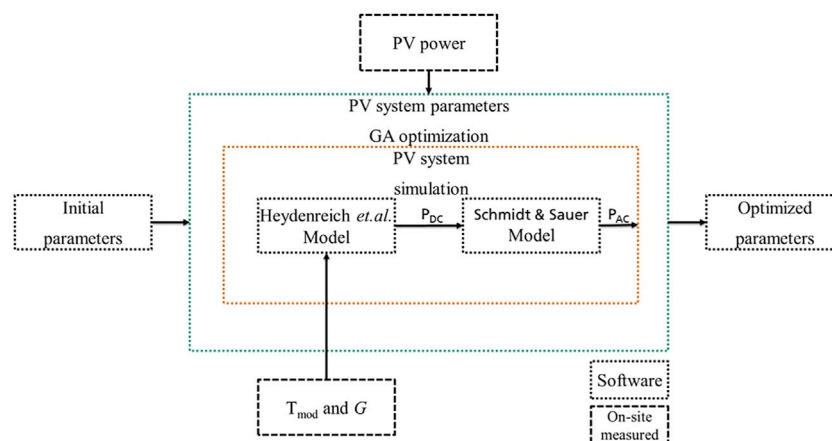


FIGURE 1
Interaction between inputs and outputs of the overall GA optimization methodology.

Using equations suggested by Heydenreich et al (2008) (Eqs. 5, 6), we simulated DC PV power (Heydenreich et al, 2008). First, the DC PV power at a temperature of 25°C, or standard test conditions (STCs) Eq. 5, was simulated, and later, we translated that simulated DC PV power to the on-site measured temperature and irradiance conditions Eq. 6.

$$\eta(G, T_{STC}) = aG + b \ln(G + 1) + c \left(\frac{\ln^2(G + e)}{G + 1} - 1 \right), \quad (5)$$

where T_{STC} is 25°C, and a , b , and c are constants defining the PV module efficiency curve at a specified G .

$$\eta(G, T_{mod}) = \eta(G, T_{STC}) (1 + \gamma(T_{mod} - T_{STC})), \quad (6)$$

where γ represents the PV module temperature coefficient, T_{mod} represents the PV module temperature measured on-site, and in both equations, and η represents the PV module efficiency at specific conditions.

To simulate AC PV power output, we used the inverter model proposed by Schmidt and Sauer (1994), accounting for 1% of cabling losses (Schmidt and Sauer, 1994).

3.2 Detection of clear-sky moments and GA optimization

To define the best climatic conditions for the parameter extraction, in the GA optimization training phase, we created two different training sets:

- The first set includes all possible conditions measured on-site i.e., overcast and clear-sky-like moments. This training dataset will be referred to in this work as *all-sky*.
- The second set filters out the overcast moments and only includes clear-sky-like moments. This training dataset will be referred to in this work as *clear-sky*.

We detected and filtered clear-sky-like moments based on the two-step process described in detail in Guzman1. First, based on the

on-site measured PV power data, a statistical clear-sky curve was created following the method implemented and proposed by Stein et al (2012) and Reno and Hansen (2016). Next, with the “detect_clearsky” function from the PVLib library (Holmgren et al, 2020), we detected clear-sky-like moments. Training datasets of both clear-sky and all-sky moments comprised only on-site measured PV power data and their correspondent on-site measured T_{mod} and G being used in this study.

In general terms, we based our GA algorithm on the technique proposed by Holland (1975). Although GA optimization is considered a traditional optimization algorithm, it has been rarely implemented in the solar industry. Moreover, inherently, the GA optimization offers an accurate and time-efficient deterministic approximation of the real parameters of unknown PV systems and subsystems. Additionally, the GA performs effectively for problems relating to dynamic environments where an optimal answer can evolve over time. In these situations, the solution space might be too big to thoroughly explore, and the ideal answer can change as the situation changes (Mori and Kita, 2000).

The novelty of this work relies on the fact that we can extract the main characteristics of an unknown PV system or subsystem by implementing a similar GA optimization to the one proposed by Holland (1975) within a stepwise process. In this work, we opted for a stepwise optimization process to reduce the compensation between parameters.

To extract the most accurate PV system parameters, we minimized the MAD (see Eq. 4) between simulated AC PV power and on-site measured AC PV power. The MAD of the best member of the population and population mean MAD are two key performance indexes to monitor throughout the GA optimization. The optimization process is interrupted if neither of the two performance indexes improves any more. A detailed description of this process can be found in Guzman1.

In the GA optimization, to create the initial population of PV system parameters to be evaluated and optimized, we began by defining the initial parameters for this work as 1-kilowatt peak (kW_p) for nominal power, −0.43 %/°C for the power temperature coefficient, and a ratio of 1 for the DC to AC power.

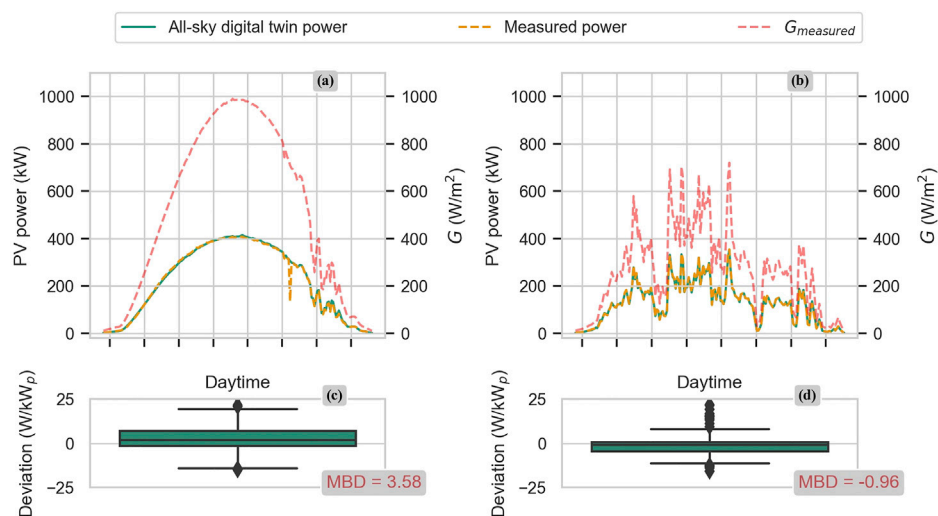


FIGURE 2

Two-day results of a digital twin from a system located in southwest Germany. In subfigure (A, B), the red dotted line shows the irradiance G measured on-site, the orange dotted line shows the AC PV power measured on-site, and the solid green line shows the AC PV power forecasted by the digital twin parametrized with a 30-days long data set considering all-sky conditions. Subfigures (C, D) show the deviation between the AC PV power measured on-site and the AC PV power forecasted. The left side of FIGURE 2 shows a clear-sky like day and the right side shows an overcast-like day.

Next, we normalized the on-site measured AC PV power by the maximum measured value. By normalizing on-site measured AC PV power, we compared it with the simulated AC PV power of a 1-kWp installed capacity system. It is important to mention that the measured G must be in the same plane of array of the PV system or subsystem. After the AC PV power is normalized, the subsequent steps are followed to complete the optimization process for the assumed 1-kWp PV system:

- With cross-validation optimization, we selected the best set of a , b , and c parameters for (Eq. 5). The cross-validation optimization process was based on a database comprising 107 sets of three parameters, described in *Guzman1*, including the results from Fraunhofer ISE CalLab efficiency measurements of 107 PV modules at different irradiance levels. We simulated DC PV power, using each one of the 107 sets of parameters, and compared it with the normalized AC PV power. We considered the lower MAD as the optimum set of parameters for the simulated PV system.
- We used GA optimization to learn the PV module temperature coefficient by minimizing the MAD between simulated DC PV power resulting from Eq. 6) and normalized-measured AC PV power.
- To optimize the DC-to-AC ratio, we used GA optimization to minimize the MAD between simulated AC PV power (based only on the efficiency section of the Schmidt and Sauer model) and normalized-measured AC PV power.



FIGURE 3

Location of the 16 real on-site measured PV systems.

TABLE 1 Nominal power and *G* sensor description for each of the 16 PV systems.

System	Nominal power (kW _p)	Sensor ^a	System	Nominal power (kW _p)	Sensor ^a
ID 1	36	1	ID 9	555	2
ID 2	899	2	ID 10	1,000	2
ID 3	999	2	ID 11	497	1
ID 4	910	1	ID 12	1,202	1
ID 5	553	2	ID 13	293	1
ID 6	713	2	ID 14	829	1
ID 7	595	2	ID 15	1,012	1
ID 8	678	2	ID 16	1,045	1

^a1 = Mencke and Tegtmeier Si reference cell; 2 = Kipp and Zonen CMP11 pyranometer.

- Finally, we used GA optimization to minimize the MAD between simulated AC PV power and measured AC PV power (non-normalized) to extract the PV system nominal power.

The results obtained from applying the PV models with the optimized parameters in this study accurately reflect the real behavior of the tested PV system. As a result, by using these optimized parameters, we can create a digital twin of the PV system or subsystem and simulate its performance by changing the irradiance and temperature conditions to current (now-cast) or future (forecast) values.

Figure 2 shows two digital twins created from on-site measurements of a system located in southwest Germany with a training dataset of 30 days length (before the day to be tested), in which all-sky conditions are considered. On the left-hand side, subplot (a) shows a PV power simulation for a clear-sky-like day: measured PV power, the measured *G*. Subplot (c) shows the deviation between the simulated and measured PV power in W/kW_p. On the right-hand side, subplot (b) shows overcast-like day results: simulated PV power, measured PV power, and measured *G*. Subplot (d) shows the deviation between the simulated and measured PV power in W/kW_p. On-site data for the optimization have been measured during the year 2020, and the results presented in this example considered only daytime measurements.

3.3 Data used in this publication

In this work, we used a database comprising 16 real on-site measured PV systems installed in Germany, which are part of the Fraunhofer ISE monitoring portfolio. The geographical location of those systems can be observed in Figure 3.

The database used here, collected between 2018 and 2020, consists of a time series of approximately 567,500 points of 5-min resolution including three main features: measured PV power, measured *T_{mod}*, and measured *G*. Table 1 shows the nominal power and the *G* sensor installed at each location of the 16 PV systems. PV systems from 36 kW_p up to 1,202 kW_p were considered in this publication.

Additionally in Section 4.3.1, we used daily observations of snow depth data from the Deutscher Wetterdienst (German Weather Service) climate data center (CDC) (Kaspar et al, 2013) for the year 2020, for all 16 locations.

4 Results and discussion

In the first part of this section, our goal was to demonstrate the impact of different lengths of training datasets on the parametrization and now-casting performance of the digital twin. We analyzed data from a PV system located in southwest Germany (ID 5) to investigate this effect. The selection of PV system ID 5 was arbitrary and was chosen out of the 16 real PV systems in our database to randomize the process and prioritize our research on the effect of different training dataset lengths on PV system parametrization.

The reported design parameters from the PV system ID 5 are the following:

- Temperature coefficient (%/°C): **-0.43**
- Heydenreich a: **0.001084**
- Heydenreich b: **-7.247061**
- Heydenreich c: **-156.5457**
- DC-to-AC ratio: **1.04**
- Nominal power (kW_p): **553**
- Year of construction: **2010**

Next, we evaluated the rest of the PV systems within the database using the best-performing length for training the digital twin. Additionally, we investigated the potential for improving now-casting accuracy by considering locally measured snow deposition information. Finally, we discuss limitations and possible future improvements at the end of this section.

4.1 Digital twin parametrization

To evaluate the effect of seasonality and the length of training data on the parametrization of the digital twin and the accuracy of now-casting, we randomly selected 1 day per week of the year 2020

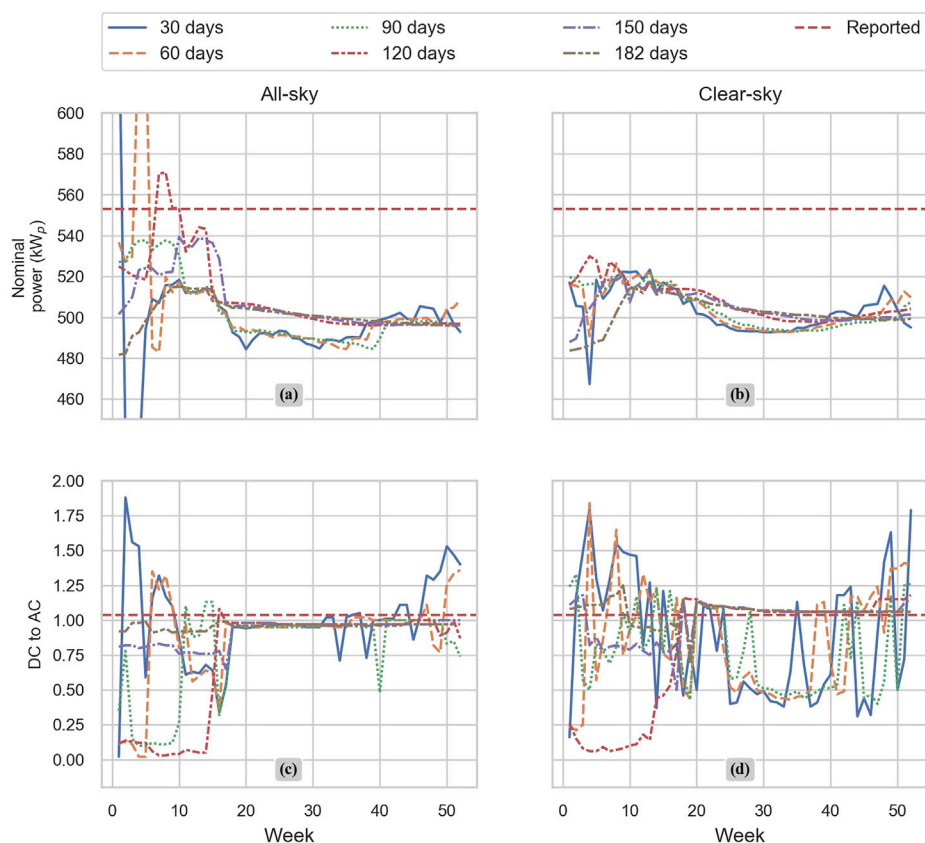


FIGURE 4

GA optimization results for nominal power and the DC-to-AC ratio. A total of 52 days were chosen, of the year 2020 considering six different training datasets for each day; all-sky and clear-sky conditions with 30, 60, 90, 120, 150, and 182 days of training datasets. The 30-day dataset is represented by the solid blue line, 60-day dataset is represented by the orange dashed-line, 90-day dataset is represented by a green dotted line, 120-day dataset is represented by the dotted-dashed red line, 150-day dataset is represented by the dotted-dashed blue line, 182-day dataset is represented by the dotted-dashed brown line, and the reported parameter is represented by a horizontal red dashed-line. Figure 4 is divided into left-hand (A, C) and right-hand (B, D) sections. The left-hand subplots (A, C) show optimized parameters for all-sky condition optimization, whereas the right-hand side subplots (B, D) show optimized parameters considering only clear-sky conditions.

(a total of 52 days). For each selected day, we used six different training dataset lengths, including 30, 60, 90, 120, 150, and 182 days prior to the selected day. We also identified clear-sky conditions within all the training datasets and trained the GA using both all-sky and clear-sky moments. Each combination of training dataset length, selected day, and all/clear-sky moments resulted in a different set of parameters (digital twin) for the PV system under consideration.

Figure 4 shows plots of optimization results for nominal power and the DC-to-AC ratio, considering 52 randomly chosen days and different training set lengths: 30, 60, 90, 120, 150, and 182 days. Optimization results for the temperature coefficient have been reported constantly throughout the 52 days ($-0.4/^{\circ}\text{C}$) and, therefore, are not shown in the figure. In general, while considering all-sky moments, the DC-to-AC ratio (see subplot c)) remains more constant than while considering only clear-sky moments. In contrast to that, optimization for nominal power remains more stable while considering only clear-sky moments (see subplot b)).

The results of a quantitative analysis are included in Table 2. The analysis includes results from the GA optimization considering

clear-sky and all-sky conditions for all the different training length datasets.

One of the advantages of parametrizing a PV system or subsystem based on only on-site measured data (including G) is the low variability of optimized parameters over time. As shown in Table 2, a training length of a minimum of 120 days is a common agreement between the best results, considering both clear-sky and all-sky moments.

The parametrization results for nominal power shown in Figure 4 are on the side of an underestimation. As mentioned previously, using only clear-sky moments seems to be more stable. As shown in Table 2, the best conditions for an accurate nominal power parametrization are as follows: all-sky conditions in combination with a 120-day training length. This combination shows a mean value of 510.55 kW_p with a MAPD of only 7.93% and an MBD of only -42.45 kW_p . In contrast to our previous publication (Guzman Razo et al, 2020), these values have reduced considerably from 10.69% and -84.24 kW_p , respectively. This is most likely due to the increase in accuracy of G which was measured on-site instead of using satellite-based irradiance information.

TABLE 2 Parametrization results of the GA optimization for PV system ID5 including all-sky and clear-sky conditions.

Sky	Training length (days)	Parameter							
		Nominal power (Reported: 553 kW _p)				DC-to-AC ratio (Reported: 1.04)			
		Mean (kW _p)	MAPD (%)	MBD (kW _p)	RMSD (kW _p)	Mean	MAPD (%)	MBD	RMSD
All	30	497.71	10.70	-55.29	61.97	0.99	21.78	-0.05	0.32
	60	504.94	9.94	-48.06	56.66	0.88	21.65	-0.16	0.36
	90	502.84	9.07	-50.16	52.89	0.79	24.94	-0.25	0.41
	120	510.55	7.93	-42.45	46.85	0.72	30.81	-0.32	0.51
	150	507.50	8.23	-45.50	47.52	0.91	12.30	-0.13	0.16
	182	501.22	9.36	-51.78	52.26	0.96	7.78	-0.08	0.08
Clear	30	503.71	8.91	-49.29	50.47	0.87	40.16	-0.17	0.47
	60	504.64	8.75	-48.36	49.36	0.86	34.87	-0.18	0.43
	90	504.44	8.78	-48.56	49.51	0.78	32.47	-0.26	0.39
	120	508.02	8.13	-44.98	45.89	0.81	29.36	-0.23	0.49
	150	504.83	8.71	-48.17	48.70	1.00	10.21	-0.04	0.15
	182	502.17	8.71	-50.83	51.43	1.06	5.70	0.02	0.08

Bold values represent the best parametrization results for both different sky conditions and different length data set.

Given that the reported nominal power value is 553 kW_p, there is still a deviation between it and the value extracted using the GA model. One possible explanation for this deviation could be attributed to a degradation rate, which according to Jordan et al (2016), is expected to be between 0.8% and 0.9% per year since the installation year (Jordan et al, 2016). For system ID5, which has been installed for 10 years to the date of the experimental data, a degradation rate of between 8% and 9% can be expected, resulting in a nominal power between 508.76 kW_p and 503.23 kW_p. The value calculated using the proposed GA model shows good agreement with the expected value. However, this should not be taken lightly as additional power losses can exist and require further investigation.

It seems that there is a trade-off between using all-sky conditions and clear-sky moments for parametrization of the AC-to-DC ratio; see Figure 4. Although all-sky conditions provide more stable results in a particular period, clear-sky moments tend to result in spreader results on the side of overestimation. However, regardless of the condition used, a training length of 182 days seems to be the most suitable for accurate parametrization; see Table 2. The best-case scenario shows a mean value of 1.06 with a 5.7% MAPD and an MBD of 0.02, which is an improvement from the MBD of -0.14 achieved in Guzman1.

As mentioned previously, a constant parameter has been estimated for the 52 test days for the power temperature coefficient. Therefore, the parametrization results of the Heydenreich et al model for PV system ID5, considering both scenario clear-sky and all-sky moments, are the following:

- Heydenreich a: **0.004326**
- Heydenreich b: **-11.275966**

TABLE 3 Accuracy results of the digital twins created for 52 randomly chosen days in the year 2020. A total of 12 different training datasets including all-sky and clear-sky conditions with lengths of 30, 60, 90, 120, 150, and 182 days.

Error metric	Training dataset length (days)					
	30	60	90	120	150	182
All-sky conditions						
MBD (W/kW _p)	3.91	4.14	4.03	2.09	3.12	3.27
MAPD (%)	1.13	1.17	1.29	1.05	0.96	0.91
RMSD (W/kW _p)	11.83	12.10	11.90	11.96	11.44	11.04
Clear-sky conditions						
MBD (W/kW _p)	3.93	4.26	4.72	3.61	4.66	4.81
MAPD (%)	0.98	1.05	1.08	1.01	0.94	0.92
RMSD (W/kW _p)	10.77	11.11	11.49	11.57	11.48	11.27

Bold values represent the best parametrization results for both different sky conditions and different length data set.

- Heydenreich c: **-182.272483**

Although the optimal conditions for parametrizing the presented model are defined based on clear-sky or all-sky conditions and the length of the training dataset, the accuracy of the now-casting must also be evaluated. For instance, if the nominal power is close to the reported value, it would receive a higher score. However, these values do not account for additional losses that are commonly present in PV systems under outdoor conditions, such as soiling and degradation.

Therefore, in the following subsection, we evaluated the accuracy of now-casting using the parameters calculated with different training dataset lengths.

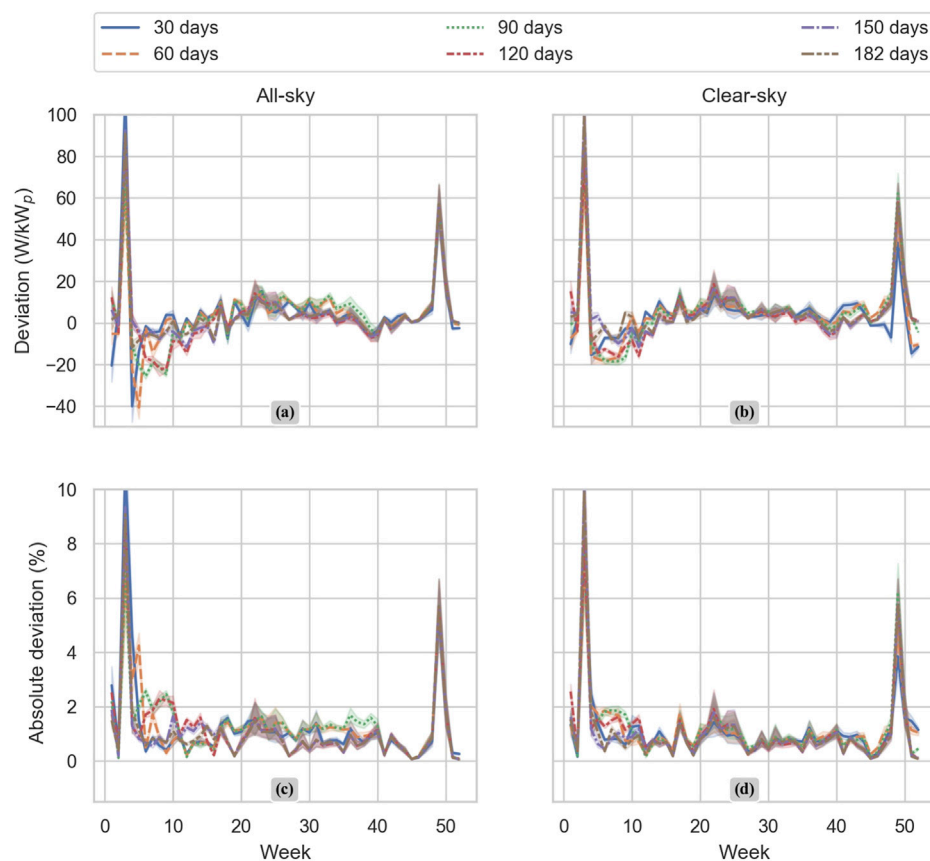


FIGURE 5

Digital twin now-casting results based on GA optimization. A total of 52 days chosen in the year 2020. Six different training datasets for each day were considered: All-sky and clear-sky conditions with 30, 60, and 90 days of training datasets. 95% confidence interval. The 30-day dataset is represented by the solid blue line, the 60-day dataset is represented by the orange dashed line, the 90-day dataset is represented by a green dotted line, the 120-day dataset is represented by the dotted-dashed red line, the 150-day dataset is represented by the dotted-dashed blue line, the 182-day dataset is represented by the dotted-dashed brown line, and the reported parameter is represented by a horizontal red dashed line. Figure 5 is divided into two vertical sections; on the left-hand side, we can see the results of the now-casting considering all-sky conditions (A, C), and the right-hand side, shows the results from the now-casting considering only clear-sky conditions (B, D).

4.2 Digital twin now-casting

To select the optimal training length for the GA algorithm presented here, in this section, we evaluate simulated PV power with parameters from the digital twin considering only daytime values. We randomly selected 52 days from the year 2020 of System ID 5 and generated a set of parameters for each of the 52 days in combination with different training lengths (30 days, 60 days, 90 days, 120 days, 150 days, and 182 days). Finally, we compared the simulated PV power with the on-site measured PV power.

To generalize and correlate the results offered here with any other PV system or subsystem, we measured the deviation in W/kW_p installed. Table 3 shows the results of now-casting for all the training datasets (30, 60, 90, 120, 150, and 182 days) and all the conditions (all-sky and clear-sky).

We evaluated the now-casting results based on the MAPD parameter. As shown in Table 3, the best combination of conditions and training length is achieved with all-sky conditions and a 182-day training dataset, resulting in an MAPD of 0.91%.

Figure 5 shows that the high variation in the parameterization, particularly in the DC-to-AC ratio, is not necessarily reflected in the now-casting results. The now-casting deviation using all-sky conditions (subfigure (a)) is consistently underestimated compared to the deviation using only clear-sky conditions (subfigure (b)), particularly for short training datasets (30–90 days). However, the absolute deviation of the now-casting is similar for both all-sky and clear-sky conditions, particularly for longer training data sets (120–182 days).

Based on the results presented here, we considered that 182 days (or 6 months) based on all-sky conditions is the minimum required length to train GA optimization. With these condition-training lengths, it is possible to achieve an MBD of 3.27 kW_p and an MAPE of only 0.91%. Previous publications, including Guzman1, reported an MAPE from 6% to 10% for now-casting tests (Ding et al, 2011; Mandal et al, 2012; Kaspar et al, 2013; Monteiro et al, 2013; Ibrahim et al, 2015; Landelius et al, 2019; Guzman Razo et al, 2020).

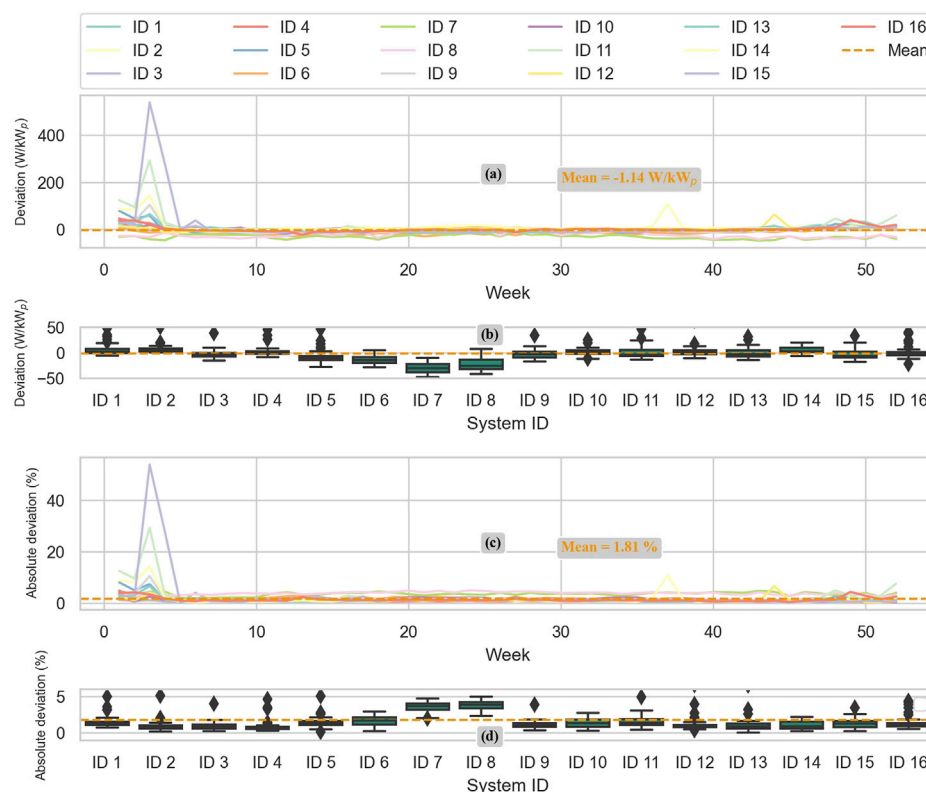


FIGURE 6

Deviation and absolute deviation of 52 days for now-casting for all the 16 real PV systems. In the upper section of the plot, subplots (A) and (B) show the deviation in W/kW_p installed between the power now-casting and the power measured on-site. In the lower section of the plot, subplots (C) and (D) show the absolute deviation in percentage between the power now-casting and the power measured on-site. Subplots (A) and (C) show the distribution of the deviation per day and the mean value over all 16 PV systems. Subplots (B) and (D) show boxplots representing the distribution of the deviation per PV system, and high deviations are considered outliers and therefore ignored (see System ID 15, week 4).

4.3 Digital twin validation

According to the results presented in the previous subsections, a training dataset length of 182 days is suggested to achieve high accuracy for both the digital twin parametrization and now-casting. To validate this suggestion, a 182-day training dataset was selected for each of the 16 monitored PV systems for the year 2020. Similar to the experiment described in the previous subsections, a random day from each week of the year 2020 was selected (52 days in total) to create a digital twin for each PV system on each selected day.

Figure 6 shows the PV power now-casting results for all 16 real PV systems. As observed, the mean deviation of all 16 real PV systems, in W/kW_p installed, indicates an under-casting, -1.14, which is influenced by high-deviation peaks in winter, particularly for System ID15. Additionally, the figure shows that the MAD for all 16 real PV systems is merely 1.81%, indicating a good benchmark for short-term PV power forecasting.

In general terms, the now-casting accuracy of all the digital twins created throughout the year 2020 for all 16 real PV suggests that their performance is time-independent, indicating that they can be implemented at any time of the year. However, there are some exceptions in winter which will be clarified in the following subsection.

4.3.1 Additional losses' information and further improvement

In the interest of accurately parametrizing PV systems based solely on on-site measured data, this publication aimed to achieve its overall goal without relying on external data sources. However, to explore the potential for improving accuracy, additional information from local weather stations was utilized. Figure 6 shows higher deviations between the digital twin-simulated PV power and the measured PV power for most of the 16 real PV systems during the first 5 weeks and the last 5 weeks of the year 2020. Considering this, in this subsection, we took into account the locally measured snow depth information from the CDC Deutscher Wetterdienst for all 16 real PV systems' locations during the year 2020.

High peaks in the winter of subplot a) from Figure 7 show a good agreement with the high-deviation peaks of the digital twin now-casting presented in Figure 6. To get a correlation between the now-casting high deviation in winter and the snow depth information, we calculated a simple linear regression between snow deposition and deviation in W/kW_p of each one of the 16 real PV systems.

Next, we use that linear regression to correct the power forecasted based on the snow information available by location. In Figure 7, it can be observed that the high deviations in winter have been reduced by approximately 75% for some specific cases (see

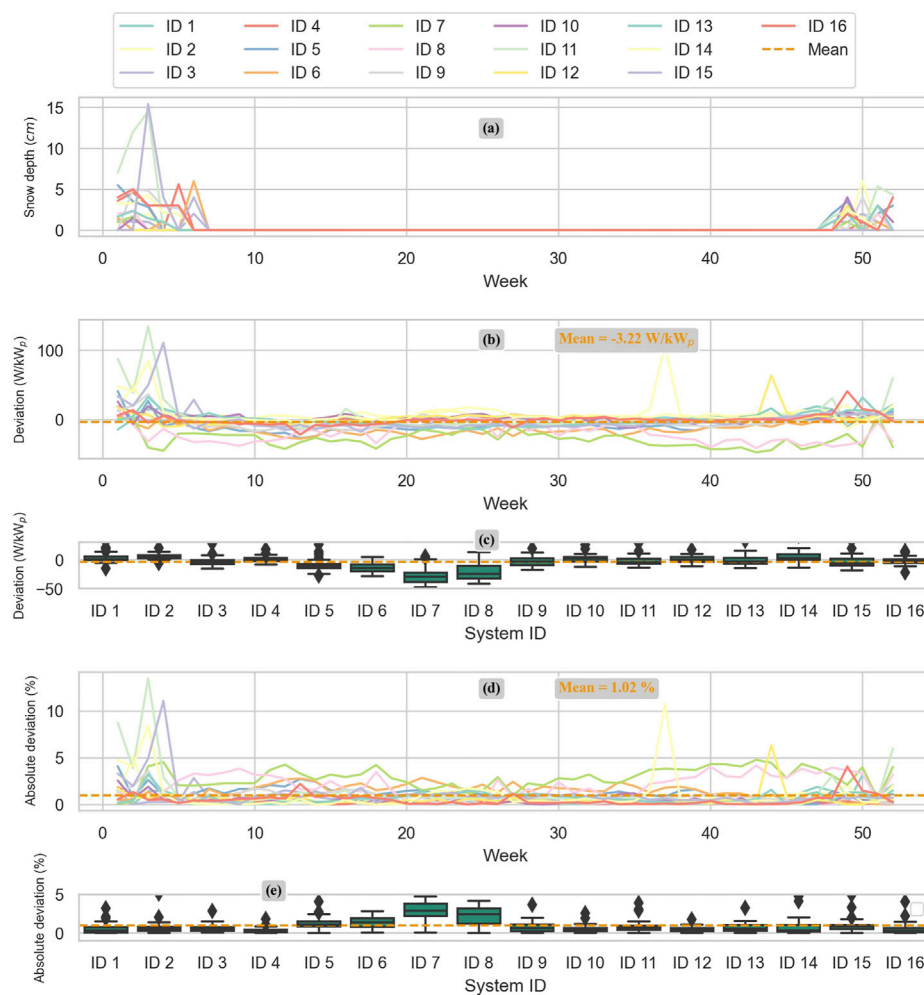


FIGURE 7

Snow deposition information for all 16 real PV systems. Deviation and absolute deviation of 52 days for now-casting for all 16 real PV systems, considering snow deposition. Subplot (A) shows the snow depth in centimeters (cm) for all the locations of the real PV systems. Subplots (B) and (C) show the now-casting deviation (in W/kW_p) after the snow information has been considered, and the correction has been performed for each of the 16 real PV systems. Subplots (D) and (E) show the absolute deviation (in %) of now-casting for all 16 PV systems after the correction for snow deposition has been implemented.

System ID 15). In general, the now-casting mean deviation of all 16 PV systems is -3.22 W/kW_p installed, underperforming constantly more evident for some specific PV systems such as PV system ID 6, ID7, and ID8. An absolute deviation of 1.02% can be observed, improving the overall accuracy by 0.79% or 44% relative to the previous calculation by only including snow deposition information for all 16 locations.

The results presented in this work suggested that PV systems with pyranometers as irradiance sensors presented lower deviation than those with reference cells installed as irradiance sensors. As suggested by Rivera and Reise, to further improve the now-casting accuracy and to reduce deviations, corrections can be applied to the values measured by reference cell sensors (Rivera Aguilar and Reise, 2020).

Moreover, additional loss factors that directly impact the power production of a PV system, such as degradation, power clipping, and soiling, could be possibly captured by some of the parameters of the GA optimization, i.e., nominal power and the DC-to-AC ratio.

Further investigation is required to confirm these assumptions and improve the model accordingly.

4.4 Limitations

We acknowledge that the GA optimization method presented here has some limitations. In addition to the loss factors mentioned in the aforementioned subsections (degradation, power clipping, and soiling), it is also important to mention that some shading effects, such as inter-row, can directly impact the optimization results. Furthermore, measuring G in a different POA will lead to biased PV power simulation, which ultimately will lead to incorrect parametrization. Additional filters and flags have to be implemented within the database to ensure that the on-site measured data are valid. Additionally, special PV system configurations, such as single- and double-axis tracked systems and bi-facial systems, require modifications to the PV power simulation model and optimization logic.

5 Conclusion

Although solutions such as GA optimization have been available over an extended period, this work proposes a novel and accurate implementation method for extracting parameters of PV systems or subsystems without prior technical information. The parameters extracted describe the main characteristics of a PV system or subsystem, which later can be translated to a digital twin. The basic parameters of a PV system or subsystem digital twin are defined based on only the on-site measured data in this work.

Based on the experiments presented here, the best condition–training length combination for the GA optimization is defined as all-sky conditions and 182 days long, with only on-site measured data. With the method proposed in this work, a digital twin is created to now-cast with an accuracy of only 0.91% MAPE and 3.27 W/kW_p MBE for PV power now-casting.

Furthermore, a validation process is presented, demonstrating the potential of parameterizing a digital twin for each PV plant within a portfolio. A season-independent digital twin is parameterized, and each of the 16 real PV plants distributed in Germany is now-casted with a mean deviation value of -1.14 W/kW_p and an MAD of only 1.81%. The model presented here can be further improved to achieve an MAD of only 1.02%, if external locally measured information is considered, i.e., snow precipitation.

Data availability statement

The raw data supporting the conclusion of this article will be made available by the authors, without undue reservation.

References

- Almeida, M. P., Perpiñán, O., and Narvarte, L. (2015). PV power forecast using a nonparametric PV model. *Sol. Energy* 115, 354–368. doi:10.1016/j.solener.2015.03.006
- Ding, M., Wang, L., and Bi, R. (2011). An ANN-based approach for forecasting the power output of photovoltaic system. *Procedia Environ. Sci.* 11, 1308–1315. doi:10.1016/j.proenv.2011.12.196
- Dirnberger, D., Müller, B., and Reise, C. (2015). PV module energy rating: Opportunities and limitations. *Prog. Photovolt. Res. Appl.* 23, 1754–1770. doi:10.1002/pip.2618
- González Ordiano, J. Á., Wacziarg, S., Reischl, M., Mikut, R., and Hagenmeyer, V. (2017). Photovoltaic power forecasting using simple data-driven models without weather data. *Comput. Sci. Res. Dev.* 32, 237–246. doi:10.1007/s00450-016-0316-5
- Guzman Razo, D. E., Müller, B., Madsen, H., and Wittwer, C. (2020). A genetic algorithm approach as a self-learning and optimization tool for PV power simulation and digital twinning. *Energies* 13, 6712. doi:10.3390/en13246712
- Heydenreich, W., Müller, B., and Reise, C. (2008). “Describing the world with three parameters: A new approach to PV module power modelling,” in 23rd European Photovoltaic Solar Energy Conference and Exhibition, Valencia, Spain, 1–5 September 2008, 2786–2789.
- Holland, J. H. (1975). *Adaptation in natural and artificial systems: An introductory analysis with applications to biology, control, and artificial intelligence*. Ann Arbor, Michigan: Mich. University of Michigan Press.
- Holmgren, W., Calama-ConsultingLorenzo, T., Hansen, C., Mikofski, M., Krien, U., et al. (2020). *pvlb/pvlb-python: v0.7.1*. Zenodo.
- Ibrahim, I. A., Mohamed, A., and Khatib, T. (2015). “Modeling of photovoltaic array using random forests technique,” in IEEE Conference on Energy Conversion, Johor Bahru, Malaysia, 19–20 October 2015, 390–393. ed. I. C. o. E. Conversion ([Piscataway, NJ]: IEEE).
- IEC (2009). *International Standard 61850 - communication networks and systems for power utility automation - Part 7-420: Basic communication structure - distributed energy resources logical nodes*. Geneva, Switzerland: Genève: Commission électrotechnique internationale. IEC IEC 61850-7-420 Accessed 2022.
- International Energy Agency (2022). *Renewables 2022: Analysis and forecast to 2025*. Paris, France: IEA.
- IRENA (2021). *Renewable power generation costs in 2021*. Abu Dhabi: IRENA.
- Jordan, D. C., Kurtz, S. R., VanSant, K., and Newmiller, J. (2016). Compendium of photovoltaic degradation rates. *Prog. Photovolt. Res. Appl.* 24, 978–989. doi:10.1002/pip.2744
- Kaspar, F., Müller-Westermeier, G., Penda, E., Mächel, H., Zimmermann, K., Kaiser-Weiss, A., et al. (2013). Monitoring of climate change in Germany – data, products and services of Germany’s National Climate Data Centre. *Adv. Sci. Res.* 10, 99–106. doi:10.5194/asr-10-99-2013
- Landelius, T., Andersson, S., and Abrahamsson, R. (2019). Modelling and forecasting PV production in the absence of behind-the-meter measurements. *Prog. Photovolt. Res. Appl.* 27, 990–998. doi:10.1002/pip.3117
- Mandal, P., Madhira, S. T. S., haque, A. U., Meng, J., and Pineda, R. L. (2012). Forecasting power output of solar photovoltaic system using wavelet transform and artificial intelligence techniques. *Procedia Comput. Sci.* 12, 332–337. doi:10.1016/j.procs.2012.09.080
- Monteiro, C., Fernandez-Jimenez, L. A., Ramirez-Rosado, I. J., Muñoz-Jimenez, A., and Lara-Santillan, P. M. (2013). Short-term forecasting models for photovoltaic plants: Analytical versus soft-computing techniques. *Math. Problems Eng.* 2013, 1–9. doi:10.1155/2013/767284
- Mori, N., and Kita, H. (2000). “Genetic algorithms for adaptation to dynamic environments - a survey,” in IECON 2000: 26th annual conference of the IEEE Industrial Electronics Society (IEEE), Nagoya, Japan, 22–28 October 2000, 2947–2952.
- Müller, B., Hardt, L., Armbruster, A., Kiefer, K., and Reise, C. (2016). Yield predictions for photovoltaic power plants: Empirical validation, recent advances and remaining uncertainties. *Prog. Photovolt. Res. Appl.* 24, 570–583. doi:10.1002/pip.2616
- Müller, B., Reise, C., Heydenreich, W., and Kiefer, K. (2007). *Are yield certificates reliable? A comparison to monitored real world results*. Washington, United States: Health IT. Unpublished.

Author contributions

DG and HM contributed to conceptualization, data processing, simulations, and analyses; CW discussed the results and improved the overall results of this publication. All authors contributed to the article and approved the submitted version.

Funding

The authors acknowledge the financial support from the Federal Ministry for Economic Affairs and Energy of Germany (BMWi) in the project ALPRO (project number 0324054A).

Conflict of interest

The authors declare that the research was conducted in the absence of any commercial or financial relationships that could be construed as a potential conflict of interest.

Publisher’s note

All claims expressed in this article are solely those of the authors and do not necessarily represent those of their affiliated organizations, or those of the publisher, the editors, and the reviewers. Any product that may be evaluated in this article, or claim that may be made by its manufacturer, is not guaranteed or endorsed by the publisher.

- Ogliari, E., Dolara, A., Manzolini, G., and Leva, S. (2017). Physical and hybrid methods comparison for the day ahead PV output power forecast. *Renew. Energy* 113, 11–21. doi:10.1016/j.renene.2017.05.063
- Reno, M. J., and Hansen, C. W. (2016). Identification of periods of clear sky irradiance in time series of GHI measurements. *Renew. Energy* 90, 520–531. doi:10.1016/j.renene.2015.12.031
- Rivera Aguilar, M. J., and Reise, C. (2020). “Silicon sensors vs. Pyranometers – review of deviations and conversion of measured values,” in 37th European Photovoltaic Solar Energy Conference and Exhibition, Marseille, France, September 2020, 1449–1454.
- Schmidt, H., and Sauer, D. (1994). Wechselrichter-Wirkungsgrade - praxisgerechte Modellierung und Abschätzung. *Sonnenenergie* 1996.
- SolarPower Europe (2022). *Global market outlook for solar power 2022-2026*. Bruxelles, Belgium: SolarPower Europe.
- Stein, J. S., Hansen, C. W., and Reno, M. J. (2012). *Global horizontal irradiance clear sky models: Implementation and analysis*. OSTI.
- Urraca, R., Huld, T., Lindfors, A. V., Riihelä, A., Martinez-de-Pison, F. J., and Sanz-Garcia, A. (2018a). Quantifying the amplified bias of PV system simulations due to uncertainties in solar radiation estimates. *Sol. Energy* 176, 663–677. doi:10.1016/j.solener.2018.10.065
- Urraca, R., Huld, T., Martinez-de-Pison, F. J., and Sanz-Garcia, A. (2018b). Sources of uncertainty in annual global horizontal irradiance data. *Sol. Energy* 170, 873–884. doi:10.1016/j.solener.2018.06.005

Frontiers in Energy Research

Advances and innovation in sustainable, reliable and affordable energy

Explores sustainable and environmental developments in energy. It focuses on technological advances supporting Sustainable Development Goal 7: access to affordable, reliable, sustainable and modern energy for all.

Discover the latest Research Topics

[See more →](#)

Frontiers

Avenue du Tribunal-Fédéral 34
1005 Lausanne, Switzerland
frontiersin.org

Contact us

+41 (0)21 510 17 00
frontiersin.org/about/contact



Frontiers in Energy Research

